Precise Scatterer Localization for Ultrasound Contrast Imaging

Konstantinos Diamantis

Submitted for the degree of Doctor of Philosophy

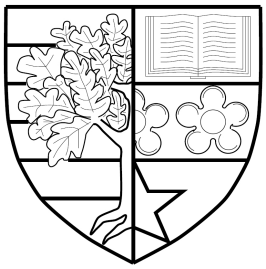

Heriot-Watt University

School of Engineering and Physical Sciences

March 2017

Abstract

This thesis is concerned with developing algorithms for the precise localization of ultrasound point scatterers with an eye to super-resolution ultrasound contrast imaging. In medical ultrasound, the conventional resolution is limited by diffraction and, in contrast to other sensing fields, point source imaging has not been extensively investigated. Here, two independent methods were proposed aiming to increase the lateral and the axial resolution respectively, by improving the localization accuracy of a single scatterer. The methods were examined with simulated and experimental data by using standard transmission protocols. Where a technique is applicable to imaging of more complicated structures than point sources, this was also examined. Further, a preliminary study was included with algorithm application to microbubbles that are currently used in contrast enhanced ultrasound. It was demonstrated that it is feasible to translate to ultrasonics, adaptive processes or techniques from optical imaging/astronomy. This way, it was possible to overcome the diffraction limit and achieve sub-wavelength localization. The accuracy gains are subject to many parameters but may reach up to two orders of magnitude, and are based exclusively on array signal processing. The latter is an important advantage since current attempts for super-resolution ultrasound are image-based which is generally undesired.

Acknowledgements

Many people have contributed to the completion of this, very ambitious when it started, interdisciplinary and interuniversity project.

First of all I would like to express my gratitude to my supervisor, Dr. Vassilis Sboros, for his continous guidance and encouragement during the past 4 years. Without his support it wouldn't have been possible to finish this thesis. I am also thankful to Prof. Alan Greenaway and Dr. Paul Dalgarno who introduced me to an unknown for me field and gave a direction to my research.

Many thanks to Mr. Tom Anderson for his valuable advice all this period, his inputs during our joint meetings and for proofreading the thesis. Next I would like to thank Dr. Mairead Butler for welcoming me when I first joined Heriot-Watt University and for her help whenever I needed it. I am also very obliged to Prof. Jørgen Arendt Jensen and would like to thank him and his group members, for accepting me in their lab in the Technical University of Denmark, where I spent almost a quarter of my PhD time, conducting all the necessary experimental work.

Finally, last but certainly not least I want to thank Maria for being so supportive and always there for me, particularly during the very difficult for me, final year of my studies.

ACADEMIC REGISTRY
Research Thesis Submission

Name*:*	Konstantinos Diamantis		
School/PGI:	School of Engineering and Physical Sciences EPS/IB3		
Version: *(i.e. First, Resubmission, Final)*	Final	Degree Sought (Award **and** Subject area)	PhD Physics

Declaration

In accordance with the appropriate regulations I hereby submit my thesis and I declare that:

1) the thesis embodies the results of my own work and has been composed by myself
2) where appropriate, I have made acknowledgement of the work of others and have made reference to work carried out in collaboration with other persons
3) the thesis is the correct version of the thesis for submission and is the same version as any electronic versions submitted*.
4) my thesis for the award referred to, deposited in the Heriot-Watt University Library, should be made available for loan or photocopying and be available via the Institutional Repository, subject to such conditions as the Librarian may require
5) I understand that as a student of the University I am required to abide by the Regulations of the University and to conform to its discipline.

* *Please note that it is the responsibility of the candidate to ensure that the correct version of the thesis is submitted.*

Signature of Candidate*:*		Date:	

Submission

Submitted By *(name in capitals):*	KONSTANTINOS DIAMANTIS
Signature of Individual Submitting:	
Date Submitted:	

For Completion in the Student Service Centre (SSC)

Received in the SSC by *(name in capitals):*			
Method of Submission *(Handed in to SSC; posted through internal/external mail):*			
*E-thesis Submitted (**mandatory for final theses)***			
Signature:		Date:	

Please note this form should bound into the submitted thesis.

Updated February 2008, November 2008, February 2009, January 2011

Contents

List of Tables

List of Figures

Glossary

CEUS Contrast Enhanced Ultrasound.

CFU Center for Fast Ultrasound imaging.

COM Centre of Mass.

CT Computed Tomography.

DAS Delay-and-Sum.

DFT Discrete Fourier Transform.

DRF Dynamic Receive Focusing.

ESPRIT Estimation of Signal Parameters by Rotational Invariance Techniques.

ESRIC Edinburgh Super-resolution Imaging Consortium.

FB Forward-Backward.

FFT Fast Fourier Transform.

FLOP Floating-Point OPeration.

FLOPS Floating-Point Operations Per Second.

FPGA Field-Programmable Gate Array.

FWHM Full-Width-at-Half-Maximum.

GPU Graphics Processing Unit.

MB Microbubble.

MCAO Multi-Conjugate Adaptive Optics.

MI Mechanical Index.

MIMO Multiple Input Multiple Output.

MLE Maximum-Likelihood Estimation.

MRI Magnetic Resonance Imaging.

MUSIC Multiple Signal Classification.

MUSLI Microbubble Ultrasound Super-Localization Imaging.

MV Minimum Variance.

MVS Minimum Variance Subband.

MVT Minimum Variance Temporal.

NACF Normalized Auto-Covariance Function.

PALM Photoactivated Localization Microscopy.

PDF Probability Density Function.

PET Positron Emission Tomography.

PMT Photo-Multiplier Tube.

PNP Peak Negative Pressure.

PSF Point Spread Function.

PSL Peak-Sidelobe-Level.

PW Plane Wave.

QDG Quadratically Distorted Grating.

RF Radio Frequency.

RMSE Root Mean Square Error.

ROI Region of Interest.

SAR Synthetic Aperture Radar.

SARUS Synthetic Aperture Real-time Ultrasound Scanner.

SAU Synthetic Aperture Ultrasound.

SD Standard Deviation.

SLM Spatial Light Modulator.

SMLM Single Molecule Localization Microscopy.

SNR Signal to Noise Ratio.

SPL Spatial Pulse Length.

STFT Short Time Fourier Transform.

STORM Stochastic Optical Reconstruction Microscopy.

TRM Time Reversal Mirror.

UCA Ultrasound Contrast Agent.

uULM Ultrafast Ultrasound Localization Microscopy.

WGN White Gaussian Noise.

List of Publications

The following publications contain research work included in this thesis:

Papers

[1] K. Diamantis, I. H. Voxen, A. H. Greenaway, T. Anderson, J. A. Jensen, and V. Sboros. A comparison between temporal and subband minimum variance adaptive beamforming. In *Proc. SPIE Med. Imag.,* volume 90400L, [Online] Available:10.1117/12.2043602, March 2014.

[2] K. Diamantis, I. H. Voxen, A. H. Greenaway, T. Anderson, J. A. Jensen, and V. Sboros. A phantom study on temporal and subband minimum variance adaptive beamforming. In *Proc. IEEE Int. Ultrason. Symp. (IUS),* pages 1072-1075, November 2014.

[3] K. Diamantis, P. A. Dalgarno, A. H. Greenaway, T. Anderson, J. A. Jensen, and V. Sboros. High resolution depth-resolved imaging from multi-focal images for medical ultrasound. In Proc. *IEEE Eng. in Med. and Biol. Soc. (EMBC),* pages 7067-7070, November 2015.

[4] K. Diamantis, P. A. Dalgarno, A. H. Greenaway, T. Anderson, J. A. Jensen, and V. Sboros. A novel array processing method for precise depth detection of ultrasound point scatter. In Proc. *IEEE Int. Conf. Acous., Speech, Sig. Pro. (ICASSP),* pages 669-673, June 2016.

[5] K. Diamantis, M. A. Dhali, G. Gibson, Y. Yan, J. R. Hopgood, and V. Sboros. Super-resolution spectral analysis for ultrasound scatter characterization. In Proc. *IEEE Int. Conf. Acous., Speech, Sig. Pro. (ICASSP),* pages 903-907, June 2016.

[6] K. B. Hansen, C. A. Villagomez-Hoyos, J. C. Bransen, K. Diamantis, V. Sboros, C. M. Sorensen, and J. A. Jensen. Robust microbubble tracking for super resolution imaging in ultrasound. In *Proc. IEEE Int. Ultrason. Symp. (IUS),* pages 1-4, September 2016.

[7] K. Diamantis, P. A. Dalgarno, A. H. Greenaway, T. Anderson, J. A. Jensen, and V. Sboros. Super-resolution axial localization of ultrasound point sources using multi-focal imaging. [Submitted to *IEEE Transactions on Biomedical Engineering*].

[8] K. Diamantis, A. H. Greenaway, T. Anderson, J. A. Jensen, and V. Sboros. Experimental performance of the sub-band Minimum Variance beamformer for ultrasound imaging. [Submitted to *Ultrasonics*].

Patents

V. Sboros, P. A. Dalgarno, K. Diamantis and A. H. Greenaway, 2017. A method of, and apparatus for, determination of position in ultrasound imaging. WO Patent 2017013443 A1.

In preparation

[1] K. Diamantis, A. H. Greenaway, T. Anderson, J. A. Jensen, and V. Sboros. Super-resolution lateral localization of ultrasound point sources using adaptive beamforming.

[2] K. Diamantis, P. A. Dalgarno, A. H. Greenaway, T. Anderson, J. A. Jensen, and V. Sboros. A parametric study on the normalized sharpness method for micrometric depth resolution in ultrasound imaging.

Chapter 1

Introduction

Ultrasound imaging is one of the most important diagnostic imaging modalities representing around 20% of all imaging examinations. Contrast Enhanced Ultrasound (CEUS) is the utilization of contrast media such as gas-filled Microbubbles (MBs), in the conventional ultrasound imaging. Medical ultrasound traditionally has dealt with imaging the structure of human anatomy. The exploitation of the MB scatter is a topic that focuses in mapping the vascular bed. Over the last 25 years it has attracted significant research interest. However in CEUS, the limited understanding of acoustic echo signals from contrast MBs hinders the improvement of the sensitivity and specificity of diagnostic imaging. This thesis proposes methods to achieve ultrasound point source super-resolution by combining the use of Ultrasound Contrast Agents (UCAs) together with techniques that have already been successfully applied to other fields of sensing. The long term goal is to generate an imaging mode that uses enhanced microbubble detection to provide superior diagnostic information to state of the art ultrasound imaging.

1.1 Ultrasound imaging

Sonography is a fast, inexpensive and harmless medical imaging technique that is nowadays widely used for diagnostic purposes. The basic principles, the artefacts and the ability of an ultrasound system to distinguish between two points are briefly described in the present section.

1.1.1 Basic principles

Ultrasound imaging is mainly based on reflections that take place when ultrasound hits the boundary between two media (organs) with a different acoustic impedance. The latter is a property of each medium indicating how promptly the medium particles move, when exposed to an acoustic wave. The impedance (Z) is given by $Z = \rho_0 c$, where ρ_0 is the mean density of the medium and c is the speed of the acoustic wave as it travels through the medium. Therefore any change in density or

compressibility results in reflection between surfaces with greater dimensions than the ultrasound wavelength, or scattering when smaller structures are concerned [1,2]. A beam of high frequency ($1 - 20$ MHz) ultrasound pulses, above the upper limit of human hearing (20 kHz) is transmitted by a transducer into the body, and the reflected echoes are collected again by the same transducer that also acts as a receiver. Those returning echoes are subsequently combined to form images from which it is possible to extract characteristics like the size and the nature of the tissue structures.

1.1.2 Artefacts

Compared to other imaging modalities such as Positron Emission Tomography (PET), Computed Tomography (CT) or Magnetic Resonance Imaging (MRI), ultrasound presents lower image quality due to certain assumptions that are made during the ultrasound propagation in the tissue [1, 3]. First the speed of sound is assumed constant and the variations through the body internal organs are ignored during the echoes processing. Second, the attenuation of the reflected echoes [4], which is responsible for the weaker appearance of targets located at greater depths, is also considered constant. Finally, the beam axis is assumed to be straight and the pulse is thought to propagate until it reaches the targets that are only on the beam axis before returning back to the transducer. However this is not the case, since an angle of the incident beam at the boundary or the lack of surface smoothness will significantly affect the backscattered echoes. It is easily understood that any divergence from the above ideal conditions, combined with the patient motion during a scan, is very likely to produce visible image artefacts.

1.1.3 Spatial resolution

Medical ultrasound has only achieved spatial (lateral and axial) resolution within the limitations of the beam diffraction (Figure 1.1), and the duration of the transmitted pulses [5, 6].

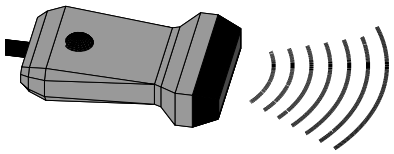

Figure 1.1: The diffraction pattern for a small linear transducer resulting from the interference of emitted wavefronts.

The lateral resolution is commonly defined as the smallest possible distance between two identical point sources, located at the same depth, that permits the display of both points as two distinct images. This distance is, at best, equal to half

the beam width but in practice it may take higher values [7]. To improve the lateral resolution, transmit focusing has been introduced, which reduces significantly the beam width at a selected depth (or multiple depths using multiple transmissions). Overall, the parameters that determine the width of a focused beam W, are summarized in:

$$W \approx \frac{F_l \times \lambda}{A}\,, \tag{1.1}$$

where F_l is the focal depth, λ is the wavelength and A is the aperture size. The wavelength is given by: $\lambda = c/f_0$, where f_0 is the transducer centre frequency. As a result with the use of transmit focusing, the beam of Figure 1.1 can be shaped differently as shown in Figure 1.2. Figure 1.2 indicates the higher lateral resolution around the focal depth, that deteriorates when moving away from it.

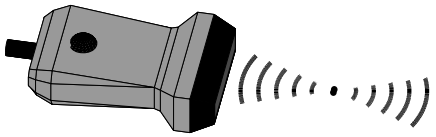

Figure 1.2: The effect of transmit focusing to the ultrasound beam for a small linear transducer.

Similar to the lateral, the axial resolution is defined as the smallest possible distance between two point sources, located on the beam axis, that enables the display of both point as two separate images. This distance is approximately equal to half the Spatial Pulse Length (SPL) [1]. The latter is defined as: SPL $= n_{osc} \times \lambda$ where n_{osc} is the number of oscillations in a pulse of ultrasound. Usually most pulses consist of $n_{osc} = 2$ cycles, resulting in an axial resolution similar to the wavelength.

Thus, ultrasound point sources can be detected, as in other wavefront sensing fields, but they will be displayed with the size of the Point Spread Function (PSF). This is the response of the ultrasound system to a point source and is comparable to the wavelength used as shown above. Higher spatial resolution can be obtained with the generation of narrow beams by using shorter pulses, transducers with higher central frequency and shorter focal depths. However, the attenuation also increases with frequency ($\approx$ 0.5 dB/MHz$\times$cm for soft tissue), decreasing the penetration depth and therefore not allowing unbounded high frequency values to be used [1, 8]. As a consequence, in order to achieve a depth of field of several centimetres, transmission frequencies are limited to a few MHz which limits the resolution to the millimetre range [8]. On the other hand, ultrasound transmission of a couple of hundreds of MHz would provide micrometric resolution but limit penetration depth to less than 1 mm [9, 10].

Should the ultrasound spatial resolution be increased beyond the conventional values, the above compromise of penetration depth versus resolution may be overcome. This has the potential to expand the application range of ultrasound imaging to a number of pathological conditions that involve alteration of the microvascular bed [11–15].

1.2 Contrast enhanced ultrasound

Over the past 25 years UCAs have been employed with the objective to increase the sensitivity of the imaging by imposing alterations in the image contrast between different structures [16, 17]. The use of MBs as UCAs was accidentally discovered in the 1960′s by a cardiologist, but it was not until the early nineties, with the introduction of stabilized biocompatible MBs, that CEUS began to be used more extensively in a number of research applications [18–20].

1.2.1 Contrast microbubbles

The MBs are microspheres with a typical diameter between 1 μm and 10 μm. They consist of a thick outer shell enclosing an interior gas. They are designed with the ability to pass through capillaries, enabling intravenous injection [21, 22]. The outer part provides durability and prevents from gas diffusion and thus disintegration of the bubbles into the blood. Transmission of ultrasound will initiate MB oscillation under the acoustic field, which leads to an observed high scattering strength (Figure 1.3).

At very low acoustic power which is usually expressed as low Mechanical Index (MI) ($< 0.05 - 0.1$), the bubbles oscillate almost symmetrically and the incident ultrasound pulse induces a linear vibration response. As the acoustic power increases the MBs begin to compress and expand in a highly non-linear manner as shown in Figure 1.3. Mechanical index values between $0.1 - 0.3$ result in non-symmetrical and non-spherical oscillations that produce a number of harmonic frequencies [19, 23, 24]. At high acoustic pressures (MI $> 0.3 - 0.6$) the MBs are destroyed.

In Figure 1.4 a measured non-linear microbubble response is shown together with its Fast Fourier Transform (FFT) from which it is possible to notice the fundamental and the harmonic spectral content [25–29]. A 6-cycle pulse was used and the MB (BiSphere, Point Biomedical, CA, USA) was insonated at 1.6 MHz for acoustic pressures in a range between 300 kPa and 1000 kPa using a Sonos5500 (Philips Medical Systems, Andover, MA, USA) research ultrasound scanner [30, 31].

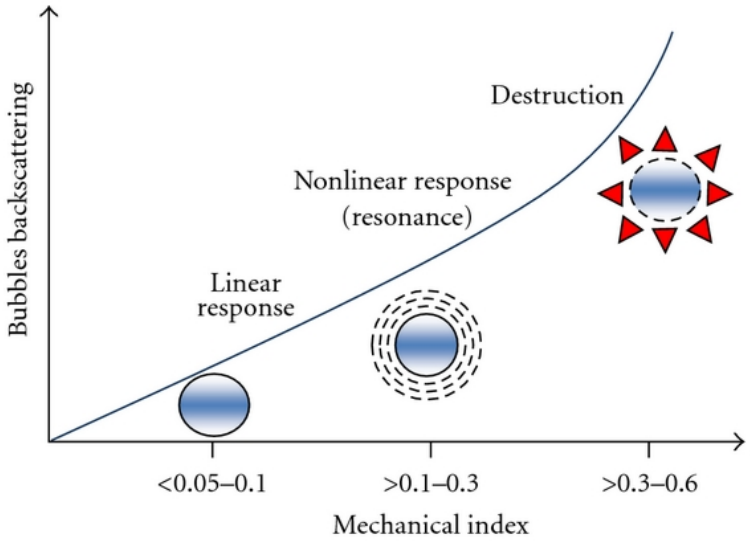

Figure 1.3: The MB behavior is depicted in respect to MI changes. The figure has been adapted from [23]. The linear MB response stage is followed by a non-linear one, as the MI increases. High MI values are causing the MB destruction with high intensity backscatter response.

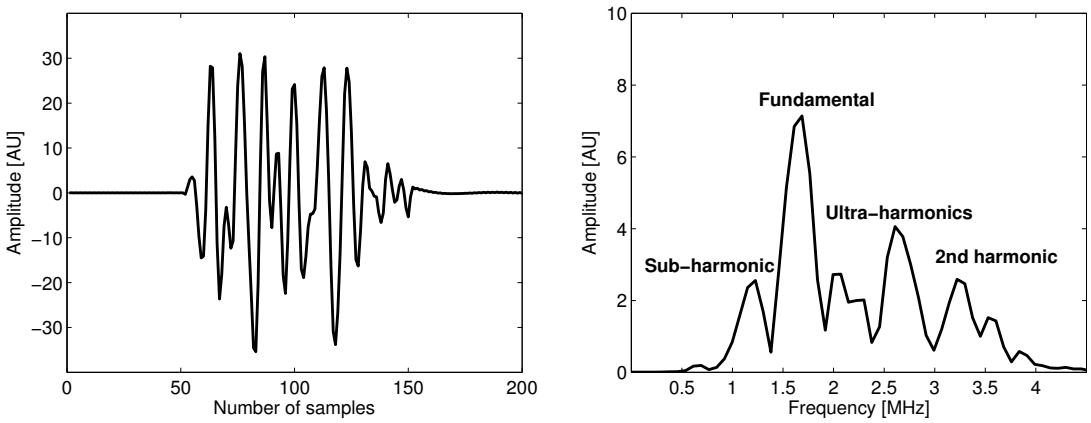

(a) MB response

(b) MB frequency spectrum

Figure 1.4: Single microbubble response and its frequency spectrum. The echo signal was acquired by a modified ultrasound transducer. The spectrum shows a fundamental frequency at 1.62 MHz which coincides with the trasmit frequency but also includes lower frequency components (sub-harmonics), randomly distributed higher components (ultra-harmonics) and an integer multiple of the fundamental frequency (2^{nd} harmonic).

1.2.2 Contrast enhancement example

The image enhancement stems from the intermediate stage of microbubble oscillation, explained in the previous subsection. For instance, the summation of non-linear responses from successive, equal in amplitude but opposite in phase, ultrasound pulses will cancel all linear content and only the area including the microbubbles

will remain, minimizing all other ultrasound echoes [32–36]. An example of the contrast improvement obtained due to the MB use is given in Figure 1.5 where the the additional information provided by the CEUS image assists in the detection of a hepatocellular carcinoma of a patient with hepatitis B virus.

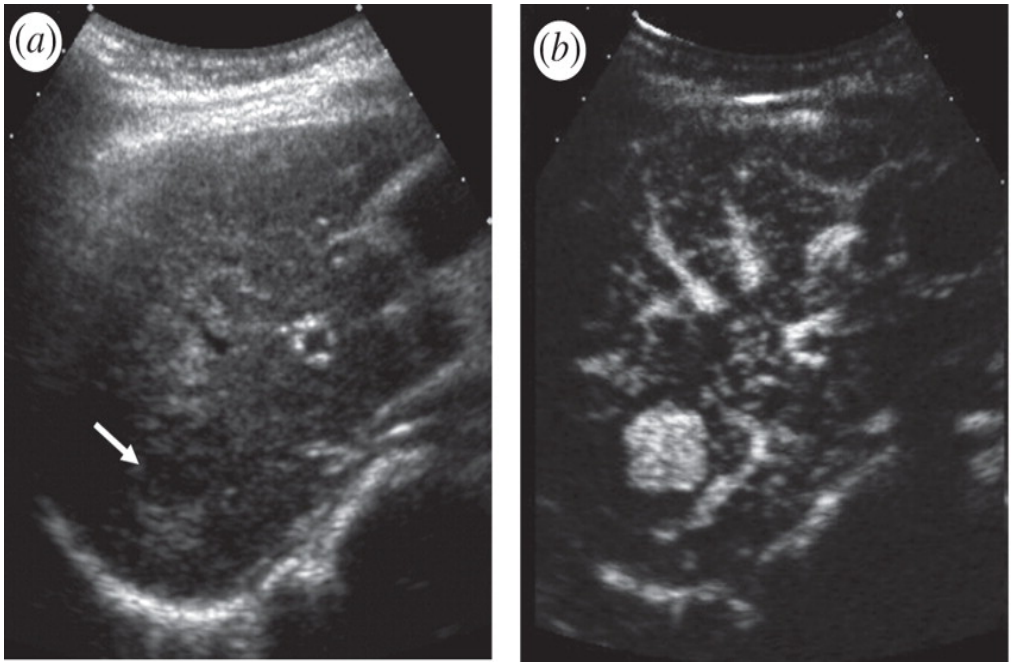

Figure 1.5: An example of improved visualization of a hepatocellular carcinoma, when using contrast imaging (b) compared to fundamental ultrasound imaging (a). From (a), a small hypoechoic mass (arrow) in the right lobe of a small cirrhotic liver is seen. Contrast imaging at the peak of arterial phase enhancement (b) reveals classic hypervascularity of the tumour. The figure has been adapted from [37].

Still, the exact microbubble behavior remains unknown and both simulation software [38,39] and theoretical models [40] have been developed in a research effort that aims to achieve the MB thorough characterization.

1.2.3 Single microbubble scatter

Some of the major limitations regarding the MB understanding namely concern the PSF variability, the 3D field variability in each pixel, and the interference pattern from microbubbles emerging from a disperse population (shell, size, etc.). The MBs are injected in high concentrations and are traditionally studied in multitudinous populations. In high concentrations, the interactions between neighboring microbubbles increase and this makes their study more difficult. Nevertheless, CEUS nowadays allows the visualization of MB signals in high sensitivity as they flow through the micro-circulations in the human body.

The signals are enhanced by signal processing techniques which mainly remove other tissue reflection and scatter and it is possible to distinguish the scattering

from single MBs and focus on their analysis [41–43]. Examination of isolated microbubbles indicates that they can be considered as efficient point scatterers [41]. This last observation makes appealing the exploration of imaging techniques ideally suited to single point sources that have not so far been applied to the field of CEUS or ultrasound in general. Such investigations may help create high precision MB localization algorithms and increase the ultrasound imaging resolution.

1.3 Motivation

Historically, ultrasound imaging has focused in imaging structures, rather than point sources. However, the combination of advanced imaging techniques with the use of contrast MBs provides a framework to explore ultrasound super-resolution. This study is motivated by the possibility that imaging methodologies able to provide resolution beyond the conventional limits in radar, astronomy or even those applied to microscopy can be applied to ultrasound. These methods are briefly discussed in this section and are followed by a short review of existing, but limited literature, available on super-resolution ultrasound imaging.

1.3.1 Advances in point-source imaging

Unlike ultrasound, point source super-resolution imaging is well-established in other fields of sensing [44,45] such as radar [46,47] or astronomy [48–51]. In radar imaging, the use of algorithms like Multiple Signal Classification (MUSIC) [52,53] or Estimation of Signal Parameters by Rotational Invariance Techniques (ESPRIT) [54,55] can provide super-resolution in the estimation of point scatterers centre position [56]. Those subspace eigenanalysis based methods or their modified versions assume a signal model based on prior data information. They then search for the signal components by solving polynomial equations or matrix eigenanalysis problems. In astronomy, the diffraction-limited resolution of a telescope used for an observation can be increased if point sources like stars are represented by Dirac δ-functions [57].

The diffraction limit has also been surpassed in numerous cases in optical microscopy [58–62] although the same fundamental physics apply both for optics [63–66] and ultrasonics [4, 67]. With the use of Single Molecule Localization Microscopy (SMLM) methods like Photoactivated Localization Microscopy (PALM) and Stochastic Optical Reconstruction Microscopy (STORM), localization of the PSF from temporally isolated particles that are spatially overlapping, can provide sub-50 nm lateral resolution [58–60]. Further, past work has extended the resolution gains to the depth dimension [68–71] where super-resolution is less established. The basis of the above methods is that the knowledge of the PSF, combined with the ability to spatially segregate adjacent emitters in time, can be used to localize particles with accuracy that overcomes the inherent diffraction limit.

1.3.2 Signal-based methods for aberration correction

So far several studies have been noted in the literature with the intention to apply to ultrasonics, imaging techniques previously used in any of the aforementioned fields [72–74]. In 1988 *Flax and O'Donnell* introduced the use of correlation approaches similar to those used in adaptive optics [49, 75, 76] and radar [77, 78] to measure phase aberrations. The method relied on simple geometric models and on cross-correlation of signals reflected from a point source to estimate precisely the arrival time differences across the transducer surface [74, 79].

In 1997 *Li* proposed an algorithm taking advantage of sensor signal redundancies to achieve phase aberration correction, as done earlier in astronomy [80, 81]. Those redundancies occur when two or more identical signals are acquired by different sensors [48, 82]. Such signals may exist in ultrasound imaging, although the different distance relations between the far-field (astronomy) and the near-field (ultrasonics) do not allow a direct translation of the method.

In 1992, *Fink et al.* introduced Time Reversal Mirrors (TRMs) in ultrasonics, which is an adaptive signal processing technique for focusing waves through inhomogeneous media. The received transducer element responses are re-emitted compensating for the aberration caused by the medium between the transducer face and the under study target, in order to obtain higher image quality [83–86].

1.3.3 Ultrasound super-resolution

Currently, the super-resolution research in ultrasound imaging is strongly related to the use of contrast agents and is based on the prior knowledge of such point scatterers. In 2009 *Fink et al.* proposed a method similar to reference beacons for adaptive focusing in astronomy with the use of a microbubble as a reference target (star in astronomy) and combined with the TRM method [87–89]. The MBs have their own particular acoustic response [27] which enables echo discrimination between them and blood or tissue. The received MB echoes from different positions have been time-reversed, amplified and re-transmitted to improve focusing in the area where the microbubbles are located. The treatment of metastasis or infiltrating tumors may benefit from such a technique which still lacks clinical application, since it is likely that the MBs, once inserted into the body, will gather in multiple metastasis.

O'Reilly and Hynynen managed to estimate MB position with super-resolution by applying three dimensional Gaussian fits to isolated microbubbles, to approximate their PSFs. This image-based method relied on the processing of the already reconstructed ultrasound data and resulted in high quality both $ex-$ and $in-$vivo images of the cerebral vasculature. The images were even comparable to ones obtained by micro-CT, demonstrating improved resolution by a factor of 3 [90–92].

The study was performed with the use of a highly diluted MB solution ($\approx 1/1000$ of the concentration normally used for diagnostic purposes) that was passing through a ≈ 250 μm tube and was scanned by a 128-element spherical transducer specifically designed for the brain. The basic concept was to maintain a low MB concentration that would enable the localization of the single MBs path as they flowed through the vessels thereby allowing the reconstruction of the cerebral vascular structure.

In a similar manner, *Viessmann et al.* suggested the deconvolution of single MB PSFs that were imaged by a clinical scanner providing a frame rate of 43 frames per second. From an approximately 30 minute acquisition, only a small percentage of the MBs were distinguished as single scattering events but this was adequate to resolve two closely spaced tubes [93]. Later as a continuation of this work, *Christensen-Jeffries et al.* achieved super-resolution imaging of the mouse ear microvasculature with 5-fold resolution gains and with the additional feature of a velocity map. This was achieved by estimating the PSF Centre of Mass (COM) from images including a number of well-separated bubbles [94]. These accomplishments show the potential of connecting well-developed advanced imaging techniques with the single MB study for ultrasound resolution beyond the diffraction limit.

However the above methods require long acquisitions that may reach up to several hours just to provide a single plane. This is because only a few MBs are distinguished in each frame. Further, they are image based and depend on thresholds or frame rejection [93, 94] while it is accepted that the Radio Frequency (RF) data have the potential for higher resolution. This is because part of the raw initial signal information is lost due to the logarithmic compression [1] that comes before the image display. A few attempts were reported to overcome the acquisition time limitations and so may be more likely to reach the clinical stage.

Couture et al. suggested the ultrasound equivalent of optical localization microscopy [95], Microbubble Ultrasound Super-Localization Imaging (MUSLI) which by high frame-rate ultrafast ultrasound imaging [96] can achieve individual MB lateral localization with up to $\lambda/38$, compensating at the same time for the previous long acquisition times. Similarly from the same group, *Desailly et al.* presented in 2013 the analog of fluorescence PALM (f-PALM) in ultrasound imaging [97], named Ultrafast Ultrasound Localization Microscopy (uULM) which achieved a smaller but also significant localization improvement with accuracy up to $\lambda/11$. Finally, they have conducted a theoretical study, that was also later confirmed experimentally, in order to estimate the maximum uULM resolution based on the acquisition setup and the standard error of their system in MB localization [98]. Their end result was that a localization precision of ≈ 10 μm can be obtained for 3 MHz ultrasound, which potentially could reveal details in the capillary level in the future.

Despite the achievements in MB localization, and the perspectives of super-resolution ultrasound in general, there is still distance between the experimental and

the clinical stage. Moreover, as explained in the Subsection 1.2.3, the understanding of MB behavior remains limited and the use of complex algorithms or imaging schemes, as the ones described above, that rely directly on contrast agents may not be the most efficient way to move the research forward and lead to actual technological advances. At the moment, there is a major gap in the literature surrounding the lack of fundamental studies of the point scatter. This lack is not allowing to specify with confidence:

- What can be achieved in terms of single scatterer localization?
- Whether or not image based methods rather than signal based are optimal for ultrasound imaging.
- What are the fundamental ultrasound related limitations?

To answer the above questions, any novel imaging technique whether it stems from another field or it has been proposed specifically for ultrasound, should be applied first to both simulated and experimental ultrasound data from linear scatterers and not straight into MBs that have additional layers of complexity (non-linear scatter, large dispersion of responses).

1.4 Objectives

This thesis aims to develop array or signal based imaging techniques that deploy raw ultrasound data processing to provide increased localization precision, that will subsequently lead to increased ultrasound spatial resolution. The work focuses mainly on point scatter investigations that will help create new imaging modes, outside the CEUS framework at an initial stage, with the microbubble imaging being the principle objective. Moreover, the outcomes of the present research will also be used, whenever applicable, to examine whether there are additional benefits in the imaging of more complicated structures than point targets. The algorithm development is accomplished either by modifying and improving already existing techniques, or by exploiting methods originating from other imaging fields with translational value in ultrasonics.

Utilizing, at a later stage, the resulting algorithms for the localization of contrast MBs may improve the image quality of ultrasound contrast imaging and may help extracting hidden MB characteristics. Since it has been proven that single microbubbles can be distinguished and since they are treated as small ultrasound point scatterers, it is expected that the proposed methods throughout the thesis will apply for the contrast agents as well.

1.5 Contributions

The key contributions are summarized in the current section. They can be divided into three main categories. Those categories namely are the signal processing part, the ultrasound point scatter localization and the microbubble imaging. A graphical representation of the objectives and all thesis contributions, as mentioned in this section, can be found in Figure 1.6.

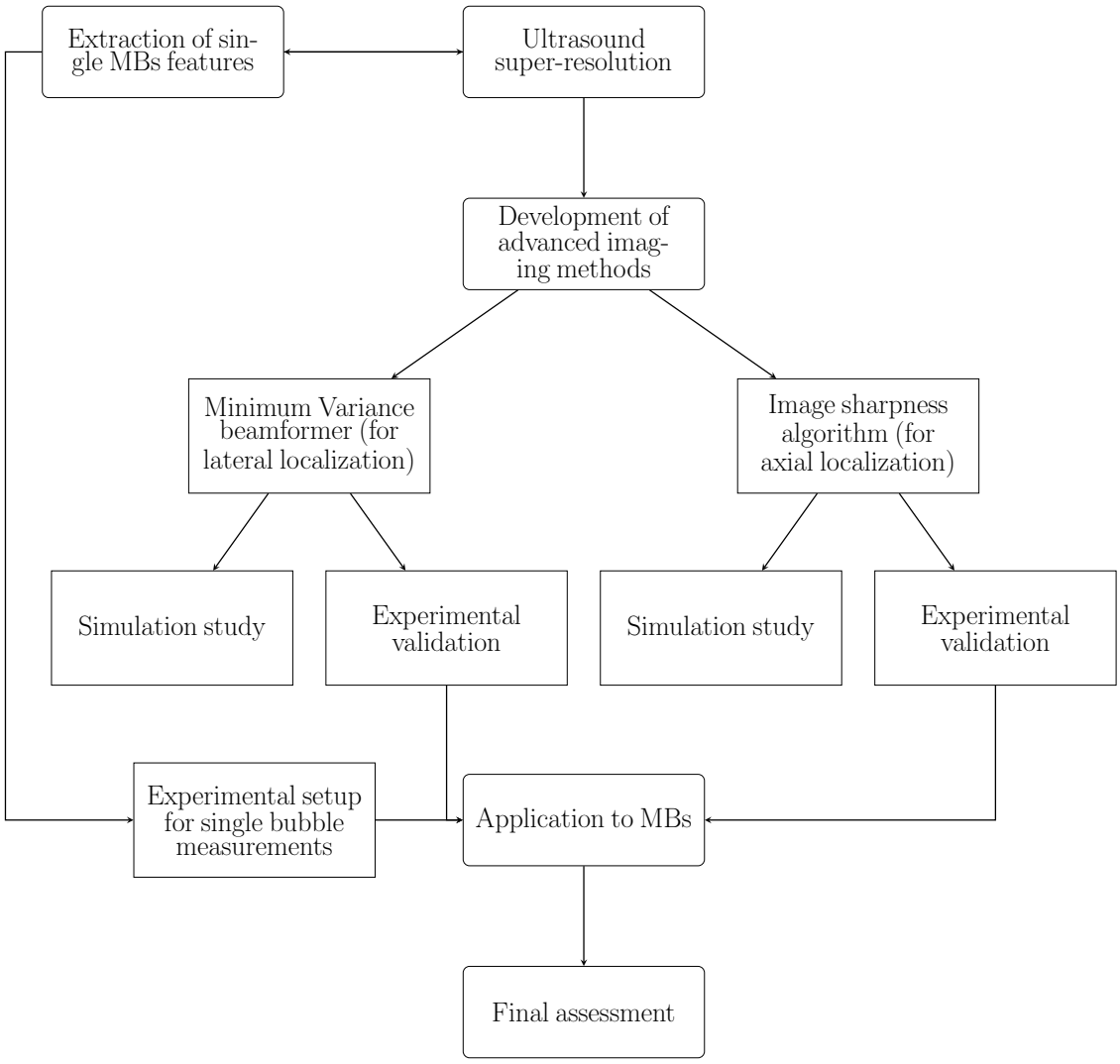

Figure 1.6: Schematic diagram of thesis objectives and contributions. The objectives are indicated by the rectangles with the rounded corners on the top of this flowchart. The remaining rectangles demonstrate the contributions and the structure in general, of the thesis.

The research related to ultrasound super-resolution is currently dominated by image processing techniques applied to images which typically contain only a small number of MBs. In this work, the signal processing methods used have either not been extensively evaluated elsewhere or are completely unknown to the field of ultrasound. Those methods were verified with simulated and experimental point scat-

terers instead of non-linear contrast MBs that cannot lead to immediate conclusions towards their efficiency.

1.5.1 Signal processing

Minimum Variance (MV) beamforming in ultrasound imaging was initially investigated. This adaptive approach has been used in ultrasound imaging over the past 10 years [99, 100] as it may provide lateral resolution improvements. However the method was intended for applications and signals of different nature [101] than the ultrasound ones, and its performance is greatly dependent on the data that are being acquired. Two implementations of the adaptive beamformer were suggested and studied with both simulated [102] in Chapter 2, and experimental [103] in Chapter 3, data in order to establish general rules towards the proper use of the MV method and define the resolution gains that can be achieved (for both point sources and structures).

The first study was followed by the development of a novel array-processing algorithm with the intention to improve the axial localization of ultrasound point sources. The proposed imaging method has been used in biological microscopy [104, 105] and was translated step-by-step to ultrasound imaging. The optical method is based on a metric extracted from the PSF of a fluorescent particle and similar kind of metric can be extracted from ultrasound point sources, making thus the method suitable for translation [106, 107]. As with the previous algorithm, the method was studied with simulated point targets in Chapter 4, and was later verified experimentally in Chapter 5.

1.5.2 Localization improvement

From the use of the adaptive beamformers, lateral localization with precision of one tenth of the wavelength was achieved, a value that demonstrates up to 20 fold improvements compared to the conventional beamformers used in ultrasound imaging. However, it should be noted that for the first time the improved localization was demonstrated using experimental ultrasound data rather than simulated data. Further, specific contrast resolution improvements were also noticed, indicating that in certain cases the adaptive approaches can be used for anatomical images as well.

Regarding the array processing method translated from optics, both the simulated and the experimental results demonstrated that it may achieve axial point source localization with an accuracy reaching values more than two orders of magnitude lower than the wavelength used. The figure is even better than the value recorded using the equivalent optical technique and is equivalent to 30 fold improvements compared to the conventional beamformers.

1.5.3 Microbubble imaging

An experimental setup that can regulate bubble movement was described. The MBs flow quasi-vertically with upward direction into a tube with a controlled flow-rate and single scattering events can be distinguished. MB data acquired from the experimental setup can be beamformed by the adaptive method or tested with the translated from the optics localization technique. The first preliminary findings indicate that the methods show potential above current conventional resolution.

1.6 Thesis overview

The introductory chapter is followed by five chapters of the main work including all methods and algorithm developments together with their simulation and experimental validation. The common layout to include a chapter with an exhaustive literature review is avoided here. The reason is that a number of disciplines and topics are presented. Techniques are being translated from other fields of sensing into ultrasound imaging. Their specific literature is reviewed in the corresponding chapters to facilitate the reading and chapter comprehension.

Chapter 2 introduces the use of an adaptive beamforming method in ultrasound imaging. The MV adaptive beamformer is presented and applied to simulated ultrasound data. Two different implementations of the method in time and frequency domain are examined, and both the resolution gains and the limitations of each approach are outlined and compared for a chosen simulation setup.

Chapter 3 presents an experimental investigation whereby the MV method is utilized in the beamforming of real ultrasound data. The acquisition setup and the scan parameters are similar to those clinically used and are described in detail. The experimental results are displayed and compared with the previously obtained simulated ones. Specific algorithm modifications regarding the MV parameters that will render the adaptive method applicable to real-time imaging are discussed.

Chapter 4 presents a signal-based algorithm based on image sharpness, that improves axial resolution in biological microscopy. The optical technique and its ultrasound equivalent are explained and key similarities and differences between them are highlighted. The main concepts of normalized image sharpness and multi-plane imaging are translated to the field of ultrasonics to obtain super-resolution axial localization for simulated ultrasound point sources.

Chapter 5 uses the sharpness algorithm to estimate the axial position of an ultrasound point scatterer in an experimental setting. The experimental results are

compared with the simulated ones of the previous chapter, and the limitations and prospects of the proposed technique in tracking the position of MBs are considered.

Chapter 6 introduces the above methods into the localization of MBs by means of an initial experimental test. First, the MV beamformer is applied to the MB data with image and metrics display followed by comparisons with the results of Chapters 2 and 3. Then, the depth position estimation algorithm is employed to extract sharpness data that are also compared with those of the Chapters 4 and 5. The assessment of the techniques and the up-to-date practical limitations are discussed.

Chapter 7 concludes the thesis with the summary of the main outcomes. The extension and improvement of the current work towards the complete position estimation of point sources are also included.

Chapter 2

Minimum Variance Beamforming - A Simulation Study

This chapter briefly reviews the evolution of adaptive beamforming in ultrasound imaging and focuses on the Minimum Variance (MV) beamformer. Time and frequency domain implementations of the MV method are introduced and applied to simulated ultrasound data. The simulation setup together with all scan and MV parameters are explained in detail and the beamformers performance is assessed through established quantitative image quality metrics. Results are compared with conventional beamforming techniques to demonstrate the benefits of the adaptive approaches. The computational load required for the generation of a single image is also assessed. The discussion aims to elucidate the trade-off between resolution gains and computational burden in light of real-time applications.

2.1 Background

Adaptive processes have been used for decades in numerous applications of array signal processing in fields such as sonar, radar, and even seismology [44, 108–110]. Improvements in transducer design as well as reduced cost and availability of hardware based processing using Field-Programmable Gate Arrays (FPGAs) enabled similar adaptive beamforming techniques to be introduced in the field of ultrasound imaging.

2.1.1 Adaptive beamforming in ultrasound imaging

The conventional Delay-and-Sum (DAS) beamformer is a widely used technique in medical ultrasound imaging. It involves the application of delays calculated by simple geometrical formulas and the use of data-independent weighting functions that optimize the beamformer output. The method is briefly described in Subsection 2.2.1. Adaptive beamforming methods aim to take advantage of image infor-

mation in order to generate higher image quality both in terms of resolution and contrast when compared to the DAS beamformer. A number of such studies include the adaptive beamformers proposed by *Viola and Walker* [111] or the one suggested by *Mann and Walker* [112] in 2002 that was the adjustment in ultrasound of the linearly constrained adaptive beamformer [113]. The latter was based on minimizing the power of ultrasound data under a number of linear constraints. A specific case of this work, with a single constraint, led to the development of the MV beamformer [114–117] that has attracted wider interest ever since. It was originally developed by *Capon* [101] with the objective to precisely localize earthquakes with the usage of seismic arrays, which is a narrowband application.

2.1.2 Minimum Variance beamforming

The MV beamformer has been expanded to broadband ultrasound data unmodified, in the time-domain, or in the frequency domain where division of transducer element signals into frequency sub-bands precedes the processing. This is to ensure that the original narrow-band condition of the adaptive beamformer is met as laid out by *Capon* [101]. The method's aim is to calculate a set of data-dependent apodization weights, which will preserve the signal from the focus point, while at the same time, minimizing all contributions from other points. This is expressed in the ultrasound case by minimizing the output power of the data and not the noise power as in [101]. The Minimum Variance Temporal (MVT) beamformer was introduced by *Synnevag et al.* [99], and was applied to both simulated and experimental ultrasound data [118, 119]. The main bulk of results throughout the literature and the comparisons with the conventional beamformers were mostly qualitative, thus making it difficult to assess the performance of the MV method within the wider ultrasound imaging context.

The Minimum Variance Subband (MVS) beamformer was first introduced by *Holfort et al.* [100] and a quantitative evaluation was performed using simulated data. Their finding was that compared to the conventional DAS beamformers, the MVS provides significant side-lobe reduction and an order of magnitude more narrow PSF main lobe in the localization of individual point scatterers. The results from a cyst phantom showed smaller contrast improvement. In general, it is accepted that the MV methods perform differently with different data types (i.e. structures or point sources) and with different ultrasound transmission apertures due to the methods adaptation to the actual data [120]. The purpose of this chapter is to investigate and develop the MV beamformers for use in medical ultrasound imaging.

2.1.3 Limitations

The principle of the MV beamformer is to isolate the main target and through an optimization process to attenuate targets that are out of phase. It has been shown that the MV performance depends on variations in the speed of sound [121] or steering vector errors [122]. This often makes the comparison between simulation and experiment difficult, since the velocity of sound is generally difficult to control experimentally. The same conclusion applies for both the MVT and the MVS, although higher performance is expected in the MVS case due to the division into frequency bands. The complexity increases with signal coherence and interference between adjacent targets, which is cumbersome to simulate. This uncertainty of the MV performance becomes even higher when real-time imaging is considered [123], and several groups have presented small modifications and parameter studies to make the method less sensitive to these changes. Such studies include the use of adaptive approaches in transmission, in addition to the most usual receive processing [124], or the use of MVT together with principal component analysis [125]. Increasing robustness is only one of the MV challenges.

Both time and frequency domain approaches are computationally demanding when compared to conventional beamforming. This is especially true in the case of MVS as unlike the single beamformer of MVT, every sub-band in the MVS method requires its own dedicated beamformer. To overcome this obstacle, the greatest research effort in this area is currently concentrated on implementing the MV beamformer using Graphics Processing Units (GPUs) [126, 127]. In this way the MV method can be possibly used for real-time cardiac ultrasound imaging [128, 129]. Alternatively, low complexity implementations have also been proposed, where only a limited number of transducer elements is used by the MV methods [130], or where the adaptive approaches are combined with conventional ones towards the development of *semi*-adaptive beamformers [131, 132].

2.1.4 Approach

It is difficult to compare the MV findings among the different MV implementations due to the use of varying scan parameters, scanned object dimensions, or performance metrics definitions throughout the investigations on ultrasound adaptive beamforming. However a basic assessment of the main implementations in time [99] and frequency [100] domain with the use of the same image quality metrics and including the calculation load is missing from the literature. In order to achieve this assessment both simulated and experimental data need to be used in separate studies due to the limitations mentioned in the Subsection 2.1.3 above. Such a comparison would help identify the exact advantages and disadvantages of each adaptive approach, and explain the inconsistency between simulated and ex-

perimental results. To this end, the first step is to perform a simulation study in such way that the simulation can be replicated in experimental form.

2.2 Methods

This section focuses on beamforming algorithm development using the established ultrasound imaging simulation software Field II [133, 134]. Beamforming is a signal processing technique used in ultrasonics for the guided sound wave transmission or reception by a transducer array. There are various options for ultrasound transmission summarized in Appendix A depending on the application, and chosen for instance for the desired depth of focus or frame rate. While the transmission takes place only once during a separate scan, the receive processing presents more interest as there are several ways to combine the received responses to achieve increased spatial resolution. This is managed by aiming to create constructive interference between the sensor signals and both conventional and adaptive methods for this are explained in the present section. The stages leading to image formation that will enable the comparisons between conventional and adaptive beamforming are included in this section. All steps of the adaptive approaches are described with emphasis on their differences and the calculation load required during the processing.

2.2.1 Delay-and-sum beamforming

In ultrasound imaging, the standard way to process the signals received by a transducer array is the DAS beamforming [135]. The transducer element signals (x_t) are time-delayed (τ), weighted (w), and finally summed to form the beamformer output as shown in Figure 2.1. The apodization weights are simply fixed window functions such as a rectangular one or a modified cosine function (Appendix B) that do not depend on the data.

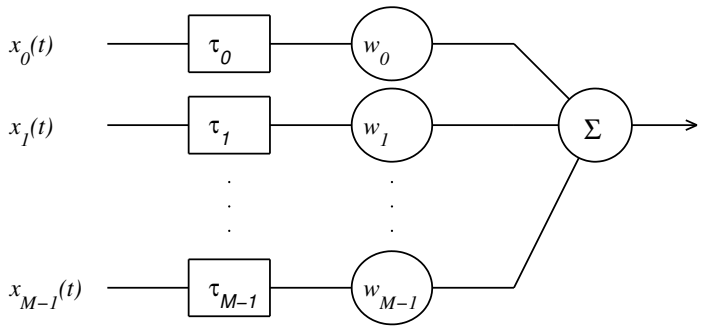

Figure 2.1: Schematic representation of the sensor signal processing by the conventional DAS beamformer.

2.2.2 Temporal Minimum Variance beamforming

As in the DAS beamformer, the MVT processes the data in a similar fashion with the only difference being the calculation of the apodization weights. This is also shown by Figure 2.2. In conventional beamforming apodization weights have predefined values, whereas in MV beamforming they are data-dependent. The output $B(t)$ of the MV temporal implementation [99] for a probe with M active elements in receive can be extracted by:

$$B(t) = \sum_{m=0}^{M-1} w_m(t) x_m(t - \tau_m) = \mathbf{w}(t)^H X(t) \,, \tag{2.1}$$

that would match with the output of a DAS beamformer for the apodization values. In Equation (2.1), t is the time vector, $\mathbf{w}(t) = [w_0(t), w_1(t), ..., w_{M-1}(t)]^H$ is the vector of the adaptive apodization weights, $X(t) = [x_0(t-\tau_0), x_1(t-\tau_1), ..., x_{M-1}(t-\tau_{M-1})]^H$ is the array of the transducer element signals, and τ_m is the time delay applied to the mth receiving element, based on its distance from the focus point.

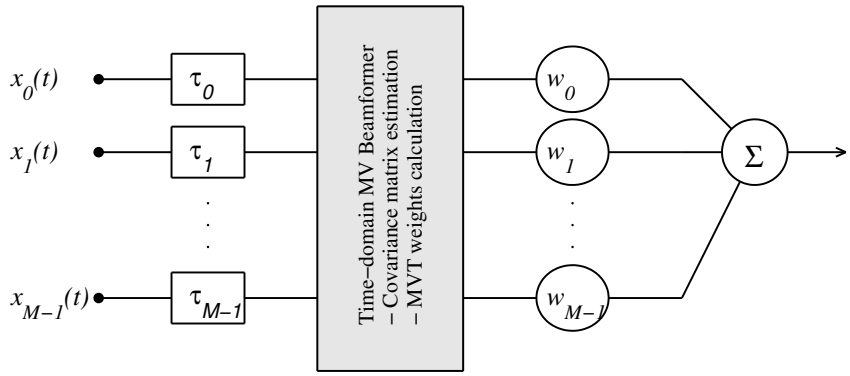

Figure 2.2: Schematic representation of the MVT beamformer.

The delayed signals $x_m(t - \tau_m)$ will at the focus be perfectly aligned, and the DAS beamformer summation and weighting aims to find the DC value of the signal along all the received elements. A rectangular weighting has fairly high sidelobes and often a von Hann or Hamming weighting is employed to lower sidelobes and to reduce signals from targets that are not perfectly aligned and in phase. The most common apodization weights are described in Appendix B. The MV beamformer is seen as a more efficient method for isolating the main target. In MV beamforming, the weights will eventually take such values, so that the variance of $B(t)$ is minimized, while the response of the focus point remains unaffected. The power $P(t)$ of the beamformer output is given by:

$$\begin{aligned} P(t) &= E\{|B(t)|^2\} \\ &= E\{|\mathbf{w}(t)^H X(t)|^2\} \\ &= E\{\mathbf{w}(t)^H X(t) X(t)^H \mathbf{w}(t)\} \\ &= \mathbf{w}(t)^H R(t) \mathbf{w}(t)\,, \end{aligned} \tag{2.2}$$

where $E\{.\}$ denotes the expectation value and $R(t)$ is the covariance matrix given by:

$$R(t) = E\{X(t)X(t)^H\}\,. \tag{2.3}$$

The MV objective can be expressed as:

$$\min \mathbf{w}(t)^H R(t) \mathbf{w}(t), \quad \text{subject } to \quad \mathbf{w}(t)^H e = 1\,, \tag{2.4}$$

where, e is the time-delay vector that is only a vector of ones, since the time delays already have been applied to the signals. Lagrangian multiplier theory [136] can then be adopted for an analytical solution to this constrained optimization problem of Equation (2.4). Given that $R(t)^{-1}$ exists, the MV weights are calculated by:

$$\mathbf{w}(t) = \frac{R(t)^{-1} e}{e^H R(t)^{-1} e}\,. \tag{2.5}$$

A single apodization weight is calculated for a single image point and this is done on a pixel-by-pixel basis for an RF dataset. The pixel size can be controlled in receive and smaller sizes, particularly in the lateral direction (where the MV improvement is noticed) can provide increased resolution benefits.

2.2.3 Subband Minimum Variance beamforming

In MVS, the Short Time Fourier Transform (STFT) is employed to divide the time delayed transducer element signals into frequency bands, and then each band is processed individually as depicted in Figure 2.3. This increases the number of calculations compared to MVT. For each focus point, $\vec{r}_p$, the Discrete Fourier Transform (DFT) is applied on a segment, thus STFT, of the adjusted transducer element signals. The mth segmented, transducer element signal $y_m(t)$ is given for $t \in [-t_d/2, t_d/2]$ where t_d is the total time duration of the segment size, and the response from the focus point will be centred around $t = 0$. The individual subband responses are then summed to derive the final MV response. The beamformer output for a single focus point, and for each frequency sub-band, ω, is given by:

$$B(\omega) = \sum_{m=0}^{M-1} w_m(\omega) Y_m(\omega) = \mathbf{w}(\omega)^H Y(\omega) \,, \tag{2.6}$$

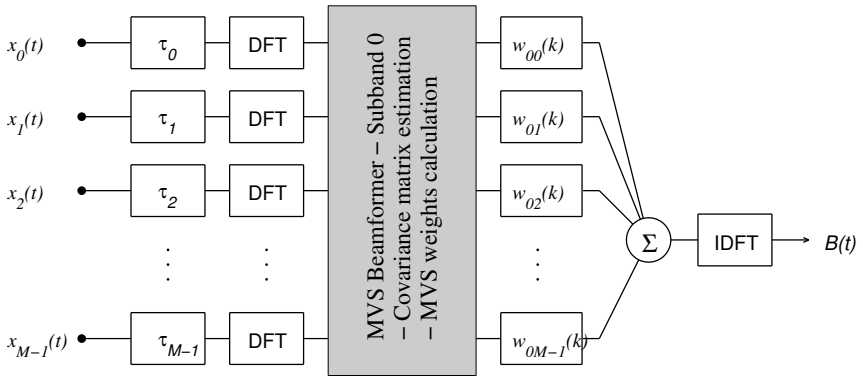

Figure 2.3: Schematic representation of the MVS beamformer for a single frequency bin.

where $\mathbf{w}(\omega) = [w_0(\omega), w_1(\omega), ..., w_{M-1}(\omega)]^T$ is the vector of the complex weights, and $Y(\omega) = [Y_0(\omega), Y_1(\omega), ..., Y_{M-1}(\omega)]^T$ is the vector of the Fourier Transform of the segmented transducer element signals. For a number of K sub-bands in total, the final beamformer output $B^*(\omega)$ can be given by:

$$B^*(\omega) = \sum_{k=0}^{K-1} \sum_{m=0}^{M-1} w_m(\omega_k) Y_m(\omega_k) = \sum_{k=0}^{K-1} B(\omega_k) \,, \tag{2.7}$$

For the MVS implementation, the power of each beamformer output $B(\omega)$ corresponding to a single frequency bin is considered and similar to Equation (2.2), is given by:

$$\begin{aligned} P &= E\{|B(\omega)|^2\} \\ &= E\{|\mathbf{w}(\omega)^H Y(\omega)|^2\} \\ &= E\{\mathbf{w}(\omega)^H Y(\omega) Y(\omega)^H \mathbf{w}(\omega)\} \\ &= \mathbf{w}(\omega)^H R(\omega) \mathbf{w}(\omega) \,, \end{aligned} \tag{2.8}$$

where $R(\omega)$ is the covariance matrix given by:

$$R(\omega) = E\{Y(\omega) Y(\omega)^H\} \,. \tag{2.9}$$

The MV objective in the MVS case can be expressed as:

$$\min \mathbf{w}(\omega)^H R(\omega)\mathbf{w}(\omega), \quad \text{subject } to \quad \mathbf{w}(\omega)^H e = 1\,, \tag{2.10}$$

By assuming that R^{-1} exists, the optimized apodization weights are given by:

$$\mathbf{w}(\omega) = \frac{R(\omega)^{-1}e}{e^H R(\omega)^{-1}e}\,. \tag{2.11}$$

The minimization goal is expressed for each frequency band and the constraint refers to the distortionless response (unity gain) from the focus point. They are therefore both independent of the implementation type [137, 138]. An important advantage of MVS, due to the MVT violation of the short-band hypothesis of MV, is the possibility of calculating different weights for each sub-band and each point as seen from Equation (2.7), which results in the filtering of the element data [139, 140].

2.2.4 Covariance matrix estimation

By omitting the dependency on time t, or frequency ω, in Equations (2.5) or (2.11) respectively, the optimized apodization weights are extracted similarly as the goal for both MV beamformers remains the same. A simple substitution of $\mathbf{w}$ to Equation (2.1) or (2.6) should in theory enable the calculation of the output of the MV beamformer for both cases. In practice, the covariance matrix has to be replaced by the sample covariance matrix $\hat{R}$, which is estimated from the data. This is because the covariance matrix changes rapidly over depth and should only be calculated from several samples instead of the whole array. Therefore, the transducer array is divided into a number of overlapping sub-arrays, from the front of the array to the end as shown in Figure 2.4, and then the covariance matrix is averaged across the array.

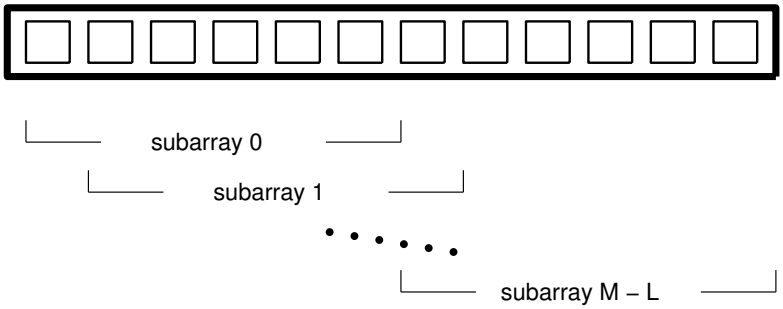

Figure 2.4: Illustration of sub-array averaging.

The sample covariance matrix can be expressed as:

$$\hat{R} = \frac{1}{M-L+1} \sum_{l=0}^{M-L} G_l G_l^H \,, \tag{2.12}$$

where L is the sub-array length, and G_l is the set of signals from the lth sub-array, which may take the form of $G_l(t) = [x_l(t), x_{l+1}(t), ..., x_{l+L-1}(t)]^H$ for MVT, or $G_l(\omega) = [Y_l(\omega), Y_{l+1}(\omega), ..., Y_{l+L-1}(\omega)]^H$ for MVS. The sub-array length is a parameter of major importance, whose value may affect the accuracy of the covariance matrix estimate, the resolution, and the number of calculation required for the weight extraction. Often values between $M/4$ and $M/2$ are selected, to make a compromise between the above aspects [141]. Once the optimized apodization weights, $\tilde{\mathbf{w}}$, have been calculated, with the use of the sample covariance matrix, the beamformer output can be given for both approaches by:

$$B(\vec{r}_p) = \tilde{\mathbf{w}}^H \frac{1}{M-L+1} \sum_{l=0}^{M-L} G_l \,. \tag{2.13}$$

2.2.5 Computational complexity

A large number of matrix multiplications are needed for estimating the adaptive apodization weights. The calculations for the estimation of a single MV weight and for a single emission will be considered here, and then the steps are exactly the same for all MV weights. To calculate the computational number required for the formation of an image resulting from a single emission, the number of image points, and weights should be multiplied by the number of calculations needed for the extraction of a single weight. Accordingly, for an image obtained from a number of emissions, another multiplication of the previously calculated number with the number of emissions used is required to extract the final number of calculations. This number is different for MVS and MVT that have both been implemented in Matlab (The MathWorks Inc., Natick, MA). The first step towards the calculation is the estimation of the sample covariance matrix, $\hat{R}$, given in Equation (2.12), that substitutes the covariance matrix, R. For this estimation, value of the sub-array L is of major importance as the matrix G_l consists of L rows and $M-L+1$ columns with the matrix G_l^H having the inverse dimensions. Therefore, for the multiplications between those two matrices $(M-L+1)\cdot L \cdot L$ multiplications and $(M-L)\cdot L \cdot L$ additions are required. The next stages include three more operations between matrices until the extraction of weights. The first one is the product of the inverse matrix, $\hat{R}$ as calculated above, with the steering vector e, resulting in $L \cdot L$ multiplications and $(L-1)\cdot L$ additions. The second one corresponds to the multiplication of the above quantity with the inverse steering vector. This output is

just a scalar, adding L more multiplications and $L-1$ more additions to the total. The third one is the ratio of the two last quantities resulting in L multiplications. The total number of multiplications and additions, $N_{f_{mult}}$ and $N_{f_{add}}$, are:

$$N_{f_{mult}} = L^2(M - L + 2 + 2/L)\,, \tag{2.14}$$

$$N_{f_{add}} = L^2(M - L + 1 - 2/L^2)\,, \tag{2.15}$$

resulting in:

$$N_{MVT} = N_{fb_{mult}} + N_{fb_{add}}\,, \tag{2.16}$$

operations for the MVT method. For the MVS method, the M transducer element signals are divided into segments with the segment size, N, depending on the excitation pulse length. If N is not equal to a power of 2 then sensor signals are zero-padded. They are then passed to the frequency domain with the use of the FFT and with a computational complexity proportional to $M \cdot Nlog_2N$ added to the total. After this point, each multiplication and addition between matrices encompasses complex numbers, and multiplication is equivalent to 6 operations and each addition to 2. The whole process is then repeated for the estimation of a single weight as many times as the number of sub-bands, N_{sub}. The total number of calculations for the MVS method is then:

$$N_{MVS} = 2K(3N_{f_{mult}} + N_{f_{add}}) + MNlog_2N\,. \tag{2.17}$$

2.2.6 Performance metrics

The comparison of the performance of the two adaptive approaches, was achieved by implementing quantitative measurements on the acquired images that enable the assessment of the lateral resolution and the image contrast. A good indicator of the lateral resolution is the lateral Full-Width-at-Half-Maximum (FWHM), which is defined as the width (in mm) of the main lobe from the PSF of an isolated point scatterer. The Peak-Sidelobe-Level (PSL) is the peak value of the first side-lobe (in dB). The image contrast (CTR) quantifies the difference between an anechoic region and a uniform scattering medium that includes such regions (cysts) and is calculated from a cyst phantom using the following equation:

$$CTR = 10 \log 10 \frac{E_{in}}{E_{out}} \,, \tag{2.18}$$

where E_{in} is the mean energy of a circular area inside a cyst and E_{out} is the equivalent quantity outside the same cyst. Finally, a Normalized Auto-Covariance Function (NACF) was used to estimate and compare the speckle of the obtained images [142]. The average speckle size can be quantified by the FWHM of the NACF with lower values, i.e. more narrow main lobe, implying better noise suppression and, thus, higher image quality. Apart from the MVT and MVS, the conventional Boxcar and Hanning [143] apodization weights (Appendix B) were also used on the same acquired data as a standard for comparison.

2.3 Simulation setup

The process of simulated data formation and acquisition is analyzed with the objective to investigate the PSF under different conditions but in the absence of extrinsic aberrations. Simulated Synthetic Aperture Ultrasound (SAU) data [144] obtained by the simulation program Field II [133, 134] were used for the comparison of the temporal and sub-band MV beamformers.

2.3.1 Field II program

Field II is a free software that runs under Matlab and can simulate ultrasound imaging using linear acoustics [145]. The software has the ability to calculate both the transmitted and the pulse-echo fields for a large variety of real transducer arrays. Further it can provide realistic images of human organs. Field II has been adopted by the wider ultrasound community to perform initial investigations on novel ways of ultrasound transmission as well as on receive processing, as it paves the way to the experimental validation very smoothly.

2.3.2 Synthetic aperture ultrasound imaging

In ultrasonics, SAU [144] is the imaging sequence in which the transmitting aperture consists of only one transducer element, while all elements are used as the receiving aperture. The single active element is emitting a spherical wave in every direction covering the whole image region, and is moved across the array. The following transducer element then becomes active, with a full synthetic aperture sequence consisting of as many emissions as the total number of transducer elements. From each emission a low resolution image can be formed. Those single emission images can be then combined so as to provide a final image of higher resolution and contrast.

The synthetic aperture ultrasound technique is similar to Multiple Input Multiple Output (MIMO) techniques used in wireless communications [146, 147], and more information about SAU and all other ultrasound transmission protocols can be found in Appendix A.

2.3.3 Simulation phantoms

Two simulated phantoms were created and used in order to evaluate the effectiveness of the MV beamformers. The phantoms are specially designed objects used in medical imaging to assess the performance of various imaging methods/devices. They were chosen here in a way, so that the specific metrics of Subsection 2.2.6 can be extracted by the resulting images. Further the simulated phantom design must ensure that at least similar acquisitions can be later performed with experimental data based on the available equipment. The purpose of the first phantom was the calculation of the PSF of the imaging system. This was done by a point phantom consisting of 12 point targets in pairs of two, separated by 4 mm laterally and located at axial depths of 30 to 80 mm. The phantom layout can be found in Figure 2.5(a). The PSFs were evaluated at different depths and the beamformers were compared in respect to lateral FWHM and side lobes.

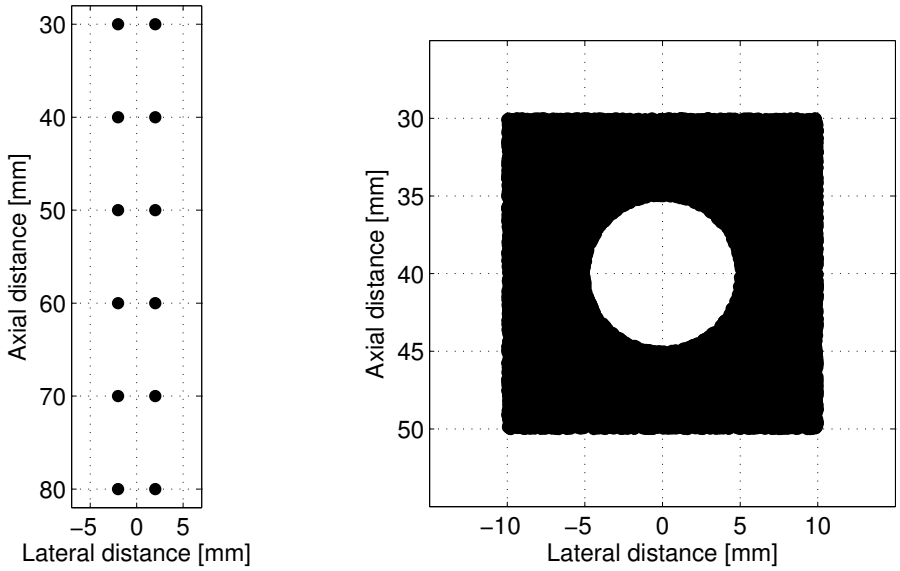

(a) Points (b) Cyst

Figure 2.5: Field II simulated phantoms layout.

The aim of the second phantom was to simulate homogeneous tissue. The phantom thus contained a circular cyst with a radius of 5 mm and centered at $(x, z) = (0, 40)$ mm, in a speckle pattern (Figure 2.5(b)). This phantom was used for the contrast evaluation of the different beamformers. The cyst phantom had 10 randomly placed scatterers within a resolution cell of $\lambda \times \lambda \times \lambda$ to ensure fully devel-

oped speckle. The contrast resolution is not the primary objective of this study that mainly focuses on point scatterers. However it is important to specify the usefulness of the adaptive beamformers and examine their performance in cases more complex than isolated individual targets.

2.3.4 Simulated imaging setup

For the simulations a 7 MHz, 128 element linear array transducer with $\lambda/2$-spacing was used. The speed of sound was set to 1540 m/s and the data were sampled at 100 MHz. All the Field II simulation parameters including the transducer definition, the way of ultrasound transmission and the receive processing, are shown in Table 2.1.

Transducer	
Transducer type	Linear array
Transducer element pitch	110 μm
Transducer element kerf	35 μm
Transducer element height	6 mm
Center frequency, f_0	7 MHz
Sampling frequency, f_s	100 MHz
Bandwidth	60% fractional
Speed of sound, c	1540 m/s
Wavelength, $\lambda = c/f_0$	220 μm
Excitation pulse	Two-cycle sinusoid at f_0
Synthetic Aperture Emission	
Receive apodization	Boxcar/Hanning/MVT/MVS
Number of transmitting elements per emission	1
Number of receiving elements, M	128
Number of emissions	128

Table 2.1: Parameters of Field II simulations.

2.3.5 Data analysis

The images that will be displayed in the Results section correspond to combined responses from a full SAU sequence, consisting of 128 emissions, for a point and a cyst phantom. For the images, the performance metrics as described in Subsection 2.2.6 were used. Further, beamformed responses and metrics from a single emission with the central element, number #64, as the transmitting aperture will be considered. This is because they are of comparable quality to those obtained from 128 averaged emissions.

2.4 Results

The point-target and the cyst phantom simulation results are presented separately. In the first case the lateral resolution was measured in various depths whereas in the second the contrast resolution was assessed.

2.4.1 Point-target phantom

The beamformed responses of the point targets are shown in Figure 2.6 with a dynamic range of 60 dB, and a sub-array length of $L = M/4 = 32$ for the MV beamformers. The number of sub-bands in the MVS case was $K = 7$.

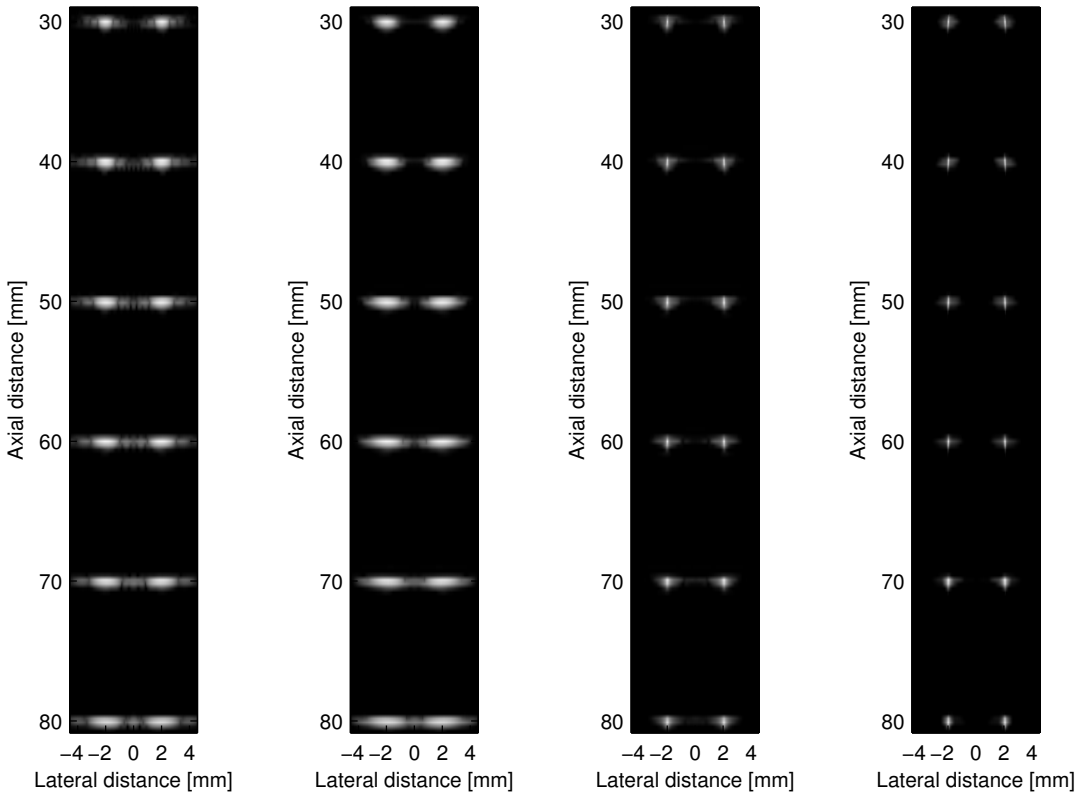

(a) Boxcar (b) Hanning (c) MVT (d) MVS

Figure 2.6: Beamformed responses of 12 point targets from 128 emissions with (a) DAS Boxcar, (b) DAS Hanning, (c) MV Temporal, and (d) MV Subband apodization. A 60 dB dynamic range display was used.

The point targets at the depth of 40 mm of Figure 2.6 are displayed separately in Figure 2.7 for more PSF and sidelobe detail since the dimensions of the whole phantom ($9\ mm \times 52\ mm$) are very big compared to those of a PSF (Table 2.2).

Figure 2.8, in which the x-axis represents the lateral distance and the y-axis the power in dB, shows the lateral variations at 40 mm and 80 mm depth for the different methods and for the case of 128 averaged emissions. The lateral FWHM and the PSL were the two criteria adopted for the performance evaluation as explained in

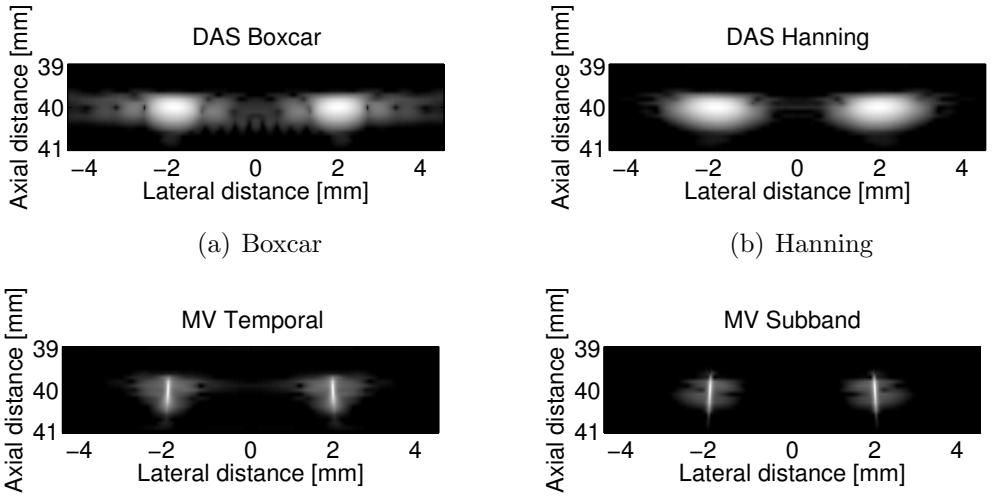

(a) Boxcar

(b) Hanning

(c) MVT

(d) MVS

Figure 2.7: Beamformed responses of the 2 point targets at 40 mm with (a) DAS Boxcar, (b) DAS Hanning, (c) MV Temporal, and (d) MV Subband. A 60 dB dynamic range display was used.

Subsection 2.2.6, and their values are shown in Table 2.2 for the targets at a depth of 40 mm. In the same table the total number of Floating-Point OPerations (FLOPs) is also found for the images of Figure 2.7. The N_{calc} numbers required for the image formation are based on the calculations needed for the extraction of a single MV weight. According to Subsection 2.2.5 those calculations were 2×10^5 for the temporal approach and the same number for the sub-band approach was 28 times higher at 5.6×10^6. Finally, the Table 2.2 also includes the metrics obtained by single emission beamformed responses at the same depth (Figures 2.9 and 2.10).

	PSL	FWHM		N_{calc}
	Full sequence (averaged over 128 emissions)			
DAS Boxcar	−31 dB	0.65 mm	2.95λ	1.16 GFLOPs
DAS Hanning	−50 dB	0.82 mm	3.73λ	1.16 GFLOPs
MV Temporal	−58 dB	0.03 mm	0.14λ	679.7 GFLOPs
MV Subband	−63 dB	0.03 mm	0.14λ	18.9 TFLOPs
	Single emission (element #64)			
DAS Boxcar	−16 dB	0.78 mm	3.55λ	9.1 MFLOPs
DAS Hanning	−40 dB	1.26 mm	5.73λ	9.1 MFLOPs
MV Temporal	−42 dB	0.04 mm	0.18λ	5.31 GFLOPs
MV Subband	−46 dB	0.03 mm	0.14λ	148.9 GFLOPs

Table 2.2: Peak-side-lobe level (PSL), lateral Full Width at Half Maximum (FWHM) and Number of calculations (N_{calc})for the beamformed responses at $z = 40$ mm, where $\lambda = c/f_0 = 220$ μm.

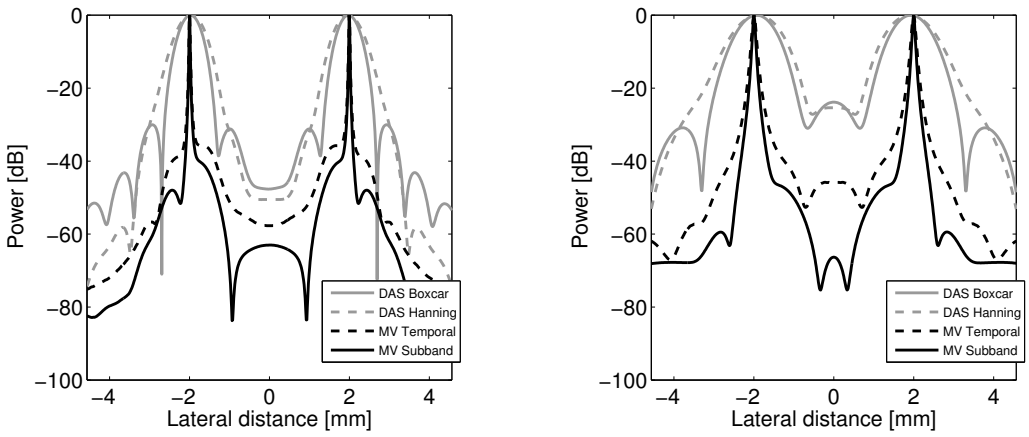

(a) $z = 40$ mm (b) $z = 80$ mm

Figure 2.8: Lateral variations of the beamformed responses from 128 emissions at a depth of (a) 40 mm and (b) 80 mm.

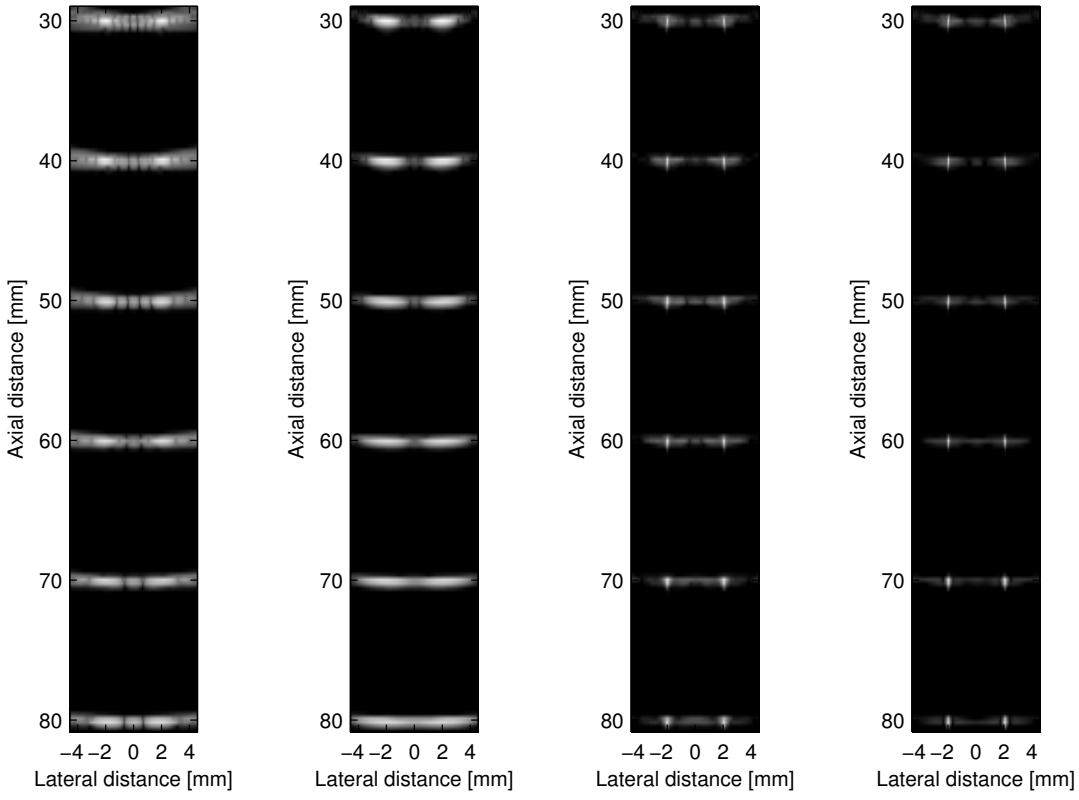

(a) Boxcar (b) Hanning (c) MVT (d) MVS

Figure 2.9: Single emission beamformed responses of 12 point targets (a) DAS Boxcar, (b) DAS Hanning, (c) MV Temporal, and (d) MV Subband. A 60 dB dynamic range display was used.

A comparison between a single and 128 emissions shows that no significant image degradation is caused by only using one emission data to form one image. This is a very important observation as it saves considerable computational time as described

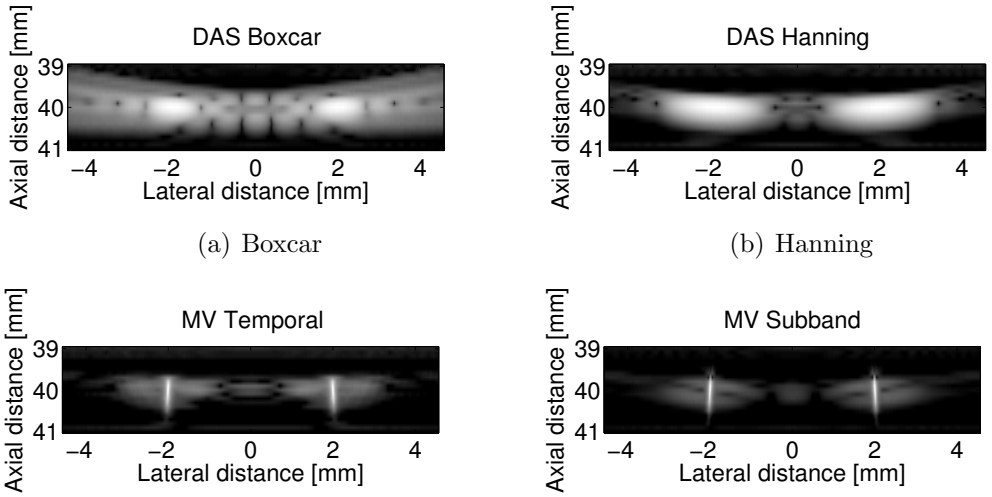

(a) Boxcar

(b) Hanning

(c) MVT

(d) MVS

Figure 2.10: Single emission beamformed responses of the 2 point targets at 40 mm with (a) DAS Boxcar, (b) DAS Hanning, (c) MV Temporal, and (d) MV Subband. A 60 dB dynamic range display was used.

in the Subsection 2.2.5. The lateral variations are also displayed here and can be found in Figure 2.11.

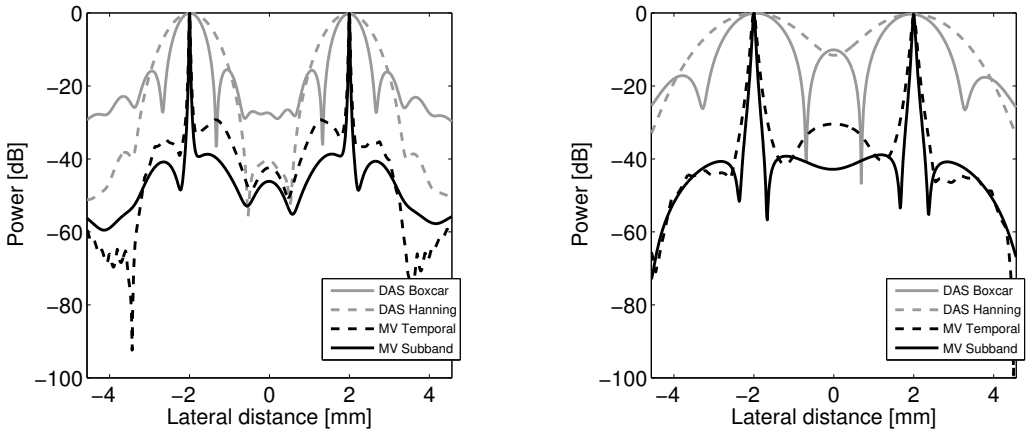

(a) $z = 40$ mm

(b) $z = 80$ mm

Figure 2.11: Lateral variations of the beamformed responses from 1 emission (#64) at a depth of (a) 40 mm and (b) 80 mm.

A full sequence of 128 emissions with one transducer element transmitting and all 128 elements receiving each time, provided a FWHM of 0.03 mm (0.14λ) for both implementations at a depth of 40 mm. This value is more than 20 times lower than that achieved by conventional beamforming. The corresponding values of PSL were -58 dB and -63 dB for time and frequency domain MV beamformers, while a value no lower than -50 dB could be obtained from either Boxcar or Hanning weights. Interestingly, a single emission with central element #64 as the transmitting aperture provided results comparable to the full sequence. The values of FWHM

were 0.04 mm and 0.03 mm and those of PSL were −42 dB and −46 dB for temporal and sub-band approaches.

From images and lateral variations, it can be noticed that the performance of all beamformers is affected by the location of the point targets. This variation of FWHM in respect to depth can be found in Figure 2.12 for both the MV and the conventional beamformers in the case of the full-sequence images. In the Figure 2.13, the equivalent PSL variation is shown for all 4 different apodization weights.

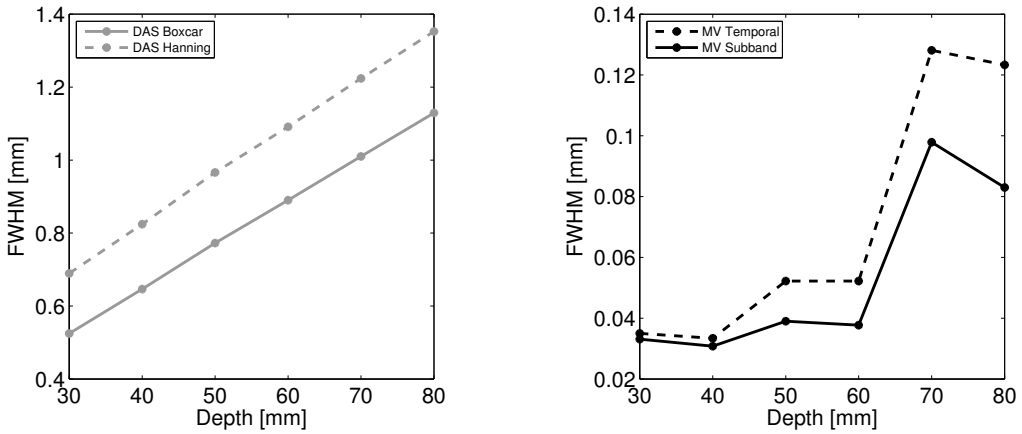

(a) Conventional (b) Adaptive

Figure 2.12: Lateral FWHM variation of the beamformed responses from 128 emissions in respect to depth for (a) conventional and (b) adaptive beamforming.

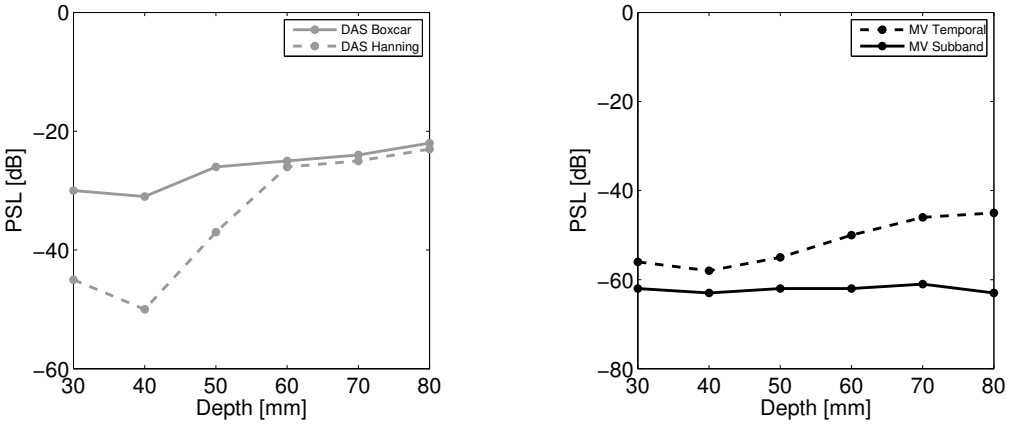

(a) Conventional (b) Adaptive

Figure 2.13: PSL variation of the beamformed responses from 128 emissions in respect to depth for (a) conventional and (b) adaptive beamforming.

The FWHM values between the two different MV approaches differ only in the fourth decimal digit at a depth of 40 mm and this difference becomes slightly more significant as the depth increases in favor of the MVS. The differences between MVT and MVS regarding the PSL values lead to similar conclusions, with the MVS slightly more effective at greater depths.

Images and metrics displayed in the current section were acquired by a lateral division of 665 image points which is equal to a lateral distance of pitch/16 between two adjacent points. Traditionally, the number of image points depends on the sampling frequency and the bandwidth during the data acquisition. However, in MV beamforming, it is possible as explained in Subsection 2.2.2, to apply further division to the image and divide it into a larger number of pixels that will reduce the lateral FWHM. In Figure 2.14 the number of image points (in the lateral direction) is plotted over the FWHM, in the case of the point targets located at a depth of 40 mm and for a single emission (element #64). The higher this number was, the lower was the FWHM but the number of calculations must be multiplied by the number of image points and thus weights.

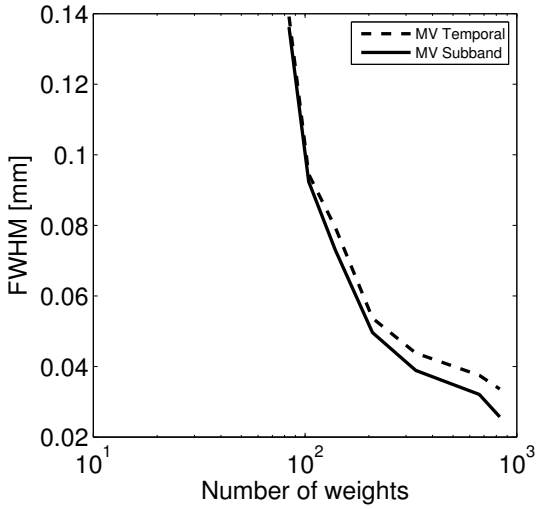

Figure 2.14: FWHM variation in respect to the total number of MV weights.

2.4.2 Cyst phantom

Images of the cyst phantom and the lateral variations, for the different methods can be found in Figure 2.15 and Figure 2.17(a) respectively. A sub-array length of $L = M/4 = 32$ was employed for the MV beamformers as in the point-target phantom case. The number of sub-bands employed by the MVS was $K = 40$. The standard number of RF samples, as they were acquired, were beamformed. Further lateral division does not affect the contrast resolution. The contrast levels for the cyst responses can be found in the Table 2.3, together with the number of calculations needed for the formation of the images of Figure 2.15, and the FWHM of the NACF that indicates the noise suppression. In the same table, the corresponding values for the case of a single emission are shown. The single emission beamformed responses and the lateral variations are displayed in Figures 2.16 and 2.17(b).

From the Table 2.3 it is seen that the contrast level between the 4 beamformers did not differ greatly in value. However, it is obvious from the images that the

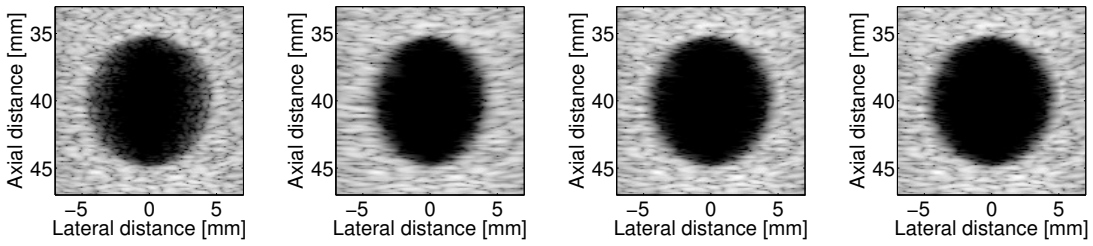

(a) Boxcar (b) Hanning (c) MVT (d) MVS

Figure 2.15: Circular cyst with radius of 5 mm and center at $(x, z) = (0, 40)$ mm. (a) DAS Boxcar, (b) DAS Hanning, (c) MV Temporal, and (d) MV Subband. A 60 dB dynamic range display was used.

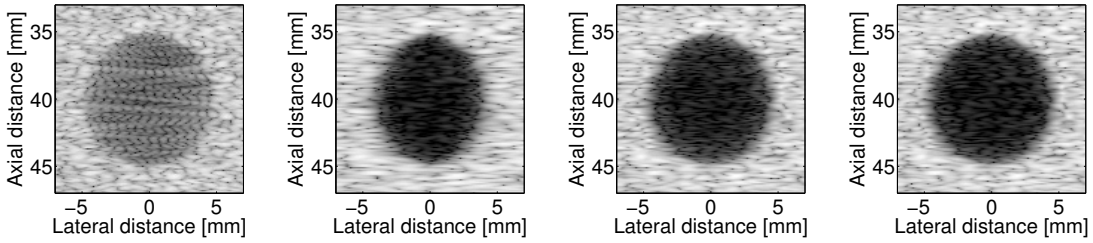

(a) Boxcar (b) Hanning (c) MVT (d) MVS

Figure 2.16: Single emission beamformed responses from the circular cyst with radius of 5 mm and center at $(x, z) = (0, 40)$ mm. (a) DAS Boxcar, (b) DAS Hanning, (c) MV Temporal, and (d) MV Subband. A 60 dB dynamic range display was used.

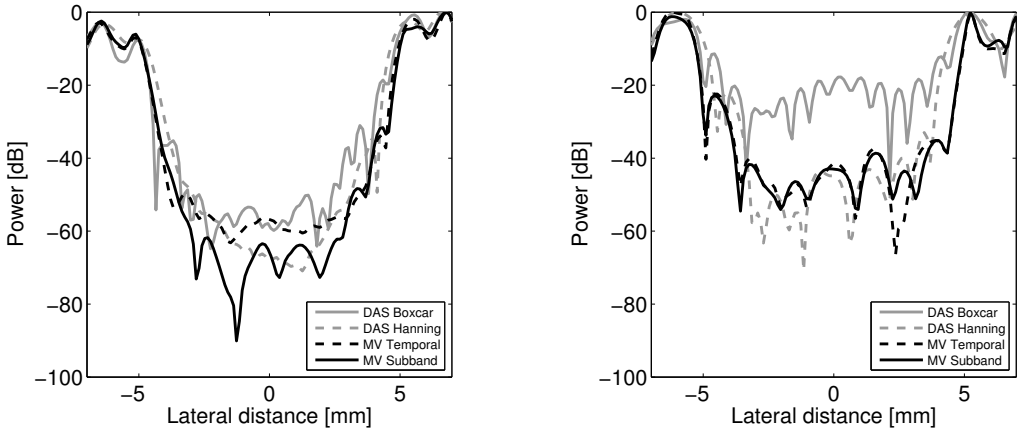

(a) 128 emissions (b) Single emission

Figure 2.17: Lateral variations at 40 mm of the beamformed responses for the cyst phantom, for (a) 128 emissions, and (b) single emission (element #64).

shape of the cyst was distorted in the case of conventional beamforming, although the same raw ultrasound data were processed by all 4 beamformers. The single emission metrics were much lower than the full-sequence ones, demonstrating lower contrast resolution. This was particularly true for the Boxcar apodization where

the contrast did not exceed −22 dB. A single MVT weight as in the point phantom case required $2 * 10^5$ floating point operations but the number rose dramatically in the MVS to $30.5 * 10^6$. This result was acquired after taking into consideration the FFT computations, the number of sub-bands, and the fact that operations were between complex numbers as outlined in Subsection 2.2.5. The difference between the two phantoms relies on the different number of sub-bands. As a consequence, the extraction of a single MV weight may require up to 152 times more calculations in the case of the sub-band approach.

	Contrast	N_{calc}	NACF FWHM
	Full sequence (averaged over 128 emissions)		
DAS Boxcar	−53 dB	1.8 GFLOPs	3.49 mm
DAS Hanning	−60 dB	1.8 GFLOPs	3.22 mm
MV Temporal	−54 dB	1.05 TFLOPs	3.36 mm
MV Subband	−63 dB	159.37 TFLOPs	3.40 mm
	Single emission (element #64)		
DAS Boxcar	−22 dB	14.1 MFLOPs	3.30 mm
DAS Hanning	−44 dB	14.1 MFLOPs	3.29 mm
MV Temporal	−42 dB	8.25 GFLOPs	3.17 mm
MV Subband	−43 dB	1.25 TFLOPs	3.19 mm

Table 2.3: Contrast, number of calculations (N_{calc}), and speckle suppression (Full-Width Half Maximum of the Normalized Auto-Covariance Function) from the cyst phantom at $z = 40$ mm, $\lambda = c/f_0 = 220$ μm.

2.5 Adaptive beamforming benefits

The initial development and quantitative assessment of the Minimum Variance (MV) methodology using simulated ultrasound data was presented in this chapter. The comparison of the obtained results and the general conclusions rising from this comparison will be discussed in the current section.

2.5.1 Point source data

It was shown that the suggested implementations of the MV methods may provide up to 20-times narrower PSF main-lobe compared to conventional beamformers in the lateral localization of point scatterers. The FWHM was equal to 0.03 mm for the MV beamformer while it took the value of 0.65 mm for the Boxcar apodization for the point target located at a depth of 40 mm (Table 2.2). The achieved FWHM values correspond to 0.14 of the wavelength ($\lambda/6$) used which demonstrates the

high performance of adaptive beamforming in comparison to the conventional DAS beamforming and beyond the diffraction limit. The additional feature of increased sidelobe suppression in the order of 13 dB (-63 dB for the MVS compared to -50 dB of Hanning apodization) was also calculated for the same target (Table 2.2). It is worth noticing that the Boxcar FWHM was lower than the Hanning but at the same time the sidelobes in Hanning were much reduced compared to the Boxcar. The MV methods were compared with the best conventional beamformer for each metric and provided a significant improvement in both aspects of PSF evaluation.

There was a decrease on the PSL when one emission was used to form an image instead of a full sequence with both adaptive and conventional apodization weights. This was expected in SAU imaging [144] since single emission images are considered of low-resolution (Appendix A) and it is the averaging over a number of emissions that usually increases the image quality. On the other hand, the lateral FWHM remained at the same levels even when only one emission was used in the MV cases. This is because the precision of the calculated adaptive weights is always high when the imaging objects are isolated points.

Computation-wise, it becomes feasible to obtain several (single-emission) frames per second of superior image quality, especially with the MVT method due to the reduced amount of data that are processed. This is possible to accomplish with the use of modern GPUs since approximately 2×10^5 operations are needed simply for the extraction of a single MVT weight. The corresponding number for the extraction of an MVS weight was 28 times higher imposing limitations to its direct use. The calculation load in the MVS case can only be managed by parallel receive processing which is lately linked with medical ultrasound adaptive beamforming [126, 127].

Both the conventional and the MV beamformers ability to resolve individual targets was reduced for scatterers at greater depths. This deterioration was expected and depends primarily on transmission since it is performed through unfocused beams with only one active element each time. However, the FWHM improvements at 80 mm (Figures 2.8(b) and 2.12) were at least 10-fold for the MV methods compared to the best conventional beamformer. Apart from the metrics values, it is obvious in Figure 2.9(b) that with Hanning apodization it was no longer possible to distinguish two individual point scatterers at the depth of 80 mm whereas at the same depth the Boxcar window resulted in an image that could be falsely intrepreted as 3 scatterers.

2.5.2 Cyst data

The cyst phantom images were employed to further evaluate the contrast resolution and shape preservation of a more complicated structure. From the analysis of the full-sequence SA images (Table 2.3 and Figure 2.15) the MVS provided 3 dB additional contrast compared to the second best beamformer (with Hanning apodiza-

tion). The difference was greater (10 dB) compared to the other two weighting functions. This indicates that the MVT was not superior in contrast resolution compared to DAS. A small cystic resolution improvement with MVS was previously shown with simulated data in [100] which is in accordance with the result of this study. Similar investigations with MV temporal implementations [120, 123] demonstrate that the MV benefits mainly concern the improved edge definition of a cyst rather than the contrast enhancements, and therefore also agree with the current MVT findings.

The cyst shape was not circular in the images of the Figure 2.15(a) and 2.15(b) meaning that only the adaptive methods managed to maintain the initial shape. This is also shown in Figure 2.5(b). Finally, the FWHM of the NACF (Subsection 2.2.6), that was introduced for the first time in the MV image analysis, showed similar values for Boxcar, MVT and MVS (less than 4% difference among the 3), whereas only the Hanning apodization resulted in 8% improvement compared to Boxcar. This indicates that the speckle suppression did not improve with the adaptive methods. The overall assessment of all the metrics and images showed that cyst phantom images benefited from the adaptive beamforming and particularly the MVS. However, the number of operations needed for a single weight extraction became even more high for the MVS (152 times higher than MVT) due to the additional processing outlined in the Methods section.

The analysis of single emission images (Table 2.3 and Figure 2.16) revealed different relations among the 4 apodization weights. Generally it was expected that the contrast resolution will decrease drastically since the images are formed only by one emission. From Figure 2.16 it is seen that the maximum performance was -44 dB and was noticed for Hanning apodization (instead of the -63 dB of the MVS in the full-sequence images). Yet, the shape distortion in the Hanning case also remained here. The Boxcar weights preserved the cyst shape as the MV methods but the contrast was significantly worse (-22 dB) compared to the other three weights. The FWHM of the NACF, with very small variations between the 4 beamformers, showed marginally lower values for the MV methods (3%) compared to DAS. The single emission imaging is advantageous in computational cost, and the MV images appeared superior than the DAS images but the overall image quality does not justify the use of the adaptive methods for such purposes neither the image formation from only one emission.

2.5.3 Time and frequency MV beamforming

A comparison between the two adaptive methods from figures and metrics throughout the chapter showed minor advantages of the MVS over the MVT with the used resolution metrics, that both outperformed the conventional beamforming approaches. This is due to the fact that only the sub-band implementation complies

with the initial narrow-band condition of the MV method [101], as analyzed also in Subsection 2.1.3. However, when the computational burden was counted in the overall performance of the each beamformer, the obtained results here pointed to the conclusion that the improvement in the MVS case was not sufficient to justify division into sub-bands. This is because the MVT can provide almost similar results compared to the MVS while its implementation can be more than 30 times faster.

Besides, it is accepted that the MV method does not provide a constant performance as was already discussed in Subsection 2.1.2. This is the major disadvantage of the adaptive approach, that also does not translate from simulations to measurements. For this reason there are various implementations and various results (the vast majority of which are qualitative) throughout the literature that cannot be compared or provide guidance for its effective use. To this front, the current implementations of both MVT and MVS need to be evaluated using real ultrasound data as similar as possible to that simulated.

The findings of this chapter were obtained by means of software simulations which did not take account of possible speed of sound variations or signal attenuation with depth. Further, the transmitting aperture consisted of a single only element and single emission beamformed images were displayed. The comparisons between the simulated and the more realistic experimental results may reveal differences between the MVT and the MVS and parameters that influence the MV performance, or even indicate the MV suitability for real-time applications in general. For instance, the usefulness of dividing the time domain sensor signals into frequency bins may be highlighted in a less-controlled, than the simulation, experimental setup.

Chapter 3

Minimum Variance Beamforming - Experimental Validation

In this chapter the previously introduced MV methods are experimentally investigated. The appropriate algorithm parameter selection is discussed so that both the MVT and the MVS are optimized for use with experimental data. The results are then analyzed and are followed by comparisons between the MV implementations and also between experimental and simulated findings. Based on the analysis, the chapter concludes with suggestions regarding the suitability of the two MV methods in a real-time application.

3.1 Background

It was stated in the Background section of Chapter 2 that several research groups have applied different MV implementations not only to simulated but also to experimental data. In general, the adaptive methods are data-dependent and therefore the performance acquired during simulations is not expected to be maintained. As in simulation, the experimental studies on MV beamforming were mainly combined with scanning point sources (wires that are positioned perpendicular to the transducer face so that they are seen as points) and cyst phantoms (tissue mimicking material that includes cylinders empty on their inside). The point target MV studies [99, 148] provide images with increased lateral resolution since the main-lobe of an MV beamformed response appears more narrow than that of the DAS beamforming. The improvement is usually not quantified since it also depends on other scan parameters [149]. The cyst phantom investigations [118, 120, 123, 150] regarding the contrast improvements show that it is only towards the edge of a cyst that the MV beamforming results in higher contrast compared to DAS.

There are also a few recent cases where the MV method has been applied to more complicated phantoms or even to RF data from *in vivo* measurements [151]. In 2012 *Taki et al.* attempted to combine MV beamforming with ultrasound vascular imag-

ing and their result was that the adaptive approach can be ideally suited for the detection of vessel stenosis [152]. In 2014 *Asen et al.* presented an MV implementation for real-time cardiac ultrasound imaging [128, 129]. Their investigation was performed using an *in vivo* cardiac data set and their result showed that MV would be feasible for such application providing improved lateral resolution. The same year, *Tracey et al.* performed a preliminary MV study with an additional beamformer constraint, for artifact suppresion on gastrointestinal ultrasonography [153].

In the present work, the same Matlab MVT and MVS scripts used in simulation were applied to wire and cyst phantom data to enable a fair comparison between simulated and experimental results.

3.2 Methods

In this section the experimental setup and the data acquisition process are outlined. The experimental data were chosen this way so that they match with the simulated point sources and the cyst of Chapter 2. The implementation of the two MV methods was given in Section 2.2 of the previous chapter and remains unchanged here. Small algorithm modifications related to the covariance matrix estimation were only suggested.

3.2.1 Covariance matrix estimation

In the previous chapter, the MV approaches were applied to the simulated data with a fixed sub-array length, $L = 32$, equivalent to 1/4 of the total transducer elements number. This value was combined by forward averaging (Subsection 2.2.4) to estimate the sample covariance matrix and proceed to the MV weight extraction. In this chapter a wider L range was studied, since the standard $L = M/4$ choice [100] did not directly show the equivalent metrics improvements as in simulation. For the same reason, apart from the forward only averaging the Forward-Backward (FB) approach was employed. The FB averaging suggests the combined use of sub-arrays from the front of the array to the end as well as from the end to the front. This results to the acquisition of a better sample covariance matrix estimate [150]. Equation (2.12) of the Chapter 2 is substituted here by:

$$\hat{R} = \frac{1}{2}(\hat{R} + J\hat{R}^T J)\,, \tag{3.1}$$

which is a more complicated one. In the Equation 3.1 J is the reversal matrix (anti-diagonal elements are 1 and all the others 0).

Both MVT and MVS apodization weights with sub-array values L ranging between $M/6$ and $2M/3$ and FB averaging were extracted from the scanned phantoms.

Generally, the sub-array division reduces the transducer element signal correlations that would affect the power calculation and consequently the MV output [119]. Smaller L values provide a more robust estimate of $\hat{R}$ but at the same time reduced resolution due to the fact that not the whole aperture is used. The opposite happens for larger L values where the sensor signal interferences is not avoided.

3.2.2 Computational complexity

The type of averaging causes a small variation to the computational complexity as this was presented in the Subsection 2.2.5. This is because the FB averaging is increasing the number of calculations required for the estimation of the sample covariance matrix. The final number of additions and multiplications becomes higher due to (3.1) and is given by:

$$N_{fb_{mult}} = L^2(M + L + 3 + 2/L)\,, \tag{3.2}$$

$$N_{fb_{add}} = L^2(M + L - 2/L^2)\,, \tag{3.3}$$

resulting in MVT number of operations $N_{MVT} = N_{fb_{mult}} + N_{fb_{add}}$. The number of operations for the sub-band implementation is given by:

$$N_{MVS} = 2K(3N_{fb_{mult}} + N_{fb_{add}}) + MNlog_2N\,. \tag{3.4}$$

3.3 Ultrasound setup

Real ultrasound data obtained by the Synthetic Aperture Real-time Ultrasound Scanner (SARUS) [154] were used for the experimental validation of the MVT and the MVS beamformers.

3.3.1 The SARUS scanner

The measurements were performed at the Center for Fast Ultrasound imaging (CFU) of the Technical University of Denmark (Lyngby, Denmark) by the in-house, experimental research ultrasound scanner SARUS shown in Figure 3.1. The SARUS scanner consists of 1024 independent channels both in transmit and receive mode and enables the implementation and evaluation of custom ultrasound imaging methods. The data are sampled at 70 MHz with 12 bit resolution, so that the system can collect data at a rate of 140 GB/s. The acquired data can then be processed in

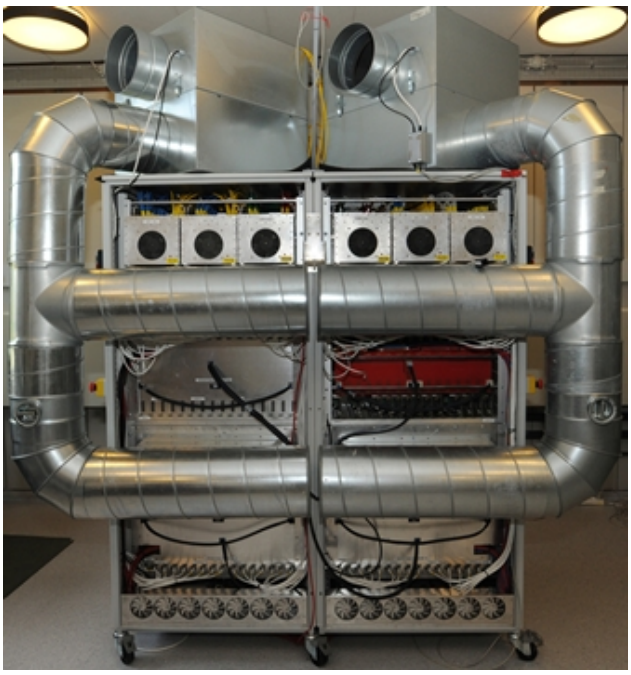

Figure 3.1: The 1024 channel research ultrasound scanner SARUS.

real time on the scanner's 320 FPGAs to obtain high quality images with synthetic aperture ultrasound imaging (Appendix A). Alternatively, data can also be stored for off-line processing.

3.3.2 Synthetic aperture ultrasound imaging

For the measurements, similar tactic as in Subsection 2.3.2 was followed. However, a transmitting aperture consisting of a single only element as in the simulation study of the previous chapter would not be practical for an actual experiment as it would limit the resolution and the penetration depth. Therefore the aperture was replaced by a number of transducer elements [139,140]. The active aperture here consisted of 128 elements, each one emitting spherical waves, and was subsequently moved across the array from one emission to the next. The RF data from 129 unfocused emissions in total were acquired from all transducer channels individually in receive and the concept of combining single emission beamformed responses was maintained. The MV methods were used to beamform a full image after each emission and the 129 single emission images were then summed to provide a final high-resolution image.

3.3.3 Phantom description

Two phantoms were used in order to verify experimentally the effectiveness of the MVT and MVS implementations. The first phantom included a number of wires held in a frame and positioned in a water tank. The wires had a diameter of 0.07 mm and were separated by 10 mm axially starting at depth of 42 mm and reaching up

to 122 mm. The phantom layout is depicted in Figure 3.2. The speed of sound, c was calculated to 1484 m/s, resulting in a wavelength λ equal to 212 μm.

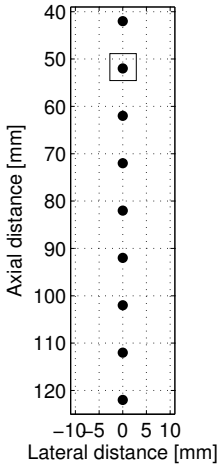

Figure 3.2: The wire phantom layout used for MV experimental validation. The MV methods were applied individually in 4 mm×4 mm areas like the one displayed here around the point scatterer positioned at $(x, z) = (0\ mm, 52\ mm)$.

The second scanned phantom was a commercial (Dansk Fantom Service, Denmark) cyst phantom. The cyst phantom contained a collection of different sized cylinders with diameters of 8, 4, 2 mm, 1 mm and 0.5 mm at various depths starting from 1 mm to 245 mm, and can be seen in the Figure 3.3. The speed of sound, c_{cyst} was 1540 m/s in the tissue mimicking material, resulting in a slightly different than above wavelength λ_{cyst} equal to 220 μm. The cylinders were positioned within a uniform scattering medium. The dimensions of the scanned area were 30 mm×60 mm. In particular, the lateral distance was between −15 mm and +15 mm and the axial from 5 mm to 65 mm depth, where only the 3 larger cysts can be found.

Figure 3.3: The cyst phantom used for MV experimental validation.

3.3.4 Experimental imaging setup

A 7 MHz, 192 element, linear array transducer with λ spacing was used to scan the two phantoms as in simulation. Data were initially sampled at 70 MHz as the SARUS scanner requires, and then the sampling frequency, f_s was decimated by a factor of 2 to 35 MHz. All the parameters of the scans are summarized in Table 3.1.

Transducer	
Transducer type	Linear array
Transducer element pitch	208 μm
Transducer element kerf	35 μm
Transducer element height	4.5 mm
Center frequency, f_0	7 MHz
Sampling frequency, f_s	70 MHz
Bandwidth	60% fractional
Speed of sound (wire phantom), c	1484 m/s
Wavelength (wire phantom), $\lambda = c/f_0$	212 μm
Speed of sound (cyst phantom), c_{cyst}	1540 m/s
Wavelength (cyst phantom), λ_{cyst}	220 μm
Excitation pulse	Two-cycle sinusoid at f_0
Peak negative pressure, PNP	2.59 MPa
Synthetic Aperture Emission	
Transmit apodization	Hanning
Receive apodization	Boxcar/Hanning/MVT/MVS
Number of transmitting elements per emission	128
Number of receiving elements, M	192
Number of emissions, N_{em}	129

Table 3.1: SARUS scan parameters.

3.3.5 Data analysis

Images and metrics that will be displayed in the Results section correspond to combined responses from a full SAU sequence, consisting of 129 emissions, for the wire and the cyst phantoms. The phantoms were chosen this way so that the specific metrics presented in the Subsection 2.2.6 can also be here extracted from the resultant images. Further, beamformed responses from the central emission (#65) where the aperture centre is above the wire targets centre, will be considered in the wire phantom case. This is because they provide similar resolution as if multiple emissions were combined [100, 102].

Small areas including only one wire as shown in Figure 3.2, were beamformed separately to avoid interference between neighboring scatterers and thus achieve the highest performance. Beamforming directly the whole RF dataset containing all

the wires, as in Subsection 2.4.1, immediately resulted in MV-derived PSFs comparable to the DAS-derived PSFs. For the MV beamforming, different values of sub-array length L, and types of averaging have been examined as outlined in subsection 3.2.1. Similar to Chapter 2, apart from the MVT and MVS, the conventional DAS beamformer using Boxcar and Hanning [143] apodization weights was also used as a standard for comparison.

3.4 Results

The section follows the structure of that in the simulation study in the previous chapter (Section 2.4), with wire and cyst phantom subsections. The additional parameter study on the covariance matrix estimation (Subsection 3.2.1), is also included for the experimental data.

3.4.1 Wire targets

Beamformed responses of single wire targets at four different depths are shown in Figure 3.4 with a 40 dB dynamic range to highlight the width of the main lobe, hence performance of the beamformers.

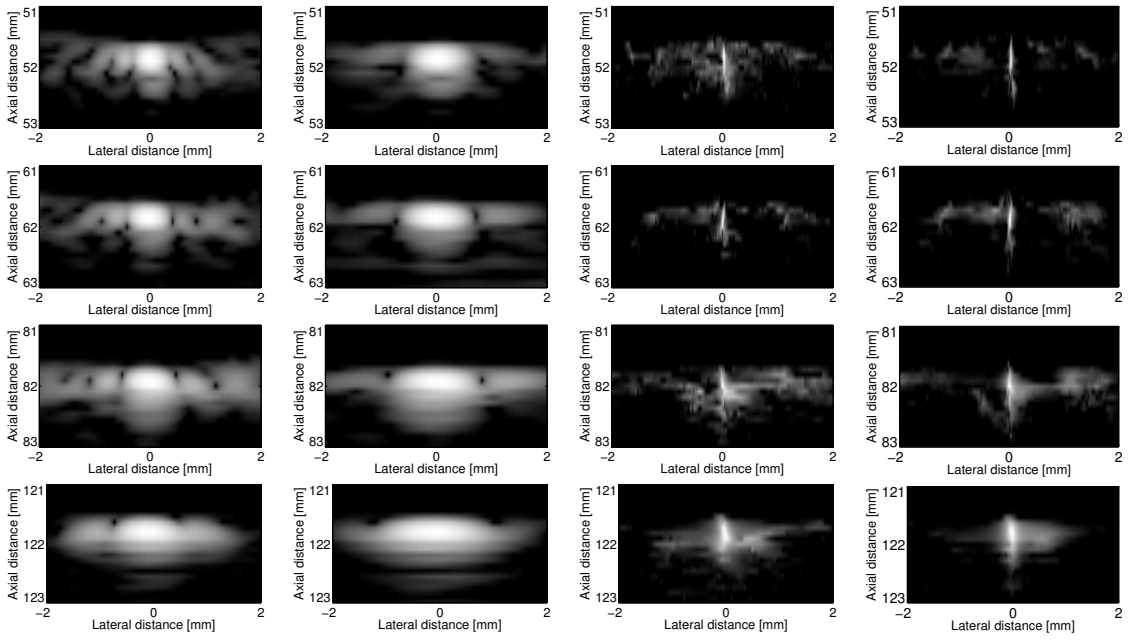

(a) DAS Boxcar (b) DAS Hanning (c) MV Temporal (d) MV Subband

Figure 3.4: Beamformed responses of 4 wire targets at different depths, from the 4 different beamformers and from 129 emissions. A 40 dB dynamic range display was used.

Signal coherence is not an issue particularly when isolated targets are studied and so a rather high sub-array length of $L = 2M/3 = 128$ combined with an FB averaging

technique was selected for display and metrics calculation. The number of subbands in the MVS case was, as in the simulation, $K = 7$. The lateral variations at 52 mm and at 122 mm depth are shown for all methods in Figure 3.5(a) and 3.5(b) respectively. The x-axis is the lateral distance and the y-axis the power in dB.

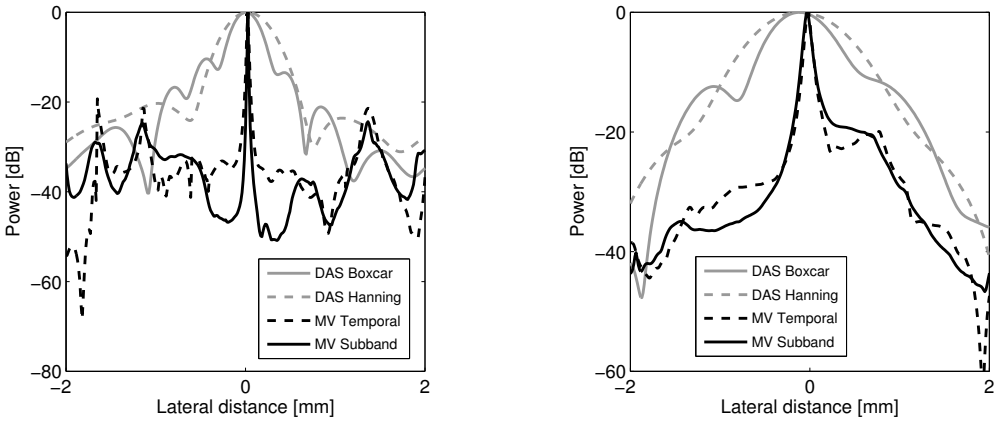

(a) 52 mm depth

(b) 122 mm depth

Figure 3.5: Lateral variations of the beamformed responses of Figure 3.4 at different depths.

In Table 3.2 the lateral FWHM, the PSL and the total number of calculations (N_{calc}) required to form an image from all 129 emissions for the first wire target displayed in Figure 3.4 can be found for both conventional and adaptive apodization weights. The table also includes the corresponding metrics obtained by single emission beamformed responses at the same depth (Figure 3.6).

	PSL	FWHM		N_{calc}
	Full sequence (averaged over 129 emissions)			
DAS Boxcar	−13 dB	0.41 mm	1.94λ	1.1 GFLOPs
DAS Hanning	−24 dB	0.65 mm	3.04λ	1.1 GFLOPs
MV Temporal	−35 dB	0.02 mm	0.08λ	39.9 TFLOPs
MV Subband	−48 dB	0.02 mm	0.08λ	1.12 PFLOPs
	Single emission (emission #65)			
DAS Boxcar	−12 dB	0.43 mm	2.03λ	8.52 MFLOPs
DAS Hanning	−22 dB	0.67 mm	3.16λ	8.52 MFLOPs
MV Temporal	−36 dB	0.02 mm	0.08λ	310 GFLOPs
MV Subband	−48 dB	0.02 mm	0.08λ	8.7 TFLOPs

Table 3.2: Peak-side-lobe level (PSL), lateral Full Width at Half Maximum (FWHM) and Number of calculations (N_{calc})for the beamformed responses at $z = 52$ mm, where $\lambda = c/f_0 = 212$ μm.

The single emission images and the lateral variations at 52 mm and at 122 mm are also displayed here and can be found in Figures 3.6, 3.7. The single emission

responses were relatively the same with the ones of Figure 3.4 at the same depth, as well as the resolution metrics values and the lateral variations. On the contrary, the N_{calc} is in this case divided by $N_{em} = 129$.

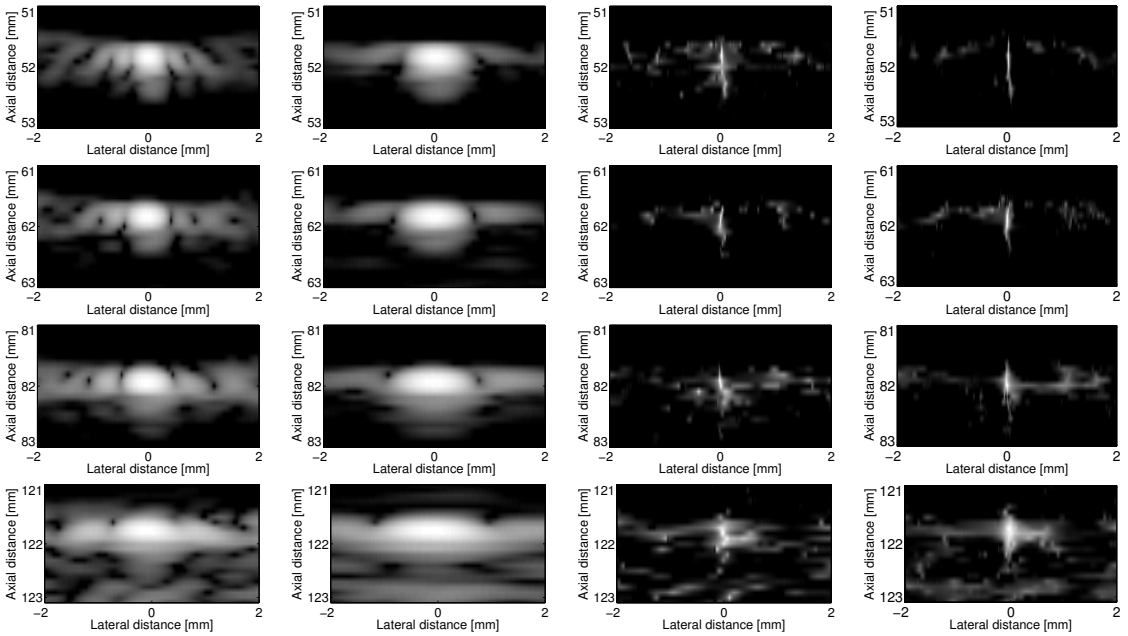

(a) DAS Boxcar (b) DAS Hanning (c) MV Temporal (d) MV Subband

Figure 3.6: Single emission beamformed responses of 4 wire targets at different depths, from the 4 different beamformers. A 40 dB dynamic range display was used.

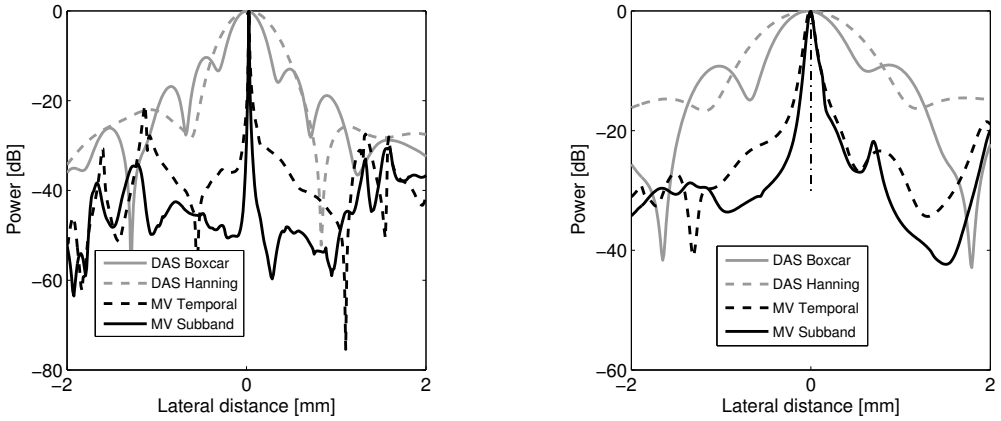

(a) 52 mm depth (b) 122 mm depth

Figure 3.7: Lateral variations of the beamformed responses of Figure 3.6 at different depths.

The lowest value for FWHM and the lowest sidelobes, thus the most precise localization, were found for the wire target at the depth of 52 mm for both conventional and adaptive weighting functions. For this target, both the MVT and MVS provided a 20 μm (or $\approx \lambda/11$) FWHM value, at least 20 times lower than the DAS can

achieve. The performance was then decreasing as the wire depth was increasing, but always remained significantly better (7-fold) for the MV approaches compared to the Boxcar or Hanning apodizations. This variation of FWHM with depth is shown in Figure 3.8(a) for the conventional beamformers and in Figure 3.8(b) for the MV approaches. In Figure 3.9 the PSL variation over increasing depths can be found for the four cases. Similarly to the FWHM, the sidelobes also became higher, when the wire was located at greater depths. Both MV beamformers showed similar performance in FWHM and PSL.

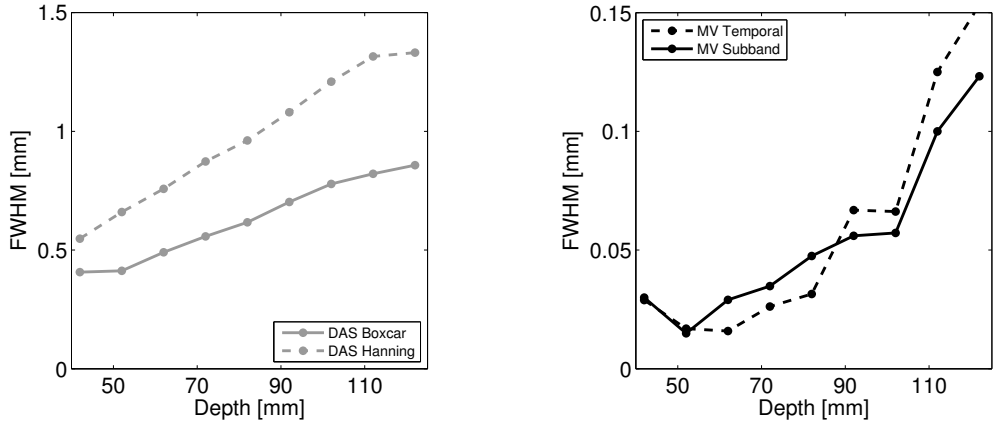

(a) Conventional (b) Adaptive

Figure 3.8: Lateral FWHM variation in respect to depth for (a) DAS beamforming, (b) MV beamforming. FB averaging was selected for the MV methods and $L = 128$.

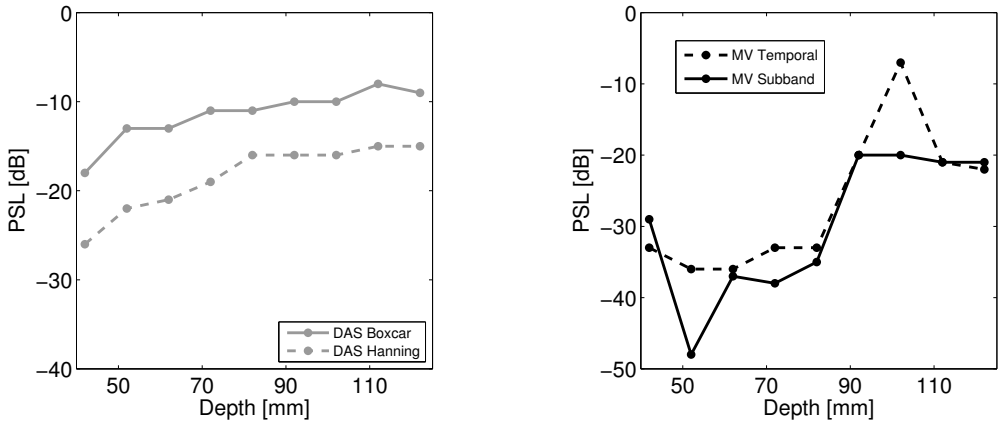

(a) Conventional (b) Adaptive

Figure 3.9: PSL variation in respect to depth for (a) DAS beamforming, (b) MV beamforming. FB averaging was selected for the MV methods and $L = 128$.

As explained in the Subsection 3.2.1, the lack of FWHM and PSL improvement in the adaptive cases with the standard MV setup in Subsection 2.4.1 of the previous chapter, led to a separate parameter study. For this sub-array length and averag-

ing investigation, single emission images were used since the MV resolution is not affected by the number of emissions. In Figure 3.10 MV single emission images of the wire at a depth of 52 mm can be found where only forward averaging was used and the sub-array length, L was equal to 48 ($M/4$). The improvement achieved by the adaptive apodization weights was limited in this case compared to the images in the first line of Figure 3.6(c) and 3.6(d). However, there is always an advantage compared to the conventional weighting. The FWHM was calculated to be 0.26 mm for both MVT and MVS which demonstrates an 1.53 fold gain compared to the best of the conventional, Boxcar weights as shown in Table 3.2. Further, the PSL remained at the same levels (-22 dB) with the one of DAS Hanning (from the same table) which is the conventional beamformer that showed the best performance for this metric.

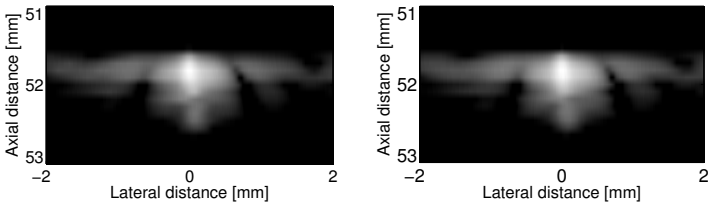

(a) MV Temporal (b) MV Subband

Figure 3.10: Single emission MV beamformed responses of target located at 52 mm, with $L = M/4 = 48$, and forward only averaging. A 40 dB dynamic range display was used and for both the MVT and the MVS measured FWHM was equal to 0.26 mm. PSL values were also identical for the two approaches and equal to -22 dB.

Figure 3.11 as in Figure 3.10 shows the equivalent MV beamformed responses in the case where $L = M/2 = 96$ and again forward only averaging.

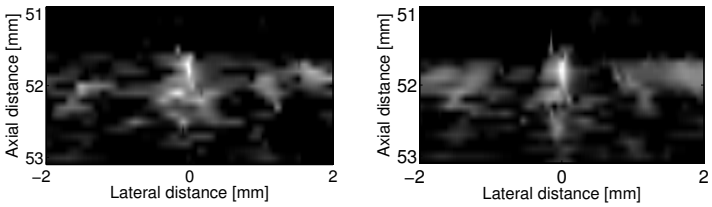

(a) MV Temporal (b) MV Subband

Figure 3.11: Single emission beamformed responses of target located at 52 mm, with $L = 96$ and forward only averaging. A 40 dB dynamic range display was used and due to high sidelobes the wire target cannot be distinguished for the MVT case. Measured FWHM was measured to 0.09 mm and PSL was equal to -30 dB for the MVS approach.

In Figure 3.11 the MVS displayed image can combine the low FWHM (similar to the one shown in Table 3.2) and lower than Hanning apodization sidelobes although the -30 dB PSL was still worse than the one achieved by $L = 128$ and FB averaging. Conversely, the MVT image (Figure 3.11(a)) appears significantly distorted to an

extent where there is no PSF to extract FWHM or PSL values. Figures 3.10 and 3.11 are two examples indicating that the MV performance is highly subject to the MV parameter selection. The FWHM and the PSL variation of the MVT and the MVS, for different values of L, are shown for both forward only averaging in Figure 3.12, and for FB averaging in Figure 3.13 for the wire target that is located at 52 mm.

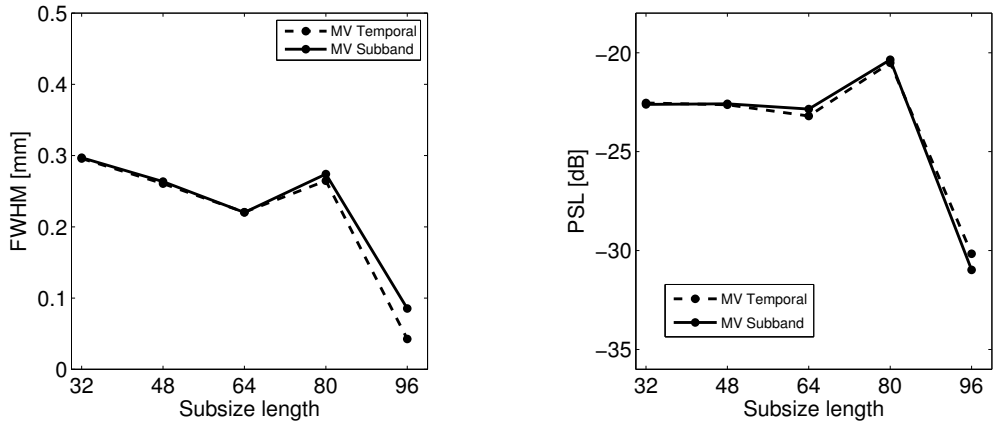

(a) FWHM (b) PSL

Figure 3.12: Lateral FWHM (a) and PSL (b) variation in respect to sub-array length for MV implementations with forward averaging.

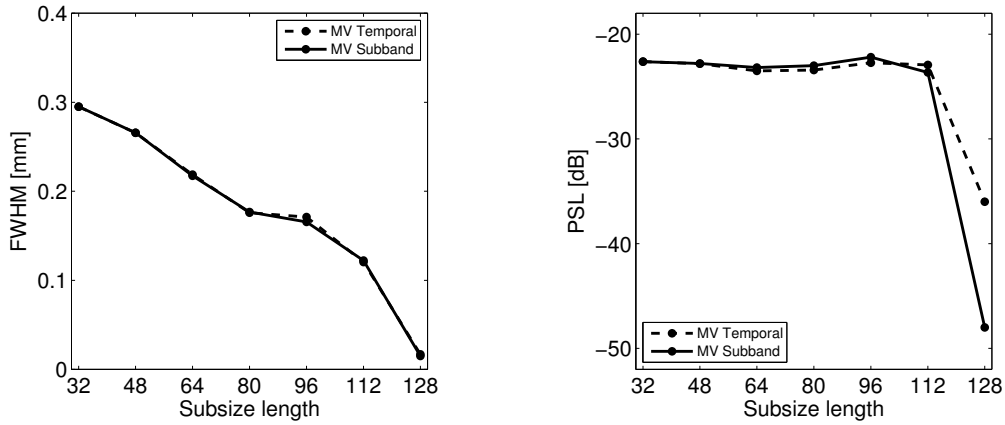

(a) FWHM (b) PSL

Figure 3.13: Lateral FWHM (a) and PSL (b) variation in respect to sub-array length for MV implementations with FB averaging.

Generally, the forward averaging provided higher FWHM and PSL values compared to the forward-backward averaging with the exception only of $L = M/2 = 96$ (Figure 3.12) where the values between the two types of averaging was similar. Further L increase, was reducing the accuracy of the estimated sample covariance matrix to a point that there was no visible PSF in the final image, to extract the FWHM or PSL values. FB averaging is a more robust method than forward only

averaging, and allowed the use of higher L values during the processing. Figure 3.13 shows that the MV beamformers outperformed greatly the conventional ones for $L = 128$, which was the value selected for initial display (Figure 3.6).

The effect of the lateral image point size on the FWHM, as in simulations, is shown in Figure 3.14 for the wire at 52 mm. All images displayed in Figures 3.4 and 3.6 correspond to an even distribution of the 4 mm lateral distance across 308 points, where each point had a length equal to $pitch/16$. As shown from the figure, smaller sizes provide improved metrics (FWHM and PSL) values with the selected length here being the optimal choice. The improvement did not continue beyond the $pitch/16$ point size, and further lateral division produced noise only images from which no wire target could be distinguished.

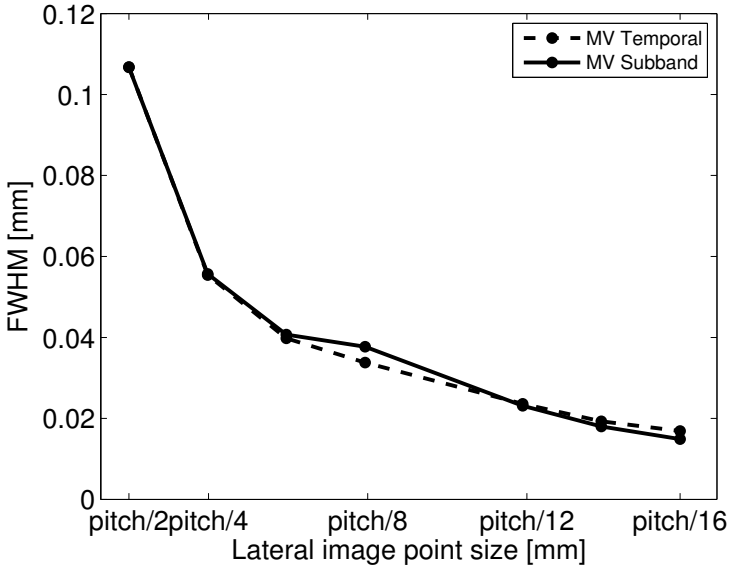

Figure 3.14: Lateral FWHM variation in respect to the lateral size of each image point for which one MV weight is calculated. Smallest size ($pitch/16$) is equivalent to highest lateral division, thus higher number of MV weights. FB averaging was selected for the MV methods and $L = 128$. For lateral sizes smaller than $pitch/16$, the beamformed responses were highly distorted and no FWHM or PSL can be calculated.

From the Figure 3.14 it can be seen that a decrease in the lateral step size from $pitch/2$ to $pitch/16$ can result in a 5 fold improvement of the FWHM, but at the same time increasing by a factor of 8 the total calculation number (N_{calc}). It is also worth noticing that between an image point size of $pitch/8$ up to $pitch/16$ the FWHM improvement cannot be considered significant. In all cases and even with the smallest lateral division (fastest implementation), the MV methods outperform any conventional apodization. The conventional beamforming performance is constant for any point size changes and was therefore not included in Figure 3.14.

3.4.2 Cysts

As in the Subsection 3.4.1, the MVT and MVS methods for the same sub-array length, L, range were used to extract the adaptive apodization weights from the cyst phantom data. However, in this study the MV methods were used to beamform whole images instead of isolated targets. In Figure 3.15 the beamformed responses of the cyst phantom are shown with a dynamic range of 60 dB. An MV parameter set providing a more robust covariance matrix estimate and lower N_{calc} was chosen for display. Both MVT and MVS were implemented with a sub-array length $L = M/4 = 48$ and forward averaging, as in simulation. The number of sub-bands in the MVS case was, as in the simulated cyst phantom, $K = 40$.

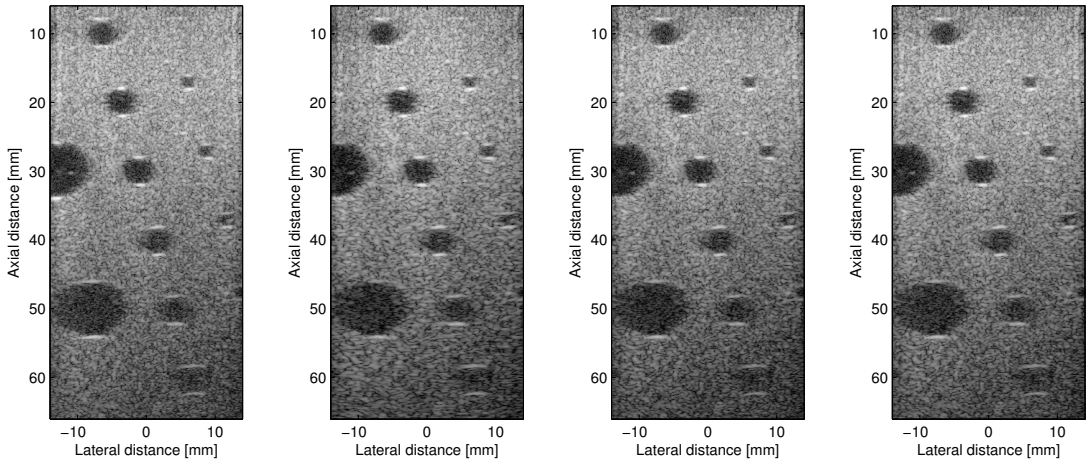

(a) DAS Boxcar (b) DAS Hanning (c) MV Temporal (d) MV Subband

Figure 3.15: Beamformed responses of the cyst phantom, from the 4 different beamformers and from 129 emissions. A 60 dB dynamic range display was used. Forward averaging was selected for the MV methods and $L = 48$

Images from the cyst at depth of 30 mm are also displayed separately in Figure 3.16 for more detail. In Figure 3.17(a) and 3.17(b), the lateral variations at the depths of 30 mm and 50 mm are shown respectively, and the calculated contrast values together with the calculation load and the FWHM of the NACF can be found in Table 3.3.

	Contrast		N_{calc}	NACF FWHM
	(30 mm)	(50 mm)	(whole image)	
DAS Boxcar	−30 dB	−11 dB	8.8 GFLOPs	3.51 mm
DAS Hanning	−29 dB	−11 dB	8.8 GFLOPs	3.67 mm
MV Temporal	−30 dB	−10 dB	258 TFLOPs	3.30 mm
MV Subband	−30 dB	−11 dB	22.4 PFLOPs	3.26 mm

Table 3.3: Contrast, number of calculations (N_{calc}), and speckle suppression (Full-Width Half Maximum of the Normalized Auto-Covariance Function) from the cyst phantom at $z = 30$ mm and $z = 50$ mm.

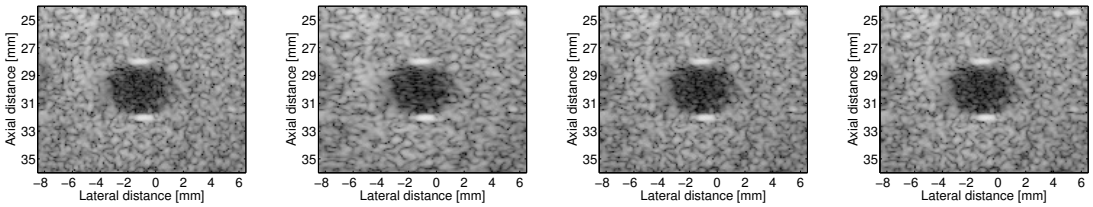

(a) DAS Boxcar (b) DAS Hanning (c) MV Temporal (d) MV Subband

Figure 3.16: Beamformed responses of the cyst centred at $(-1\ mm, 30\ mm)$, from the 4 different beamformers. Images are shown with a dynamic range of 60 dB. Forward averaging was selected for the MV methods and $L = 48$.

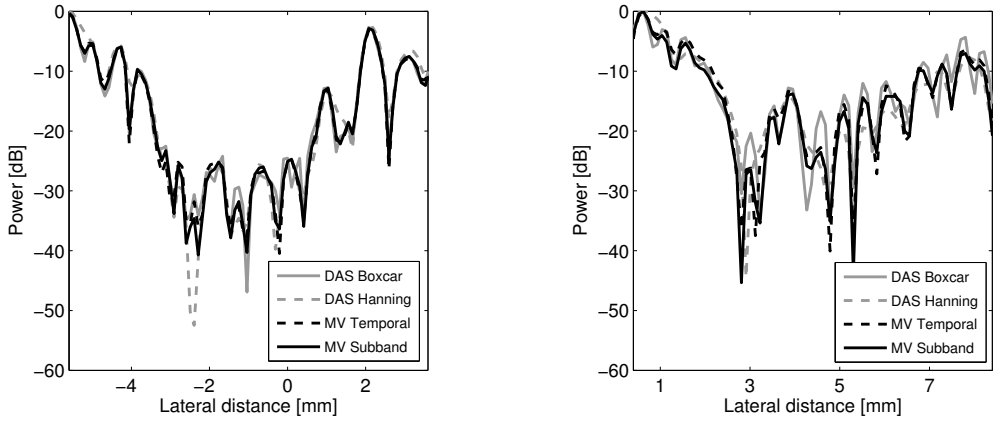

(a) 30 mm depth (b) 50 mm depth

Figure 3.17: Lateral variations of the beamformed responses of Figure 3.15 for cysts at different depths.

Visually the 4 beamformed responses of the cyst phantom in Figure 3.15 appear very similar which was verified by the quantitative perfomance evaluation (Table 3.3). The contrast was calculated between -29 and -30 dB from the cyst centred at (-1 mm, 30 mm) and between -10 and -11 dB from the one centred at (3.5 mm, 50 mm) demonstrating no practical advantage in favor of the adaptive apodization weights. The FWHM of the NACF was found 10% and 11.6% lower for MVT and MVS respectively compared to Hanning response indicating that MV methods were able to suppress the speckle slightly better compared to the DAS beamformers. Images in Figure 3.16 show more clearly that the round shape of the cyst centred at (-1 mm, 30 mm) was distorted to a certain degree. Also visible in all 4 images were two strong scattering features above and below the cyst which are the specular reflections from the interfaces between the cysts (cylinders) and the background. Similar conclusions were reached for any L size between $M/6$ and $M/2$, regardless of the averaging type and the lateral division as the contrast or shape do not change with the adaptive approaches. The parameter setup used for the maximum resolution images of Figure 3.4 ($L = 2M/3$, FB averaging) was also

replicated and applied to the cyst phantom to illustrate the varying MV behavior for the two phantoms and the two MV responses (Figure 3.18).

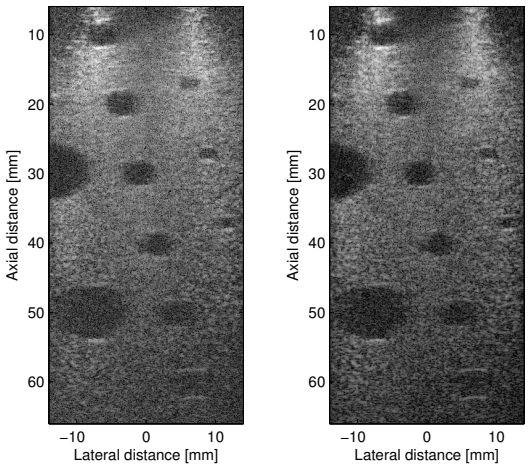

(a) MV Temporal (b) MV Subband

Figure 3.18: Beamformed responses of the cyst phantom, with $L = 128$ and FB averaging. A 60 dB dynamic range display was used.

The intensity values representing the uniform scattering medium vary and the top of the phantom for both MVT and MVS presents alternating bright and dark vertical zones. This became altogether darker at greater depths. Due to this intensity variation, the contrast resolution did not exceed -15dB at 30 mm, whereas the cyst at 50 mm was hardly visible. The equivalent FWHM values of the NACF, for MVT were 37.24% lower whereas for MVS there was further reduction equal to 41.81% compared to DAS Hanning. Results demonstrate that the specific MV settings were able to suppress the speckle in a much higher degree than DAS beamformers, but with minor differentiation between them. Finally, compared to Figure 3.15, the bright spots above and below the cysts were either weak or completely absent.

3.5 Adaptive beamforming benefits

In the present chapter, a quantitative assessment of the Minimum Variance (MV) methodology, and particularly the MVT and MVS implementations, was investigated for the first time using experimental ultrasound data. In this section, comparisons between simulated and experimental findings will take place and finally the perspectives of using the MV methods in real-time imaging will be discussed.

3.5.1 Point source data

From the above analysis, it was shown that adaptive apodization weights may achieve extremely low lateral FWHM values as $\lambda/11$ (or 20 times better than conventional weights) while at the same time keeping the sidelobes below -40 dB in the

lateral localization of isolated point sources. As it was highlighted in the Subsection 2.1.4 of the previous chapter, a comparison of findings between the various MV implementations would be inappropriate due to the sensitivity of the method on a large number of parameters. However, such low values have never been presented in the adaptive beamforming literature for medical ultrasound [100, 118, 155], which provide $\lambda/6$ at best. Further, single emission over full-sequence images were mainly examined as they showed the similar PSF appearance with additional computational time gains. Excluding the calculation load that will be examined separately in Subsection 3.7, the general conclusion from the wire target analysis is that there is little difference between MVT and MVS. This agrees with previous comparison based on simulation results (Subsection 2.4.1). However with the experimental data, this superior performance was obtained only when the MV approaches are applied to individual targets as described in Subsection 3.3.3 and not for the entire image. A detailed comparison between simulation and experimental results will follow in Subsection 3.6.

3.5.2 Cyst data

In the absence of individual targets, and when beamforming larger areas or the entire RF dataset, the gain of the adaptive method was minimized and the performance became equivalent to that achieved by conventional weighting. This applied for the wire phantom and became more evident in the cyst data processing. The cyst shape in Figure 3.16 seemed slightly more circular in the case of MVS but in general it was not possible to identify a significant advantage of the MV methods over conventional ones in terms of contrast improvement or speckle suppression. Interestingly, the use of high sub-array length L, where the effect of signal coherence was not avoided, the MV images (Figure 3.18) appeared considerably different from the ones in Figure 3.15. The scattering medium did not appear homogeneous and the intensity variation throughout the image was of compromised quality. As a consequence the contrast significantly deteriorated and the penetration depth was further limited. However, cyst edges were better defined and the specular reflections, that ideally shouldn't be there, were avoided to a great extent.

These results are not in full accordance with previous simulations where in addition to the shape maintenance there was some contrast improvement with the MV methods and especially with the MVS [100, 102]. However, the Subsection 3.4.2 is in general agreement with the recent studies on cystic resolution as outlined in Section 3.1. Considering the additional computational load it appears that there is no clear benefit in using the MV methods in structural/anatomical imaging. Both wire and cyst phantom experiments strongly suggest that the MV efficiency depends on the relation between the number of available transducer element signals and the number of scatterers to be resolved. The above conclusion renders the adaptive

beamforming suitable for combination with sparse implemented elsewhere [156,157].

3.5.3 Time and frequency MV beamforming

There are a few examples showing different behavior between the MVT and the MVS. First, there was a noticeable 12 dB (-36 for the MVT and -48 dB for the MVS) PSL difference in favor of the MVS for the wire target that is closest to the transducer surface (Table 3.2). This was reflected by the PSF appearance where the target was clearly defined for the MVS derived image (Figure 3.6(d), first row), while sidelobes were visible in the MVT case (Figure 3.6(c), first row). Second, in the MVT, unwanted signal contributions around a wire at greater depths, were not always well suppressed. This could result in images where wire targets were poorly defined for the temporal implementation, as it can be seen from Figures 3.6(c) at the depth of 82 mm (third row) or 122 mm (fourth row).

Finally, from the MVT responses of Figure 3.6(c) it can be noted that the peaks on the images did not line up vertically with depth in the third (82 mm) and particularly in the fourth row (122 mm). This is more easily observed by the lateral variations at the greatest depth in Figure 3.7(b), where only in the MVS case the curve peak was aligned around $x = 0$ mm (Figure 3.7(b), vertical dashed-dotted line). A comparison between the black continuous (MVS) and the black dashed (MVT) lines in Figure 3.7(b) shows that whereas the right sides of the two lines were adjoining (up to -15 dB), there was some deviation on the left sides revealing a wire centre shift with the MVT processing. All these appear as small differences between the MVT and the MVS, but together they show a marginal superiority of the MVS and lower precision of the MVT calculated weights. This suggests that the sub-band division of the broadband ultrasound signals may be the optimal choice as the theory indicates [101].

3.6 Comparison with simulation

An overview between the Results sections of the Chapters 2 and 3, demonstrates that in general terms, simulation and experimental measurements agree with each other. The acquisition setups, the MV parameters used in each study and the obtained metrics in the two cases will be compared in the present subsection.

3.6.1 Imaging setup

The specifications of the simulated transducer of the previous chapter were not identical with the transducer characteristics used during the experiment. The most important difference is that the simulated transducer consisted of 128 elements and had a pitch equal to $\lambda/2$ while the actual transducer had 192 element and a λ

pitch. In addition, the speed of sound was constant during the Field II simulations (1540 m/s) and was calculated based on the water temperature [158] during the experiment (1484 m/s). The transmitting aperture was also adjusted in the present chapter from 1 to 128 elements. The single element unfocused transmissions can be suitable for scanning a small collection of simulated point scatterers but would result in poor images in an experimental setting when phantoms are scanned. Therefore a larger aperture was used emitting, as in simulation, spherical waves.

Further, the chosen phantoms here were not identical to the simulated ones. There were two columns of point scatterers at increasing depths in the simulation study reaching 80 mm (Figure 2.5) while there was only one column in the wire phantom (Figure 3.2) where the furthest wire was located at a depth of 122 mm. Moreover, for the simulation a single cyst was examined while the experimental phantom included a number of varying-sized cysts at different depths. The availability of these phantoms for the simulation and mainly experimental setups dictated their use in the respective investigations, as it was deemed unnecessary to have new phantoms made for either study. This is because all phantom layouts allow the use of exactly the same metrics (Subsection 2.2.6) in order to evaluate the beamformers performance in each case.

The MV methods were applied in the simulation with a sub-array length, $L = 32$, which equals to a sub-aperture that is 1/4 of the total aperture. Further, forward only averaging was employed and this combination resulted in the numbers and images displayed in Chapter 2. On the other hand, in the experiment, the equivalent parameter values, $L = 48$ (since the transducer had 192 elements) and forward averaging resulted in the images and metrics shown in Figure 3.10 which did not meet the expected from the adaptive beamformers standards based on the simulation results. For this reason, the MV parameter study was only introduced in the present chapter until the MV benefits appear. This happened for the images acquired with much larger sub-aperture $L = 128$, which corresponded to 2/3 of the 192-element array and with the use of FB averaging to ensure a more robust estimation of the sample covariance matrix. The above choices had an effect on the number of calculations needed for the extraction of a single MV weight as the total N_{calc} depends on L^3, indicating that in the case of the large aperture $(128/32)^3 = 4^3 = 64$ times more floating point operations were needed.

3.6.2 Resolution metrics

The resolution metrics comparison between simulated and experimental MV results can again be divided into two parts, one referring to the point scatterers and one referring to the cysts. A close look in the Tables 2.2 and 3.2 shows that in simulation both the MVT and the MVS were able to provide lateral FWHM with values approximately around 0.14λ, while the experimental results were slightly improved

reaching values up to 0.08λ. This does not imply any differences between simulated and experimental MV results and is simply due to the larger aperture used in the measurements. This is also reflected in the FWHM values of the conventional apodization that were higher for the simulated data compared to the experimental ones. For example, the DAS boxcar provided 0.65 mm FWHM in simulation while the experimental result was 0.41 mm. Importantly, the comparison between DAS and MV results showed a 20 fold improvement achieved by the MV beamforming both in Chapters 2 and 3. The FWHM variation with depth was also very similar for both experimental and simulated point targets (Figures 2.12 and 3.8). The highest value of the lateral FWHM was $\lambda/2$, which demonstrates decreased performance compared to the best case ($\approx \lambda/11$) but was still improved compared to any conventional weighting function. Finally, another similarity of experiment and measurement regarding the FWHM is that whether it was calculated from full sequence or single emission images takes similar values.

The PSL showed higher discrepancy between experimental and simulated results (Tables 2.2 and 3.2). In simulation the sidelobes appeared 15 dB lower for MVS than in the measurement (-48 dB for the experiment compared to -63 dB for the simulation) and the difference became greater for the MVT (22 dB). For the point scatter at different depths there was a difference ranging between -10 and -15 dB. This is because the current simulation setup is limited in incorporating ultrasound noise, speed of sound variation or contributions from neighbouring targets due to sidelobes (Figures 2.13 and 3.9).

The relation between MVT and MVS is not always the same in experiment and simulation. In simulation MVS appeared always slightly superior than the MVT with small differences that did not exceed 5% for either FWHM or PSL. In the experiment, the FWHM may be marginally lower for the MVT in some cases. Further as explained in Subsection 3.5.3, there are point targets that were not clearly visible with the MVT (Figure 3.6(c), third line). It is thus safe to conclude that the experiment was generally consistent with the simulation in the point scatter investigation as the advantage of the MV was clear and any other discrepancies were small enough to be justified by the differences between simulation and experimental envirnoments.

Conversely, the experimental data of the cyst showed no significant improvement with the MV methods compared to DAS beamforming. This is in slight disagreement with the simulated results of the previous chapter. In Figure 2.15 the contrast resolution was more than 10 dB improved in the MVS case compared to the DAS Boxcar and 3 dB compared to Hanning. This difference combined with the distorted shape of the cyst in the Hanning case, demonstrated that mainly the MVS and secondarily the MVT outperform the conventional methods. Such difference was absent in the experimental data as shown in Figures 3.15 and 3.16 and in Table 3.3. The

table calculations demonstrate an overall decreased contrast resolution compared to simulation. The calculated contrast did not exceed −30 dB, while it reached −63 dB in simulation. Further, it was not possible to form experimental images of the cyst phantom only by using RF data from a single emission. The insignificant difference between the 4 apodization methods in the experiment disagrees with the simulation results. In the experiment where the MV utilized $L = 128$ (Figure 3.18), images of reduced contrast, only half as good when compared to the conventional beamformers, were obtained. At the same time the reflections between interfaces disappeared indicating a peculiar MV advantage. This is something that could not be studied during simulation since the Field II program calculates the ultrasound field at a specific point in space as function of time without taking into account interactions from other points. Hence, such phenomenon would be absent and the specific MV parameter setup was never applied to the simulated data.

3.7 Implication for real-time imaging

The above findings invite further work to assess the MV implementations in both the localization of point sources as well as structural imaging. For instance, the combination of the MVT or primarily the MVS, with chirp-coded excitation [159, 160] instead of the standard pulses (Table 3.1) can lead to improved performance and overall image quality. Further, the use of a transducer with higher bandwidth and the generation of broader pulses could amplify the need for dividing the signals into frequency bins, which may lead to further optimization. The target is to define cases in ultrasound imaging where the benefits of adaptive beamforming can be emphasized.

The MVT and the MVS performance with the current experimental setup overall appear similar but the MVT provided a reduced computational penalty. There was a 28-fold lower calculation number for the MVT compared to MVS for each wire target image, which increased to 87-fold for the cyst phantom images. The difference between the N_{calc} (Tables 2.2 and 3.3) stems from the image size since much larger area was scanned in the cyst phantom case. The relative difference between MVT and MVS was not stable due to the different number of frequency bands in the two measurements ($K = 7$ for the wire-phantom and $= 40$ for the cyst phantom respectively). Despite the MVT computation gains, considering current state of the art computing both MVT and MVS would be useful, if an off-line processing choice is applicable.

In practical terms, with the use of modern GPUs, whose peak performance reaches several tera-Floating-Point Operations Per Second (FLOPS), the current best case scenario would be one frame per 3 seconds for the MVT whereas more than a minute would be required per frame for the MVS. Yet, when the point tar-

gets are considered, the exploitation of single (or reduced) emission frames could render the MV methods more applicable to real time imaging. In that case it would be feasible to reach frame rates of approximately 2 and 50 frames per second for the MVS and the MVT respectively. The above numbers that are based on Table 2.2 could be improved, if priority is not given to optimizing resolution as shown from Figure 3.14. Since the RF data from each emission were beamformed individually with the current MV implementations, the parallel computing can be an option to reduce the computational time and thus increase the frame rate that can be achieved. Further in the MVS, each frequency band is also processed individually and could potentially allow for parallelization.

Although the applicability of the MV method remains open for B-mode imaging, the results show that it appears particularly attractive for use in point source imaging. The emerging field of research in super-resolution ultrasound contrast imaging which is based on the assumption of single point scatter, is an obvious future research target. Whereas super-resolution imaging is currently image-based, the MV beamformer offers a complementary method on the processing of signals. The advantage of using such a method does not only rely on the improved localization (FWHM), but also on the contrast (PSL). This signifies the potential for a reduced variability of PSF and reduced background clutter or noise. Both these improve the statistics of detecting microbubbles in an image, further improving accuracy and reproducibility of image processing and the final outcome. The lack of improved axial localization using the MV method is not a major obstacle as the PSF has a very well defined shape, which may facilitate the image analysis implemented elsewhere.

Chapter 4

A Normalized Sharpness Method for Axial Scatter Localization

The previous work has dealt with the lateral localization which motivates the research in the axial dimension. In this chapter the possibility to improve the axial localization is examined through a novel array processing method for precise depth detection of ultrasound point scatter. The method is translated to ultrasonics from optical microscopy. Both the optical technique and the ultrasound equivalent are described with examples to demonstrate all the common characteristics that render this translation applicable. Moreover, the differences between the two fields regarding the ways of transmission and the nature of the point sources are also discussed. For the ultrasound implementation, simulation software is used to permit the development of the algorithm and to help in the design of the experimental procedure for testing.

4.1 Axial localization in optical microscopy

The optical method proposed by *Dalgarno et al.* [104] and *Dalgarno et al.* [105] in 2010 for depth estimation of fluorescent particles in biological microscopy, serves as a basis for the ultrasonic algorithm and as a consequence it is outlined here first. The method makes use of a simple metric called *image sharpness* [161, 162], a small microscope attachment called a *diffraction grating* [163–165] and a maximum likelihood algorithm. This method provided approximately 8 nm ($\lambda/40$) depth resolution when applied to images of unresolved targets that are not background-limited.

4.1.1 Image sharpness

Image sharpness is a pixel-based measure of image quality often used as a criterion in auto-focusing algorithms [166–168]. It has also been widely used in astronomy for correction of distorted images [162, 169]. The sharpness metric can be seen as a

descriptor of field aberration, which is dominated by defocus. Its main characteristic is that it takes higher values at minimal aberration and presents increasingly lower values as defocus increases. Consequently, maximum sharpness occurs at the region corresponding to the best focus. In optics, it is usually defined as the integrated square (2^{nd} order) intensity over the emitter [104, 105, 170]. The intensity is given by the product of the energy of a single photon multiplied by the number of photons per second per unit area (photon flux). However, there is no unique way to assess the sharpness function and the definition varies depending on the application each time [161, 167, 171, 172]. For the specific optical method [104, 105] a normalized version of the sharpness was adopted and it was given by:

$$S_{opt} = \sum_{k=1}^{K}(n_k^2 - n_k)/(\sum_{k=1}^{K} n_k)^2 \,, \tag{4.1}$$

where S_{opt} is the normalized image sharpness, K is the number of pixels, and n_k is the recorded intensity value of the k^{th} pixel. The subtraction in the numerator is to avoid photon bias at low photon budget level. It has a very small effect on the sharpness value for high-flux data, but becomes more important when analyzing low-flux data [105].

To demonstrate the optical sharpness, a $3D$ confocal microscopy [173] scan was performed with fixed fluorescent particles (FluoSpheres, Molecular probes, ThermoFisher scientific, UK). For the scan, a Leica SP5 (Leica Microsystems Ltd, UK) confocal microscope housed at the Edinburgh Super-resolution Imaging Consortium (ESRIC), was used. The fluorospheres were captured by a Photo-Multiplier Tube (PMT), as they were moving along the z-axis (depth) with a z-step size equal to 130 nm. The total displacement was 8 μm, the emission wavelength varied between $580 - 650$ nm and the diameter of the particles which are shown in Figure 4.1 was 100 nm.

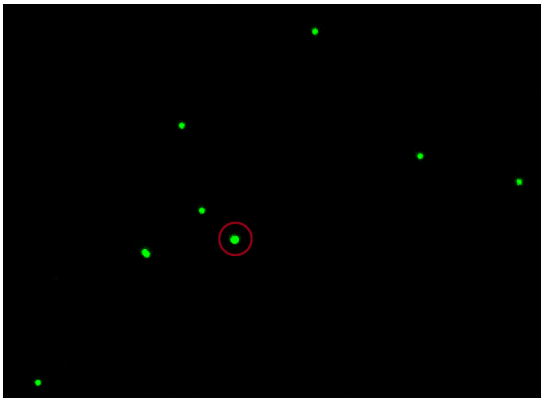

Figure 4.1: A PMT captures a collection of fluorospheres. The pixel size 48.1 nm $\times$48.1 nm for the confocal microscopy scans. The area inside the red circle contains only one bead to be examined.

Confocal microscopy aims to improve optical resolution by placing a spatial pinhole at the confocal plane of the optical path, before collection by a point detector. Due to the pinhole effect, out-of-focus and off-axis light is excluded from collection as illustrated in Figure 4.2. Confocal microscopy thus provides improved optical sectioning over widefield imaging, at a cost of imaging acquisition speed.

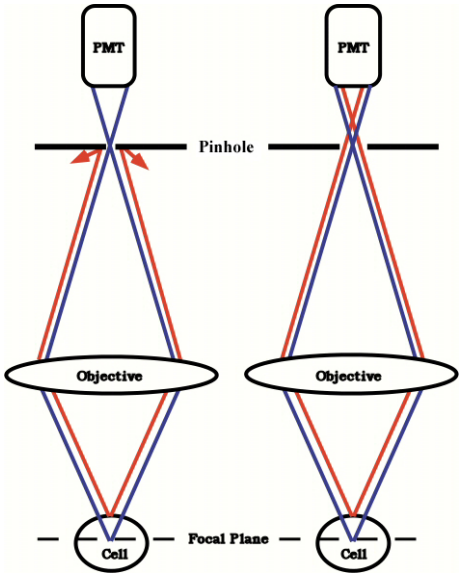

Figure 4.2: The left subfigure shows a small pinhole opening that allows data only from a thin optical plane (blue) to be acquired, while data having a different focal plane (red) are deflected. The larger pinhole on the right enables the acquisition of both in-focus and out-of-focus data. The figure has been adapted from [173].

Confocal imaging approximates the classical focused ultrasound transmission, described in Appendix A, and thus is the most accurate optical analogy for translating the optical sharpness method. The possible acquisition of results similar to those shown in [104, 105] would mean that the sharpness metric could potentially be adopted in ultrasound imaging. Two individual datasets were collected with different pinholes as in Figure 4.2. The diameter of the pinhole is measured in respect to the Airy diameter [173], d_{Airy}, a quantity calculated by:

$$d_{Airy} = \frac{1.21\lambda}{NA} M \,, \tag{4.2}$$

where λ is the wavelength, NA is the numerical aperture and M is the magnifying factor of the objective. For the first dataset, a smaller pinhole size, equal to a single Airy unit was selected, which is considered to provide the optimal signal/noise ratio [174] as shown in Figure 4.3. In the second scan, a larger value equal to 4.5 Airy units was used for a more widefield-like measurement. Several fluorospheres are found in Figure 4.1 but a region or interest (red-circled area of the figure) that includes a single particle was used for a single sharpness calculation.

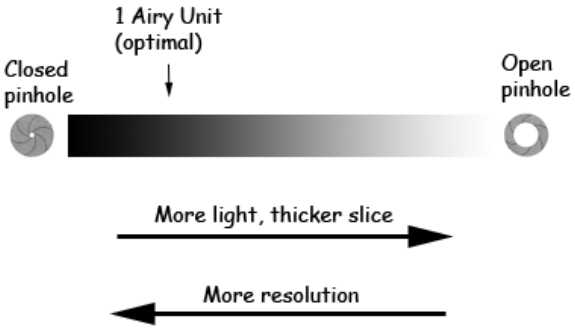

Figure 4.3: One airy unit offers maximum sectioning and thus axial resolution, without compromising light. Larger pinhole size than one airy unit increases the amount of collected light. This additional out-of-focus light blurs the image and adds to background. The figure has been adapted from [174].

In Figures 4.4(a) and 4.4(b) the normalized image sharpness obtained by Equation (4.1) is plotted over particle displacement for the confocal microscopy images with pinhole sizes of 1 and 4.5 Airy units respectively. The image sharpness takes higher values as the particle moves closer to the focus and then starts decreasing rapidly and symmetrically when moving away from it. The Lorentzian function fits well the sharpness data providing high correlation coefficients, r, equal to 0.992 (Figure 4.4(a)) and 0.989 (Figure 4.4(b)) for those two cases. The sharpness data form the so-called sharpness curves (S-curves). The r values demonstrate the similarity with the corresponding S-curves extracted in [104, 105] for widefield datasets.

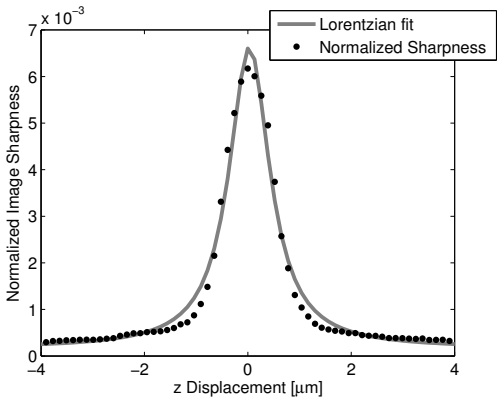

(a) 1 Airy unit

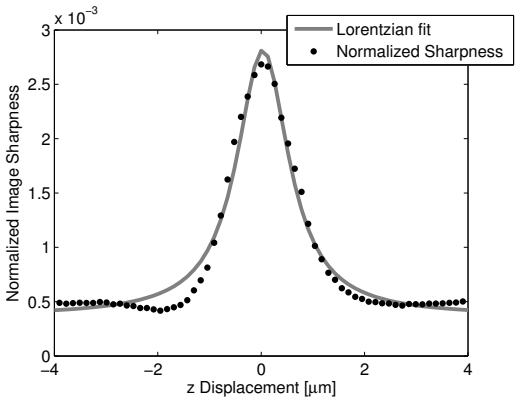

(b) 4.5 Airy units

Figure 4.4: Image sharpness data and their Lorentzian fits, acquired from confocal data in optical microscopy with different pinhole sizes a) 1 Airy Unit (true confocal) and b) 4.5 Airy Units.

Between the Figures 4.4(a) and 4.4(b), the smaller pinhole size resulted in a narrower curve where the distance between peak and lowest sharpness values was 6×10^{-3}. For the larger pinhole size the curve main-lobe was much wider and the

equivalent distance between maximum and minimum sharpness was only limited to 2.2×10^{-3}. Their differences are best shown in Figure 4.5 where the S-curves from the sharpness data of Figure 4.4 are scaled to 1 and overlaid. Overall the results show that the sharpness variation follows a reproducible pattern, from which depth information may be extracted, for different light transmissions.

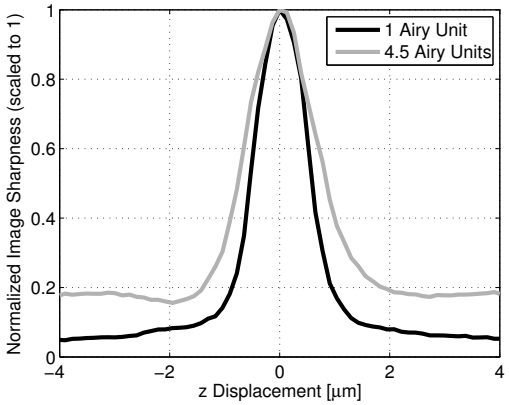

Figure 4.5: Direct comparison of the resulting S-curves from the sharpness data of Figure 4.4. The normalized sharpness values were scaled to 1 due to the different amplitudes from the two scans.

4.1.2 Multi-plane imaging

The confocal microscopy example of the previous subsection can only provide a single object plane/S-curve. However, a single S-curve would give an ambiguous dissemination of position, as one sharpness value corresponds to two possible axial positions. Further, there is near-zero sharpness dependence to position around focus, where sharpness is flat. As a result, a single plane would not allow for accurate determination of axial position beyond a wavelength depth either side of focus [104, 105, 175]. Multi-plane imaging, where multiple planes of the same object are captured simultaneously, removes the ambiguity by providing multiple references to translate sharpness to absolute axial position.

There are two requirements in order to achieve multi-plane imaging. The first is to split light into multiple images, and the second is to include a slight defocus term for each of those images. This can be accomplished in several ways such as beamsplitting or by means of Spatial Light Modulators (SLMs). One approach for multi-plane imaging in optics is through the use of a diffraction grating [176]. The grating consists of a series of slits and one such example is shown in Figure 4.6. Through diffraction it is possible to split incident light into interfering waves as explained in [177] and described in Figure 4.6. In its simplest version the slits are straight lines as depicted in Figure 4.7(a). With such a grating, incident light is separated into equal images in each order. For a simple binary phase grating over 84% of incident light can be balanced between the 0^{th} and $+1, -1$ diffraction orders, providing a simple way to beamsplit incident signal. Two orthogonal gratings can

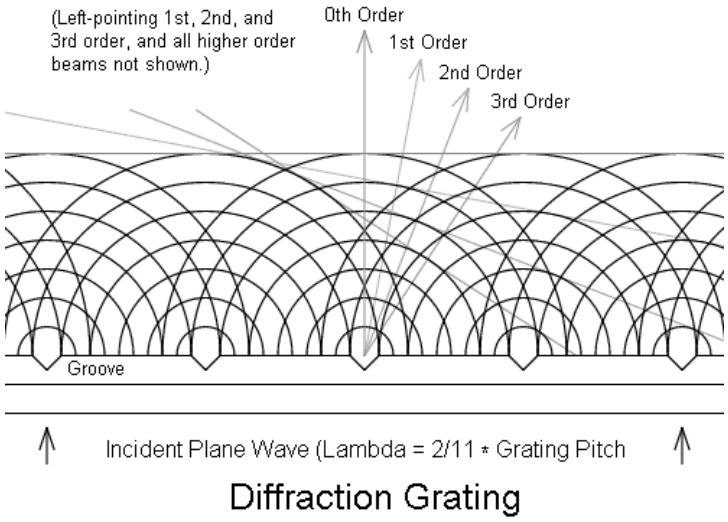

Figure 4.6: The grating splits the transmitted light and creates interference patterns that will eventually lead to the formation of new wavefronts. The figure has been adapted from [177].

provide 9 image planes with minimal optics. To introduce the defocus term needed for each order, a Quadratically Distorted Grating (QDG) is used. In Figure 4.7(b) the QDG version can be found where the straight lines are substituted by arcs of a number of circles, centred in the same point but with different radii.

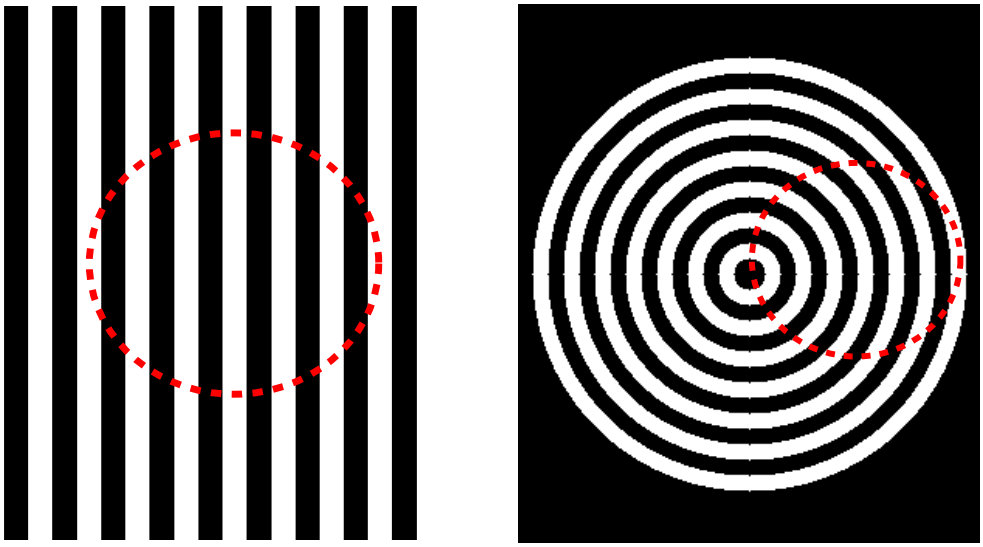

(a) Straight line grating

(b) Quadratic grating

Figure 4.7: Two differently-shaped diffraction gratings with the ability to split incident light into interfering waves. In (a) a straight line grating is shown in the circled area. In (b) the corresponding red-circled area consists of arcs of a circle resulting in a quadratically distorted diffraction grating as used in the current method.

The QDG imposes a phase change to the wavefronts scattered into the non-zero diffraction orders, so that the wavefront curvature is altered [177]. As a consequence, it has focusing power in the non-zero orders and its behaviour can be compared to the one of a lens with a different focal length in each diffraction order. By combining the QDG with a relay lens, with the QDG positioned directly in the plane of the relay lens, the system lens-grating introduces order-dependent focusing power and the focal length, f_m, of the combination is given by:

$$f_m = \frac{fR^2}{R^+2fmW_{20}}\,, \tag{4.3}$$

where f is the focal length of the relay lens, R is the radius of the grating aperture and mW_{20} is the path-length difference introduced by the curvature at the edge of the aperture in the m^{th} diffraction order. A single QDG acts as a set of lenses of positive, neutral and negative power. It is therefore possible to acquire a single image which includes at least 3 object planes at the same time [164, 165]. It is thus also possible to extract 3 sharpness values simultaneously for each position of a particle mounted on a precision translation stage as it moves in the z-axis.

4.1.3 Optical data example

An example image of multiple object planes can be found in Figure 4.8. The image consists of 100 nm fluorescent beads adhered to a glass slide in an aqueous solution with a standard cover slip on top. The figure is divided into three images each one corresponding to a different diffraction order.

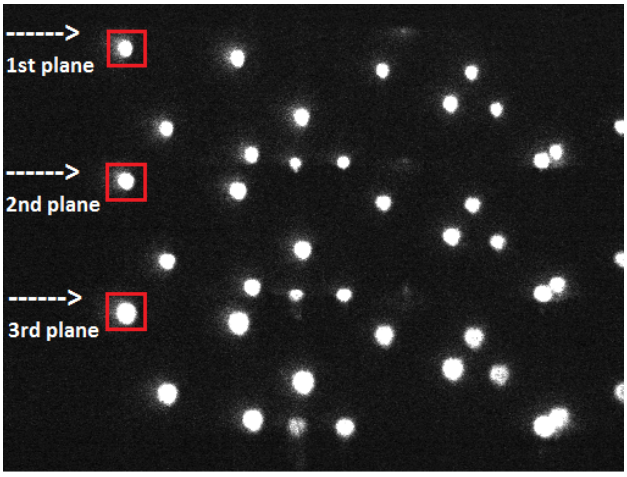

Figure 4.8: Three different planes of fluorescent beads. From the image that corresponds to a specific axial position, 3 sharpness values can be extracted for each one of the particles.

The smaller PSFs size noticed in the top plane imply the best-focused image for this specific depth thus higher sharpness value. On the other hand, the bottom

plane is equivalent to an out-of-focus image. This resulted in lower sharpness values for each of these particles. For this particular measurement, data from 41 different positions of the z-axis stage (each position corresponding to an image number) were acquired. The three resulting S-curves, formed by connecting the sharpness value of each depth and of each plane, can be seen in Figure 4.9. The individual normalized sharpness curves in this figure were estimated over the red box containing the top left PSF of the Figure 4.8 excluding all other point targets or background.

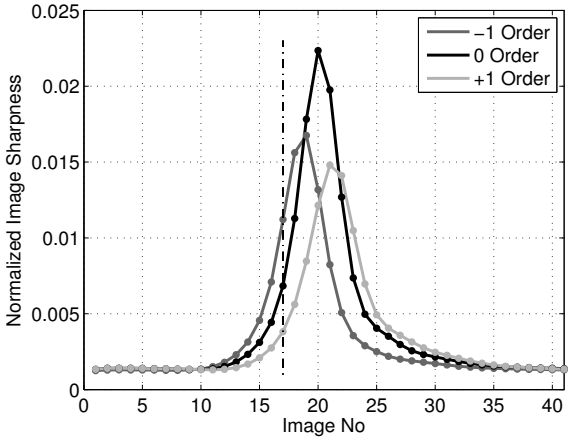

Figure 4.9: Three different S-curves extracted from a series of images similar to that shown in Figure 4.8 for the top left particle of Figure 4.8. The vertical dashed/dotted line highlights the contributions of the aforementioned image. The curve amplitude differentiation is due to the diffraction of light in three orders $(-1, 0, +1)$.

Figure 4.8 provides sharpness values over 520 nm from the central position in the direction of the -1 diffraction order (from position #17). For this image the measured sharpness values were 11.21×10^{-3}, 6.84×10^{-3} and 3.81×10^{-3} for the respective diffraction orders $-1, 0, +1$. The highest, and closest to the curve peak, sharpness was noted for the -1 light order, as expected. For the orders 0 and $+1$ the calculated sharpness was lower and hardly overcame the half-maximum values (11.18×10^{-3} and 7.39×10^{-3}) of the two curves respectively. From the Figure 4.9 it can also be observed that the amplitude of the median curve was higher than the other two since it refers to the 0^{th}-order, which has the largest proportion of the diffracted light.

4.1.4 Maximum Likelihood Estimation

Multi-plane image sharpness provides a simple way to return an axial position of a point emitter. In practice, this requires relating a single multi-plane data set to a known calibration standard, done through a Maximum-Likelihood Estimation (MLE). The MLE is an established statistical method to estimate the parameters of a dataset to a known model. The objective of the algorithm is to provide an

estimate of the particle depth position by deploying the sharpness knowledge. The 3 S-curves do not coincide and have their peaks in different positions as in-focus images, and thus maximum sharpness values, occur for different depths.

A single measurement is subject to background noise or instrument movement errors. In order to determine the variation on the calibration data, the measurements are repeated several times. In Figure 4.10 the mean S-curve and the Standard Deviation (SD) are shown after re-producing the previous result of the Figure 4.9 for 10 times. This consecutive data collection was realized during a single set of measurements where the translation stage was continuously moving back and forth.

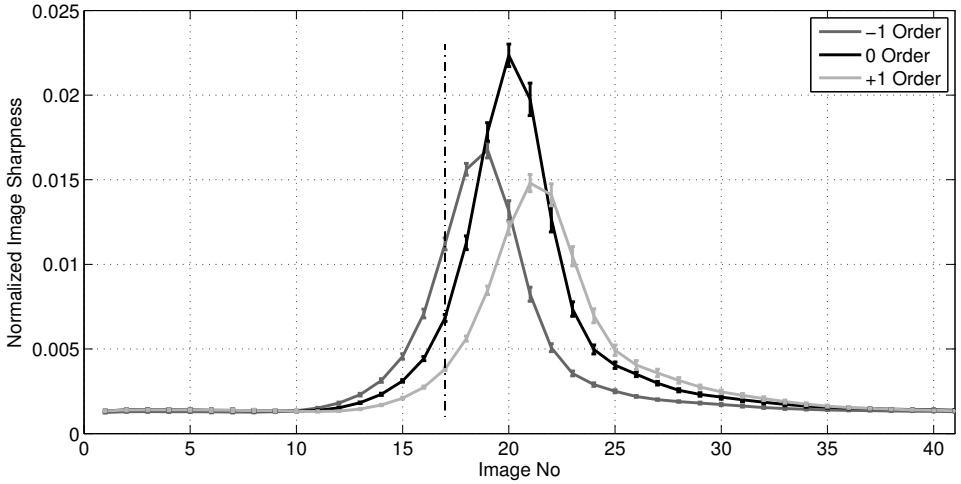

Figure 4.10: Three mean S-curves, one for each of the 3 diffraction orders $(-1, 0, +1)$, are displayed. The sharpness standard deviation in each depth position is also represented as vertical lines of varying length. The sharpness data are extracted by repeating the procedure that led to the Figure 4.9 for 10 times.

All measurements made in each diffraction order are used for the estimation of the Probability Density Function (PDF), $P(S_{opt,d}|z)$. This is the probability that a specific normalized sharpness value, $S_{opt,d}$, will be measured experimentally from the image of a target located at depth z, where d denotes the diffraction order. Since the sharpness calculations in different diffraction orders do not depend on each other and with z being known, the probability for the set of D sharpness measurements in all diffraction orders when a particle is located at z can be written as:

$$L(S_{opt,1}, S_{opt,2}, ..., S_{opt,D}|z) = \prod_{d=1}^{M} P(S_{opt,d}|z) \,, \tag{4.4}$$

where L is the likelihood for the set of sharpness measurements $S_{opt,1}, S_{opt,2}, ..., S_{opt,D}$ and D is the number of diffraction orders in which images are simultaneously recorded. The maximum likelihood estimator of the particle depth, z, is the value of z for which L is maximized given an actual dataset $S_{opt,1}, S_{opt,2}, ..., S_{opt,D}$ and the

calibration PDFs, $P(S_{opt,d}|z)$. For the PDF a Gamma distribution was selected as it fits best with the Lorentzian-like shape of the S-curves [178, 179] and with the theoretical estimation of the variance on the measured sharpness, and is given by:

$$P(S_{opt,d}|z) = \frac{e^{\bar{S}^2_{opt,d}} \bar{S}^{\alpha-1}_{opt,d}(z)\beta^{-\alpha}}{\Gamma(\alpha)}\,, \tag{4.5}$$

where $\alpha = \bar{S}^2_{opt,d}(z)/\bar{\sigma}^2_d$, $\beta = \bar{\sigma}^2_d/\bar{S}^2_{opt,d}(z)$, $\bar{S}_{opt,d}(z)$ represents the mean S-curve, $\bar{\sigma}^2_d$ the variance, both extracted by the repetitive measurements and after interpolation of those two quantities takes place, and Γ is the Gamma function. The estimated depth position is finally compared with the true position, which is provided by the position control of the translation stage. For optical work, as previously published, results showed that on exemplary data an average accuracy of 8.1 nm was possible around the peaks of the S-curves and that this number slightly deteriorates to 12.5 nm when a larger area is taken into consideration [105]. The estimated values however remain more than 40 times lower than the wavelength used (532 nm).

4.2 The ultrasound sharpness equivalent

The optical technique outlined above may be translated to an ultrasound imaging method. It is perfectly suited to ultrasound due to the ability to beamform multiple planes without the need for any additional equipment. This involves transducer array signal processing and additional statistical post-processing. The algorithm development is achieved through the use of Field II [133, 134] simulation software that can create near-realistic experimental measurement conditions. Figure 4.11 demonstrates the ultrasound PSF variation in respect to depth and to focal length. In the figure, a moving scatterer was simulated in an initial attempt to produce equivalent setup conditions with the ones used in [104] and the optical experiment above.

For use with ultrasound, the sharpness method requires that single point targets must be considered. The area of interest is denoted with the white box in the top left subfigure of the Figure 4.11. Similar to the structure of Section 4.1, the concepts of image sharpness, multi-plane imaging and MLE are introduced in the field of ultrasound imaging, with the same objective, that is the axial localization of point scatterers.

4.3 Normalized sharpness assessment

The calculation of ultrasound sharpness remains unchanged in principle (Subsection 4.3.1), for an ultrasound image containing only a single point target (Fig-

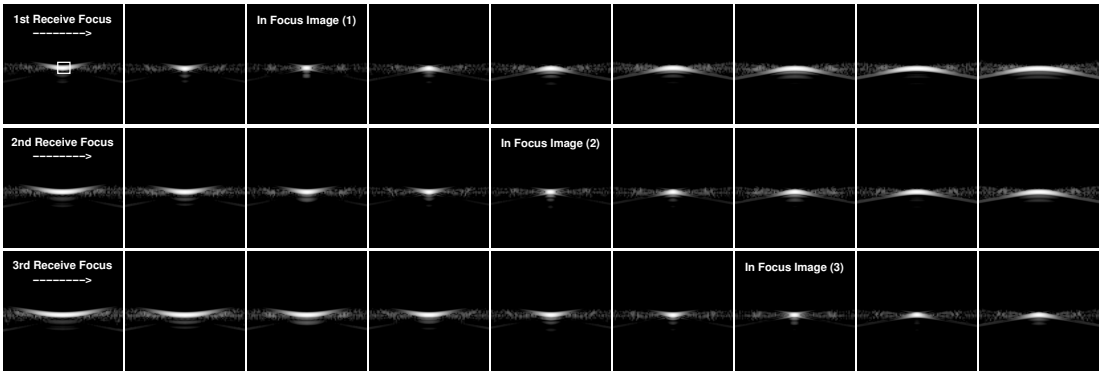

(a) -4mm (b) -3mm (c) -2mm (d) -1mm (e) 0mm (f) 1mm (g) 2mm (h) 3mm (i) 4mm

Figure 4.11: A point target imaged at different axial displacements from an initial position (e). Each image corresponds to an area of 10×10 mm^2. The same dataset was beamformed with three different foci in receive, in every 2 mm. A 60 dB dynamic range display was used.

ure 4.11(a)). However, in ultrasound imaging it is also possible to access the raw RF data from which the final image is formed and avoid distortions from image format conversions. Hence, there is the signal alternative for the sharpness assessment (Subsection 4.3.2). In cases where the rule of a single scatterer analysis is not preserved, sharpness variation becomes irregular over axial displacement and this is discussed in Subsection 4.3.3.

4.3.1 Image derived sharpness

Compared to Equation (4.1), the subtraction in the numerator is neglected, since ultrasound point scatter data are not flux-dependent. Therefore, sharpness is now given by:

$$S_{us} = \sum_{k=1}^{K} n_k^2 / (\sum_{k=1}^{K} n_k)^2 \,, \tag{4.6}$$

where S_{us} is the normalized image sharpness, K is the number of pixels, and n_k is the recorded intensity value of the k^{th} pixel, exactly as they were defined in the optical method. In Figure 4.12 the normalized image sharpness variation is plotted over axial displacement for the point target of Figure 4.11 when the intermediate focal length is employed (2nd row). In Figure 4.12 the best Matlab Lorentzian and Gaussian fits of the resulting sharpness curve are also displayed in (a) and (b) respectively.

This is done in order to model the ultrasound sharpness behavior and find the analogy between optical and ultrasound S-curves. The correlation coefficient of the ultrasound data to the Lorentzian in Figure 4.12(a) was $r = 0.986$ while the fit to the

Gaussian in Figure 4.12(b) was below 0.90. It can also be observed in Figure 4.12 that the Gaussian function cannot describe accurately this image quality metric, while the Lorentzian presented very close resemblance to the data curve.

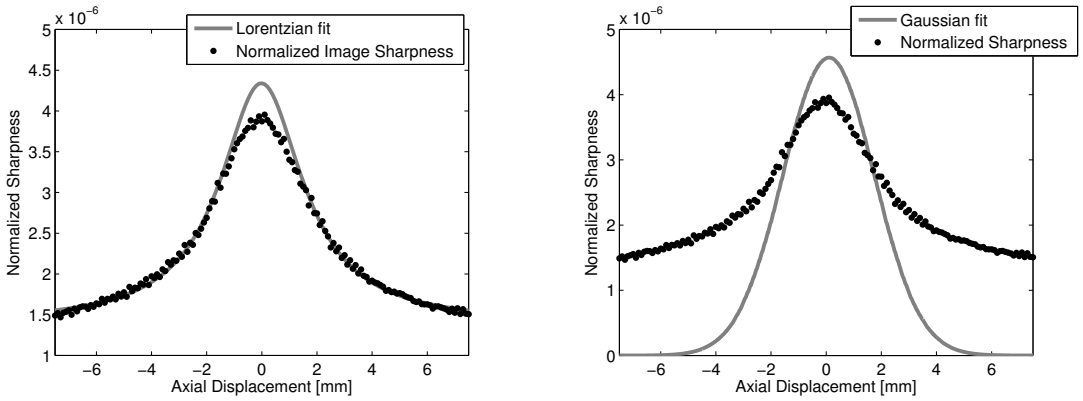

(a) Lorentzian fit

(b) Gaussian fit

Figure 4.12: An example of ultrasound image sharpness data together with the best (a) Lorentzian and (b) Gaussian fit. The sharpness data correspond to the intermediate row of the Figure 4.11.

4.3.2 Signal derived sharpness

Following the raw RF data acquisition, the transducer element signals are rectified and then the Hilbert Transform [180] is employed to provide a pre-image signal free from image processing bias [4]. At this stage, before reaching the image formation, an alternative ultrasound sharpness may be derived based on those Hilbert amplitudes. As a result the optical pixel intensity used in [104, 105] is replaced with the square of the signal amplitude and the ultrasound sharpness function is given by:

$$S = \sum_{q=1}^{Q} E_q^4 / (\sum_{q=1}^{Q} E_q^2)^2 \,, \tag{4.7}$$

where S is the normalized image sharpness calculated from the Hilbert data and E_q^2 is the squared envelope value of the q^{th} sample. The metric is calculated over Q samples in total, that include a single point source. In theory, the new sharpness definition is expected to be more precise and suitable for this algorithm, since the raw information is exploited prior to further processing.

In Figure 4.13 the normalized sharpness from the Hilbert amplitudes is plotted over axial displacement for the same Field II simulated point target as in Figure 4.12. The best Lorentzian and Gaussian fits can also be found in Figure 4.13(a) and 4.13(b) respectively with higher correlation coefficients (0.997 and 0.995) apparent this time, compared to the ones found in Subsection 4.3.1. Both functions seem to model

accurately the sharpness variation over depth. The Gaussian fit describes the edges more accurately, whereas the Lorentzian results in a marginally better fit of the peak.

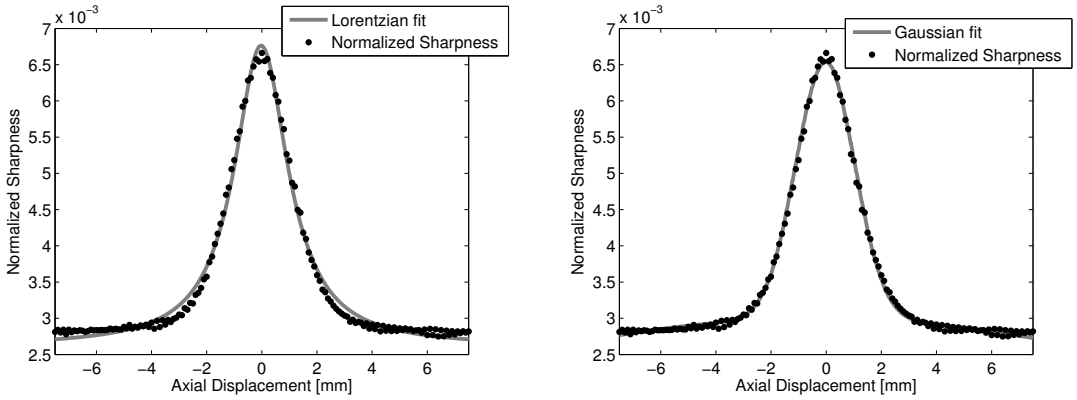

(a) Lorentzian fit

(b) Gaussian fit

Figure 4.13: An example of ultrasound sharpness data together with the best (a) Lorentzian and (b) Gaussian fit. Unlike the Figure 4.12, the sharpness data were extracted by the transducer element signals rather than from scan-converted images, and correspond again to the intermediate row of the Figure 4.11.

Overall, the sharpness variation of the Figure 4.13 is closer than that of the Figure 4.12, to the optical sharpness variation (Figure 4.4). The difference between Figure 4.13 and Figure 4.12 relies on the sharpness values away from focus where the drop in the latter is not as rapid as noted for the sharpness extracted by ultrasound signals or the optics curve. The curve shape is an important feature for the algorithm as it determines its depth detection capability. For this reason the term normalized image sharpness will be replaced by the term normalized signal sharpness or simply normalized sharpness when it refers to ultrasound data.

4.3.3 The single scatterer assumption

An ultrasound image may contain more than one closely spaced scatterers. This would mean that the Region of Interest (ROI) selection may be prone to errors as a result of the number of scatterers that are actually included within it. It can be observed from Figure 4.11 that particularly in the out-of-focus images (Figure 4.11(a) third row, (i) first row), the PSF sidelobes may spread laterally up to ± 5 mm from the scatterer centre. This is because with the use of a fixed receive focus the DAS spatial resolution is only good around the focal point and deteriorates greatly away from it (Subsection 1.1.3).

As a consequence there is a high chance of close or overlapping PSFs in case the ROI includes a whole PSF. In order to solve this problem and avoid extra signal on the outer part, the ROI can be centred on the PSF but a box of size much smaller than the PSF can be then used for the sharpness calculation. Evidence form optics

shows that this actually is possible, as long as the box size same is kept the same from calibration to measurement [104, 105].

Therefore the ROI may be defined as a box centred at the centre of the PSF and of a size adequate to encompass the PSF main lobe at all defocus conditions, as shown in Figure 4.11(a) where the white box has dimensions 1.3×1.3 mm^2. In this example the box size is not important as there is only one scatterer in the image. In general in order to create the calibration curves the PSF centre must be approximately known and then the ROI is selected around it as mentioned above. In situations where the measuring area is not ideal, i.e more than one scatterers (at different depths) or only part of a scatterer are included in the ROI, the sharpness data will be affected. Thus the sharpness curves will not accurately reflect the calibrated standard and quantitative measurments will become difficult. Two examples of such distorted S-curves are given in Figure 4.14.

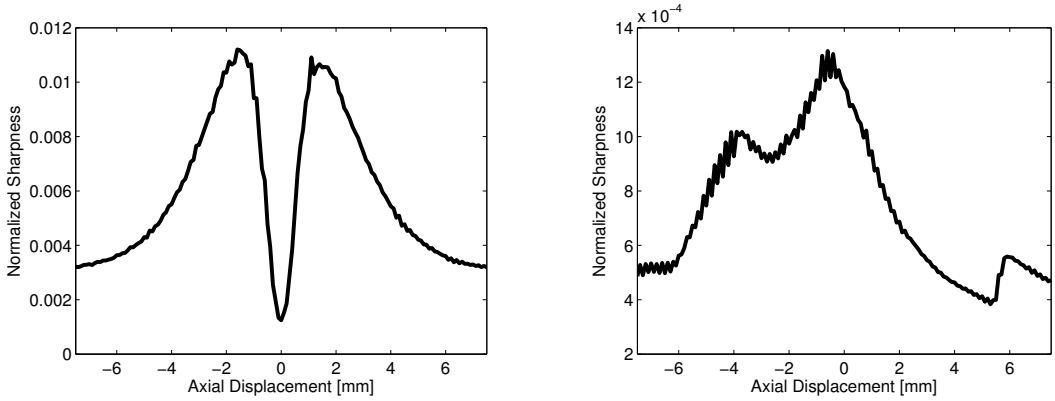

(a) Half scatterer

(b) Multiple scatterers

Figure 4.14: S-curves where (a) only a part of a single point target is included in the ROI for the sharpness calculation, and (b) multiple point targets are inside this area.

In 4.14(a), the sharpness was calculated for an area that included a scatterer cut in two while moving across the z direction. When the PSF became smaller as in Figure 4.11(e) (2nd row), the point almost disappeared from the selected area and a curve minimum instead of a maximum appeared. Note that outwith this area the general sharpness features was reproduced but at a lower magnitude, due to the inherent symmetry in the PSF. In Figure 4.14(b) the sharpness was calculated for an area including two scatterers at different depths. As a result the curve maximum was substituted from two local lower maxima, each one corresponding to the depth when each scatterer was in-focus. In both instances, the Lorentzian curve shape was not preserved indicating the presence of multiple targets or the possible absence of a whole PSF.

4.4 Multi-foci beamforming

The multi-plane imaging of the optical method (Subsection 4.1.2) is substituted in ultrasonics by multi-foci beamforming. The same principles can be directly translated to ultrasound imaging, however the multiple focusing is achieved by conventional beamforming, requiring no additional hardware and is thus considerably simpler to implement than the optical equivalent.

In the ultrasonics case the receive focus provides higher flexibility, compared to the transmit, as the element signals can be stored after the transmission and beamformed offline, or even in real time, in multiple ways. The conventional method to process the received transducer element signals is the DAS beamformer that was already defined in Subsection 2.2.1 by Equation (2.1) and Figure 2.1 of the 2^{nd} Chapter. The beamformer output, $B(t)$ depends on the τ_m that is the time delay applied to the mth element used both in transmit and receive given by:

$$\tau_m(r_p) = \frac{2}{c}\sqrt{(x_m - x_p)^2 + (z_m - z_p)^2}\,, \tag{4.8}$$

where (x_m, z_m) is the location of the m^{th} receiving element, $r_p = (x_p, z_p)$ is the focus point, and c is the speed of sound. From Equation (2.1) and Equation (4.8) it can be seen that $B(t)$ can be calculated for any r_p. In this way the requirement for three simultaneous images in [105] can be easily met. Three different receive foci can be implemented and each of the three beamformer outputs will produce a different image of the same object as in Figure 4.11. Similarly to the optical method, the example of Figure 4.13 can be now expanded to different τ_m and multiple images can be captured for each position from the raw scatter data. The different receive foci (or else τ_m) must be selected close enough so that they ensure the generation of overlapping S-curves, and at the same time, far enough to ensure that the S-curves will peak at different depths. The three S-curves of a single point scatterer are shown in Figure 4.15 as a function of point displacement in correspondence to the three different selected receive foci. The receive foci were positioned at the centre of the scatterer displacement and at ± 2 mm away from it, to fit the above requirement.

A comparison between the sharpness data of Figure 4.13 and the middle S-curve of the Figure 4.15 shows that the second one presents a more steep decrease around the peak although the same data were used for the sharpness calculations. The difference is attributed to different distances between two successive sharpness measurements which slightly affects the curve shape. This will be extensively studied in Subsection 4.9.2.

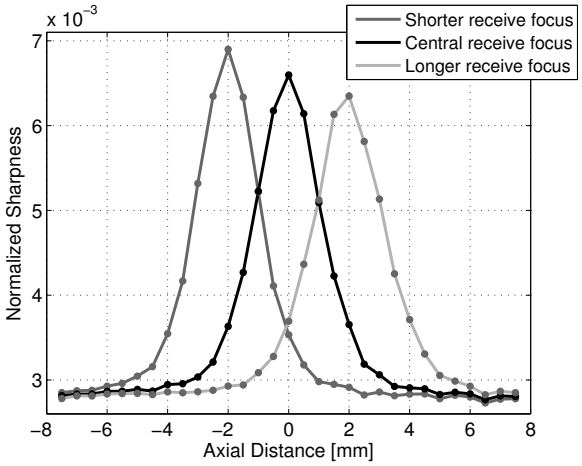

Figure 4.15: Three different S-curves extracted from a series of ultrasound images that include a single scatterer as in Figure 4.11. The curve peak differentiation is due to the increasing distance of the receive focus to the transducer surface.

4.5 Maximum Likelihood Estimation

The MLE is employed in the ultrasound analogue, as in Subsection 4.1.4, to extract precisely the axial location of a single point source using known calibration data (i.e. the sharpness values). The estimate is unique, since each position is characterized by three distinct sharpness values. The calibration data are derived from repetitive measurements of point sources moving in depth. The ultrasonic analogue involves multiple frame acquisition, as a point scatterer is positioned at each axial distance. The varying measurements are enabled by repeating the data acquisition procedure in the presence of realistic noise, which then leads to the calculation of the mean S-curves and the respective standard deviation. The addition of noise is discussed separately in the Subsection 4.7.4.

The ultrasound sharpness data may then be fitted by either a Lorentzian or Gaussian function that are both good approximations of a mean S-curve peak and slopes as shown in Figure 4.13 [106, 107]. Alternatively, the data may simply be interpolated using the Matlab spline interpolation function. At all cases, the fitted data are oversampled by a factor K, to provide sub-resolution sampling for maximizing the techniques accuracy. To be more specific, the distance between 2 successive sharpness measurements (z-step) after the fitting/interpolation stage becomes z-step/K. The fitted or interpolated data are then used for the estimation of the PDF, $P(S_j|z)$. This is the probability that a specific normalized sharpness value, S_j, will be assigned to a point source located at depth z, where j denotes the focus in receive. Equations 4.4 and 4.5 (Section 4.1.4) are adjusted to the ultrasound data. The sharpness calculations are independent from the receive focus and z is also known as in the optics analogue. Hence, the probability for the set of N sharpness measurements for all receive foci, when a point source is located at z,

can be expressed as:

$$L(S_1, S_2, ..., S_N|z) = \prod_{j=1}^{N} P(S_j|z) \,, \tag{4.9}$$

where L is the likelihood for the set of sharpness measurements $S_1, S_2, ..., S_N$ and N is the number of the receive foci. The maximum likelihood estimator of the point depth, z, is the value of z for which L is maximized given an actual dataset $S_1, S_2, ..., S_N$ and the calibration PDFs, $P(S_j|z)$. For the PDF a Gamma distribution was selected as it fits best with the Lorentzian shaped S-curves and their variance, and is given by:

$$P(S_j|z) = \frac{e^{\bar{S}_j^2} \bar{S}_j^{\alpha-1}(z)\beta^{-\alpha}}{\Gamma(\alpha)} \,, \tag{4.10}$$

where $\alpha = \bar{S}_j^2(z)/\bar{\sigma}_j^2$, $\beta = \bar{\sigma}_j^2/\bar{S}_j^2(z)$, $\bar{S}_j(z)$ represents the interpolated mean S-curve, $\bar{\sigma}_j^2$ the interpolated variance and Γ is the Gamma function. A set of three measured sharpness values are the PDF's input and the output is the depth estimate for which the PDF becomes maximum with an estimation error equal to the modulated step. This estimate is compared with that already known, from the simulation setup. Two PDF examples are plotted over depth in Subsection 4.7.2, once the simulation is described and the initial results shown.

4.6 Ultrasound simulations using Field II

In this section the simulation setup is explained including the transducer definition, the phantoms, and the transmission of ultrasound, used for the initial development of the normalized sharpness algorithm. The aim is to develop the technique in simulation so that the future experiment can be informed. All simulations were carried out with Field II [133, 134, 181] software and Matlab scripts were utilized for the data post-processing.

4.6.1 Simulation setup

A phantom consisting of a single point scatterer at a depth of 40 mm, was created and used as a target to replicate the optical situation. The phantom was scanned by single Plane Wave (PW) emissions (Appendix A), made by a 7 MHz, 192 element, linear array simulated transducer with λ spacing. The central transducer element was located above the point target. The speed of sound, c was set to 1540 m/s and all the parameters of the scan are given in Table 4.1.

Transducer	
Transducer type	Linear array
Transducer element pitch	208 μm
Transducer element kerf	35 μm
Transducer element height	4.5 mm
Center frequency, f_0	7 MHz
Bandwidth	60% fractional
Speed of sound, c	1540 m/s
Wavelength, $\lambda = c/f_0$	220 μm
Excitation pulse	Two-cycle sinusoid at f_0
Plane Wave Emission	
Transmit apodization	Hanning
Receive apodization	Hanning
Receive focus depth	38/40/42 mm
Number of transmitting elements	192
Number of receiving elements, M	192
Number of emissions	1
Particle Movement	
Highest point	$(x, z) = (0, 32.5)$ mm
Lowest point	$(x, z) = (0, 47.5)$ mm
Total distance covered	15 mm (axially only)
z-step between succesive emissions	0.1 mm

Table 4.1: Simulation setup parameters

Raw data from a single unfocused emission were acquired from all 192 channels individually in receive. The data were stored and then a new phantom was created, with the point scatterer moved 100 μm in direction away from the transducers surface until it reached the depth of 47.5 mm. The process was followed for the opposite direction, until the point scatterer reached a depth of 32.5 mm. Therefore, there were 151 acquisitions overall with the point target covering a distance of exactly 15 mm. For the initial investigation, ten sharpness datasets were created where White Gaussian Noise (WGN) with a Signal to Noise Ratio (SNR) equal to 10 dB was added to the raw signals.

For each acquisition the data were beamformed with three different foci in receive. The central receive focus was selected at a depth of 40 mm, that is the target's initial position and then the two other values were at -2 mm and $+2$ mm of the starting depth. For curve fitting stage a factor $K = 1000$ was used and the depth vector following the sharpness data oversampling, was also updated and the new z-step was 0.1/1000 mm.

4.6.2 Data analysis

The conventional axial resolution was defined in Subsection 1.1.3. Here, the excitation pulse was a two-cycle sinusoid at f_0 (Table 4.1) resulting in a theoretical resolution limit equal to the wavelength used ($2\lambda/2$). The proposed method aims to increase the axial resolution by improving the the localization accuracy of a single scatterer.

The accuracy of the normalized sharpness method was indicated by the depth deviation of the method's z-estimate to the actual scatterer position, or d_{dev} in short. Since there are 10 simulation repetitions, d_{dev} resulted from the Root Mean Square Error (RMSE) from all 10 cases. The average d_{dev} was calculated for several depth ranges of the total scatterer displacement, as in the optics equivalent (Subsection 4.1.4). For each depth range, the standard deviation of the average d_{dev}, or in short d_{SD}, was also calculated as an extra indicator of the measurements' uncertainty. Both d_{dev} and d_{SD} were compared, as in the optics example, with the wavelength used.

4.6.3 Algorithm summary

All the steps from the ultrasound transmission up to the received data processing and the extraction of the depth estimates are shown here under the following algorithm representation (Algorithm 1) as a summary of the current section.

Algorithm 1 Ultrasound sharpness algorithm for precise depth detection

```
for z = z_start to z_end do
    Create a Field II phantom including a point target at depth z
    for i = 1 to NumFrames do
        Emit ultrasound pulses from an active aperture
        (in PW all elements are used for transmission)
        Collect and store raw RF data from all emissions
        for j = 1 to N do
            Beamform acquired data according to eq. (2.1)
            with fixed focus j in receive
        end for
    end for
end for
Calculate all sharpness values S_{z,i,j} based on eq. (4.7)
Calculate statistical measures from sharpness data
  -Extract mean sharpness values for each position
  -Extract the standard deviation from mean values
Plot mean S-curves and associated deviation over depth
Interpolate/fit data by a K factor
Select the PDF model and insert interpolated data
Receive depth estimates and compare with actual depth
```

4.7 S-curves from plane wave emission

Plane wave transmission was initially adopted as the best approximation to the optical equivalent [105] where particles are self-illuminated and thus no focused transmission applies. The unfocused beams offer the advantage of covering the whole image region with only one emission, which allows for high frame rate and multiple acquisitions [106].

By following the steps of Algorithm 1 and by using the scan parameters of Table 4.1, for each of the three receive foci, 151 normalized sharpness values are calculated leading to the generation of three S-curves. In Figure 4.16 three sharpness datasets (mean and SD) can be found together with their Lorentzian and Gaussian fits. A random example of 3 PSFs linked each one to a sharpness value is also included. In comparison to Figure 4.11 the images of Figure 4.16 show the effect of noise addition in the displayed point scatter image. While the surrounding area becomes slightly more blurry which deteriorates with depth in the presence of noise, the PSF appearance is kept the same in both cases.

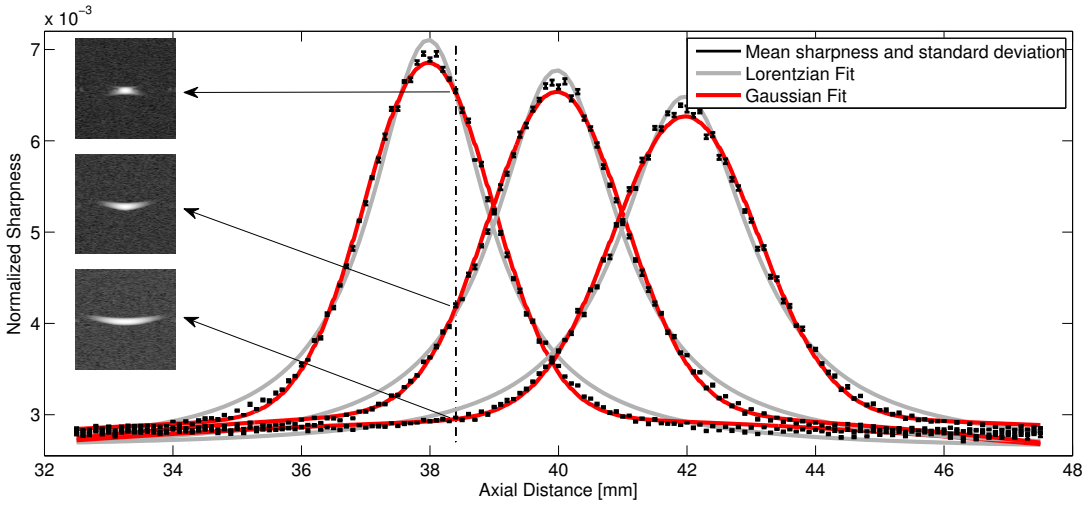

Figure 4.16: Mean sharpness is plotted over axial displacement for three receive foci (38 mm, 40 mm, 42 mm), with the corresponding Lorentzian and Gaussian fits. The error bar represents the sharpness SD in each depth. The displayed data result from ten Field II acquisitions in each z-position for a simulated point target moved 15 mm axially around an initial depth (40 mm). Each curve's peak is located at the position of each receive focus. A set of 3 randomly selected PSFs from each focal plane for the same axial position are also shown as an example. Each image is 6×6 mm^2 and a 60 dB dynamic range display was used. Mean sharpness values were calculated to 6.548×10^{-3} ($\pm 6 \times 10^{-6}$), 4.197×10^{-3} ($\pm 6 \times 10^{-6}$) and 2.972×10^{-3} ($\pm 2 \times 10^{-6}$) for the 1^{st}, 2^{nd} and 3^{rd} receive focus respectively for the point target located at 38.4 mm.

4.7.1 Accuracy from signal derived sharpness

Figure 4.17 shows the three mean S-curves in (a), together with the d_{dev} in (b). Figure 4.17 includes the resulting depth deviations when a Lorentzian function, a Gaussian function or spline interpolation were used to model the mean S-curves. The same functions were used to model the sharpness SD that, although it doesn't follow any specific trend, presents higher values around the peak of an S-curve and lower at the edges. In the figure, the ultrasound wavelength used, is also displayed as a standard of comparison.

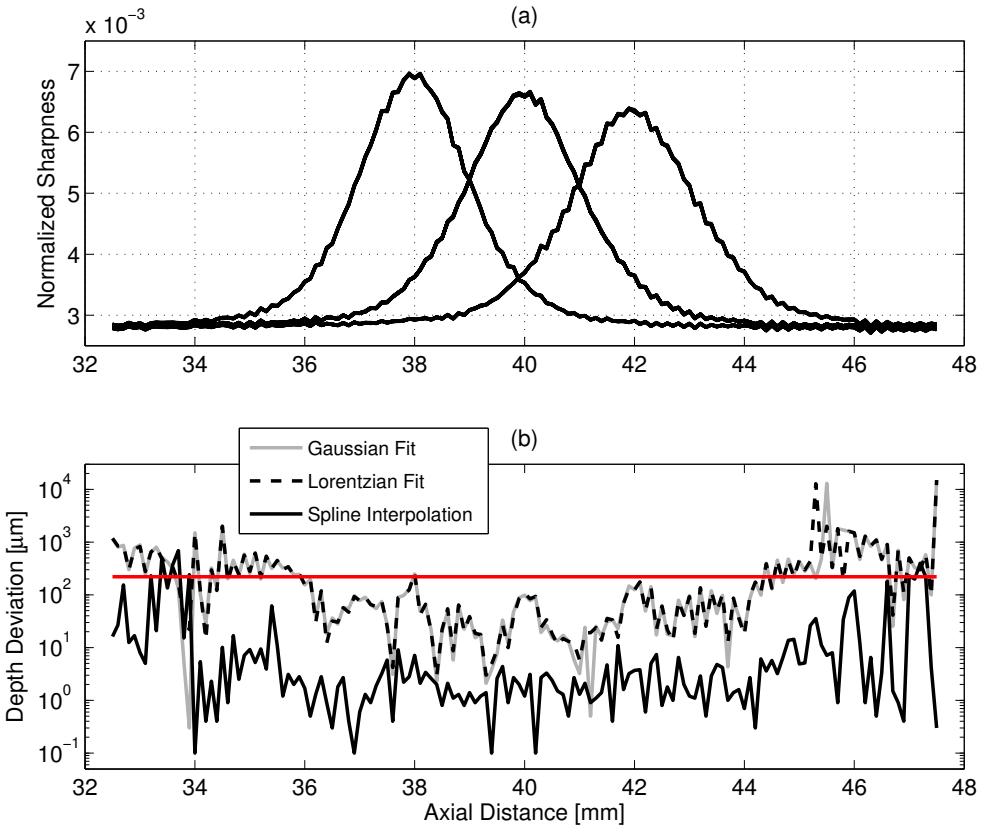

Figure 4.17: (a) A set of three normalized S-curves from a simulated ultrasound point target moving in depth. Data were generated by unfocused PW ultrasound transmission and by beamforming with three different foci in receive. The d_{dev} is shown in (b) for each depth position and for the different fitting functions used to approximate the calculated sharpness data. The red line in (b) indicates the wavelength used.

The algorithm does not perform uniformly for the total 15 mm distance. The d_{dev} increases greatly near the displacement edges. When the Lorentzian fit was used to model the mean sharpness, the average d_{dev} was equal to 29.6 μm ($\approx 0.13\lambda$) for a depth range of 3.3 mm, between 38.4 mm and 41.7 mm. This range roughly covers the area around the peak of the central S-curve and one adjacent slope of each of the

other S-curves. The d_{SD} for the same range was calculated to 27.3 μm ($\approx 0.12\lambda$). The calculations show resulting values in the range of $\approx \lambda/10$. Outside this specific distance, the d_{dev} increases reducing the method's performance. Similar numbers in terms of axial localization precision ($\approx \lambda/10$) and depth range were acquired when the Gaussian fit was used. The Gaussian and the Lorentzian d_{dev} curves are insignificantly different as shown in Figure 4.17(b). In this case the average d_{dev} was equal to 28.14 μm ($\approx 0.13\lambda$) between 38.3 mm and 41.7 mm (3.4 mm in total), with a d_{SD} equal to 26.2 μm ($\approx 0.12\lambda$).

The spline interpolation provides significantly increased accuracy in the scatterer localization (Figure 4.17). The interpolated sharpness data (mean S-curves and standard deviation) are the best fit to the actual measured sharpness values than any other fitting functions. Therefore, the d_{dev} was greatly reduced and reached values in the range of $\lambda/100$, with exact values depending on the distances that the accuracy is measured. The reported average d_{dev} was 2.03 μm ($\approx 0.0092\lambda$), between 38.1 mm and 41.8 mm (3.7 mm in total), with d_{SD} equal to 1.83 μm ($\approx 0.0083\lambda$). However, unlike the previous cases, the d_{dev} here was kept relatively low for a longer z distance.

In order to make this more clear, the d_{dev} in the spline interpolation case was plotted separately over axial distance in Figure 4.18. A slightly smoothed version of the depth deviation was included to describe how the accuracy changes with depth. The smoothed deviation may help identify high and low precision areas and potentially make the normalized method assessment more systematic. Zooming into this curve shows that there is a 2.26 μm ($\approx 0.01\lambda$) average d_{dev} with a d_{SD} of 2.01 μm ($\approx 0.0091\lambda$) for an 8 mm depth range (between 36 mm and 44 mm).

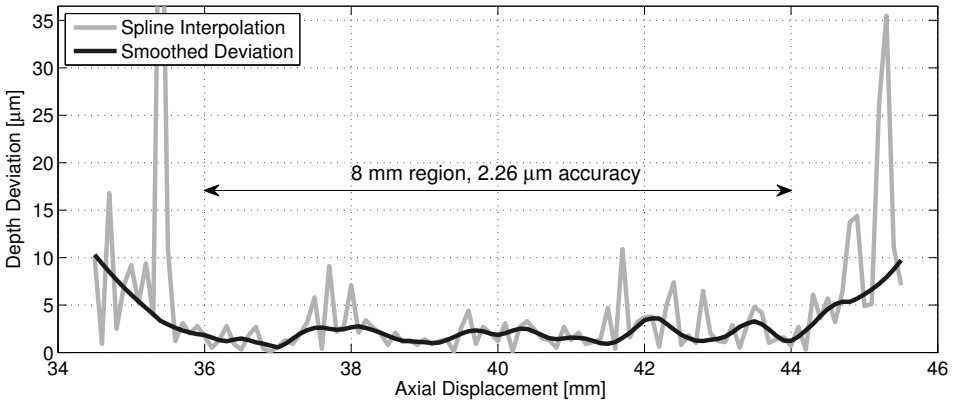

Figure 4.18: Actual and smoothed versions of the depth deviation recorded when spline interpolation was used to model the measured sharpness data. The average d_{dev} for an 8 mm depth range covering the slopes of all 3 S-curves was equal to 2.26μm. Outside the limits of $[-4, +4]$ mm from the central position (40 mm), the sharpness method's performance decreases but the accuracy of the localization always remains significantly below the wavelength.

4.7.2 The probability density function

Despite the generally low average d_{dev} calculated in the spline interpolation data processing, it can be noted from Figure 4.18, that some depth estimates are more accurate than others. Each depth estimate, and thus its accuracy, depends on the PDF maximum noticed during the MLE analysis. Usually, a high and more narrow PDF will result into a more precise estimate while the d_{dev} is likely to be higher for lower-peaked wider PDFs. In Figure 4.19, two examples of the Gamma PDF are shown around the area of their maximum.

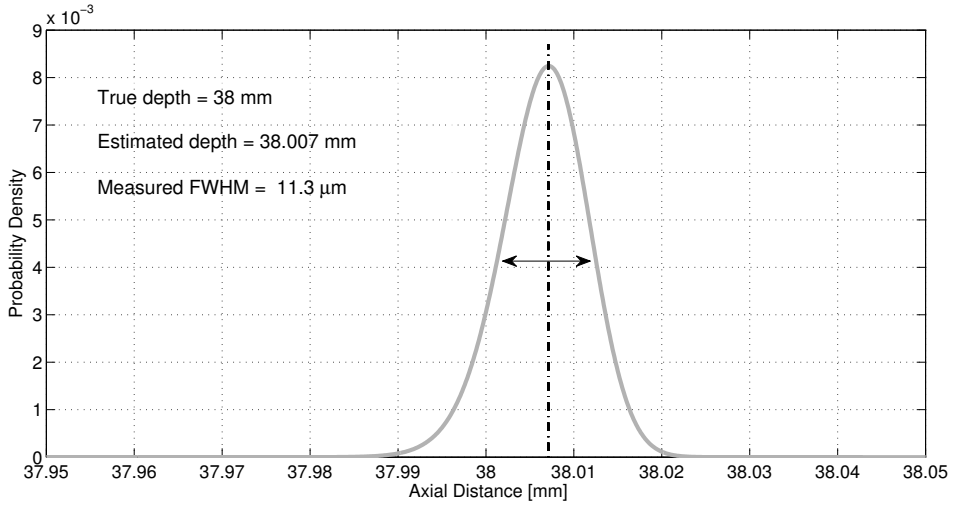

(a) PDF at 38 mm

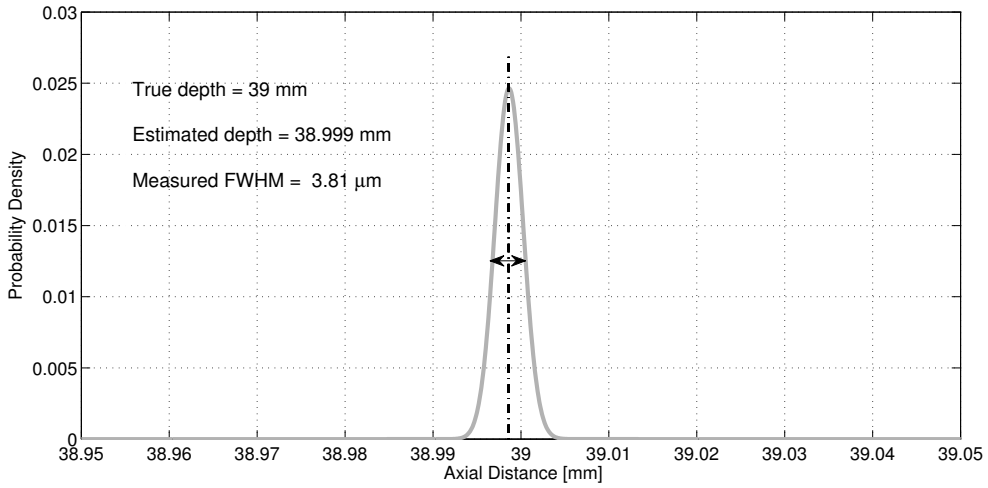

(b) PDF at 39 mm

Figure 4.19: Probability density function plotted over depth when the scatterer was located at (a) 38 mm and (b) 39 mm. The PDF maximum indicates the normalized sharpness method's estimate for this position. In (a) the maximum was found at 38.007 mm resulting in a d_{dev} equal to 7.1 μm. In (b) the maximum was at 38.999 mm resulting in a d_{dev} equal to 1.4 μm.

The true point scatterer position was 38 and 39 mm respectively for the two subfig-

ures. From Figure 4.18 it may be seen that at depth equal to 38 mm, the d_{dev} was relatively high (7.1μm) whereas a smaller one (1.4 μm) was noticed for the sharpness method's estimate at 39 mm. Indeed the 7.1 μm was the d_{dev} of the curve maximum (equal to 8.2×10^{-3}) from 38 mm and the FWHM was 11.3 μm (Figure 4.19(a)). The corresponding numbers of Figure 4.19(b) were 0.024 for the peak value and 3.81 μm for the FWHM while the d_{dev} was equal to 1.4 μm. The calculation of the PDF FWHM enables further comparisons with the axial FWHM of the DAS beamformer used here. The axial FWHM is also a good indicator of the axial resolution and can be used for comparisons in the same way the lateral FWHM was used in Chapters 2 and 3 for the lateral resolution assessment.

In Figure 4.20(a), the PSF of the scatterer located at 40 mm is shown, where the receive focus was set at 40 mm. The −6 dB decrease shows the axial FWHM which was equal to 174.19 μm. Here a 40 dB dynamic range display was selected as only the width of the main lobe is of major interest. In Figure 4.20(b), an alternative FWHM calculation is shown corresponding to the Hilbert envelope of the RF signal that passes through the centre of the scatterer, resulting in this Gaussian-shaped curve [182]. Following the Hilbert transform [180], the axial FWHM was calculated again at 174.19 μm. Whereas the lateral FWHM is subject to the focus and changes greatly with axial displacement, the axial one remains unaffected as a target moves deeper.

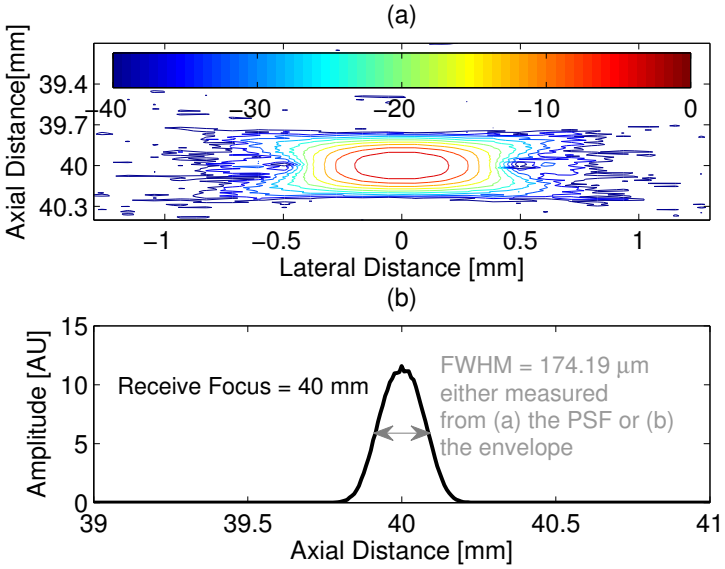

Figure 4.20: Axial FWHM assessment (a) from the PSF contour following the logarithmic compression and (b) from the Hilbert derived envelope of the RF signal through the centre of the scatterer. The simulated scatterer was located at 40 mm depth and a 40 dB dynamic range display was used.

In Figure 4.21(a) all the PDF FWHM from the spline interpolation processing and the DAS axial FWHM as calculated above, are plotted over axial distance. The

PDF FWHM curve presents similar curvature with the d_{dev} of the spline interpolation in Figure 4.17(b), with lower values at the middle of the scatterer displacement and higher at the edges. For an 8 mm range (from 36 mm to 44 mm) the average PDF FWHM was not higher than 7.54 μm ($\approx 0.03\lambda$) or 23 times lower than the DAS axial FWHM. The improvement is best demonstrated in Figure 4.21(b) where the Hilbert envelope of Figure 4.20(b) is plotted with the PDF at the same depth (40 mm). The PDF main lobe was significantly narrower and the ratio of the two FWHMs shows a $\approx$ 21 fold more accurate localization in favor of the normalized sharpness method.

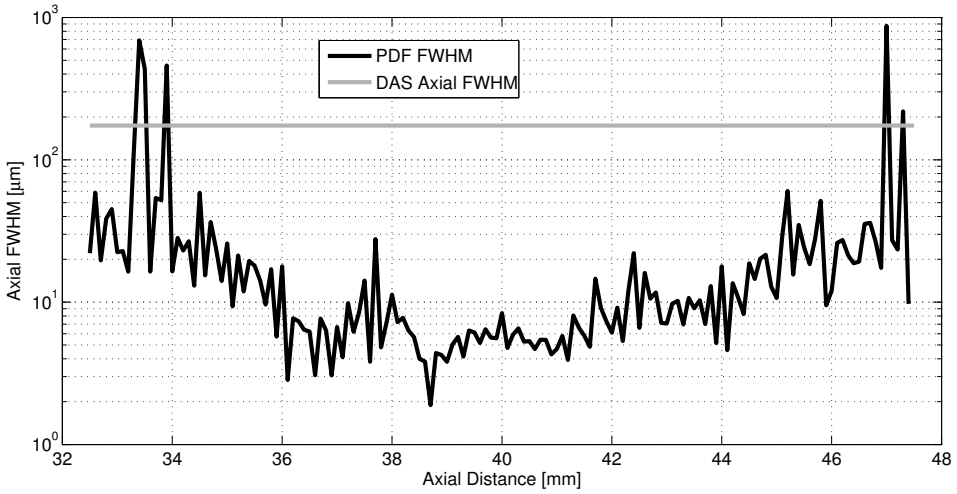

(a)

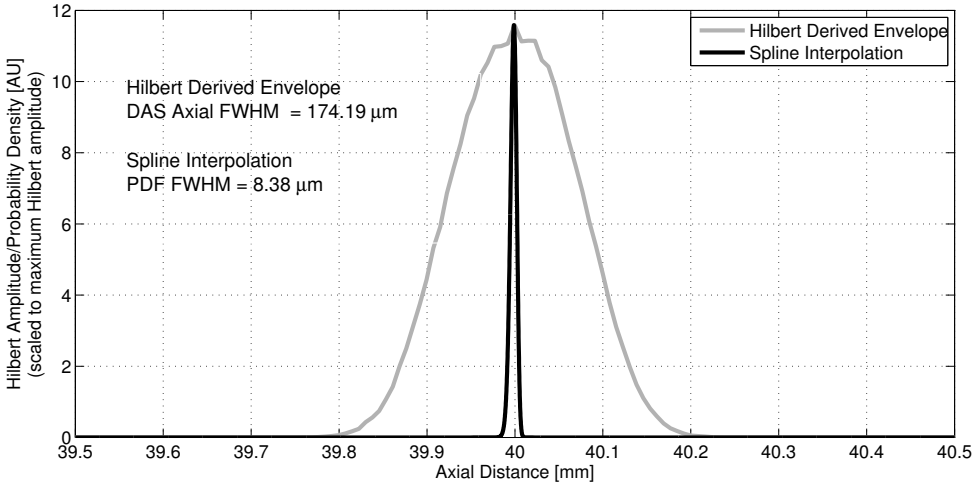

(b)

Figure 4.21: (a) The constant DAS axial FWHM is shown in comparison to the resulting FWHM from all 151 PDFs for each depth position, when spline interpolation was used for the sharpness analysis. The PDF at 40 mm depth was scaled to the maximum Hilbert amplitude and plotted together with the envelope at the same depth in (b).

4.7.3 Accuracy from image derived sharpness

In Figure 4.22(a) the three mean S-curves extracted by image data instead of signals are displayed, and in Figure 4.22(b) the d_{dev} can be found. The figure compares to Figure 4.17 and the same data were used for the image and accuracy analysis that follows. The Lorentzian or Gaussian functions are unable to provide a precise fit for the image sharpness values (Figure 4.12), and as a consequence the method was only examined with spline interpolation fitted data. Therefore, only one d_{dev} curve from those data in Figure 4.22(b) was displayed and compared with the wavelength.

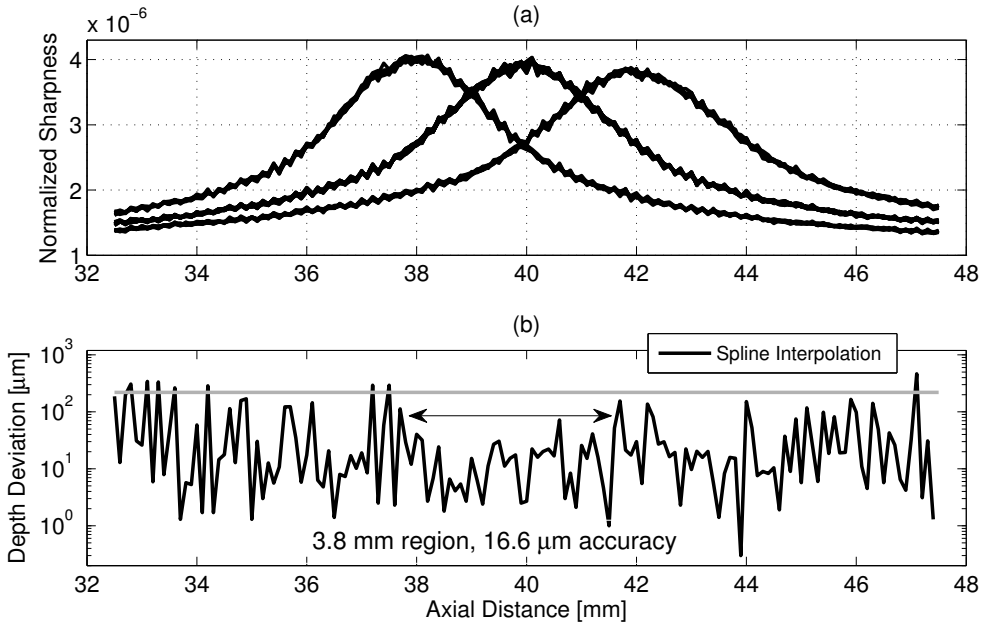

Figure 4.22: (a) A set of three normalized image sharpness curves from a simulated ultrasound point target moving in depth. The same data as in Figure 4.17 were used. Three sharpness values for each scatterer position result in a d_{dev} equal to 16.6 μm for a 3.8 mm distance as shown in (b). The gray line in (b) indicates the wavelength used.

An average d_{dev} of 16.6 μm ($\approx 0.075\lambda$) was reported for a depth range of 3.8 mm, between 37.8 mm and 41.6 mm. This range involved the same area around the peak of the middle S-curve that was mentioned in the previous subsection. The d_{SD} of the average d_{dev} was calculated to 15.49 μm ($\approx 0.074\lambda$). However, this result corresponds to much lower localization precision, compared to the sharpness that was calculated directly from the raw data (≈ 2 orders of magnitude lower than the wavelength). For a longer 8 mm range (from 36 mm to 44 mm), the average d_{dev} was 30.93 μm and the associated d_{SD} had a higher value (53.81 μm), which led to several inaccurate depth estimates for the same range. The results here confirm that signal derived sharpness is superior to the image derived one as suggested in Subsection 4.3.

4.7.4 Noise study

The first simulations and the initial PW results of the normalized sharpness algorithm were examined with an SNR equal 10 dB added to the transducer element signals. This way it was possible to introduce realistic sharpness variability and enable a difference between measurements that is then deployable through the use of the MLE. In the present subsection, the simulation process of the Subsection 4.6.1 was repeated with different SNR values. A range between 0 dB and 30 dB SNR was selected and the d_{dev} was calculated as in Subsection 4.7.1. The sharpness was derived from raw signals and spline interpolation was employed. In order to make an objective comparison, the average depth deviation is calculated for an 8 mm range in all cases, from 36 mm to 44 mm. The outcome of this study is found in the Figure 4.23.

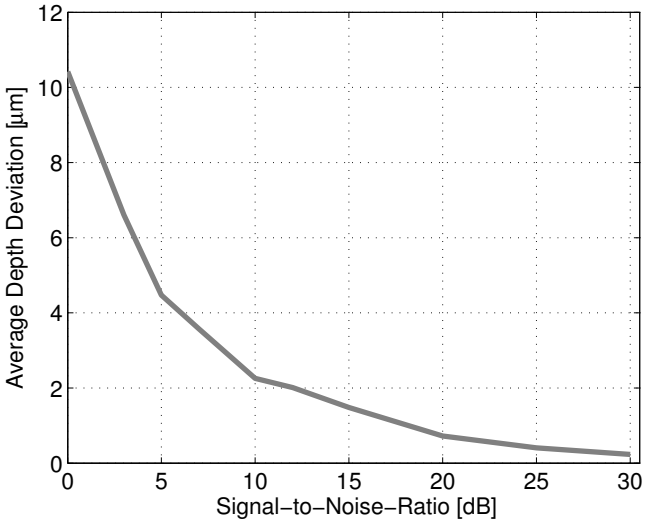

Figure 4.23: Average d_{dev} over different SNR values added to the ultrasound RF signals. Lower SNR thus higher noise, increases the d_{dev} reducing this way the method's performance.

From the Figure 4.23 it is seen that in the extreme cases that the noise was equal to the signal (SNR= 0 dB) the average d_{dev} rose to 10.42 μm. This value was significantly increased compared to the 2.25 μm of the 10 dB but still is equivalent to $\approx 0.05\lambda$. As the SNR increased the d_{dev} continued to decrease reaching the value of 0.23 μm when the noise was equal to 30 dB, very close to a noise-less condition. There was no further variation of the y axis values beyond 30 dB. Moreover, the d_{dev} and d_{SD} were quite similar and therefore d_{SD} was not plotted separately in the graph.

Overall the SNR value of 10 dB that was used for the simulations so far, is an average choice away from both extremes, that can sufficiently describe an equivalent experimental setup with a real point target in this thesis. To demonstrate the sharpness variation when different amount of noise was used, two mean sharpness

data together with their associated SDs are shown in Figure 4.24. Figure 4.24(a) corresponds to 0 dB noise, from which it is seen that the edge data were no longer flat, the peak decreased by 15% in amplitude and the sharpness SD was up to 10 times higher compared to Figure 4.24(b) where the 20 dB sharpness data are shown. This SD difference explains the d_{dev} variation of Figure 4.23.

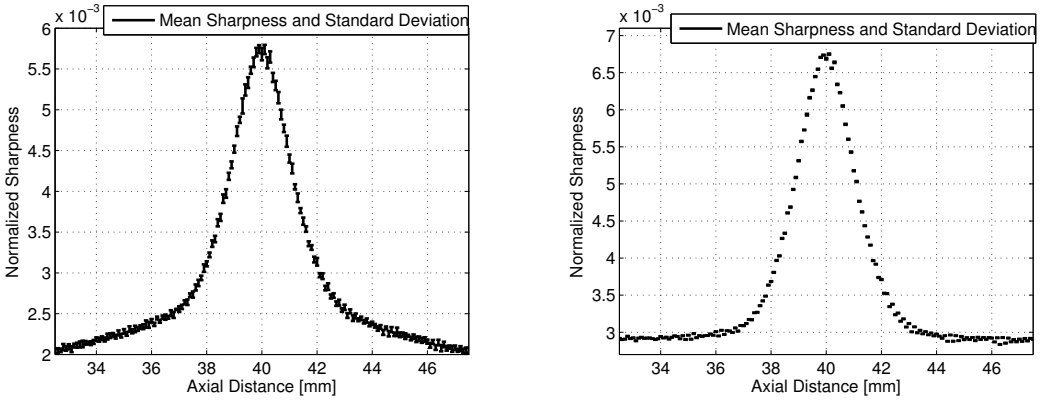

(a) SNR = 0 dB (b) SNR = 20 dB

Figure 4.24: Mean sharpness and sharpness SD over axial distance, when a) 0 dB and b) 20 dB of white Gaussian noise was added to the RF signals. The receive focus was set to 40 mm.

The differences between 0 dB and 20 dB, are best shown in Figure 4.25 where the S-curves from the sharpness data of Figure 4.24 are scaled to 1 and overlaid. The result shows that the shape of the peak and the slopes remained unchanged but the edges were elevated when the SNR was lower.

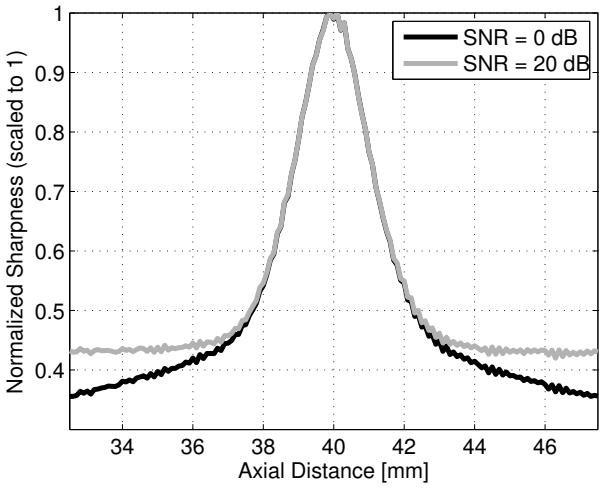

Figure 4.25: Direct comparison of the resulting S-curves from the sharpness data of Figure 4.24. The normalized sharpness values were scaled to 1 due to the different amplitudes.

4.8 Other transmission protocols

The purpose of the current section is to examine the impact of different transmission protocols. The procedure of Algorithm 1 was repeated with all the ultrasound transmission described in Appendix A. In Subsection 4.8.1 synthetic aperture ultrasound transmission was used instead of plane wave. In Subsections 4.8.2, 4.8.3, 4.8.4 the focused transmission was employed and three individual cases were explored. In the first one, the transmit focus was set to 30 mm which is higher than the scatterer highest position (32.5 mm), in the second the transmit focus was set to 40 mm which coincides with the centre of the total displacement and finally in the third case the focal depth was set to 50 mm, lower than the scatterer lowest position (47.5 mm). The same noise was added to the signals (SNR = 10 dB).

4.8.1 Synthetic aperture ultrasound imaging

Synthetic aperture ultrasound (SAU) [144] can offer similar benefits to the ones of the PW imaging, and is used in various ultrasound applications [183, 184]. Due to the smaller aperture used, lower resolution images are acquired from single SA emissions but this way a very high frame rate is maintained. Figure 4.26 is the equivalent SA sharpness derivation of Figure 4.17. The spline interpolation was used since it outperformed the other fitting functions (Subsection 4.7.1). The transducer specifications and the particle movement part of the Table 4.1 were maintained whereas the updated transmission section is in Table 4.2.

Synthetic Aperture Emission	
Transmit apodization	-
Receive apodization	Hanning
Receive focus depth	38/40/42 mm
Number of transmitting elements	1 (#96)
Number of receiving elements, M	192
Number of emissions	1

Table 4.2: Transmission parameters (Synthetic aperture)

The reported average d_{dev} was 2.3 μm ($\approx 0.01\lambda$) for an 8 mm depth range covering the slopes from the extreme S-curves. The d_{SD} was calculated to 1.88 μm ($\approx 0.0085\lambda$). The average d_{dev} can also be measured for a smaller 3.5 mm region (from 38.3 mm to 41.8 mm) as in Subsection4.7.1 where the equivalent numbers for d_{dev} and d_{SD} were 1.71 μm ($\approx 0.0078\lambda$) and 1.32 μm ($\approx 0.006\lambda$) respectively. These results are similar to the plane wave transmission performance (Subsection 4.7.1). Particularly the calculated d_{dev} for the longer (8 mm) distance is the same.

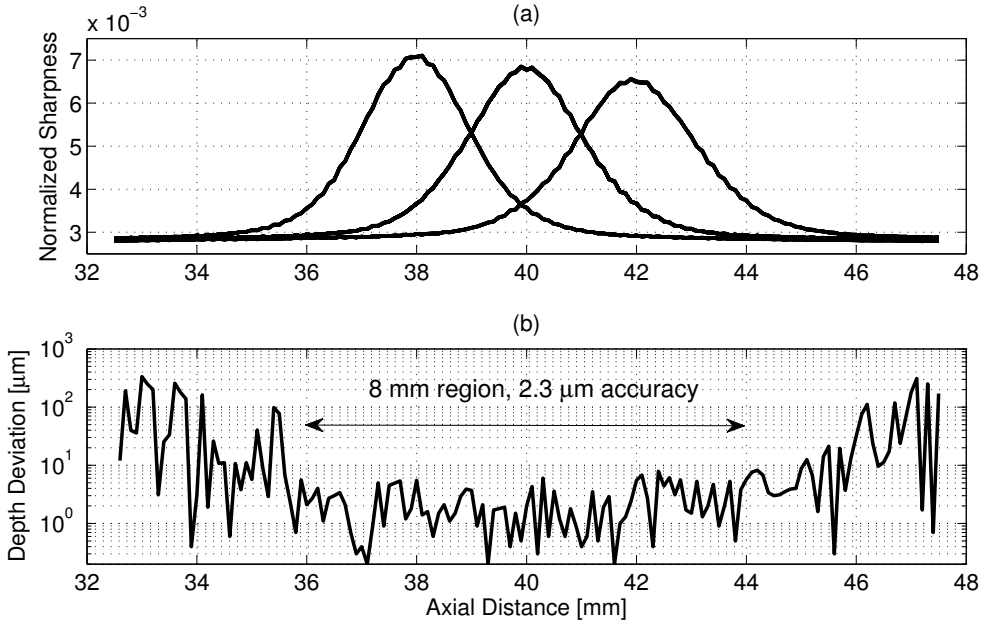

Figure 4.26: (a) A set of three normalized S-curves from a simulated ultrasound point target against depth. Data were generated by a single synthetic aperture ultrasound transmission and by beamforming with three different foci in receive. Three sharpness values for each scatterer position result in an average d_{dev} equal to 2.3 μm for an 8 mm depth range as shown in (b).

4.8.2 Shorter transmit focus

Focused transmission is commonly employed in today's state-of-the-art ultrasonic imaging machines. In this study, the transmit aperture consisted of 64 elements, and the scanning was performed by translating the 64 active elements over the aperture and focusing at the selected depth. More than one emission was required to cover the whole image region which reduced the maximum available frame rate by a factor equal to the number of emissions, here 128, compared to the PW or SA situation. The speed of sound, c was set to 1540 m/s and the wavelength was $\lambda = c/f_0 = 220$ μm as previously. The transmission parameters can be found in Table 4.3. The S-curves and the depth deviation to scatterer actual position are shown in Figure 4.27 again as derived by the spline interpolated sharpness data.

The average d_{dev} for the shorter transmit focus was 2.56 μm ($\approx 0.012\lambda$) for the common 8 mm depth range between 36 mm and 44 mm that was examined in all previous cases for the interpolated data. The d_{SD} was calculated to 3.01 μm ($\approx 0.014\lambda$) slightly higher than in Subections 4.7.1 or 4.8.1. When the average d_{dev} was calculated for a smaller optimal 3 mm distance (between 38 mm and 41 mm), it reached the value 1.81 μm ($\approx 0.0082\lambda$), where the d_{SD} was 1.62 μm ($\approx 0.0074\lambda$).

Figure 4.27(a) shows that the transmit focus affected the S-curve shape. More specifically the left halves of all curves were slightly shifted to higher sharpness

Linear Sweep	
Transmit apodization	Hanning
Receive apodization	Hanning
Transmit focus depth	30 mm
Receive focus depth	38/40/42 mm
Number of transmitting elements	64
Number of receiving elements, M	192
Number of emissions	128

Table 4.3: Transmission parameters (focused beams)

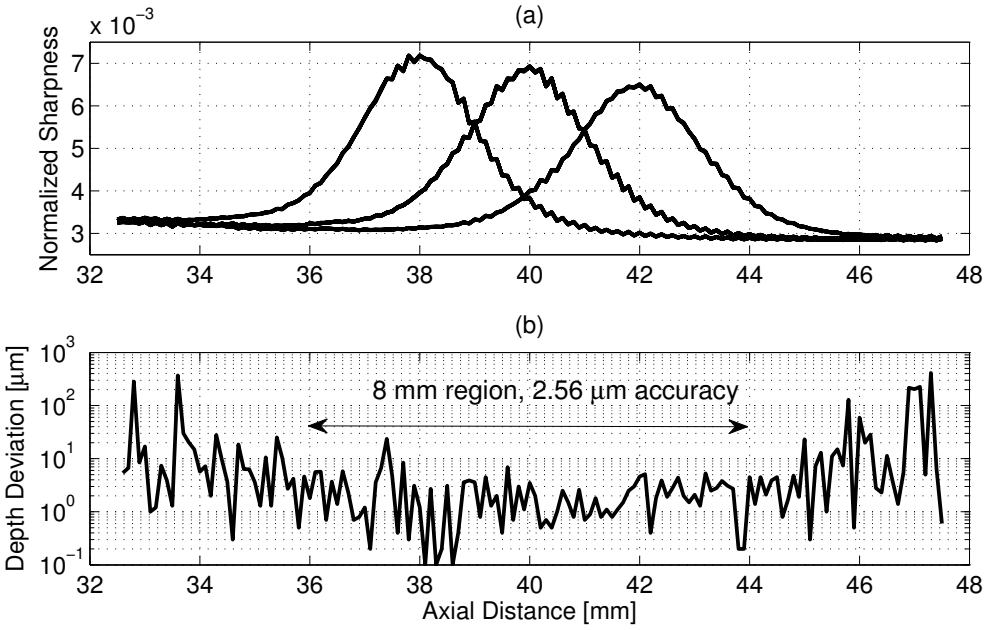

Figure 4.27: (a) A set of three normalized S-curves from a simulated ultrasound point target moving in depth. Data were generated by focused at 30 mm ultrasound emissions and by beamforming with three different foci in receive. Three sharpness values for each particle position result in average d_{dev} equal to 2.56 μm for an 8 mm depth range as shown in (b).

values and increased variability was observed in the right halves at depths away from the transmit focus. This is due to the introduction of focusing in transmit which slightly distorts the curve symmetry in contrast to the previous unfocused beams. In order to highlight the transmit focus effect, the measure of *skewness* [185] was employed through the Matlab function with the same name. It is a metric of data asymmetry around the sample mean, with positive values implying that the data are spread out more to the right and the opposite stands for negative values. Two skewness values of the S-curves corresponding to the shortest receive focus (38 mm) from Figures 4.17(a) and 4.27(a) were measured and compared selectively. Both curves should have positive skewness based on the metric's definition but in

Figure 4.27(a) the value is expected to be lower due to the shift towards the left. Indeed the values were 1.52 for the focused transmission case and 1.70 for the PW example where normally between curves corresponding to the same receive focus and unfocused transmission, there is no difference up to the 2^{nd} decimal digit. Despite the changed curve shape, the precision of the localization was generally not affected by this focused transmission apart from a small decrease (from 3.7 mm to 3 mm) in the depth area where the optimal results appeared. This is because the general Lorentzian-like shape is always preserved and at all cases, the interpolated data fit very well the calculated sharpness.

4.8.3 Intermediate transmit focus

In the case where the transmit focus was positioned in the middle of the total depth (40 mm), the obtained average d_{dev} was 3.04 μm ($\approx 0.014\lambda$) for the 8 mm depth range between 36 mm and 44 mm and the d_{SD} was equal to 3.41 μm ($\approx 0.016\lambda$), as shown in Figure 4.28.

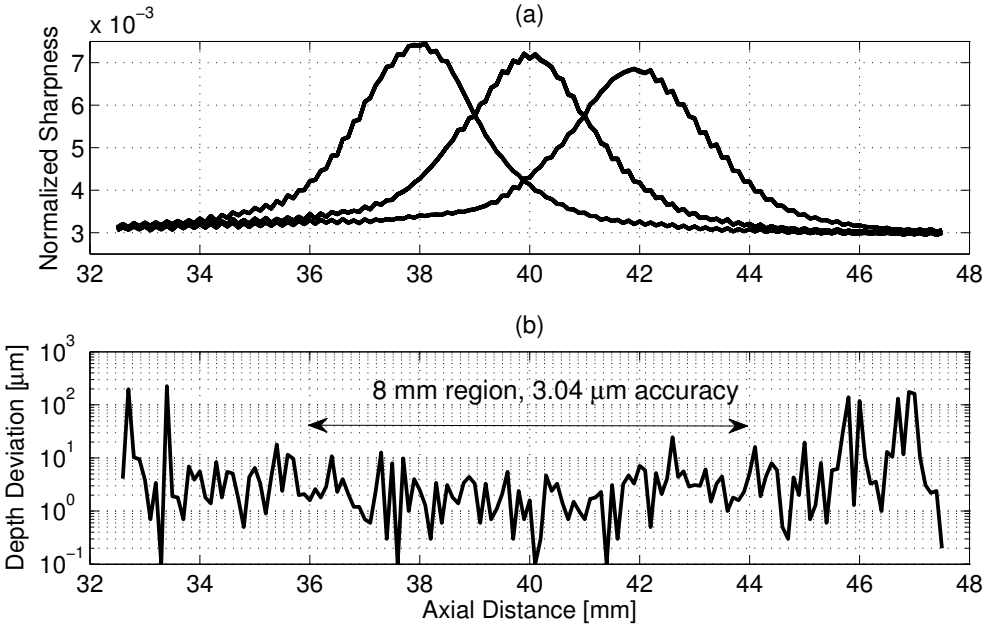

Figure 4.28: (a) A set of three normalized S-curves from a simulated ultrasound point target moving in depth. Data were generated with transmit focus at 40 mm and by beamforming with three different foci in receive. Three sharpness values for each particle position result in average d_{dev} equal to 3.04 μm for an 8 mm range as shown in (b).

The optimal accuracy was achieved at a 3.6 mm distance (from 38 mm to 41.6 mm) with an average d_{dev} equal to 1.87 μm ($\approx 0.0085\lambda$) and a d_{SD} equal to 1.39 μm ($\approx 0.0063\lambda$). The achieved accuracy was again comparable to that shown in Subsection 4.7.1. Moreover, the current simulation presents some similarity to the PW

or SA cases, in the sense that the focus was selected this way so that it does not affect the curve shape.

4.8.4 Longer transmit focus

The last focused emission results are shown in Figure 4.29, where the focus was set to 50 mm. This simulation was rather similar to the case with the shorter transmit focus. Here, the right half of each curve appeared slightly shifted to higher values and in the left halves that were furthest away from the focus flickering was introduced. The small skewness difference between two S-curves in Figures 4.29 and 4.17 was maintained as in Subsection 4.8.3 but moved to opposite direction. The average d_{dev} was 2.97 μm ($\approx 0.014\lambda$) for a 9 mm depth range between 36 mm and 45 mm this time. The range was extended 1 mm further than usual as the calculated d_{dev} did not change between 44 mm and 45 mm. This number came with a d_{SD} equal to 2.55 μm ($\approx 0.012\lambda$). There was also a small 2.5 mm area (between 38.5 mm and 41 mm) where the average d_{dev} was reduced to 1.76 μm ($\approx 0.008\lambda$) with also a small d_{SD} equal to 1.61 μm ($\approx 0.0073\lambda$).

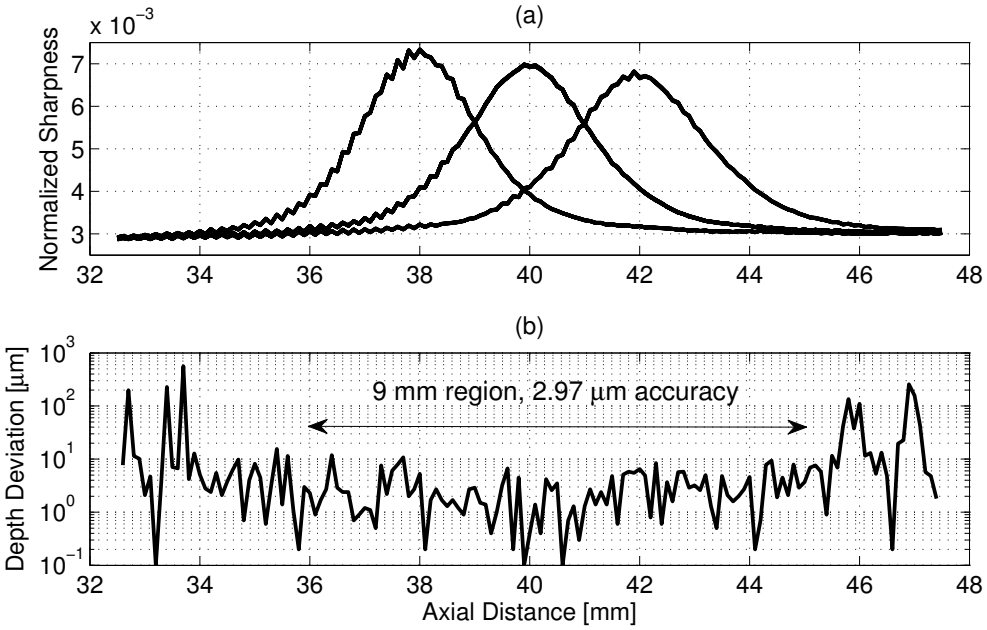

Figure 4.29: (a) A set of three normalized S-curves from a simulated ultrasound point target moving in depth. Data were generated by focused at 50 mm ultrasound emissions and by beamforming with three different foci in receive. Three sharpness values for each particle position result in average d_{dev} equal to 2.97 μm for an 9 mm distance as shown in (b).

4.9 Other algorithm optimization

In this section, simulations were produced in an attempt to perform additional parametric studies that will refine the sharpness method for ultrasound scatter localization. The PW ultrasound transmission was employed throughout the section. In Subsection 4.9.1, the Algorithm 1 was applied to a scatterer who's central position different from the one shown in Table 4.1 (0 mm, 40 mm). Then, studies on the effect of z-step size and with multiple S-curves follow in Subsections 4.9.2 and 4.9.3 respectively. Finally, the optimal separation between two successive receive foci was investigated in Subsection 4.9.4.

4.9.1 Sharpness at different initial positions

Simulations similar to those of Section 4.7.1 were performed first with scatterer's central position other than (x, z)=(0 mm, 40 mm). The movement was always limited to the axial direction and the length between initial and final position remained 15 mm. Different axial and lateral coordinates were tested in order to study any possible sharpness variations. Initially, the x coordinate only changed and this means that the scatterer under study was no longer centred below the transducer. The x range extended from -7.5 mm to $+7.5$ mm. In Figure 4.30 the mean sharpness values and the sharpness SD are shown for two different cases for illustration.

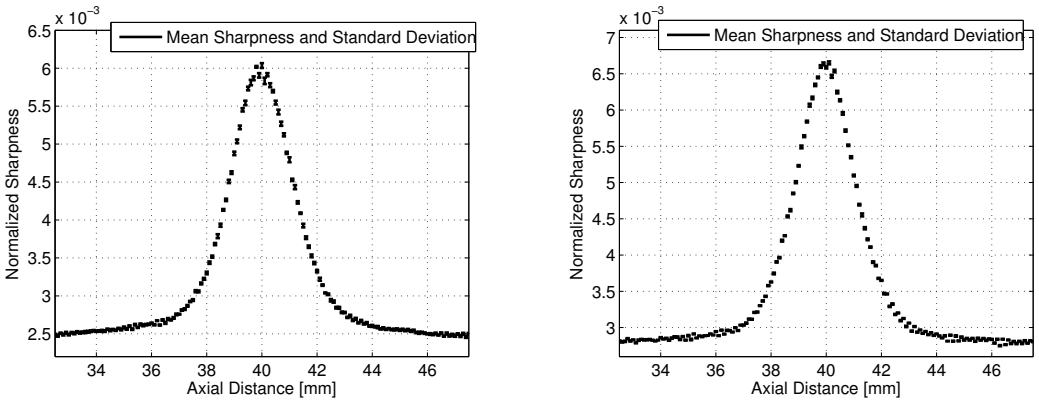

(a) (−7.5 mm, 32.5 mm) (b) (0 mm, 32.5 mm)

Figure 4.30: Mean sharpness and sharpness SD over axial distance, for 2 different initial scatterer lateral positions. In a) the simulated point begins its movement from (x, z)=(−7.5 mm, 40 mm) and in b) from (x, z)=(0 mm, 40 mm).

In Figure 4.30(a), the scatterer initial position was (−7.5 mm, 40 mm) and in 4.30(b) the original case (0 mm, 40 mm) was repeated for comparison. The sharpness data did not reveal significant differences between the two cases apart from a small amplitude decrease (lower sharpness values by 9.5%) noticed in the first case. Essentially the difference is simply a scaling factor as shown in Figure 4.31.

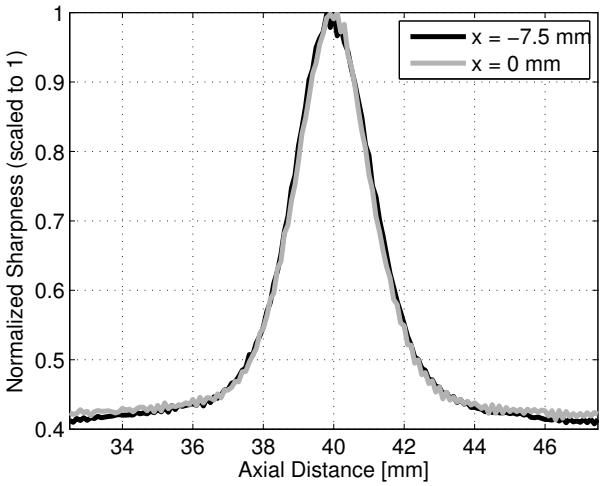

Figure 4.31: Direct comparison of the resulting S-curves from the sharpness data of Figure 4.30. The normalized sharpness values were scaled to 1 due to the different amplitudes.

This can be attributed to imperfect alignment with the transducer longitudinal since away from the beam axis the signal amplitude becomes lower. The latter resulted in a lower sharpness, given that the sharpness calculation was done by Equation (4.7). The curve similarity was reflected by the accuracy obtained, as this was not altered by more than $\pm 3\%$, from the numbers shown in Subsection 4.7.1 in all lateral positions tested. The findings show that the performance of the algorithm is not significantly affected by a different lateral position.

The performance of the sharpness method for a scatterer moving at different depths was also studied here. As previously, the movement was limited to depth only where the total distance covered is 15 mm in 151 steps. In Figure 4.32 the average d_{dev} for an objective 8 mm area, [−4 mm, 4 mm] around the scatterer central position was displayed over the scatterer's central depth position. The central depth position was moved in steps of 10 mm starting from (x, z)=(0 mm, 30 mm) and reaching (x, z)=(0 mm, 90 mm). In the last case the scatterer range extended from 82.5 mm to 97.5 mm. The receive foci were adjusted appropriately for each case. For example these were set to 88 mm, 90 mm and 92 mm to match with the requirements of the last simulation. Due to absorption, scattering and reflection effects, normal in ultrasonic imaging, as the transmit/receive path increases (longer depth), the situation can arise where a point target is only just visible. As a result it may be difficul or even impossible to apply the sharpness algorithm. The effect on the accuracy of the scatterer axial localization is expected to be similar to that of increased noise added to the RF signals (Subsection 4.7.4).

Indeed there was a quasi-linear relation between depth and average d_{dev} as shown by the Figure 4.32. When the centre of displacement was located at 90 mm the average d_{dev} was equal to 19.06 μm ($\approx 0.087\lambda$) which was increased compared to

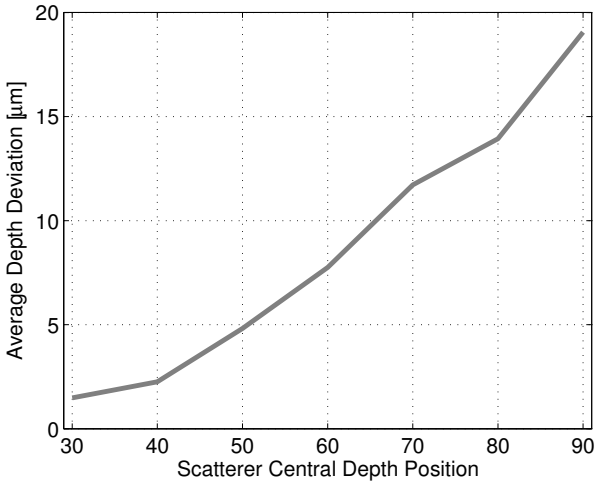

Figure 4.32: Normalized sharpness method average d_{dev} for different central depth positions of the point scatterer.

the 2.26 μm of the standard example (at 40 mm) but still remains better than $\lambda/10$. As an example in Figure 4.33 mean sharpness and sharpness SD are shown, when the scatterer was located at a depth of 60 mm and 80 mm.

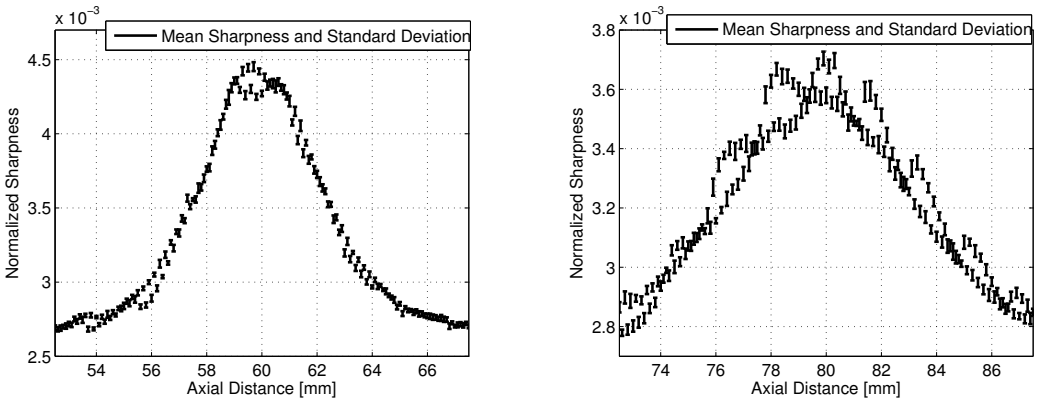

(a) 60 mm

(b) 80 mm

Figure 4.33: Mean sharpness and sharpness SD over axial distance, when the central depth position of displacement was a) 60 mm and b) 80 mm.

Figure 4.33 shows that at increasing depths, the curve edges became less flat, the fluctuations increased, the maximum sharpness dropped by 33% in 4.33(a) and 44% in 4.33(b) compared to Figure 4.30(b) which is the initial example, and that the SD reached values more than one order of magnitude higher. The average d_{dev} in the two cases was 7.76 μm ($\approx 0.035\lambda$) and 13.94 μm ($\approx 0.064\lambda$) respectively. The increased SD (Figure 4.33) and the reduced S-curve slopes (Figure 4.34) justify why the efficiency of the sharpness algorithm was reduced.

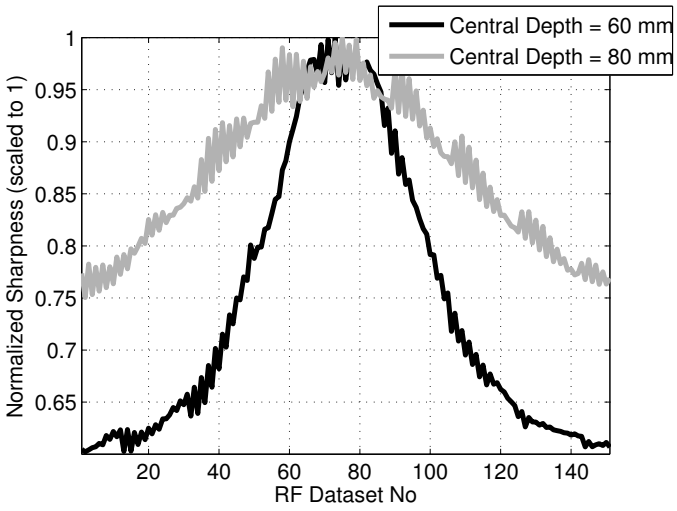

Figure 4.34: Direct comparison of the resulting S-curves from the sharpness data of Figure 4.33. The normalized sharpness values were scaled to 1 due to the different amplitudes.

4.9.2 Study on z-step size

In this study several different z-steps were examined between two successive recorded signal responses. The normalized sharpness algorithm was tested using the same transmit and receive protocols as in the example of Section 4.7. The z-steps ranged from 50 μm ($\approx \lambda/4$) up to 660 μm ($\approx 3\lambda$). The simulation results are shown in Figure 4.35 where the z-step size is plotted versus the acquired average d_{dev} in each instance. The average d_{dev} was calculated as in Figures 4.23 or 4.32 for an approximately 8 mm depth range but in this case particularly for the larger z-steps it was not always possible to examine the exact depth range due to the absence of samples at 36 mm or 44 mm.

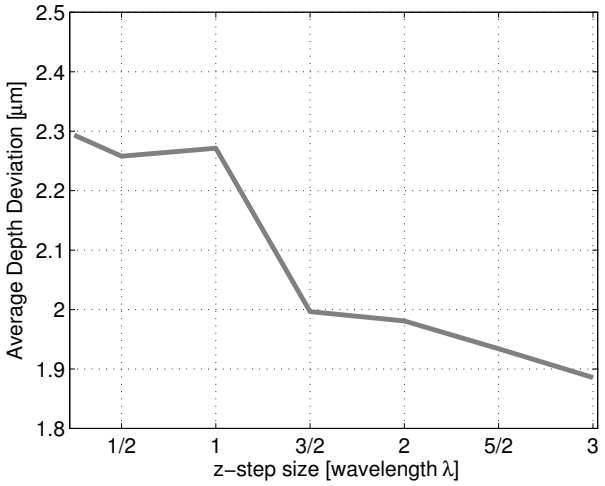

Figure 4.35: Normalized sharpness method average d_{dev} for different z-steps between successive scatterer positions.

Figure 4.35 shows that the average d_{dev} was maintained at the same levels (between 2.26 μm and 2.28 μm) for the three smallest z-steps but then dropped below 2 μm when the step increased, to reach the optimal value for the largest z-step which was equal to 1.88 μm ($\approx 0.0085\lambda$). Figure 4.36 shows the resulting mean S-curves when the z-step was 200 μm and when the z-step was larger and equal to 500 μm.

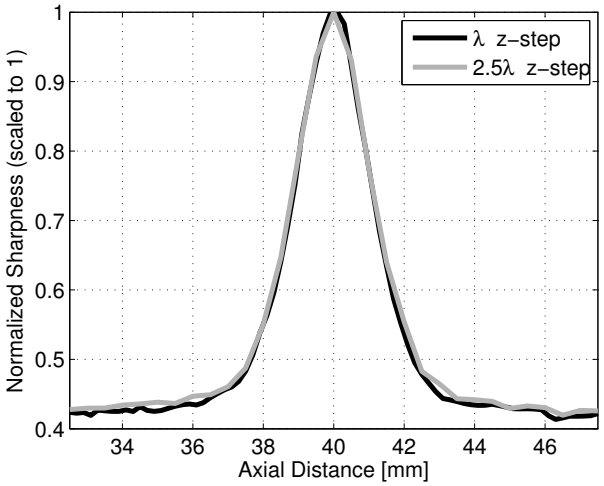

Figure 4.36: Direct comparison of two mean S-curves. In the first the z-step was approximately equal to the λ and in the second the z-step was approximately equal to 2.5λ.

Figure 4.36 shows that an S-curve extracted from a limited number of samples may result in a curve peak slightly more steep compared to the one in Figure 4.30(b). The average d_{dev} was equal to 2.27 μm ($\approx 0.01\lambda$) and was extracted by 42 samples in total in when the z-step was equal to λ while for 2.5λ z-step size, the equivalent number was 1.93 μm ($\approx 0.0088\lambda$) but from 17 only samples. The latter is a small number and not as reliable as the first one. The current tests indicate that the algorithm was not affected by z-step changes. Larger z-steps may potentially provide marginally increased accuracy (reduced d_{dev}) although the difference is insignificant from the smallest to the largest step size. On the other hand, reduced sampling on the calibration data, increases the possibility that the change over the peak is not recovered (Figure 4.36).

4.9.3 Multiple S-curves

An increased number of S-curves was considered in this subsection to further increase the depth range of high accuracy localization, which will be applicable of any given depth for ultrasound imaging. The initial implementation included only 3 foci to imitate the original optical analogue but ultrasound imaging that uses electronic focusing upon receive does not impose any limitations to the number of receive foci. Therefore the previous PW data, were beamformed with 11 different foci in receive

where the focus was set successively from 35 mm to 45 mm with 1 mm distance between two of them. Spline interpolation was used again to fit the sharpness data and the outcome can be found in Figure 4.37 where the 11 S-curves are shown in (a) and in (b) there is the d_{dev} to the scatterer true position.

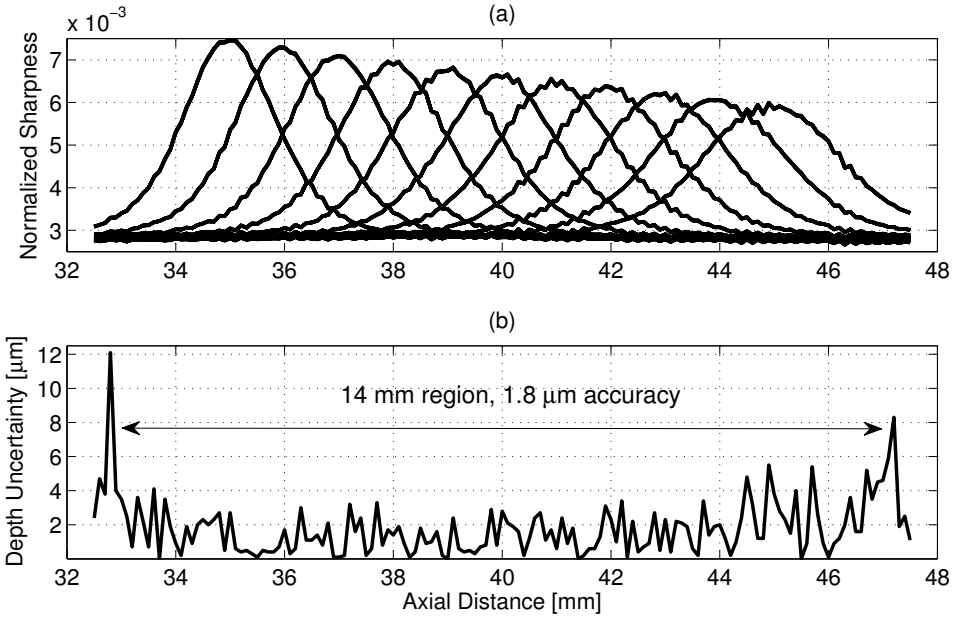

Figure 4.37: (a) A set of eleven normalized S-curves from a simulated ultrasound point target moving in depth. Data were generated by unfocused PW ultrasound transmission and by beamforming with eleven different foci in receive. Eleven sharpness values for each scatterer position result in average d_{dev} equal to 1.8 μm for a 14 mm distance as shown in (b).

The smallest d_{dev}, thus maximum accuracy, was calculated for a 3.6 mm area between 38.2 mm and 41.8 mm, and had a value equal to 1.15 μm ($\approx 0.0052\lambda$) with a d_{SD} equal to 0.86 μm ($\approx 0.0039\lambda$). Such values ($\lambda/191$) indicate the maximum improvement reported in this chapter. When almost the whole distance (14 mm) covered by the scatterer was considered the calculated d_{dev} was still matching with the best results acquired in other sections but for smaller areas. To be more specific, by excluding 0.5 mm at the end of each d_{dev} curve edges, the resulting value was 1.8 μm ($\approx 0.0039\lambda$) and the d_{SD} was equal to 1.27 μm ($\approx 0.0058\lambda$).

In Figure 4.38 the average d_{dev} is plotted separately for more detail and a smoothed version of the d_{dev} is included to describe how the accuracy changes with depth exactly as in Figure 4.18. Zooming into this curve shows that there are further areas that can be distinguished combining super-resolution axial localization for longer depth ranges. The average d_{dev} for a 12 mm depth range, [−6 mm, 6 mm] from the central position, was 1.45μm ($\approx 0.0066\lambda$) with a d_{SD} of 1.16μm ($\approx 0.0053\lambda$). From the Figure 4.38 it is obvious though that the uncertainty increased for the last 2 mm of the previously measured distance and hence, a final

calculation was made for the 10 mm range between 34 mm and 44 mm. For those depths, the average d_{dev} was calculated to 1.29 μm ($\approx 0.0058\lambda$) and the d_{SD} was equal to 0.95μm ($\approx 0.0043\lambda$).

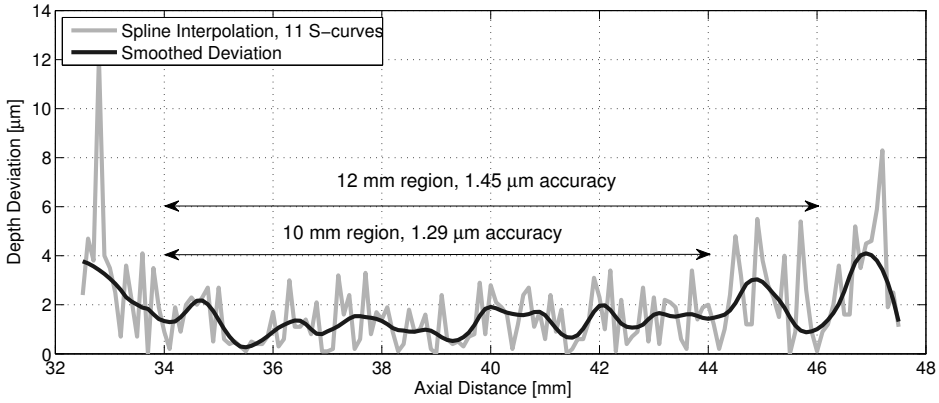

Figure 4.38: Actual and smoothed versions of the d_{dev} recorded when spline interpolation was used to model the 11 S-curves. The average d_{dev} for a 12 mm depth range covering 80% of the total scatterer displacement was equal to 1.45μm. When the range was reduced to 10 mm, (between 34 mm and 44 mm) the sharpness method's performance further increased reaching an average d_{dev} of 1.29μm.

4.9.4 Axial separation between S-curves

From the introduction of the ultrasound normalized sharpness algorithm, the axial separation between two successive receive foci was fixed to 2 mm. The peaks of the 3 S-curves also maintained this 2 mm difference (38 mm, 40 mm, and 42 mm) as shown in Figure 4.17. The choice was based on the assumption that if the slopes of 2 sharpness curves overlap to a great extent (the right slope of one curve and the left of the next one) the localization will be done at maximum resolution as it is the steep part of the curve (slopes) that provides minimum d_{dev}.

In the previous subsection for the first time the distance between two foci in receive beamforming was reduced to half (1 mm). Reducing this distance though was the only way to fit more than 7 S-curves in the 15 mm axial scatterer movement. Keeping an 1 mm distance between curve peaks presents the advantage of having all 3 curve slopes close as shown in Figure 4.38 but may slightly limit the depth range where the d_{dev} becomes low. In the present simulation study, the 3 S-curve example was examined by testing different distances between the 3 curves following the optics example [186]. The smallest distance was 1 mm where the 3 S-curves peak at 39 mm, 40 mm, and 41 mm respectively and the largest axial separation was 5 mm where the equivalent curve peaks were located at 35 mm, 40 mm and finally 45 mm. In Figure 4.39 the average d_{dev} is plotted over the distance between successive receive foci positions.

The average d_{dev} was calculated again between 36 mm and 44 mm for comparison.

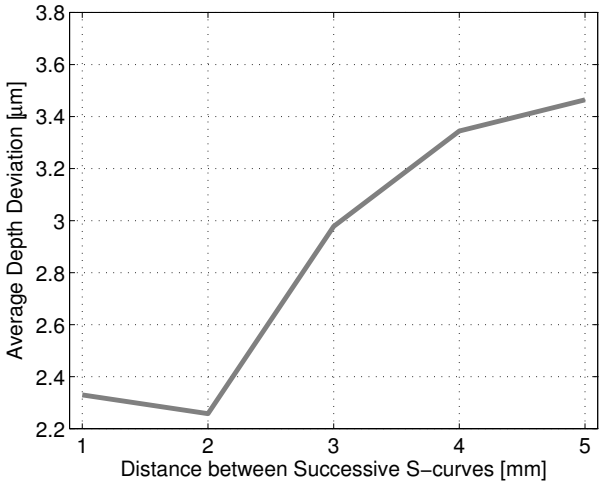

Figure 4.39: Average d_{dev} of the normalized sharpness method for a range of distances between successive receive foci positions.

Figure 4.39 shows that there is an increasing trend for d_{dev} as the distance between receive foci increases, apart from the first 2 cases that provided the lowest values. This result was expected, based on the discussion at the beginning of the subsection, since the more the curve slopes are spread, the less accurate the depth estimates are likely to be.

However, the result displayed in Figure 4.39 is not the only guide to the receive protocol and to the subsequent implementation of the sharpness method. Different combinations of parameters may provide different levels of accuracy and super-resolution depth range. For instance a possible selection of 3 receive foci at 37 mm, 40 mm and 43 mm may be producing higher uncertainty for an 8 mm range but may be more suited if a longer range is of interest. A trade between the two parameters was not identified and it may be possible to optimize both. The current study can be expanded to exclude S-curve peaks, and further reduce the axial separation between peaks, since it is the curve's slopes area where the method performs best.

4.10 Real imaging development

An axial super-resolution localization ultrasound imaging method was developed through the use of the image sharpness metric. This metric was applied to simulated data for a point source located over a range of depths. The investigation here utilized a simulation environment as a first test of the technique. It was shown that PSF-based localization methods can successfully be applied to ultrasound data and achieve improved depth resolution. The underlying aberrations are similar for optics [63] and ultrasonics [4] but the difference in wavelengths (~ 220 μm compared to ~ 500 nm), resulted in micrometric and nanometric depth resolution, respectively.

The axial localization may be achieved with a maximum accuracy of 1.15 μm

(subsection 4.9.3) which corresponds to $\lambda/191$ where the conventional axial resolution is equal to λ. However, even a reduced perfomance as the one noticed for low SNR cases (Susection 4.7.4) or when applying the method at greater depths (Subsection 4.9.1), can be a significant improvement. The technique also proved to work with all used transmissions without significant performance differences between them. These conclusions are relevant to *in vivo* imaging and combining several emissions, as explained in Appendix A, may be a way of increasing image quality thus achieving a higher SNR for the entire image depth. Increasing the number of emissions though, causes an increased total acquisition time, which may also affect the tracking sensitivity of the moving scatterers in different frames.

The sharpness technique, similar to the Minimum Variance beamformers of the past 2 chapters, may add to the existing super-resolution methods. However, both tissue and the complex structure of the human body increase ultrasound aberrations at the position of focus. To determine whether the sharpness method is viable under real conditions, it is necessary to conduct experimental work with an actual ultrasound scanner imaging real point scatterers.

Chapter 5

Experimental Validation of the Sharpness Method on Linear Scatter

In this chapter the normalized sharpness method is applied to experimental ultrasound data. The newly developed algorithm is verified using a linear point target i.e. a custom wire phantom. The scanning is performed by a commercial linear array and the different sharpness algorithm implementations are assessed. The data acquisition process and the measurement setup are similar to the simulation in Chapter 4. This enables comparisons between experimental and simulated findings as between the Chapters 2 and 3.

5.1 Ultrasound Setup

The measurement setup and the custom phantom created for the sharpness method verification are described in detail here. The transmit and receive processing together with all the scan parameters are also outlined. The general case of unfocused ultrasound transmission was preferred to obtain symmetric S-curves. As explained in Chapter 3, single element emissions will result in low SNR images and thus they have been avoided. An initial schematic diagram of the whole setup used for the experimental validation is depicted in Figure 5.1.

5.1.1 Experimental phantom

As in Chapter 3, a wire phantom was used to replace the point target of the simulation study (Chapter 4). In this case, a single wire that can be moved in depth was required. Therefore a large multiple-wire phantom (such as the one in Figure 3.2, Subsection 3.3.3) was not suitable and a custom one was used. An image of the phantom before inserting in the water, can be found in Figure 5.2.

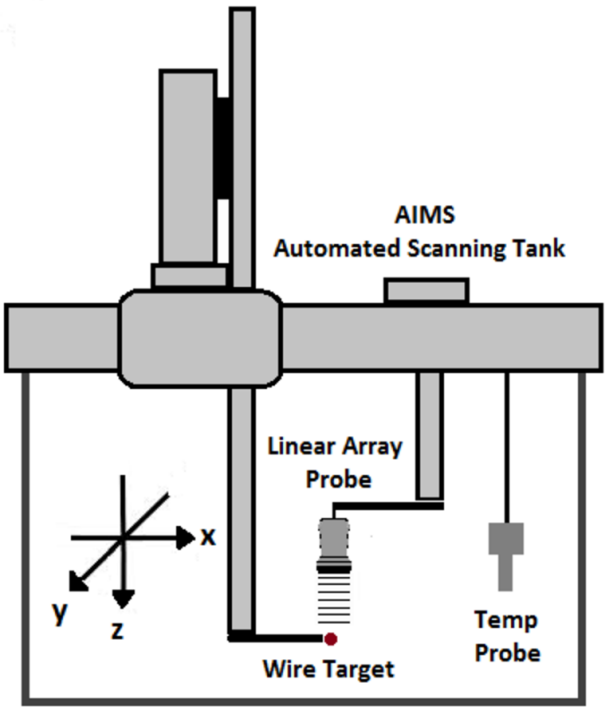

Figure 5.1: Illustration of the measurement setup: A wire target was mounted on the scanning tank. The wire was moved from an initial position across the z-dimension and RF data were acquired for every displacement.

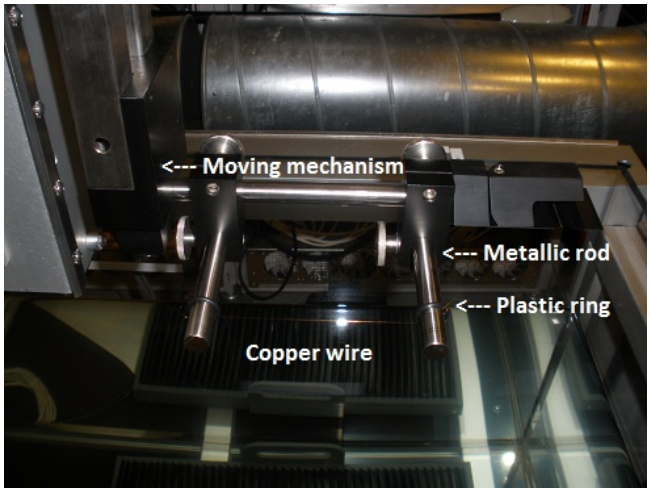

Figure 5.2: The custom phantom used for the experimental validation, consisted of a single 0.07 mm diameter copper wire. The wire was mounted on metal rods attached to a linear stage by means of plastic rings. This arrangement allowed movement of the wire in the axial direction.

A 0.07 mm diameter copper wire was mounted on the AIMS III [187] positioning setup (Onda Corporation, Sunnyvale, CA). The wire was attached to the positioning setup between metal rods allowing it to be lowered into a water tank. Plastic clips on the rods ensured that the wire was held in tension. A picture of the entire setup and the probe used for the scans can be found in Figure 5.3. The transducer was

positioned above the phantom with the field of view normal to the wire so that the wire is depicted as a point scatter in the ultrasound image. The transducer was fixed in this position with a holder and aligned such that the central element is exactly above the wire. The custom phantom can be moved by means of the AIMS III in all directions. For the purposes of the current experiment all coordninates apart from the z-axis were kept constant.

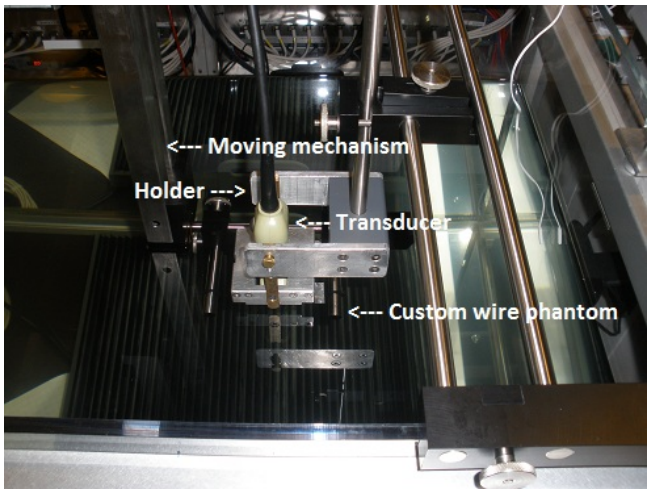

Figure 5.3: Picture of the setup from above. The BK8804 linear array probe was attached to a fixed holder and positioned vertically above the wire target.

5.1.2 Data acquisition

A 7 MHz, 192 element, linear array probe was employed to scan the custom phantom. All the scan parameters can be found in Table 5.1. The measurements were performed in the CFU, as those of Chapter 3, using the 1024 channel experimental ultrasound scanner SARUS [154]

Plane wave transmission was employed, using all the transducer elements as the transmitting aperture. RF data from the unfocused emissions were acquired from each of the 192 channels individually in receive. Data were produced across 15 mm, between 32.5 mm and 47.5 mm from the transducer face. Ten frames were acquired at each axial position of the wire target before moving to the next. After each emission the data were stored and when all 10 emissions (frames) were completed, the wire target was moved to the next location in the axial direction.

This was accomplished by using the AIMS III scanning tank, which was controlled using a Matlab interface. This high accuracy system has a minimum movement step equal to $1/92\ mm = 10.87\ \mu$m. The ratio 1/92 is attributed to the stepper motor system that was used to position the wire phantom into the tank. Hence, the resulting positioning resolution was at worst 10.87 μm. However, to avoid potential mechanical inaccuracies with the minimal stepper mode increment step sizes of

Transducer	
Transducer type	Linear array
Transducer element pitch	208 μm
Transducer element kerf	35 μm
Transducer element height	4.5 mm
Centre frequency, f_0	7 MHz
Bandwidth	60% fractional
Speed of sound, c	1484 m/s
Wavelength, $\lambda = c/f_0$	212 μm
Excitation pulse	Two-cycle sinusoid at f_0
Peak negative pressure, PNP	2.48 MPa
Plane Wave Emission	
Transmit apodization	Hanning
Receive apodization	Hanning
Receive focal depths	38 mm/40 mm/42 mm
Number of transmitting elements	192
Number of receiving elements, M	192
Number of emissions	1
Wire Movement	
Highest point	$(x, z) = (0, 32.5)$ mm
Lowest point	$(x, z) = (0, 47.5)$ mm
Total distance covered	15 mm (axially only)
z-step between succesive emissions	108.7 μm

Table 5.1: Experimental setup parameters

108.7 μm were used. Consequently the total distance of 15 mm was covered in 139 steps.

5.1.3 Data analysis

For every acquisition the data were beamformed in three different foci in receive with the use of an in-house built beamformation toolbox BFT III [188]. The toolbox is written in C++ with a Matlab interface and is meant for off-line beamforming of ultrasound transducer element signals. It is the equivalent to Field II beamforming but for real instead of simulated data. It is being used extensively at the CFU where Field II was also created.

The same Matlab scripts written for the simulation study of the sharpness methodology were used for the experimental data post-processing with minor adjustments to accommodate for software compatibility issues. The receive foci were selected again to be at 38 mm, 40 mm and 42 mm, and in Figure 5.4, five random PSFs corresponding to five different axial positions, where the receive focus was set to 40 mm, are shown as an example.

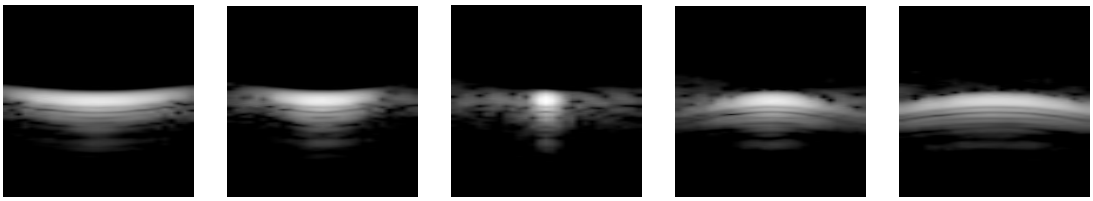

(a) 32.5 mm (b) 36.25 mm (c) 40 mm (d) 43.75 mm (e) 47.5 mm

Figure 5.4: Ultrasound images of the wire target as captured by the SARUS scanner. These simulate well point scatter and the PSFs of five different displacements accross the entire range are displayed here. The receive focus was set at 40 mm, therefore (c) is an in-focus image. Each image includes an area of 6×6 mm^2 and a 60 dB dynamic range display was used.

The sharpness data were subsequently fitted or interpolated by a factor of 1000 and inserted to the Gamma PDF (Subsection 4.5). Due to the interpolation, the z vector was also divided by 1000, taking the value of 108.7 nm. Similar to the simulation study a set of three sharpness values, as calculated from a single acquisition, were the input to the algorithm and the output was a depth position estimate. This was the depth for which the PDF presents its maximum value.

The true position of the wire is known from the control of the positioning system. Depth estimates for all 139 datasets were calculated and compared with the actual positions. The accuracy of the normalized sharpness method was also quantified here by the d_{dev} and the d_{SD}, the same measures that were defined in Subsection 4.6.2 of the previous chapter. The excitation pulse was, as in Chapter 4, a two-cycle sinusoid at f_0 (Table 5.1) resulting again in a conventional axial resolution equal to the wavelength used ($2\lambda/2$).

5.2 Normalized sharpness assessment

For the PSFs of the Figure 5.4, the normalized sharpness may again be calculated either from the resulting images or by the signals as described in the Section 4.3. A ROI box around the wire centre enclosing an area of 2.3×2.3 mm^2 was assumed and the calculation was limited to this area which as previously includes the PSF main lobe in all cases.

5.2.1 Image derived sharpness

In the first instance a single sharpness dataset was extracted from images based on Equation (4.6). In Figure 5.5 the normalized image sharpness variation is plotted over axial distance for the point target of the Figure 5.4. In the same figure the best Lorentzian and Gaussian fits of the sharpness values are also displayed in (a) and (b) respectively. The correlation coefficient in Figure 5.5(a) was calculated

to 0.952. With the exemption of the right slope, the best Lorentzian fit failed to describe adequately the peak, the left slope and both edges sharpness data, which was reflected by a relatively lower r value compared to the equivalent of the previous chapter. Further, the Gaussian function was able to fit the experimental image sharpness data with a correlation coefficient 0.873 as shown in Figure 5.5(b). Such correlation coefficient is of limited predictive value and shows that the Gaussian fails to fit any of the image sharpness features.

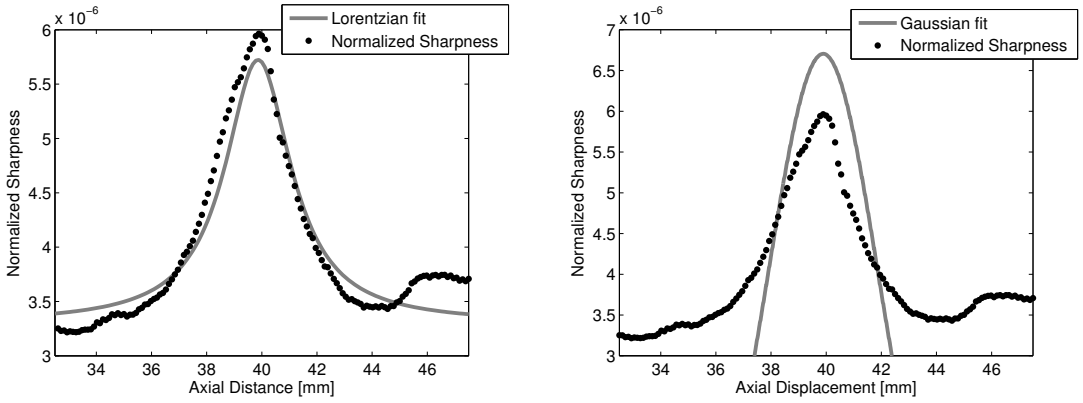

(a) Lorentzian fit

(b) Gaussian fit

Figure 5.5: An example of ultrasound image sharpness data together with the best (a) Lorentzian and (b) Gaussian fit. The sharpness data correspond to the intermediate receive focus of Figure 5.4 (40 mm).

5.2.2 Signal derived sharpness

The normalized sharpness showed improved correlation with the two models when it was calculated using the Hilbert amplitudes based on Equation (4.7). In Figure 4.13 the normalized sharpness from the Hilbert amplitudes is plotted over axial distance for the same experimental wire target data as in Figure 5.5. The best Lorentzian and Gaussian fits can be found in Figure 5.6(a) with an r value equal to 0.997, and in Figure 5.6(b) where r was calculated to 0.993. These values are significantly higher compared to those of the previous subsection (5.2.1).

Particularly the Lorentzian function, that resulted in the highest correlation displayed in both Chapters 4 and 5, was a very good fit for the peak and the slopes with a very small deviation around the sharpness edges. The Gaussian function was not an ideal fit around the curve peak but described well the curve edges. These results show that the sharpness should be derived from RF data in order to provide high precision localization. Thus, for the rest of the analysis in the present chapter sharpness was derived from the RF data.

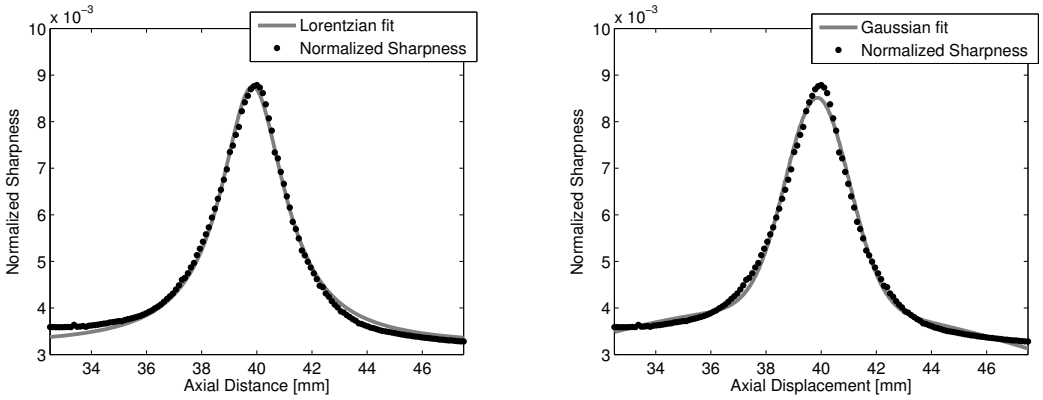

(a) Lorentzian fit

(b) Gaussian fit

Figure 5.6: An example of ultrasound sharpness data together with the best (a) Lorentzian and (b) Gaussian fit. The sharpness data were extracted by the transducer element signals, and correspond to the intermediate receive focus of Figure 5.4 (40 mm).

5.3 S-curves from plane wave emission

The steps of the Algorithm 1 were followed as in simulation. In Figure 5.7 three sharpness datasets (mean and SD) can be found together with their Lorentzian fits.

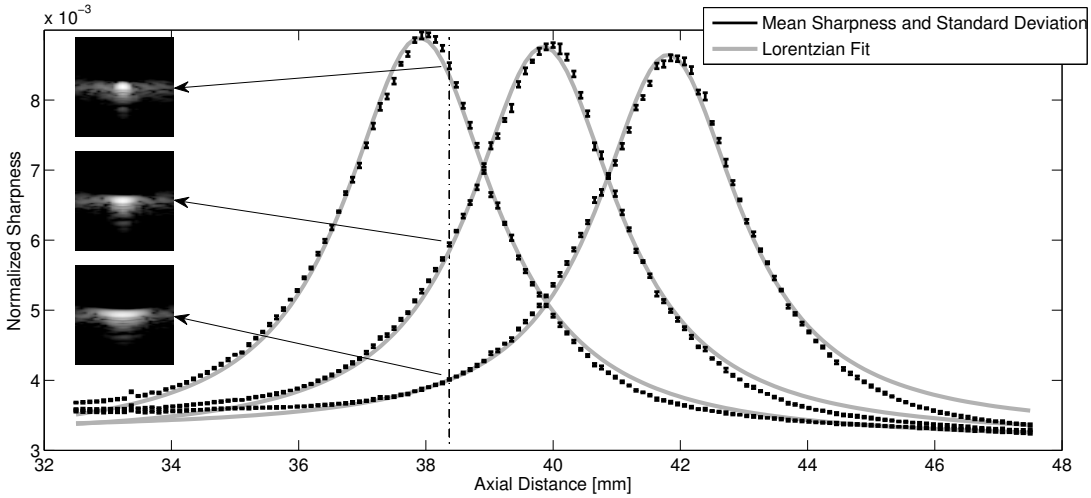

Figure 5.7: Mean sharpness is plotted over axial displacement for three receive foci (38 mm, 40 mm, 42 mm), with the corresponding Lorentzian fits. The error bar represents the sharpness SD in each depth. The displayed sharpness data result from 10 experimentally acquired frames in each z-position for a wire target moved 15 mm axially around an initial depth (40 mm). Each curve's peak is located at the position of each receive focus. A set of 3 randomly selected PSFs are also shown as an example. Each image is 6×6 mm^2 and a 60 dB dynamic range display was used. Mean sharpness values were calculated to 8.491×10^{-3} ($\pm 1.4 \times 10^{-5}$), 5.938×10^{-3} ($\pm 9 \times 10^{-6}$) and 4.053×10^{-3} ($\pm 6 \times 10^{-6}$) for the 1^{st}, 2^{nd} and 3^{rd} receive focus respectively for the point target located at 38.37 mm.

Instead of repetitive Field II scans the 10 frames were acquired sequentially before moving the scatterer to the next position. A random example of 3 PSFs (3 images) linked each one to a sharpness value is also included in Figure 5.7. The PSFs correspond to a similar axial position as in Figure 4.16 but the position cannot be identical due to the modified z-step. A comparison between the images of Figures 4.16 and 5.7 shows that both simulated and experimental PSF appearance remains very similar. The area around the PSF in the experimental study indicates that the 10 dB SNR of WGN added to the RF signals in the simulation study (Subsection 4.7.4) were noisier compared to the current experiment.

5.3.1 Accuracy from signal derived sharpness

Figure 5.8 shows the three mean S-curves in (a), together with the d_{dev} in (b). The figure, in correspondence to Figure 4.17, includes the depth deviations when a Lorentzian function, a Gaussian function or spline interpolation were used to model the mean S-curves and their SD, and the ultrasound wavelength used.

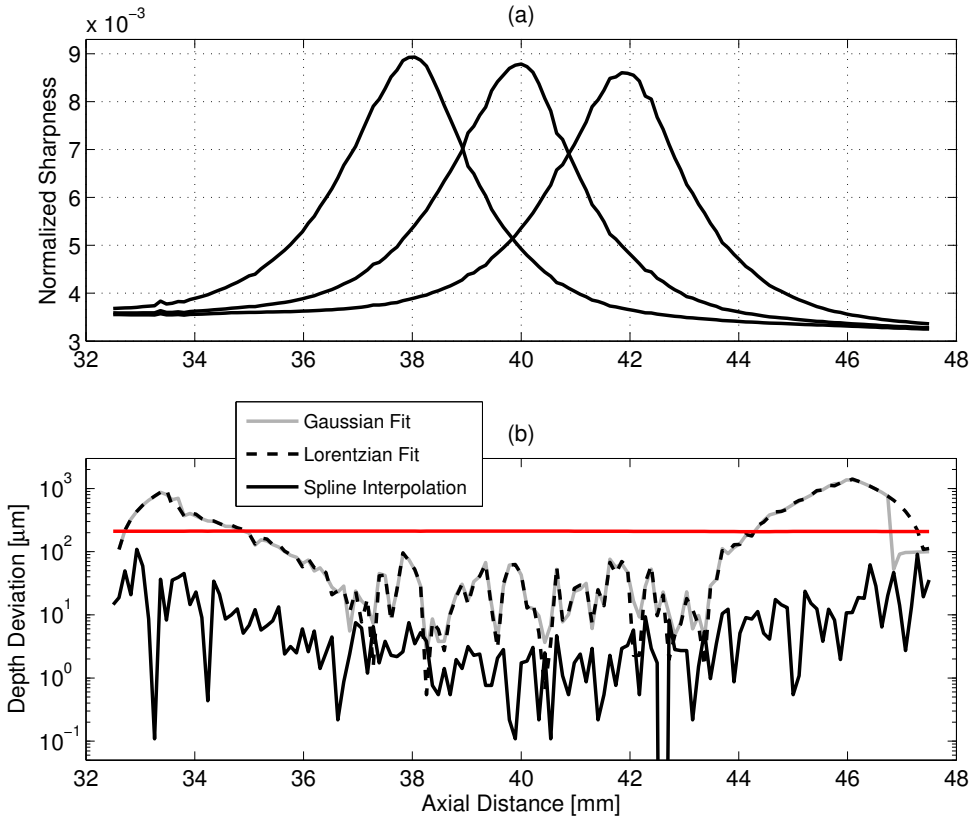

Figure 5.8: (a) A set of three normalized S-curves from the wire target moving in depth. Data were generated by unfocused PW ultrasound transmission and by beamforming with three different foci in receive. The d_{dev} is shown in (b) for each depth position and for the different fitting functions used to approximate the calculated sharpness data. The red line in (b) indicates the wavelength used.

Figure 5.8(b) shows, as previously, that the d_{dev} is not constant for the total displacement. When the Lorentzian fit was used to model the mean sharpness, an average d_{dev} of 26.8 μm ($\approx 0.13\lambda$) was found for a depth range of 6 mm distance either side of the central focus, corresponding roughly to the depth range between the half-value of the lower and upper S-curves of the extreme foci. The d_{SD} was calculated to 22.4 μm ($\approx 0.11\lambda$).

Further, an extended 8 mm region provided an average d_{dev} of 32.5 μm ($\approx 0.15\lambda$), and a d_{SD} of 29.1 μm ($\approx 0.14\lambda$). Outside the above range, the uncertainty of an estimate increased reducing the method's accuracy. The Gaussian fitting resulted in similar axial localization precision ($\approx \lambda/8$) and depth range. The difference between Gaussian and Lorentzian d_{dev} curves was apparent around the displacement edges that do not belong to the high accuracy range. The average d_{dev} in this case was 27.3 μm ($\approx 0.13\lambda$) between 37 mm and 43 mm (6 mm in total), with a d_{SD} equal to 23.5 μm ($\approx 0.11\lambda$). The localization accuracy was greatly improved when the sharpness data were simply interpolated. As in simulation, this is due to the fact that the sharpness SD (Figure 5.7) cannot be approximated by neither a Lorentzian nor a Gaussian function. The d_{dev} was found equal to 1.83 μm ($\approx 0.0086\lambda$) for a 4 mm region that covered the area around the peak of the central S-curve and one slope of each of the extreme foci S-curves (between 38 mm and 42 mm). The corresponding d_{SD} was equal to 1.60 μm ($\approx 0.0075\lambda$). The d_{dev} in the spline interpolation case can again be plotted separately over axial distance for more detail (Figure 5.9).

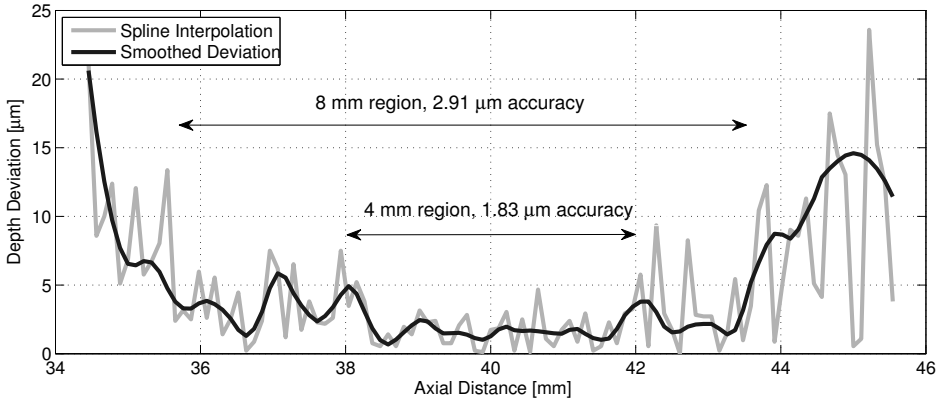

Figure 5.9: Actual and smoothed versions of the depth deviation recorded when spline interpolation was used to fit the measured sharpness data. The average d_{dev} for a 4 mm depth range covering the area around the central S-curve was equal to 1.83 μm. The d_{dev} was also maintained relatively low, at 2.91 μm for a larger 8 mm area between 35.6 mm and 43.6 mm.

In Figure 5.9 the logarithmic y-axis was omitted and a smoothed version of the d_{dev} was added to describe how the accuracy changes with depth. Zooming into this curve shows a d_{dev} of 2.91 μm ($\approx 0.014\lambda$) with a d_{SD} of 3.22 μm ($\approx 0.015\lambda$) for an 8 mm distance (between 35.6 mm and 43.6 mm).

5.3.2 The probability density function

Following the example of Subsection 4.7.1, in Figure 5.10, two instances of the Gamma PDF are shown around the area of their maximum.

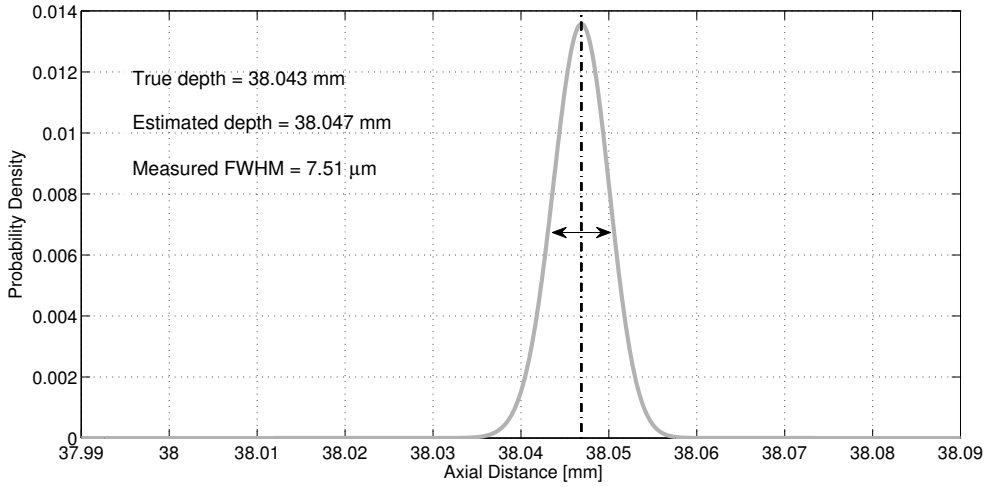

(a) PDF at 38.043 mm

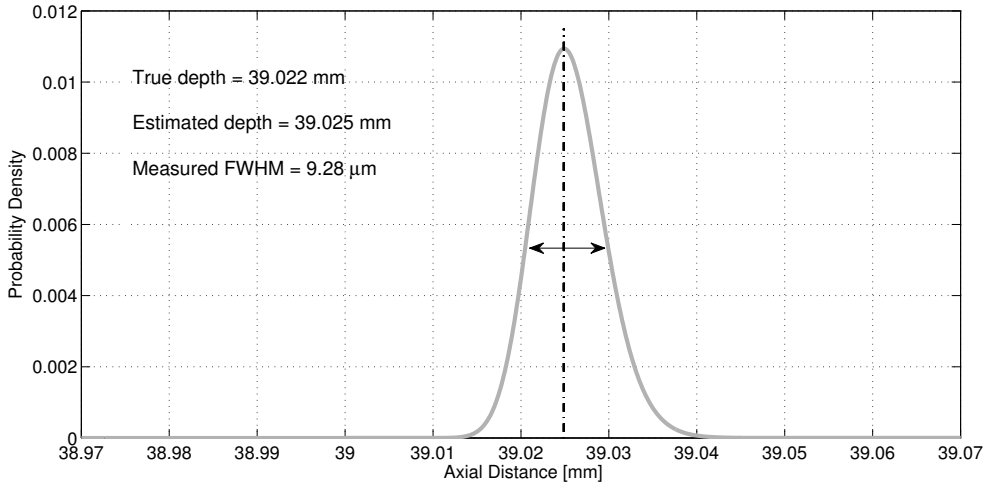

(b) PDF at 39.022 mm

Figure 5.10: Probability density function plotted over depth when the wire was located at (a) 38.043 mm and (b) 39.022 mm. The PDF maximum will indicate the normalized sharpness method's estimate for this position. In (a) the maximum was found at 38.047 mm resulting in a d_{dev} equal to 3.48 μm. In (b) the maximum was at 39.025 Mm resulting in a d_{dev} equal to 3.15 μm.

The true point scatterer position was 38.043 and 39.022 mm respectively for the two subfigures. From Figure 5.9 it may be seen that around the 38 mm area the d_{dev} was relatively high but presented a local minimum at the selected point (3.48 μm). The d_{dev} was lower around 39 mm but with a local maximum at the second selected point (3.15 μm). The two PDFs are comparable in amplitude and lobe width compared to those in Figure 4.19. The two maxima were equal to 0.0135 and 0.011, and the

FWHM was calculated at 7.51 μm and 9.28 μm for the Figures 5.10(a) and 5.10(b) respectively.

As in Subsection 4.7.2 of the previous chapter, the calculation of the PDF FWHM allows the comparison of this quantity with the axial FWHM of the DAS beamformer. The DAS axial FWHM is assessed first by means of the Figure 5.11, which is similar to Figure 4.20 but referring to the wire target this time.

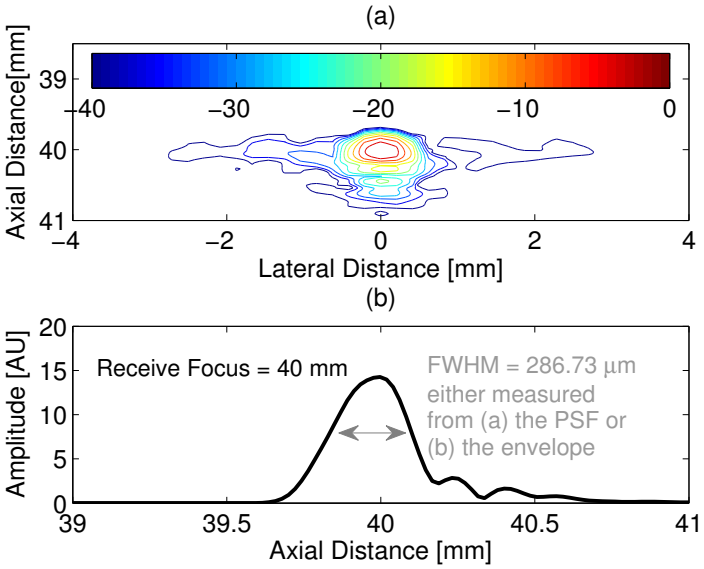

Figure 5.11: Axial FWHM assessment (a) from the PSF contour following the logarithmic compression and (b) from the Hilbert derived envelope of the RF signal through the wire centre. The wire target was located at 40 mm depth and a 40 dB dynamic range display was used.

In Figure 5.11(a), the PSF which appears in the middle panel of the Figure 5.4, is displayed. The -6 dB decrease shows the axial FWHM which was equal to 283.73 μm. A 40 dB dynamic range display was selected as only the width of the main lobe is of major interest. In Figure 5.11(b), the alternative way to calculate the axial FWHM is shown, through the RF signal that passes from the centre of the wire. Following the Hilbert transform [180], the axial FWHM was calculated again at 283.73 μm. The same calculation was repeated for all 139 experimental datasets with minimal differentiation among the results.

In Figure 5.12(a) all the PDF FWHM from the spline interpolation processing and the DAS axial FWHM as calculated above, are plotted over axial distance. The PDF FWHM curve followed as in the simulation study (Subsection 4.7.2), the shape of the d_{dev} corresponding to the spline interpolation in Figure 5.8. For an 8 mm range (from 36 mm to 44 mm) the average PDF FWHM was 9.46 μm ($\approx 0.045\lambda$) or 30 times lower than the DAS axial FWHM. The improvement is best demonstrated in Figure 5.12(b) where, as in Figure 4.21(b) of the previous chapter, the Hilbert envelope of Figure 5.11(b) is plotted with the PDF at the same depth (40 mm).

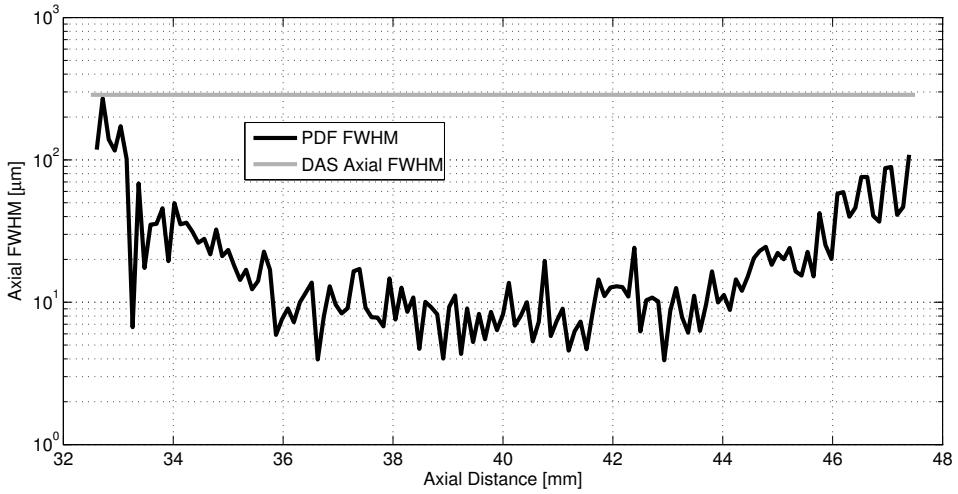

(a)

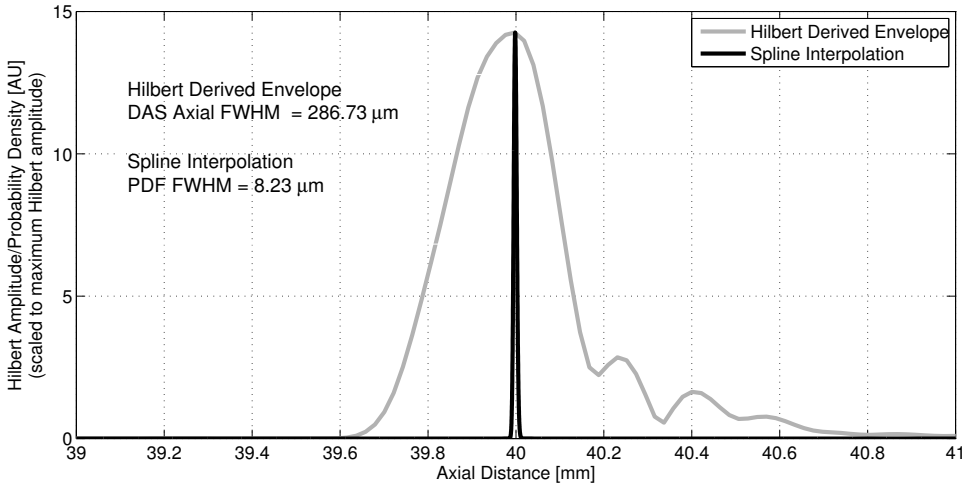

(b)

Figure 5.12: (a) The constant DAS axial FWHM is shown in comparison to the resulting FWHM from all 139 PDFs for each depth position, when spline interpolation was used for the sharpness analysis. The PDF at 40 mm depth was scaled to the maximum Hilbert amplitude and plotted together with the envelope at the same depth in (b).

The PDF main lobe was significantly narrower and the ratio of the two FWHMs shows a ≈ 35 fold more accurate localization in favor of the normalized sharpness method.

5.3.3 Accuracy from image derived sharpness

In Figure 5.13(a) the three mean S-curves extracted by image data are displayed, and in Figure 5.13(b) the d_{dev} can be found. The same acquisitions that were used for the Figure 5.8, were also used for the analysis here. The Lorentzian or Gaussian

functions did not provide a good fit for the image sharpness values (Figure 5.5), and therefore the method was only examined with spline interpolation fitted data. Hence, there is only one d_{dev} curve in 5.13(b) which is compared to the wavelength used (212 μm).

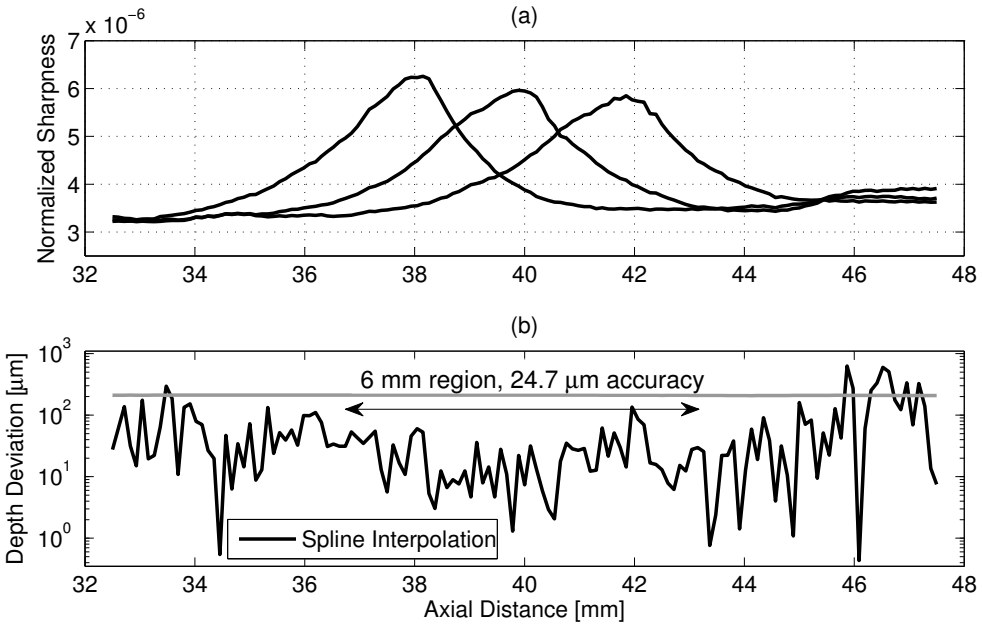

Figure 5.13: (a) A set of three normalized image sharpness curves from the wire target moving in depth. The same data as in Figure 5.8 were used. Three sharpness values for each scatterer position result in average d_{dev} equal to 24.7 μm for a 6 mm distance as shown in (b). The gray line in (b) indicates the wavelength used.

An average d_{dev} of 24.7 μm ($\approx 0.12\lambda$) was found for a depth range of 6 mm, between 37 mm and 43 mm. This range included the central receive focus [-2 mm,$+2$ mm], extended for ± 1 mm. The d_{SD} was calculated to 24.2 μm ($\approx 0.12\lambda$). However, this result is lower than that acquired when the sharpness was measured from signals. The average d_{dev} also remained similar (27.4 μm) for a longer 8 mm depth range, from 36 mm to 44 mm, with the associated d_{SD} at 26.3 μm.

5.3.4 Study on z-step size

A study that examined the data sampling effect (z-step) similar to that of Subsection 4.9.2 was performed with the experimental ultrasound data. The wire target data were acquired with a specific z-step equal to 108.7 μm. Undersampling of this was only possible. A z-step range from 108.7 μm ($\approx \lambda/2 - 139$ steps) up to 652.2 μm ($\approx 3\lambda - 24$ steps) was investigated. The average d_{dev} for an 8 mm range (between 36 mm and 44 mm) is plotted over z-step in Figure 5.14. For the larger z-steps it is not always possible to examine the exact depth range due to the absence of samples at 36 mm or 44 mm.

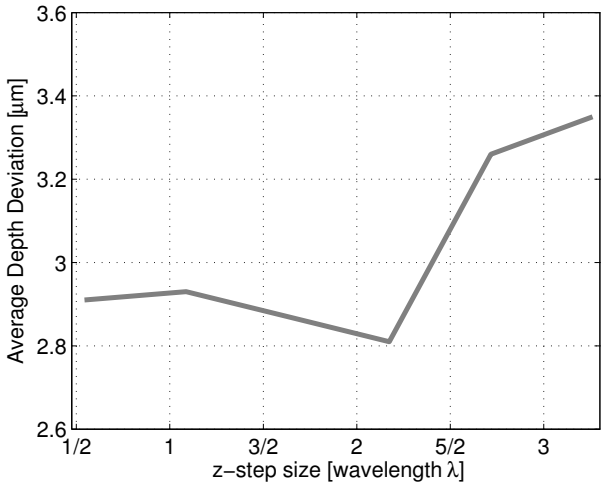

Figure 5.14: Normalized sharpness method average d_{dev} for different z-steps between successive wire target positions.

Figure 5.14 shows that the average d_{dev} presented small variations between 2.81 μm and 2.93 μm, for the first four z-steps (up to 2.1λ). At larger z-step the d_{dev} increased above 3 μm to reach the maximum value for the largest z-step which was equal to 3.35 μm ($\approx 0.016\lambda$). This value was still equal to $\lambda/63$. Although the average d_{dev} variation in Figures 4.35 and 5.14 is insignificant, a comparison between the experimental and the simulation studies indicates a slightly different algorithm performance for the larger steps. The average d_{dev} was decreased in the simulation and increased during in the experiment. However, all results from the larger z-steps were subject to errors due to the limited number of observations from which the average d_{dev} was calculated. For instance, the presence of one extremely low or one extremely high d_{dev} value can greatly affect the average. In the Figure 5.15, two mean S-curves resulting from different z-steps are plotted over axial distance.

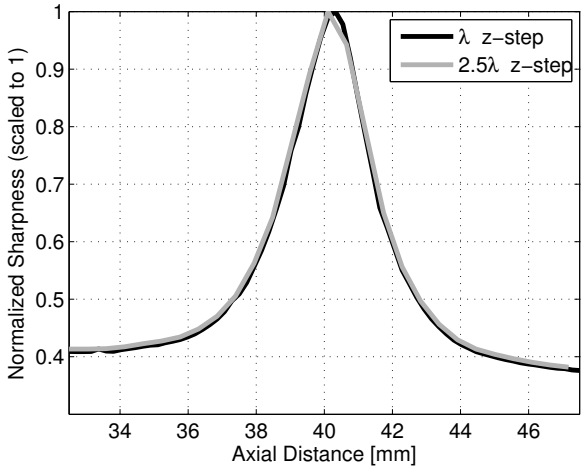

Figure 5.15: Direct comparison of two mean experimental S-curves. The two different z-step used were $\approx \lambda$ and $\approx 2.5\lambda$.

In the first case the z-step was equal to 217.4 μm and in the second, a larger step was used equal to 543.5 μm. From the Figure 5.15 it is seen that, similarly to the simulated data, the undersampling is causing a small loss of detail around the peak of an S-curve. For this reason adequate (or over-) sampling for the S-curve generation is strongly recommended.

5.3.5 Multiple S-curves

As in simulation (Subsection 4.9.3), more than three foci in receive were used to create more S-curves and cover a realistic penetration depth. Although this is not limited to a specific number, here again, 11 foci were selected. The receive foci were set successively from 35 mm to 45 mm with 1 mm distance between them. The previous trend of decreasing amplitude S-curves as the receive focus position increases (Figure 4.37) is now hardly present. The spline interpolation was used to fit the sharpness data and the results can be found in Figure 5.16 where the 11 S-curves are shown in (a) and the d_{dev} in (b).

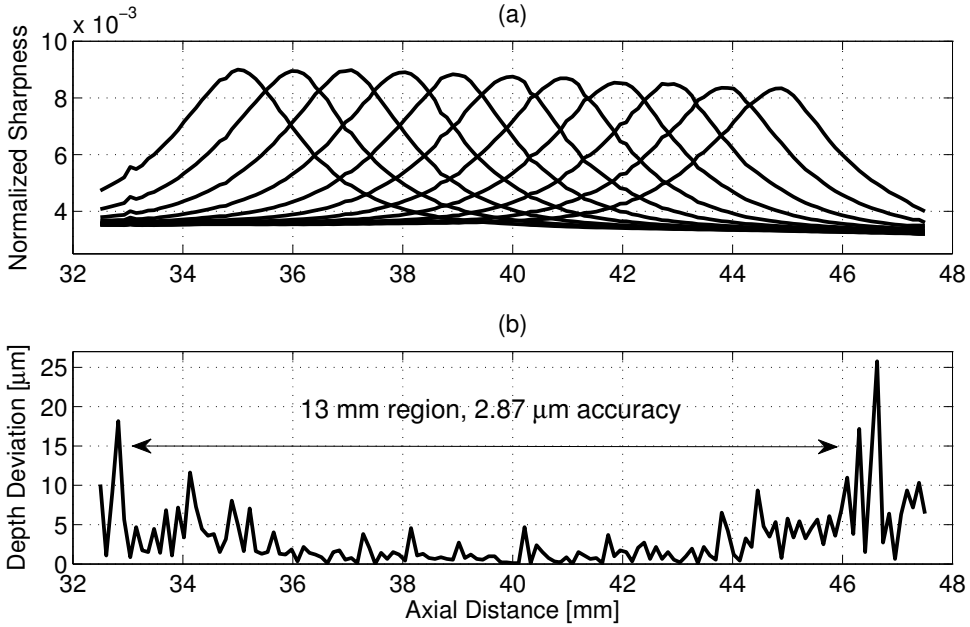

Figure 5.16: (a) A set of eleven normalized S-curves from a wire target moving in depth. Data were generated by unfocused PW ultrasound transmission and by beamforming with eleven different foci in receive. Eleven sharpness values for each scatterer position result in average d_{dev} equal to 2.87 μm for a 13 mm distance as shown in (b).

From the Figure 5.16(b), it is shown that increasing the number of S-curves further improved the results acquired in Subsection 5.3.1. The smallest average d_{dev}, thus maximum accuracy, was calculated for a 4.1 mm area between 37.9 mm and 42 mm, and had a value equal to 1.08 μm ($\approx 0.0051\lambda$) with the d_{SD} being

1 μm ($\approx 0.0047\lambda$). When a longer 13 mm distance was considered, from 33 mm up to 46 mm, the calculated average d_{dev} also remained relatively low compared to other values presented in this chapter. In particular it was estimated at 2.87 μm ($\approx 0.014\lambda$) with a d_{SD} equal to 2.85 μm ($\approx 0.014\lambda$).

In Figure 5.17 the d_{dev} curve is plotted alone for more detail and its smoothed version was also added. A closer look into this curve shows that there are further areas that can be distinguished combining super-resolution axial localization for longer depth ranges. The average d_{dev} for a 11.6 mm depth range, from 33.9 mm to 45.5, was 2.23 μm ($\approx 0.0105\lambda$) with a d_{SD} of 2.20 μm ($\approx 0.0104\lambda$). The accuracy was also calculated for another 8 mm region between 35.3 mm and 43.3 mm. For those depths, the average d_{dev} was 1.19 μm ($\approx 0.0056\lambda$) and the d_{SD} was 1.05μm ($\approx 0.005\lambda$).

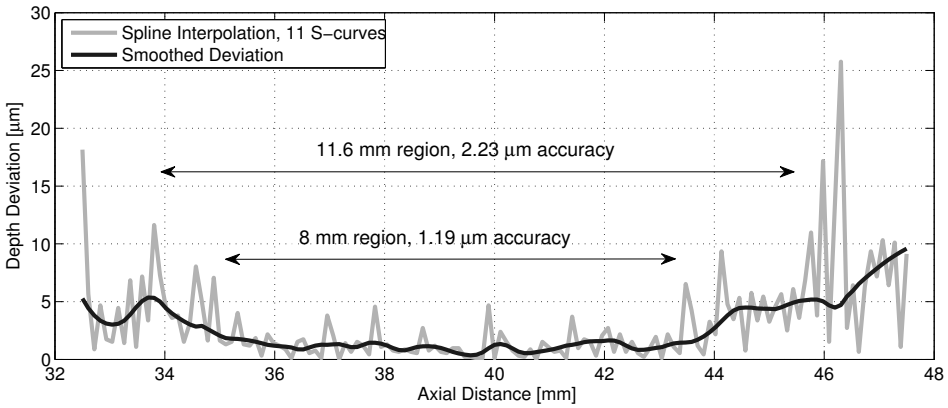

Figure 5.17: Actual and smoothed versions of the d_{dev} recorded when spline interpolation was used to model the 11 S-curves. The average d_{dev} for a 11.6 mm depth range covering 77.3% of the total scatterer displacement was equal to 2.23 μm. When the range was reduced to 8 mm, (between 35.2 mm and 43.2 mm) the sharpness method's performance further increased reaching an average d_{dev} of 1.19 μm.

5.3.6 Axial separation between S-curves

The last subsection (5.3.5), where the distance between two successive foci was reduced to 1 mm instead of 2 mm, motivated a study regarding the optimal foci separation for the experimental data. Therefore, the 3 S-curve example was examined by testing different distances between the 3 curves. The shortest distance was, as in simulation, 1 mm where the 3 S-curves peak at 39 mm, 40 mm, and 41 mm respectively and the longest distance is 5 mm where the equivalent curve peaks are located at 35 mm, 40 mm and finally 45 mm. In Figure 5.18 the average d_{dev} is plotted over the distance between successive receive foci positions. The average d_{dev} was calculated between 36 mm and 44 mm in all cases.

Figure 5.18 shows that for distances between 1 mm and 4 mm the average d_{dev} was maintained at similar levels around 2.9 μm. The average d_{dev} increased to 3.9 μm

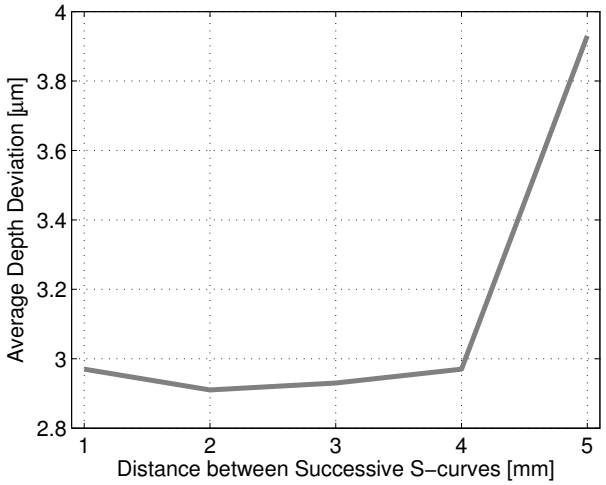

Figure 5.18: Average d_{dev} of the normalized sharpness method for a range of distances between successive receive foci positions.

($\approx 0.018\lambda$) only in the maximum distance between two receive foci (5 mm). The result shows similar performance to Figure 4.39 (Subsection 4.9.4) for the shortest distances (1 mm and 2 mm) and also for the longest one (5 mm) but presents differences for the two intermediate distances (3 mm and 4 mm). For those cases in simulation the average d_{dev} was increased whereas it remained low during the experimental study. The difference is attributed to slight variations in the S-curve shape between simulation and experiment.

A comparison between the Figures 4.16 and 5.7 shows that in the second case the S-curve was wider (with FWHM equal to 5.37 mm compared to 4.64 mm) and had a higher peak (0.0088 compared to 0.0067). This resulted in slopes that cover longer distances and thus maintain the high accuracy (lower uncertainty) for most S-curve combinations. However, it must be noted again that different distances between the foci affect not only the average d_{dev} but also the depth range for which this precision is noticed. The purpose of the current subsection, and of the corresponding one in the simulation study, was to highlight that the slopes are the most useful part of an S-curve. This is because it is more straightforward to match a depth position with a specific sharpness value in this area as shown from the figures of the last two chapters.

5.4 Comparison with simulation

The principle of axial super-resolution ultrasound localization through the use of the calibrated sharpness metric was validated with experimental ultrasound data. The Sections 4.7 and 5.3 of Chapters 4 and 5 that refer to the PW, demonstrate that in general terms the achieved uncertainty reaches similar values both for simulated and experimental ultrasound data. The section here focuses in understanding the

differences between these resuls and discuss the potential usefulness of the method in microbubble tracking.

5.4.1 Imaging setup

The specifications of the simulated transducer used in Chapter 4 were selected to this way to match exactly with the characteristics of the transducer used during the measurements (BK8804, BK Medical, Herlev, Denmark). One difference between the scan parameter values is the small speed of sound variation that was 1540 m/s during the Field II simulations but was calculated to 1484 m/s based on the water temperature [158] during the experiment. This difference caused a small change in the wavelength (220 μm compared to 212 μm). Further, whereas the starting depth of the point scatterer, and the total displacement is maintained the same for both cases, the z-step between two succesive scatterer positions was slightly larger in the experimental setup (108.7 μm from 100 μm) due to instruments limitations as explained in Subsection 5.1.1.

Finally, the DAS axial FWHM was in this experimental study (Subsection 5.3.2) considerably higher (283.73 μm) than that calculated in Subsection 4.7.2 for the simulated point target (174.19 μm). The difference was due to the larger width of the wire compared to the simulated point target. For the same reason the selected ROI for the sharpness calculation was also larger in the experimental case (2.3 mm×2.3 mm) compared to simulation (1.3 mm×1.3 mm).

During the simulation study several transmitting apertures and strategies were used. The conclusion of the previous chapter was that the unfocused transmission should generally be employed due to the high number of emissions needed for a single image formation in focused ultrasound. However, the focused ultrasound trasmission showed similarly high levels of accuracy in the single scatterer axial localization, and thus should be considered when high noise or depth penetration problems limit other emission protocols. The initial experimental procedure here is simple and avoids such challenges, aiming to investigate the principle of sharpness method as close as possible to the simulation. Single element SAU was not chosen because of the very low resolution resulting images as explained in Chapter 3. A solution involving a larger number of elements in transmission could have been used as in Subsection 3.3.2, but in the end plane wave was preferred as it is a better match with the original optical method.

5.4.2 Axial localization precision

The figures and the results of the present experimental study can be directly compared with those of the simulation and this is facilitated by the similar structure of the two chapters. Figures 4.22 and 5.13 are examined first where the normalized

sharpness is calculated based on the ultrasound images as in [104,105]. In the simulation study an average d_{dev}, equal to 16.6 μm was found over a 3.8 mm depth range while in the experimental study, the equivalent d_{dev} was 24.7 μm but was maintained over a longer range (6 mm). Although it was concluded that calculating the sharpness using images is not recommended (Section 4.3), the comparison showed a noticeable 33% improvement in the simulation case.

In Figures 4.17 and 5.8 the normalized sharpness was calculated using the Hilbert amplitudes. The average d_{dev} when either a Lorentzian or a Gaussian function were used to fit the sharpness data was not lower than 28.1 μm, a value maintained for a 3.5 mm depth range. The equivalent result from the experimental data analysis showed very little difference in the average d_{dev}, which was 26.8 μm and the high-accuracy localization area was extended to 6 mm. When the spline interpolation was considered for the simulation study, the average d_{dev} was varying between 1.83 μm and 2.26 μm depending on the selected depth range. The corresponding accuracy in this chapter was between 1.83 μm and 2.91 μm again based on several depth ranges. This demonstrates that in point scatter simulations a lower uncertainty can be maintained for longer areas.

The best results in both cases were acquired when the number of S-curves was increased to cover almost the whole simulated or wire target displacement, in Figures 4.37 and 5.16. In simulation, the average d_{dev} varied between 1.16 μm and 1.8 μm. In the measurement, the corresponding average d_{dev} varied between 1.08 μm and 2.87 μm. The number is similar for simulation and experiment when measuring the accuracy for shorter distances, but for longer ranges the simulation results were superior. The comparisons between the simulation study and the experimental validation show only small differentiations, given the fact that the wavelength used in the two cases was similar (220 μm for the simulation and 212 μm for the experiment). Note, the experimental result is always subject to the stepper motor system error which introduces some uncertainty to the actual wire position, that is necessary for the calculation of the d_{dev}.

Further, the normalized sharpness method's PDFs were also compared with the DAS axial FWHM in an alternative way to evaluate the axial resolution. The average PDF FWHM was 7.54 μm during the simulations and equal to 9.46 μm in the experimental study for an 8 mm depth range. The simulation result was better in absolute values but the experimental result was more significant since the DAS axial FWHM was 63% higher in the second case, due to the wire size. In general, Figures 4.21 and 5.12 show the potential for a future algorithm implementation without the actual scatterer position being a prerequisite. All other comparisons regarding the PSF appearance, S-curve width or amplitude were discussed in Section 5.2, Subsection 5.3.5 or during the studies on the z-step size and the axial separation between the S-curves of the present chapter. All those issues originate from the

addition of noise during the simulations. Overall, the closeness of the experimental results to the simulated ones, confirms the high performance of this sharpness method in achieving true super-resolution axial localization.

5.5 Combination with adaptive beamforming

The combination of the normalized sharpness algorithm with other beamforming techniques that improve the lateral resolution, may result in a complete description of the position of a single scatterer. The Minimum Variance (MV) or Capon beamformer [101] was extensively discussed in the Chapters 2 and 3 of the present thesis. Two implementations that are able to maintain similar high accuracy lateral localization (down to $\lambda/10$) in both simulation and experimental setup, were provided [102, 103]. The method is, like the sharpness one, based on the RF data. As a consequence the centre of a PSF of a scatterer could be fully assessed by the two methods with additional signal processing.

The sharpness method is a proof of principle study requiring further validation, whereas the MV beamformer is an already used algorithm among the ultrasound beamforming methods. The connection between the two relies on the fact that the same raw ultrasound data can be beamformed off-line in different ways as already explained in Subsection 4.4. Upon acquisition, the RF point-scatterer data may be initially beamformed with the adaptive method based on the processing described on Chapter 2. This will result in an initial estimate of a scatterer position, that may be later used to define the ROI around the PSF, where the sharpness value is calculated.

This procedure does not apply for the study of this or the previous chapter, since the simulated or wire target position was already known because of the Field II program and the translation stage respectively. Therefore there was no reason to determine the scatterer centre before the sharpness calculation, as explained in Subsection 4.3.3. However when the target position will be unknown, adaptive beamforming has the ability to provide an improved lateral localization or even distinguish two closely spaced scatterers that may appear as one with conventional beamforming. Finally, both methods are compatible with an unfocused transmit protocol and do not require a large number of emissions to function effectively. This makes the received transducer element signals suitable for processing in both ways.

5.6 Possibilities in microbubble tracking

An obvious application in ultrasound is the detection of contrast microbubbles, which can be visualized using pulsing strategies [34–36] that enable the subtraction of background tissue echoes such that a situation similar to a wire target is achieved.

It is established that despite the size of the bubbles it is possible to distinguish single scattering events due to their high scattering cross-section [41]. However, the use of high concentrations of microbubbles produces images that, for clinical applications, deploys intensity measures to provide a qualitative assessment of vascular kinetics.

The sharpness method is limited to the axial only direction and may be considered as a signal-based adjunct to the already existing methods aiming to precisely determine the position of a point source. Currently ultrasound super-resolution is based only on image processing. It has been accomplished either by identifying the PSF COM [93, 94] or by fitting three dimensional Gaussians [90–92] to ultrasound reconstructed data to approximate the PSF as outlined in Subsection 1.3.3. The COM is though dependent on high SNR and easily skewed by small tilt changes in the system, and the fitting functions are of limited value for axially displaced PSFs. The possibility to surpass the diffraction-limited resolution is therefore reliant on exploiting the otherwise lost detail from the ultrasound RF data, when converting them to images. A signal-based technique, such as the normalized sharpness method could further optimize any method that is nowadays available in real-time imaging.

However a potential microbubble application would require the control of the contrast agent density in an image, since each sharpness value must be evaluated only from a small area around a single PSF (Subsection 4.3.3). This is because with this restriction, the aberrations including (and dominated by) the focus errors are well-defined, symmetric and can be contained within a single analysis frame, as explained in the last two chapters. The ultimate objective will be the expansion of the sharpness method to the estimation of all three coordinates of a point source and potentially of microbubbles. Ultrasound scanning with modern $2D$ array probes could be explored to extract sharpness values that will correspond to a total position instead of a z-position [46].

Chapter 6

Application to Microbubbles

This chapter uses the methods as developed in Chapters 2-5 to perform a preliminary experimental study with microbubbles. The Minimum Variance beamformers and the normalized sharpness method are used here in an attempt to achieve high accuracy lateral and axial localization respectively. Both methods are implemented with small alterations from their initial presentations in Chapters 2 and 4. Their initial results are displayed and then compared with those of the previous chapters. Finally, possible future steps for further improvement are discussed.

6.1 Ultrasound setup

The setup was designed to allow individual bubbles to be distinguished in the image as described in earlier work [30, 189]. This is an important condition for both the MV beamformers and the normalized sharpness method, as they were developed for point scatter applications. A schematic representation of the complete experimental setup is shown in Figure 6.1.

6.1.1 Experimental phantom

The phantom consisted of a water tank in which a 200 μm diameter cellulose tube was mounted as shown in Figure 6.2. The tube was held in position with the aid of two (blue) fixed strings located at different depths across the tank.
The cellulose tube was connected through a syringe and additional tubing to an infusion pump containing the microbubble suspension. The pump pushed the bubbles through the phantom tube in and out of the tank. The setup intended the creation of a vertical microbubble path in relation to the face of the transducer. The transducer central beam could then be aligned with the tube and make sure that the microbubble movement is only axial and not lateral. However, the formation of right angle bends in the cellulose tube as imposed by the fixed wires would compromise the flow. To avoid this, the tube was not stretched thus taking a curved shape as shown in Figures 6.1 and 6.2.

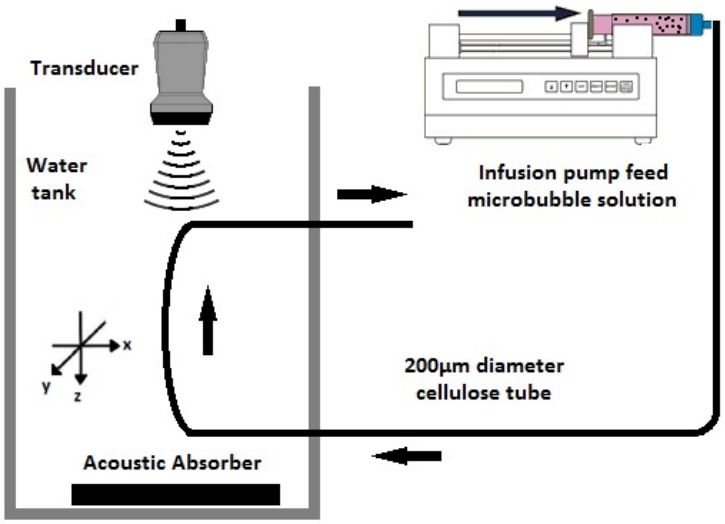

Figure 6.1: Illustration of the experimental setup for a preliminary attempt to achieve microbubble localization. The transducer acquired the data from MBs that were located in the parabolic part of the tube in the centre of the tank, that enforced upward flow.

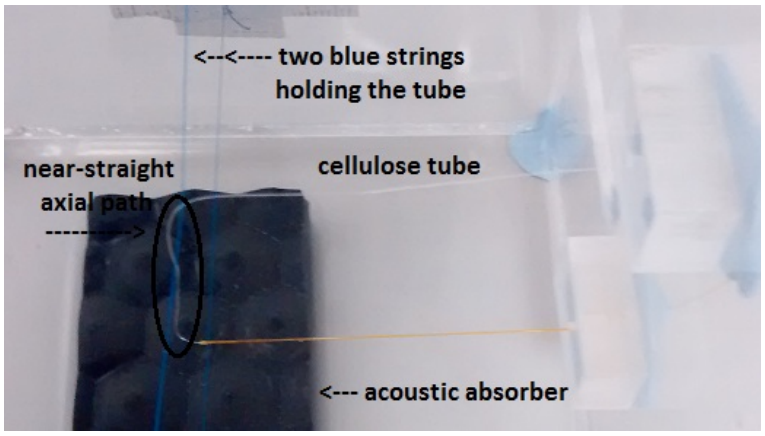

Figure 6.2: Picture of the tank before it was filled with water. The tube through which the micobubbles flow was held in a near-straight position in the middle of the tank by means of fixed wires. This ensured that the tube can be located fully within the $2D$ plane of the ultrasound image. The acoustic absorber ensured that multiple reflections were avoided.

The microbubbles used for this experiment were kindly provided by Prof. Klibanov. They are non-commercial and their preparation is detailed in [190]. They were lipid-shelled and their diameter varied between $1-10$ μm. The infusion pump contained 0.1 mL of bubble solution mixed with 150 mL of water. This was found to provide an adequate dilution of the MB for the experiments undertaken. Higher microbubble concentrations provide strong echoes, and thus a bright image along the tube, and were initially used to align the transducer with the tube. The pump was then set to 5.6 mL/hour flow rate V, which given the tube diameter R, resulted into a 5 cm/s average MB velocity c_{mb} based on the following equation:

$$c_{mb} = \frac{4V}{\pi \times R^2} \,, \tag{6.1}$$

This calculated velocity is within the range found in human blood vessels [191]. The infusion pump was positioned above a magnetic stirrer with a small magnetic bead inside the syringe that contained the MB solution, to secure an even distribution of the MBs in the water. In this experiment, there were no fixed targets and despite the control of microbubble movement, by means of the infusion pump, the scatterer location was not precisely known as previously (Subsection 5.1.1).

6.1.2 Scanner

The data were acquired in the CFU (Lyngby, Denmark) using the SARUS scanner as in the experimental studies of Chapters 3 and 5. The on-line processing of the received signals did not allow a live preview of the data. This preview was provided by the use of a second commercial scanner, Pro Focus 2202 Green Ultrasound (BK Medical, Herlev, Denmark). The transducer was firstly connected to that scanner until the initial alignment and the concentration were adjusted to make sure that single microbubbles were visualized in the image. Then, the transducer was relocated to the SARUS scanner in order to proceed with the data acquisition. This procedure proved to be problematic as the scanners had different settings and the concentration in the SARUS scanner appeared a lot higher. This limitation was not possible to address at the time of the experiments, and would only be possible after the analysis of the data. An image of the whole setup is shown in Figure 6.3.
As in the previous experiments that used the SARUS scanner, the data were initially sampled at 70 MHz, and then the sampling frequency, f_s was decimated by a factor of 2 to 35 MHz.

6.1.3 Data acquisition

An 8 MHz 128-element linear array transducer (BK8670, BK Medical, Herlev, Denmark) with 1.5λ element spacing was used to scan the custom-made tube phantom. The speed of sound, c was calculated to 1488 m/s, resulting in a wavelength λ equal to 186 μm. All the parameters of the scans are summarized in Table 6.1.

Synthetic transmit aperture was used as in Subsection 3.3.2. This transmission is also compatible with the normalized sharpness method (Subsection 4.8.1). The images were formed only by single emissions since the microbubble movement did not allow the averaging over a number of emissions. The SA offers fast acquisitions and the data from each emission were collected and were subsequently beamformed to provide the microbubble images.

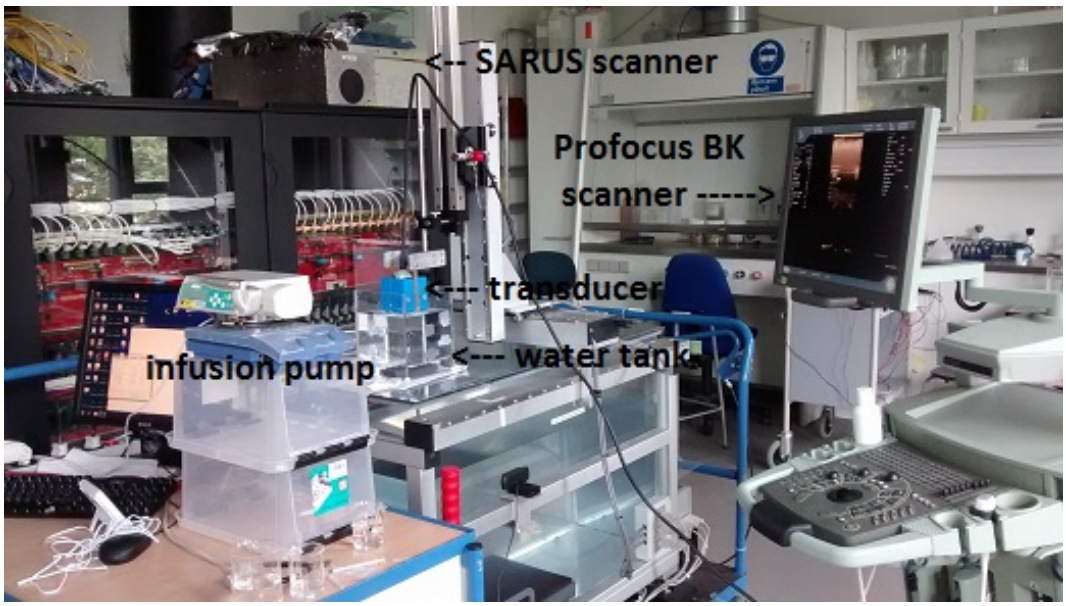

Figure 6.3: Experimental setup for imaging microbubbles inside the tube. Two ultrasound scanners were used for setting up the experiment and the data acquisition respectively. The same transducer was used in both and was clamped into the phantom.

Transducer	
Transducer type	Linear array
Transducer element pitch	300 μm
Transducer element kerf	35 μm
Transducer element height	4 mm
Center frequency, f_0	8 MHz
Sampling frequency, f_s	70 MHz
Bandwidth	60%
Speed of sound, c	1488 m/s
Wavelength, $\lambda = c/f_0$	186 μm
Scanning depth	30 mm - 90 mm
Excitation pulse	Six-cycle sinusoid at f_0 weighted by a 50% Tukey window
Peak negative pressure, PNP	2.57 MPa
Synthetic Aperture Emission	
Transmit apodization	Hanning
Receive apodization	Boxcar/Hanning/MVT/MVS
Receive focal depths (for sharpness)	45 mm/48 mm/51 mm/54 mm
Number of transmitting elements	64
Number of receiving elements, M	128
Number of emissions, N_{em}	1

Table 6.1: Scan parameters of the microbubbles measurement.

The maintenance of a low MI is another prerequisite in this study as explained in Subsection 1.2.1 of the Introduction. This is because high Mechanical Index (MI) values may result in MB destruction or inertial cavitation [192–195]. For this

reason, the data acquisition followed a similar strategy to that in [196, 197], where the MI was calculated for the same transducer and the SARUS scanner. The active aperture was used to emit an unfocused spherical wave where the MI dropped off quickly below the transducer surface. The peak MI is the ratio of the Peak Negative Pressure (PNP) (in MPa) and the square root of the transducer's center frequency (in MHz). In Figure 6.4 the MI map from [196] is shown for depths between 10 mm and 17 mm and for a 10 mm lateral distance. The MI was calculated at 0.91 and the peak value was for $(x, z) = (1.5 \text{ mm}, 10 \text{ mm})$. The value then was then approaching 0.5 at a depth of 17 mm and continued to further decline for the scanning depths of the measurement (30 mm to 90 mm). Although no data are available for the depth of interest in this study it can be estimated that the MI was below 0.3, which is a non-destructive MI for the microbubbles.

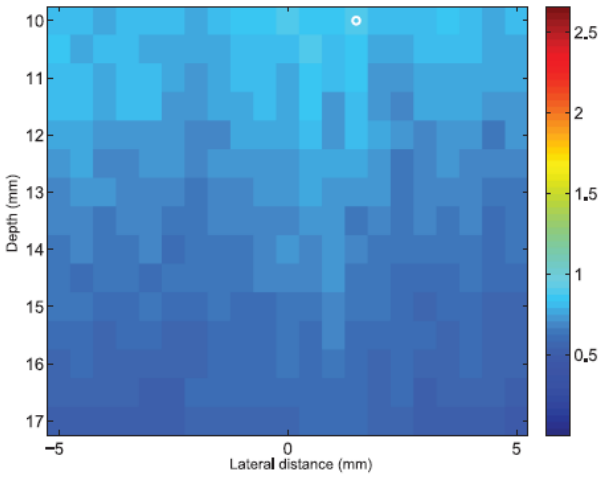

Figure 6.4: The MI map adapted from [196] is shown across an image for depth between 10 mm and 17 mm and 10 mm laterally for the SA transmission protocol used. The white circle indicates the position of the peak value.

6.2 Receive beamforming and data analysis

The acquired MB data were beamformed using the MV and DAS methods. Different receive foci were used in the DAS case for the normalized sharpness algorithm implementation. The processing is outlined in the following two subsections.

6.2.1 Minimum Variance beamforming

The adaptive apodization weights for both the MVT and the MVS were calculated based on the Equation (2.5), found in Subsection 2.2.2, and (2.11) in Subsection 2.2.3 respectively. The experimental validation (Subsection 3.4.1) of the adaptive methods in Chapter 3 showed higher performance when:

- A larger aperture was used.
- The forward-backward averaging was used for the calculation of a more robust sample covariance matrix (Subsection 3.2.1).

- The adaptive processes were applied to small areas instead of entire images (Subsection 3.4.1).
- A lateral subdivision beyond the pitch size was employed.

Using the above as a guide an extensive MV parameter study was avoided here for the microbubble implementation. Forward-backward averaging and a sub-array length $L = 2M/3 = 85$ were used. In absolute numbers the L was lower than the value selected in Chapter 3, but since the transducer used here consisted of 128 elements, the sub-array length was adjusted accordingly. Likewise, the lateral subdivision as discussed in Subsection 3.4.1 and Figure 3.14 reached the value $pitch/24$ instead of $pitch/16$ since the pitch size was %50 higher in this case compared to the number shown in Table 3.1. The number of sub-bands in the MVS case was $K = 55$.

Small areas with dimensions 10mm ×4mm, were beamformed separately to avoid calculating the sample covariance matrix over a large number of samples and then the image parts were merged to produce the final images. In this case, it was not feasible to beamform images with single scatterers since they were injected to the tube in difficult to control concentrations. However, it was possible to determine individual MBs from the beamformed images. For those MBs the lateral resolution can be again assessed, using the same metrics (lateral FWHM and PSL) defined in Subsection 2.2.6 of Chapter 2. The number of calculations (N_{calc}) was also measured based on the Equations (3.2), (3.3) and (3.4). Similar to Chapter 3, apart from the MVT and MVS, the conventional Boxcar and Hanning [143] apodization weights were also used as a standard for comparison.

6.2.2 Normalized sharpness algorithm

The normalized sharpness calculation used Hilbert data and was given by Equation (4.7) in Subsection 4.3. The same equation was mainly used for the experimental validation with the wire phantom in chapter 5 and is also adopted for the MB study. Further, the studies in Chapters 4 and 5 concerned only a single scatterer that was moving axially in relation to the beam and the normalized sharpness was calculated in each position. Thus, the only differentiation between frames was the relative distance between the scatterer and the position of the receive focus. This resulted in the sharpness variation over depth and subsequently into the formation of a symmetric S-curve.

In this MB study here the above concept was preserved, but instead of tracking individual bubbles over a large number of frames, multiple bubbles located at different depths were used simultaneously to extract a single curve. The normalization factor in Equation (4.7) compensates for bubble echoes of different intensity [198], that may be due to their size or the local PSF characteristics. Note that the PSF is not unique and is a function of displacement in all directions. Overall, compared

to previous chapters, this approach may lead to the acquisition of fewer frames to form an S-curve. Indeed, for the normalized sharpness method 150 frames were beamformed with around 10 manually distinguished microbubbles in each frame. Hence, the total number of the individual microbubbles used in this study, was approximately 1500. The sample is similar to the corresponding ones of the previous chapters but with smaller acquisition number. More specifically, in the simulation study (Section 4.6) there were 151 acquisitions including a single scatterer and were repeated for 10 times (1510 acquisitions/scatterers). During the wire-target measurement, the scatterer sample was slightly reduced to 1390 due to the 139 acqusitions per repetition (Section 5.1).

The raw received data were beamformed in multiple ways with the standard DAS process by the use of an individual receive focus each time. The beamformation toolbox BFT III [188], was used as in the Chapter 5. Closely spaced bubbles were rejected upon manual inspection due to the single PSF hypothesis of the algorithm. For the inspection, images beamformed with a Dynamic Receive Focusing (DRF) were preferred. This is because, the fixed-focus receive beamforming yields overall low resolution images apart from the focus position. The DRF that is also available by the BFT III, assumes multiple focal zones instead of only one (fixed focus). With this feature it was more likely to quickly locate MBs that may be merged throughout the whole image. Hence, a rough initial estimate of MB positions could be provided. Combined with the use of the Matlab *imagesc* function and image magnification tools, the DRF may result in the identification of single scatterers centres and thus, of the ROIs around them that may be used later for the sharpness processing. In contrast to the experimental study of the Chapter 5 where the true depth of the scatterer was precisely known, the experimental procedure here did not include this information. The development in Chapters 4 (Subsection 4.7.2) and 5 (Subsection 5.3.2) showed that the PDF may also provide the true deviation of the method. Thus, the results here will be focused on the obtained PDFs.

6.3 Minimum Variance beamforming results

The section follows the structure of the wire phantom Results section in the simulation study of Chapter 2. The beamformed images and the lateral resolution metrics are shown in Subsection 6.3.1 and a comparison with previous MV results comes next (Subsection 6.3.2).

6.3.1 Images & metrics

Single emission beamformed responses of a randomly chosen frame for the MB phantom are shown in Figure 6.5 with a 40 dB dynamic range. Overall the scanned area

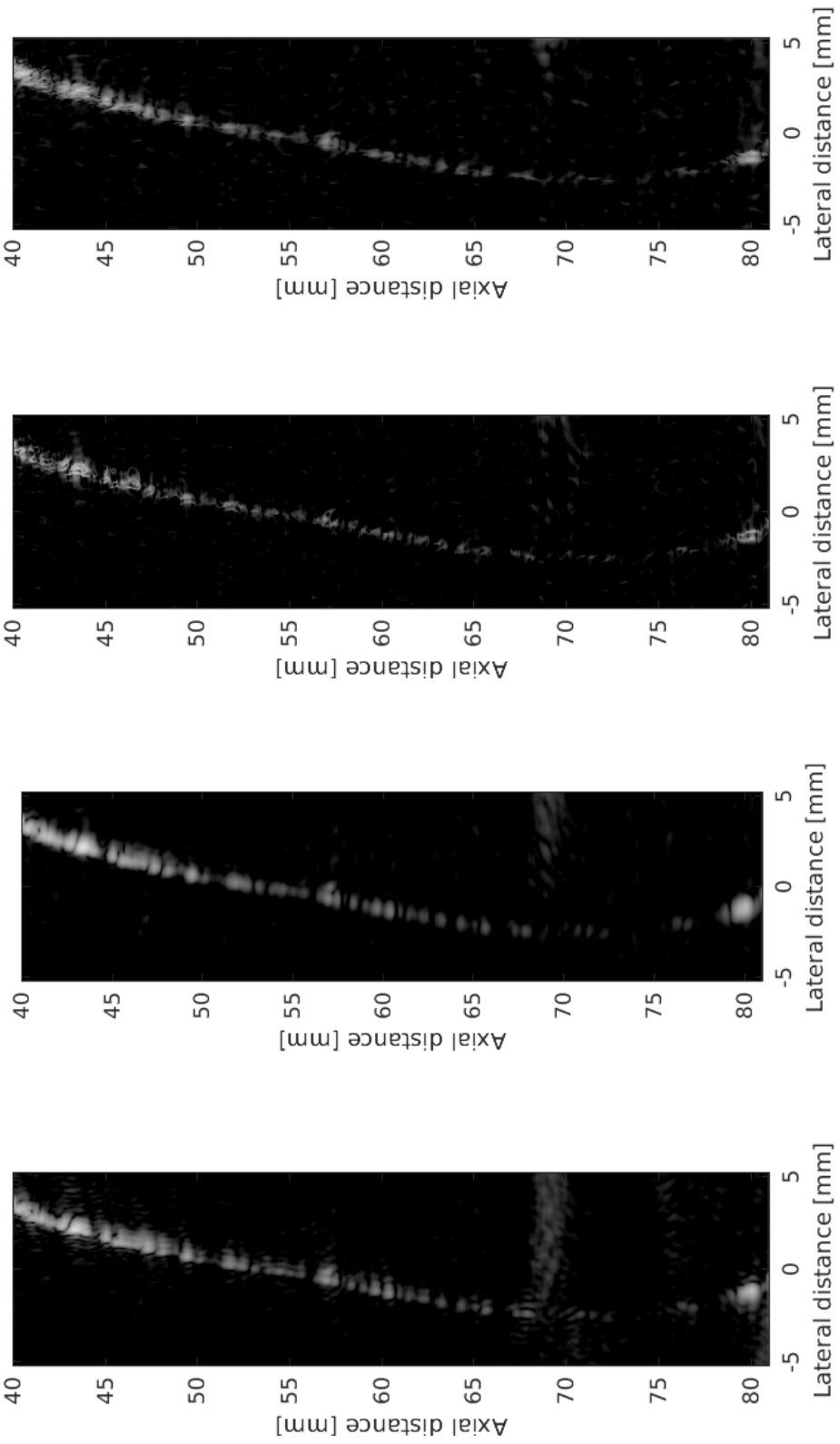

(a) Boxcar (b) Hanning (c) MVT (d) MVS

Figure 6.5: Beamformed responses of microbubbles inside the tube phantom from a single SA emission with (a) DAS Boxcar, (b) DAS Hanning, (c) MV Temporal, and (d) MV Subband apodization. The dynamic range of the display was 40 dB.

extended from -10 mm to 10 mm laterally and from a depth of 30 mm up to 90 mm axially (an area of 20×60 mm in total). Each of the images shown had dimensions (10.5 mm by 41 mm), so concentrating only on the path containing the MBs. The shape of the tube is curved and appears thinner in the MVT and the MVS cases (Figures 6.5(c) and 6.5(d)) compared to DAS Boxcar or Hanning (Figures 6.5(a) and 6.5(b)). This implies an improvement of lateral resolution that was expected with the adaptive beamforming compared to the conventional DAS. Further, additional unwanted reflections that appear in the first two subfigures of the Figure 6.5 (at a depth of 70 mm and for a lateral distance between 0 mm and 5 mm) were avoided with the adaptive beamforming.

At the top of the images (between 40 mm and 50 mm) the concentration of the contrast agents was higher. On the other hand the concentration was very low at a depth range between 70 mm and 75 mm and isolated microbubbles were possible to visualize. This was noticed in most frames and is an effect of the increased MI compared to the bottom of the image. As shown previously the microbubble number with echo above the noise of the system correlates with MI [41]. Thus, the bottom of the image offers improved opportunity to isolate single MB echoes in the image. A quantitative comparison of the different beamformers was achieved by plotting the lateral variations of intensity at various depths for all methods in Figure 6.6. Data from the top of the Figure 6.5 were avoided due to the high density of the microbubbles at that part. In Table 6.2 the lateral FWHM and the PSL measured by the graphs displayed in Figure 6.6 can be found for both conventional and adaptive apodization weights. The N_{calc} is not included in the Table since it was not calculated for each bubble (scatterer) as in the previous chapters but for the whole images. The numbers were 23 MFLOPs for the conventional apodization weights and 1.44 TFLOPs for the MVT and 319 TFLOPs for the MVS, based on the Subsections 2.2.5 and 3.2.2.

Figure 6.6 and Table 6.2 demonstrate that there are significant resolution gains for applying the adaptive beamforming. The improvement of the lateral resolution as this was defined in Subsection 1.1.3 of the Introduction, becomes more prominent for closely spaced microbubbles. There are instances in Figure 6.5 where the conventional apodization weights failed to distinguish the presence of two MBs and resulted into a single large PSF. Figure 6.7 displays a closer look at the result of the four beamformed responses at the depths $z = 71.47$ mm, and $z = 80.2$ mm for more clarity. The lateral variations at the depth of 80.2 mm are also shown in Figure 6.8. At this depth, the Boxcar apodization resulted in FWHM equal to 0.68 mm (3.65λ) and in PSL equal to -17 dB. The equivalent numbers for Hanning apodization are 0.89 mm (4.78λ) and -28 dB for the two metrics respectively. On the other hand, for the MV approaches two distinct bubbles were identified. The first bubble is centred at $(x, z) = (-1.4$ mm, 80.2 mm) and the FWHM is 0.29 mm (1.56λ) and

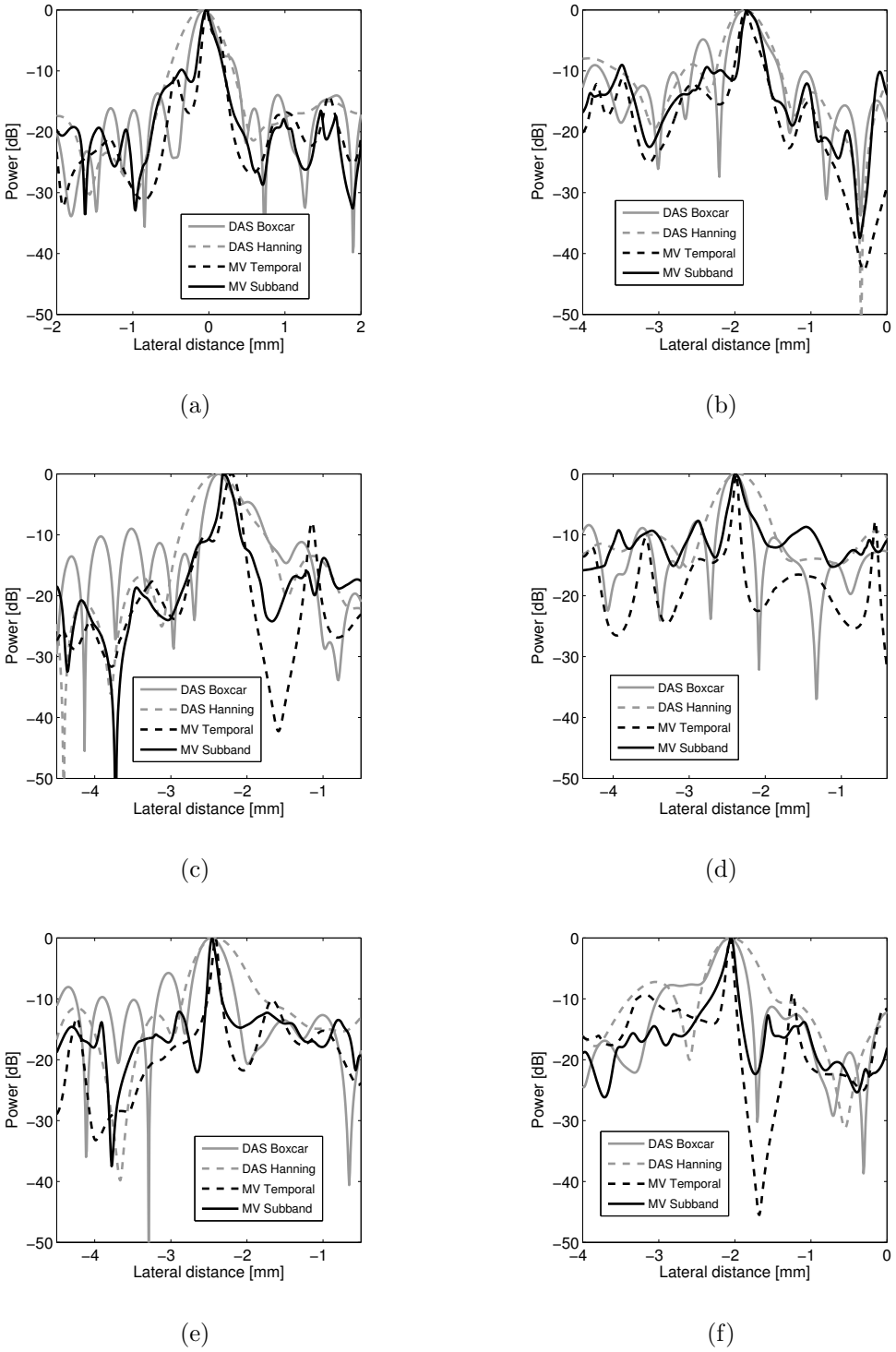

Figure 6.6: Lateral variations of the beamformed responses of Figure 6.5 at various depths: (a) 54.34 mm, (b) 60.55 mm, (c) 67.27 mm, (d) 70.87 mm, (e) 71.47 mm and (f)76.89 mm.

the second at $(x, z) = (-1.1 \text{ mm}, 80.2 \text{ mm})$ with FWHM equal to 0.21 mm (1.13λ) for the MVT. The corresponding numbers for the MVS were 0.34 mm (1.82λ) and 0.24 mm (1.29λ). The PSL was calculated at -22 dB and -20 dB for the left and right bubble respectively of Figure 6.8 (second row), both for the MVT and the MVS.

	PSL	FWHM	
Microbubble centred at $(x, z) = (0.03$ mm, 54.34 mm)			
DAS Boxcar	-7 dB	0.39 mm	2.10λ
DAS Hanning	-15 dB	0.64 mm	3.44λ
MV Temporal	-11 dB	0.27 mm	1.45λ
MV Subband	-10 dB	0.25 mm	1.34λ
Microbubble centred at $(x, z) = (-1.31$ mm, 60.55 mm)			
DAS Boxcar	-10 dB	0.62 mm	3.35λ
DAS Hanning	-13 dB	0.69 mm	3.73λ
MV Temporal	-12 dB	0.33 mm	1.76λ
MV Subband	-10 dB	0.35 mm	1.89λ
Microbubble centred at $(x, z) = (-2.39$ mm, 67.27 mm)			
DAS Boxcar	-11 dB	0.69 mm	3.71λ
DAS Hanning	-14 dB	0.78 mm	4.20λ
MV Temporal	-18 dB	0.24 mm	1.30λ
MV Subband	-19 dB	0.24 mm	1.30λ
Microbubble centred at $(x, z) = (-2.39$ mm, 70.87 mm)			
DAS Boxcar	-8 dB	0.39 mm	2.10λ
DAS Hanning	-10 dB	0.75 mm	4.03λ
MV Temporal	-14 dB	0.09 mm	0.48λ
MV Subband	-9 dB	0.21 mm	1.13λ
Microbubble centred at $(x, z) = (-2.46$ mm, 71.47 mm)			
DAS Boxcar	-6 dB	0.62 mm	3.35λ
DAS Hanning	-13 dB	0.77 mm	4.14λ
MV Temporal	-10 dB	0.11 mm	0.59λ
MV Subband	-13 dB	0.13 mm	0.70λ
Microbubble centred at $(x, z) = (-2.05$ mm, 76.89 mm)			
DAS Boxcar	-8 dB	0.51 mm	2.74λ
DAS Hanning	-8 dB	0.75 mm	4.03λ
MV Temporal	-9 dB	0.11 mm	0.59λ
MV Subband	-14 dB	0.19 mm	1.02λ

Table 6.2: Peak-side-lobe level (PSL) and lateral Full Width at Half Maximum (FWHM) for the beamformed responses of single bubbles at different depths, where $\lambda = c/f_0 = 186$ μm.

To increase the confidence that the MVT and the MVS images at the second row of the Figure 6.7 indeed include two distinct targets, a Field II simulation was performed. The simulation setup was similar to the one described in Subsection 6.1.3 and two point scatterers were simulated at the positions where the two MBs were located based on the MV processing. The result is displayed in the third row of Figure 6.7, with DAS apodization again providing images containing a single PSF, while the MVT and MVS beamformed responses include two separate PSFs. For this simulation, the Boxcar apodization resulted in FWHM equal to 0.81 mm (4.35λ)

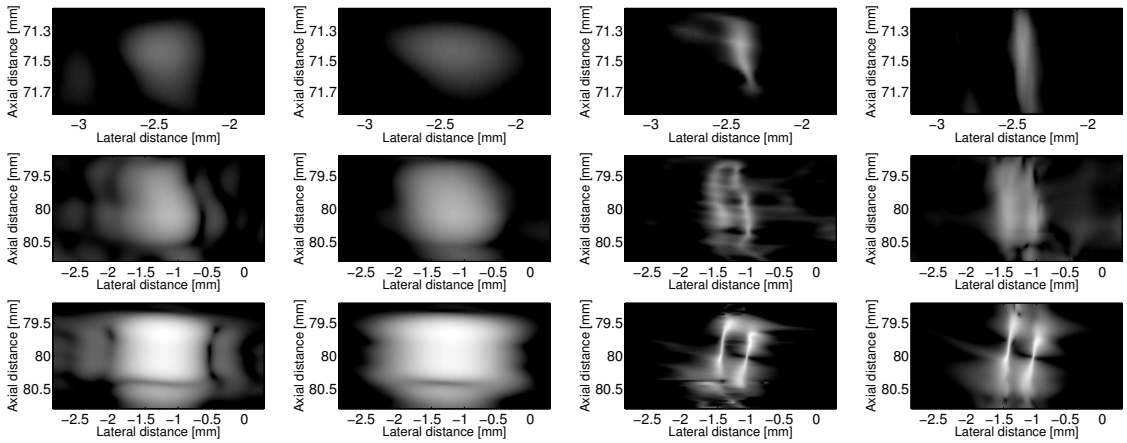

(a) DAS Boxcar (b) DAS Hanning (c) MV Temporal (d) MV Subband

Figure 6.7: Beamformed responses of the microbubbles at 71.4 mm and at 80.2 mm depths, and of two simulated Field II targets at a depth of 80 mm with (a) DAS Boxcar, (b) DAS Hanning, (c) MV Temporal, and (d) MV Subband apodization. Images are shown with a dynamic range of 40 dB.

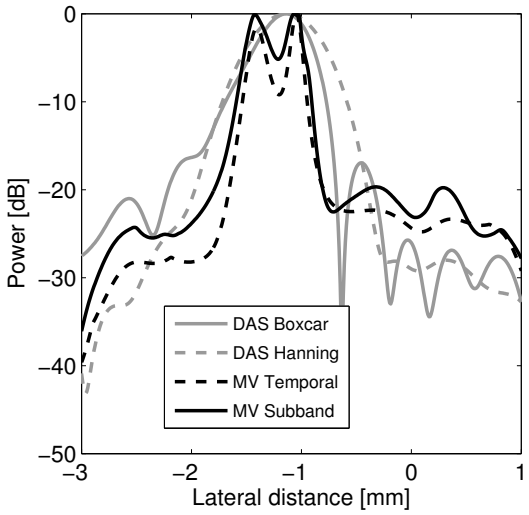

Figure 6.8: The lateral variations of power in dB at 80.2 *mm* in Figure 6.6.

and in PSL equal to −17 dB. The equivalent numbers for Hanning apodization are 1.02 mm (5.48λ) and −33 dB for the two metrics respectively. On the other hand, from the two MVT PSFs, the FWHM was measured to 0.08 mm (0.43λ) and 0.05 mm (0.27λ) respectively with a common PSL of −22 dB. The corresponding numbers for the MVS were 0.09 mm (0.48λ) and 0.06 mm (0.32λ), with a PSL equal to −18 dB. The last two rows of Figure 6.8 present close resemblance, and the simulation confirms that both the MV methods were able to distinguish two individual scatterers where the DAS beamformers could only identify one.

6.3.2 Comparison with results of Chapters 2 and 3

The MV beamforming was applied to images containing non-linear ultrasound scatterers. The MB results shown in Table 6.2 (for microbubbles at different positions), enable the comparisons with previously acquired simulated and experimental results with linear scatter. The metrics in this table demonstrate that adaptive apodization weights can improve the lateral FWHM and the PSL values compared to conventional ones. However the level of improvement is not the same with the one recorded in the previous chapters, where between 5 and 20-fold more narrow PSF main lobes were acquired with the same technique using the linear scatter (Subsection 3.6.2). Particularly, FWHM values of up to 20 μm (or $\lambda/10$) and PSL even below -40 dB were reached (Subsection 3.4.1).

Here the lowest FWHM value was 0.09 mm (or 0.48λ) and was noticed for the MB located at $(x, z) = (-2.39$ mm, 70.87 mm). This number implies a 4 fold improvement compared to the best conventional beamformer (Boxcar) at the same depth (Figure 6.6(d)). In addition, the greatest improvement was reported for the MB located $(x, z) = (-2.46$ mm, 71.47 mm). The MVT FWHM was 0.11 mm marginally higher than the best case mentioned above, but the Boxcar FWHM was equal to 0.62 mm, demonstrating 6-fold gains using the MVT for that microbubble (Figure 6.6(e)). The results from all other bubbles show that the FWHM was improved in the adaptive approaches by a factor that varied between 1.5 and 6. Importantly, the improvement at depths greater than 70 mm was very similar to the one provided using the wire target (Subsection 3.4.1).

The sidelobes were much higher and closer to 0 dB (maximum power) for all four beamformers, compared to the results of previous studies (Subsections 2.4.1 and 3.4.1). They therefore could not be compared directly and in absolute values. In this study, the lowest PSL value was -19 dB and was noticed for the MB located at $(x, z) = (-2.39$ mm, 67.27 mm) for the MVS (Figure 6.6(c)). At the same time, the best conventional beamformer result did not overcome -14 dB for this individual microbubble. With this exception, the Table 6.2 shows that the Boxcar apodization resulted in very high PSL values (between -6 dB and -11 dB) and thus sidelobes. The other three apodization weights (Hanning, MVT and MVS) showed similar performance and PSL values that range between -9 dB and -15 dB with no obvious variation pattern.

The optimal results mentioned in this subsection were acquired in random order regardless of the MB position, since the metrics values primarily depend on the variable MB signal. The metrics thus, do not provide a correlation with depth as found with the linear scatter work before. This was confirmed from the standard DAS beamforming results in Table 6.2. In general, the high bubble concentration appears to reduce the utility of the calculated adaptive weights. In this study there was less control on the MB concentration and thus beamforming ROIs with only

one scatterer as in Chapter 3 was rather rare. The interference between neighboring microbubbles was hence not avoided and this affected negatively the precision of the covariance matrix estimate. Nevertheless, resolution gains were still present and so the results obtained here confirm that adaptive beamforming is well-suited for lateral MB localization.

A comparison between the MVT and the MVS ignoring the computational burden, shows as in the Chapters 2 and 3, similar performance. Furthermore, where single microbubble events were beamformed the results looked similar to those of the linear scatter. The metrics here show a slight improvement in the MVT case, but the MVS may result in better microbubble definition as it can be seen by comparing Figures 6.7(c) and (d). In those figures, the presence of two individual scatterers was more obvious in (d) whereas in (c) the scatterer on the left was more likely to be perceived as noise. Computation-wise the MVT benefit over the MVS is very important (220 times reduced) based on the numbers given in the previous subsection.

6.4 Normalized sharpness method results

The section follows the sharpness methodology as this was developed in Chapters 4 or 5 using the same microbubble data as above. The derivation of the MB sharpness data is first analyzed and then several examples of the probability density function, that provides the depth estimates, are displayed .

6.4.1 Region of interest definition

Four different beamformed responses of the same image frame used in the MV analysis (Figure 6.5), are shown in the Figure 6.9. From the figure it is possible to see the effect of shifting the receive focus position on the lateral resolution (wider PSF main-lobe and significantly higher side-lobes). The receive foci were chosen to 45 mm, 48 mm, 51 mm and 54 mm to cover the effective range between 38 mm and 61 mm depths (23 mm in total). The depth range here was selected based on the MB presence, and was extended compared to the 15 mm depth displacement of the previous chapters (Subsections 4.6.1 and 5.1.1). Therefore a 4^{th} receive focus was implemented and as a consequence a 4^{th} S-curve was formed to cover the total 23 mm displacement and compensate for the difference.

From each image in Figure 6.9 it was possible to estimate a small number (≤ 10) of separated MBs and then the next frame was examined. Single scatterers were visible only for a small area around the selected focus each time, whereas away from the focus the MBs presented high sidelobes. Each image in Figure 6.9 is similar to those in Figure 4.11 of Subsection 4.6.1. However, away from the receive focus position and when the bubble density was too high, the confidence in locating the centre of a single microbubble was significantly reduced.

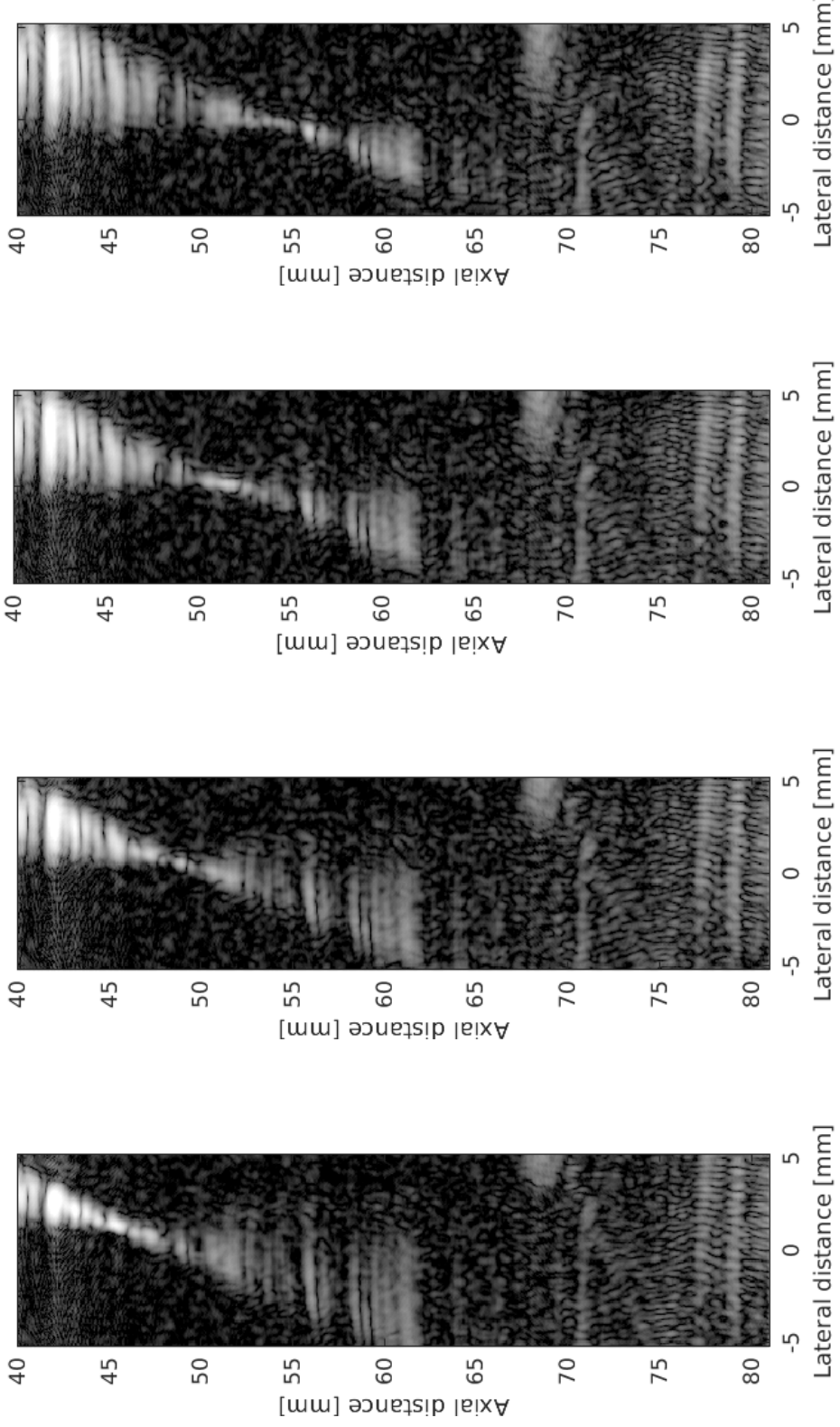

(a) Receive focus at 45 mm (b) Receive focus at 48 mm (c) Receive focus at 51 mm (d) Receive focus at 54 mm

Figure 6.9: Single emission beamformed responses of the microbubble phantom with 4 individual fixed foci in receive. The dynamic range of the display was 40 dB.

For this reason the advanced focusing and the image scaling tools described in Subsection 6.2.2 were employed. Their use led to the generation of Figure 6.10 for the same data presented in Figure 6.9, which makes easier the distinction of single scattering events. In essence, this intermediate stage described in this subsection assists in the single MB centre approximation that is necessary for the algorithm as explained in Subsection 4.3.3. This process enables the ROI definition, with the black box shown in Figure 6.10(b) being an example. However, the sharpness values that form an S-curve were extracted from the original Hilbert data as described in Subsection 4.3.2.

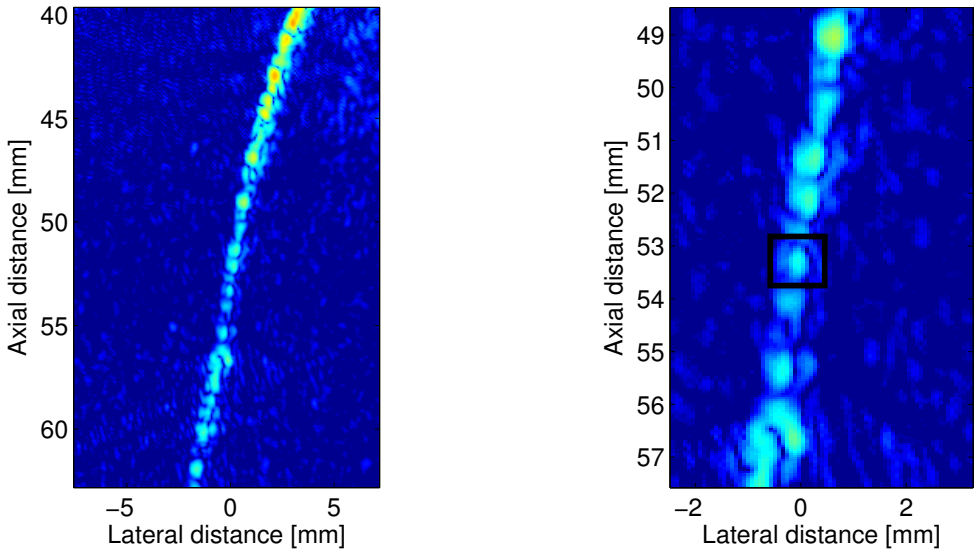

(a) 15 $mm \times 23$ mm close-up (b) 6 $mm \times 9$ mm close-up

Figure 6.10: Two, color-scaled close-ups from the beamformed responses of the bubble phantom with dynamic focusing in receive, to provide a rough estimate of individual microbubble centres.

6.4.2 Normalized sharpness assessment

Figure 6.11 shows the mean sharpness and its Standard Deviation (SD) in four cases, one for each receive focus of Figure 6.9 (45 mm, 48 mm, 51 mm and 54 mm). The mean and the SD values originated from random microbubbles that were passing from similar depths and not from identical successive measurements as shown in Figure 5.7. As a consequence, unlike the previous studies, the number of observations varied at different depths. Further the distance between two successive sharpness values was not controlled and therefore different observations had different distances from their neighbors. Figure 6.11 also includes the best Lorentzian and Gaussian fits of the four sharpness datasets. In Figure 6.11(a), the correlation coefficients, r, between mean sharpness and the two fits were 0.979 and 0.975 for Lorentzian and Gaussian respectively. Those coefficients take values slightly over 0.98 when only

the slopes and the peak of an S-curve are considered. The corresponding values in Figure 6.11(b) are 0.973 and 0.976 for the Lorentzian and the Gaussian functions.

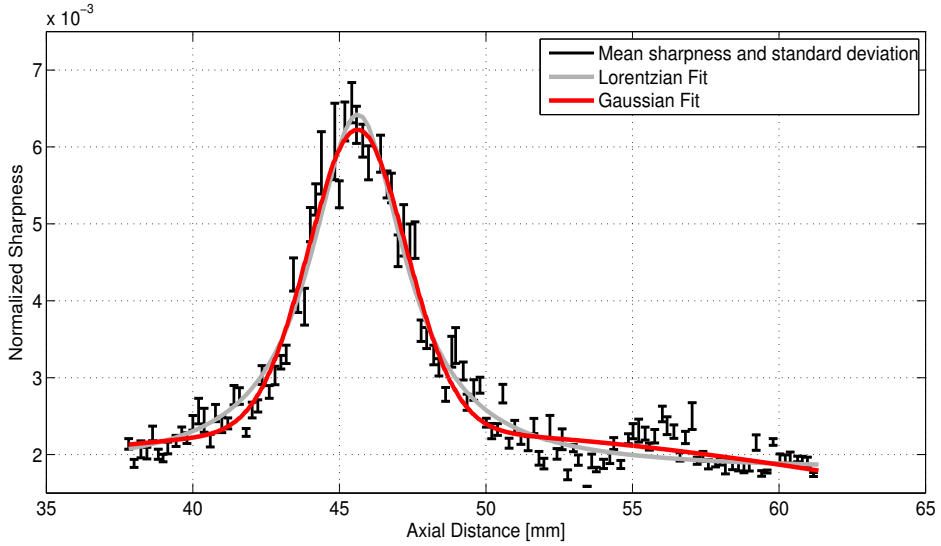

(a) Receive focus at 45 mm

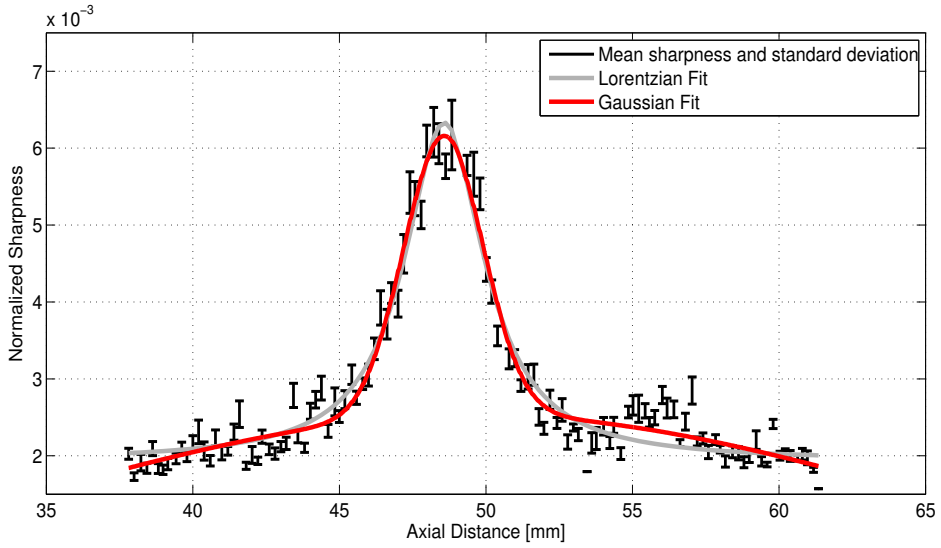

(b) Receive focus at 48 mm

Figure 6.11: Mean sharpness and standard deviation together with the best Lorentzian and Gaussian fits for the same 4 receive foci used in Figure 6.9: (a) 45 mm, (b) 48 mm.

A receive focus at greater depths decreases the sharpness peak value and slightly lowers the correlations. In Figure 6.11(c) the correlation coefficient r values, were equal to 0.957 and 0.963 for the Lorentzian and the Gaussian fitting functions and did not improve when the curves edges are excluded. In Figure 6.11(d) the respective values were 0.968 and 0.969. The Figure 6.11 is in correspondence to the Figure 5.7. However, the sharpness values were fluctuating around the displacement

edges and the standard deviation was also higher, so each sharpness dataset was plotted separately.

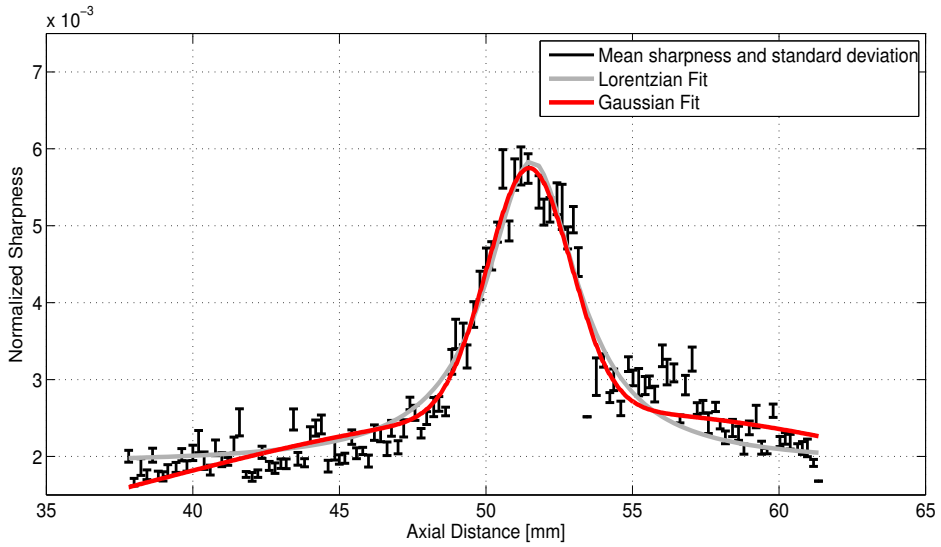

(c) Receive focus at 51 mm

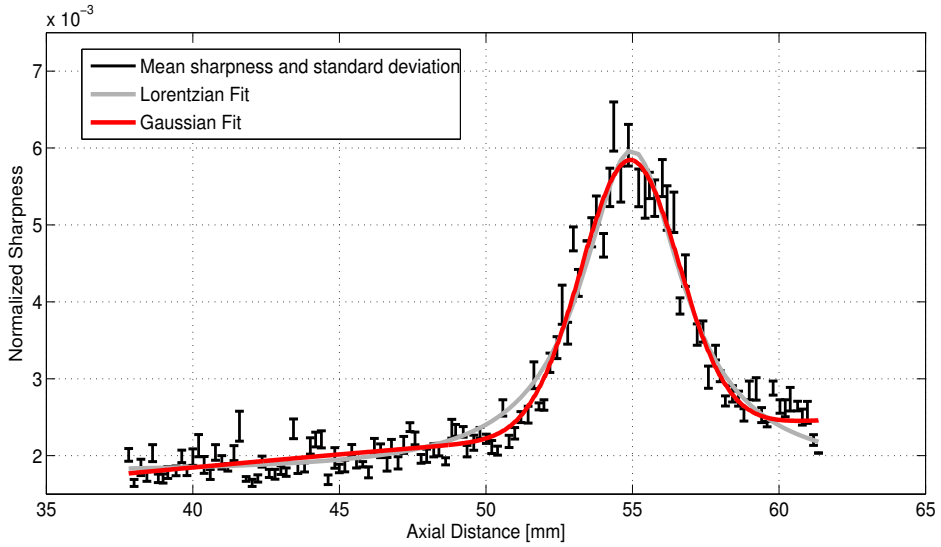

(d) Receive focus at 54 mm

Figure 6.11: (continued) Mean sharpness and standard deviation together with the best Lorentzian and Gaussian fits for the same receive foci used in Figure 6.9: (c) 51 mm and (d) 54 mm.

In the Figure 6.12 the 4 sharpness curves corresponding to the sharpness data of the Figure 6.11 are displayed. The figure is similar to Figures 4.17(a) or 5.8(a) of the past two chapters and results into depth estimates for individual microbubbles based on the spline interpolation processing (Subsection 4.7.1). However, the comparison (Figure 4.17(b) and 5.8(b)) of the normalized sharpness method depth estimates with the scatterer actual position is here missing since the latter was not precisely known.

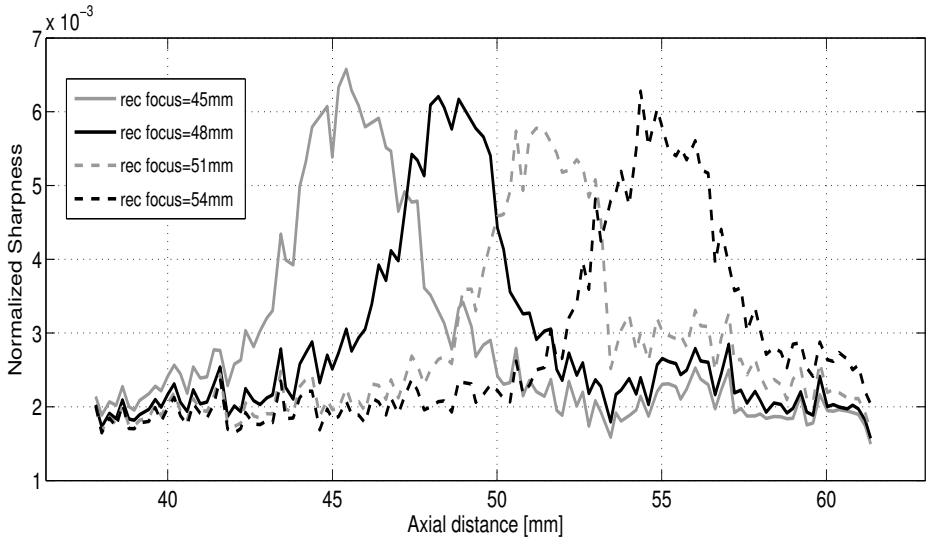

Figure 6.12: A set of four normalized S-curves from 150 experimentally acquired microbubble frames. Data were generated by unfocused synthetic aperture ultrasound transmission and by beamforming with four different foci in receive.

6.4.3 The probability density function

Following the example of Subsections 4.7.2 and 5.3.2, in Figure 6.13, two instances of the Gamma PDF are shown around the area of their maximum. In Figure 6.13(a) the microbubble centre depth position was 50.25 as estimated from Figure 6.10(b), based on the DRF beamforming. The PDF maximum was located at 50.314 mm and this would result in a d_{dev} equal to 64 μm ($\approx 0.34\lambda$) supposing that the microbubble centre was precisely known. This was not the case here, since with the given sampling frequency (Table 6.1), the axial distance between 2 RF samples was ≈ 40 μm in the conventional DAS beamforming. The PDF FWHM was calculated to 165.42 μm ($\approx 0.89\lambda$) although some smaller peaks were also present in curve, unlike the PDFs shown previously in Figures 5.10 or 4.19. Likewise in Figure 6.13(b), the microbubble centre depth position was 51.30 and the PDF maximum was located at 51.378 mm. This would provide a d_{dev} equal to 78μm ($\approx 0.42\lambda$). The PDF FWHM was calculated to 310.68 μm ($\approx 1.67\lambda$) and a smaller peak in the PDF was again observed. Note that due to the longer excitation (6-cycles - Table 6.1) the conventional axial resolution in the present scan was reduced to $6 * 186$ μm$/2 = 558$ μm. This value corresponds to the minimum axial separation between two targets.

A final PDF example can be found in Figure 6.14, regarding the microbubble in the black box of Figure 6.10(b). For this target, the Hilbert envelope is plotted with the PDF around the same depth (53.25 mm) as in Figures 4.21(b) or 5.12(b). The PDF maximum, i.e. the depth prediction of the method for this scatterer was 53.226 mm. The PDF had a FWHM equal to 115.91 μm ($\approx 0.62\lambda$) and resulted in a more clear peak compared to the examples of the Figure 6.13. For this reason it is more appropriate for a direct comparison with the DAS axial FWHM. The Hilbert

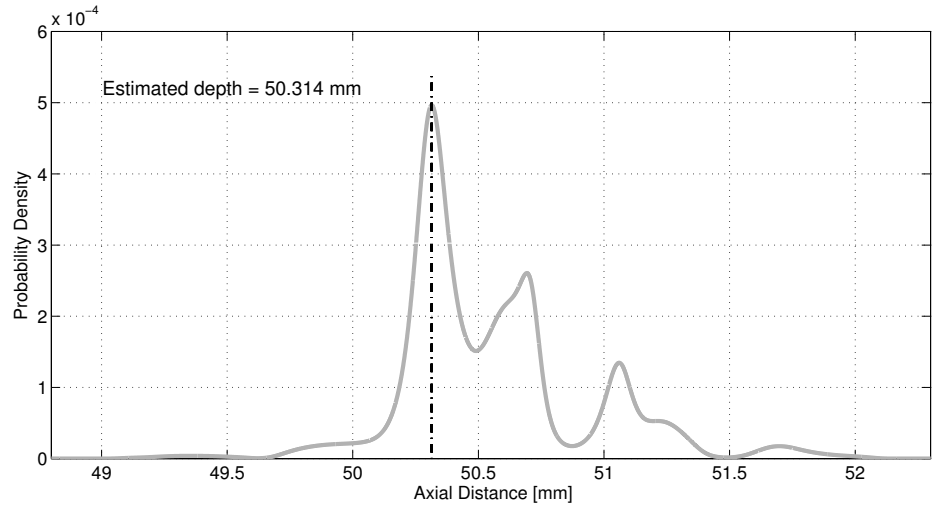

(a) PDF at 50.25 mm

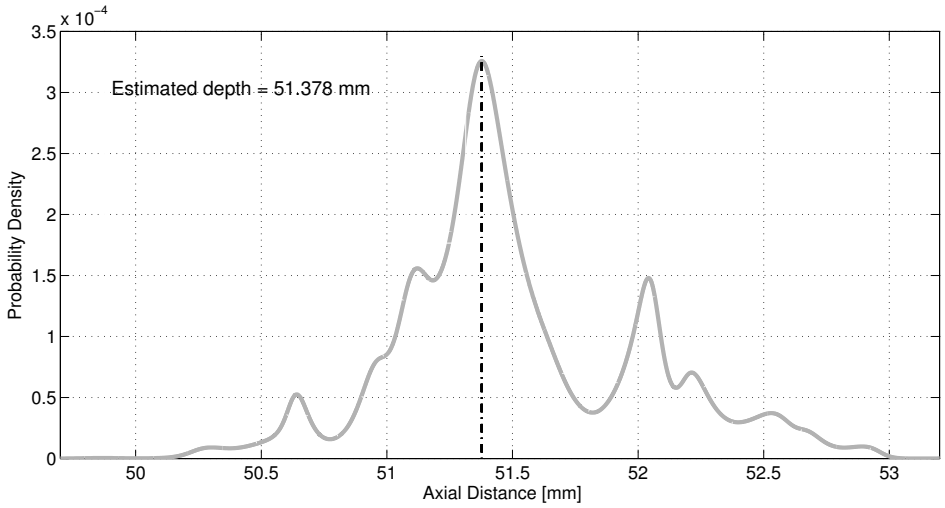

(b) PDF at 51.30 mm

Figure 6.13: Probability density function plotted over depth for two microbubbles approximately centred at depths (a) 50.25 mm and (b) 51.30 mm. The PDF maximum will indicate the normalized sharpness method's estimate for this position. In (a) the maximum is found at 50.314 mm and in (b) at 51.378 mm.

envelope resulted in an axial FWHM equal to 604.06 μm ($\approx 3.25\lambda$). The two calculated FWHM indicate a that a 5-fold improvement in the axial localization for the normalized sharpness method is feasible with the normalized sharpness method.

6.4.4 Comparison with Chapters 4 and 5

The normalized sharpness method was adjusted here to the non-controlled movement of the non-linear scatterers and to the absence of repetitive measurements. The behavior of the sharpness metric was preserved with higher sharpness appearing for those microbubbles closer to the receive focus, and rapid reduction away from

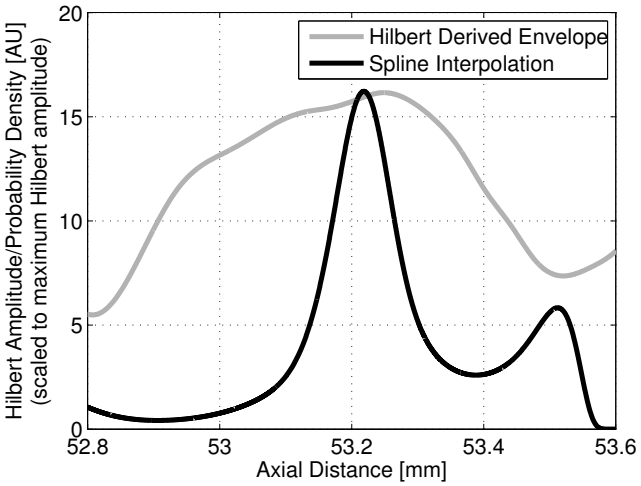

Figure 6.14: The PDF of the microbubble approximately centred at 53.25 mm depth, is scaled to the maximum Hilbert amplitude and plotted together with the envelope of the same MB. The DAS axial FWHM was calculated to 604.06 μm whereas the PDF FWHM was calculated to 115.91 μm.

it. The Lorentzian or Gaussian fitting functions remain a good fit for the sharpness values and describe adequately the sharpness variation in respect to depth. However, in this MB study the S-curves (Figures 6.11 appear to have increased fluctuations when compared to the sharpness data displayed in Figures 4.16 and 5.7.

Consequently, the sharpness standard deviation was increased and reached values more than one order of magnitude higher than those noticed for the wire target. Overall the MB sharpness data were similar to the results of Subsection 4.7.4 where increased noise was added to the RF signals (Figure 4.24(a)) and Subsection 4.9.1 where sharpness was calculated at greater depths (Figure 4.33). The above fidning highlights the signal to noise limitation of the measurement. Further, from the Figure 6.12 it must be noted that the S-curve peak did not always coincide with the depth equal to the chosen receive focus (for instance the curve corresponding to a receive focus at 45 mm). This is because the peak depends on the existence of strong MB signal exactly at the receive focus depth. In the case where this was not present or where there was no microbubble at this depth then the S-curve peak was located at the depth closest to where a MB exists, which shows that the data sampling here was not optimal.

In order to compensate for possible S-curve distortions or peak shifts as explained in the previous paragraph, a longer foci separation (3 mm instead of 2 mm) between successive receive foci was selected compared to Chapters 4 and 5. This is because, the standard 2 mm distance would increase the probability to obtain S-curves with overlapping peaks due to the compromised quality of the currently acquired ultrasound data. Increasing this distance by 1 mm though is not expected to affect the algorithm performance as already studied in Subsections 4.9.4 and 5.3.6.

The above constraints, limited the comparisons with the Chapters 4 and 5 only to the study of the resulting PDFs. From Figures 6.13(a) and 6.14 it was shown that it was possible to acquire a sub-wavelength PDF FWHM or even obtain 5 fold improvements in situations where there was increased confidence for the presence of a single event (clear PDF). Importantly, the conventional axial resolution was lower due to the longer spatial pulse length (558 μm compared to 220 μm of the simulation study), and the DAS axial FWHM, unlike the linear scatter case, was subject to variations due to the increased PSF variability of the microbubbles. The result here, although it shows some potential, it cannot be generalized, and remains far from the 23 and 35-fold gains that were achieved in the Subsections 4.7.2 and 5.3.2 respectively.

6.5 Comments on the experimental setup

Overall, both MV and sharpness methods resulted in promising findings, in their initial application to microbubble data. Improving the experimental setup is expected to improve both methods' performance. The current setup limitations and possible solutions are discussed in this section for each method individually.

6.5.1 Minimum Variance beamforming

The MV beamformer is established as a method to process the responses captured by an ultrasound imaging system that utilizes transducer arrays. In the present study, this adaptive method was combined for the first time, with SAU transmission and experimental microbubble data. Although the method's performance did not reach the level achieved by simulated or fixed-linear target experimental results, there was a significant lateral resolution improvement both in terms of lateral localization, and separation of two closely spaced scatterers, compared to conventional beamforming. Further improvements may depend on the quality of the collected data which is not directly linked to the beamforming performance.

For instance, a lower MB concentration would potentially allow the use of the MV methods in small ROIs that only include one scatterer. This way the signal coherence caused by nearby MBs could also be limited and the maximum MV benefits may converge to the results found in the linear scatter case. Indeed, at a depth around 70 mm where the MBs concentration was small (Figure 6.5), the used metrics were similar to those using the wire phantom. This did not happen for the top of the images in Figure 6.5 where the MB concentration was high.

Further, the single emission acquisition protocol used for this measurement performs best for the area below the transducer centre, while the cellulose tube containing the MBs was not perfectly aligned with the beam axis (Figure 6.5). This may be compromising the MV performance in this study. In addition, the image

background is noisier than before (Chapters 2 and 3) and it is likely that the averaging over a number of emissions will also improve the overall image quality and reduce the PSF side-lobes. This number cannot increase significantly as the MBs are moving and may decorrelate, but the use of a few emissions (≤ 5 due to acquisition time limitations) at different angles would be feasible to implement. This way a high frame rate could be maintained and the transmission protocol could cover an extended field of view.

6.5.2 Normalized sharpness method

The normalized sharpness algorithm requires further development and investigation in order to assess all sources of error and determine the method's true potential in terms of localization precision. This was not possible with the current measurements but a future experimental setup must exploit the knowledge from the data here. The present study demonstrates that the sharpness metric can be an indicator of depth position for ultrasound contrast imaging, since it follows a specific pattern in respect to receive focus position. The ultrasound transmission and the experimental setup misalignment discussed at Subsection 6.5.1 are also relevant for the sharpness method.

The accurate axial movement is critical for this technique to perform optimally and this was not achieved here. In Subsection 4.9.1 of Chapter 4 it was pointed out that the calculated sharpness for two scatterers at the same axial but at different lateral positions will take different values (Figure 4.30). The mixing of various lateral positions (from -3 mm up to $+1.5$ mm as shown in Figure 6.9) contributed to the S-curves distortions and increasing the sharpness standard deviation. Another important point that was emphasized throughout the Chapters 4 and 5 and in the beginning of the present chapter is that the sharpness value must be calculated from a small area where only a single target is present. To ensure this, scatter has to appear sparse, thus increasing the possibility of single scatter events. The low resolution of the original image did not allow the distinction of several microbubbles that are located within the resolution cell of the image. In addition, even when a single microbubble can be identified, the sidelobes from neighbouring MBs may interfere with the sharpness measurement and contribute an additional systematic error to the sharpness value.

Moreover, the initial MB centre determination, accomplished by the use of the DRF is still subject to improvement. The PSF centre needs to be approximated more accurately as the centre co-ordinates will be used to finally define the small area of interest, where the sharpness is calculated. This could be achieved by using MV beamforming instead of DRF in the intermediate algorithm stage discussed in Subsection 6.4.1. This was not implemented here simply due to processing time limitations since the improved performance of the adaptive method comes

at the expense of very high computation number (Subsection 6.3.1). This is not prohibitive for the future, as parallel MV processing may be used (Subsection 3.7). The measurement of an accurate microbubble position for the necessary algorithm calibration can also benefit from the MV processing. Otherwise this must be done in a different way, before applying the method *in vivo* where the true scatterer position will not be available. For instance, if the flow rate is kept constant and the MB concentration is absolutely controlled, then the velocity of each microbubble could be estimated and with time as a given, the MB position will be known as well.

The experimental design was compromised by the use of two different scanners with different sensitivity and settings. The acquisitions were made using a scanner with no display. The scanner used for the initial visualization did not have the same MI as the one shown in Figure 6.4. As a consequence there was no similarity in the data between the two scanners and MB concentration was different during the data acquisition. This can be resolved if adequate time is allowed between data processing and the next experiment, which means that the microbubble administration can be informed by the data. Since the offline processing takes time to optimize and the data were captured in CFU (Lyngby, Denmark) it was not possible to capture subsequent datasets with optimized concentrations and transmit protocols.

In addition, and as informed from the current study, since it is difficult to create a straight path for the microbubbles (Subsection 6.1.1), a transducer alignment with a smaller range of $15 - 20$ mm with minimal lateral displacement from the whole cellulose tube could be achieved. Alternatively, a tubeless phantom where MBs are free flowing in the liquid may enable the acquisition of enough single scatter data for the entire image with adequate sampling. This may provide an S-curve cover for all depths. All these changes may significantly improve the normalized sharpness method performance.

Chapter 7

Conclusion and Future Work

The research work in this thesis focused on ultrasound point source localization with a view to provide a new method for ultrasound contrast imaging. This chapter presents a summary of the conclusions drawn from Chapters 2 to 6, and makes suggestions for future directions of this work.

7.1 Conclusion

The conclusions of the two different methods are outlined separately and are followed by a review of the current microbubble lateral and axial localization.

7.1.1 Lateral localization accuracy

In Chapter 2, the time and the frequency domain approaches of the Minimum Variance beamformer were compared with simulated ultrasound data. The temporal implementation is a direct translation of a method initially designed for earthquake localization while the frequency domain implementation introduces processing (signal division in frequency sub-bands) that exploits the broadband nature of ultrasound signals. The adaptive methods provide, at the expense of computational time, a set of optimized apodization weights which, in theory, attains lateral localization and contrast resolution beyond the conventional limits.

In simulation, the point scatterer data processing showed that the two different MV implementations may achieve up to 20-fold resolution metrics improvement compared to what conventional beamforming techniques provide. The above conclusion concerns the identification of a single target and the level of improvement depends on the target's distance from the transducer face. The adaptive beamforming showed also some rather insignificant benefits in the cyst structure (shape preservation and 10 dB contrast resolution improvement). Overall, the sub-band approach appeared slightly superior but the number of calculations required for the weight extraction is up to 30 times lower for the temporal implementation. Finally, it was possible

to form high quality MV images produced by single emissions which may partially compensate for the computational burden the adaptive methods introduce.

In Chapter 3, the same two adaptive methods were applied to experimental ultrasound data that were acquired using a research scanner. The calculation of the MV apodization weights is however, data-dependent and therefore identical performance between simulation and measurement was not expected. There were several uncontrolled parameters, such as the speed of sound variations or signal interference that affected the adaptive beamforming performance during experiments. Indeed, the application of the same beamforming scripts to the experimental point scatter data provided limited resolution benefits compared to the simulation results (Figures 3.10 and 3.12). This leads to the conclusion that adaptive weighting is useful only in an aberration-free environment. A parametric study was performed focusing on the effect of the aperture size and investigated the accuracy of the sample covariance matrix. Both are involved in the MV weight calculation. By changing these it was possible to identify optimal parameters and achieve resolution metrics values for point scatter lateral localization from single emissions similar to those in the simulations.

The changes included larger apertures, two-way sub-array averaging and beamforming small parts of an image instead of large areas. To the author's knowledge lateral FWHM values lower than $\lambda/10$, that were obtained here, have never been obtained in the ultrasound imaging literature before. On the other hand, the simulation contrast resolution gains were not confirmed experimentally. It is important to note that experimental conditions are difficult to simulate. These include the point scatterer centre displacement, the presence of redundant signal contributions or the reflections created at the interfaces of different media. Between the two adaptive approaches, the temporal and sub-band implementations showed similar performance, while the already shown calculation benefits in favor of the temporal approach remain.

7.1.2 Axial localization accuracy

The aim of Chapter 4 was to provide increased accuracy in the axial localization of point sources. A Field II simulation helped to develop and test a newly introduced array processing method for the accurate axial localization of ultrasound point sources. The axial resolution of an ultrasound scanner mainly depends on the pulse duration and the specifications of the ultrasound scanner. Therefore increasing the axial resolution is not directly connected to beamforming. The technique utilizes simple conventional beamforming and the measure of sharpness, as calculated from the raw ultrasound signals. The investigated method originated from biological microscopy where it was used for providing depth resolution of moving particles. In microscopy, the method made use of multi-plane imaging and of the image sharpness

metric to achieve depth resolution down to a few nanometers, equivalent to $\lambda/50$ of the wavelength used in this field.

The algorithm showed to be appropriate for ultrasound imaging and relatively easy to implement since it doesn't rely on time consuming beamforming strategies as the MV methods or on external hardware components as in the optics. The multi-plane imaging was substituted by conventionally beamforming the ultrasound RF data with several fixed foci in receive mode. The sharpness metric was calculated using the RF signal amplitudes around a simulated point scatterer. The metric followed a Lorentzian-shaped curve with higher values as approaching to the receive focus position, and lower moving away from it. Further, multiple shaprness curves could be formed, one for each used receive focus. As a consequence a single depth position can be fully characterized by multiple sharpness values that stem from the respective foci. This resulted into a depth prediction of a few microns accuracy or equivalent to $(\lambda/2)/100$. The method showed also to be robust, presenting small performance variations for scatterers at greater depths, at low SNR simulated envinoments, at different data sampling rates and when using different ultrasound transmission protocols.

The simulation study of the Chapter 4 was followed by the experimental validation of the sharpness algorithm in Chapter 5. Similar to Chapters 2 and 3, an experimental setup was created in such way as to match the initial presentation of this method. A wire target was mounted on a translation stage and was moved depth-wise in preset increments. The acquisition of multiple frames per scatterer depth position allowed the calculation and the study of the sharpness variance under real-time conditions. The study showed that the experimentally calculated sharpness is analogous to that simulated when white Gaussian noise in a range between 10 and 20 dB is added to the RF signals. The use of a high precision positioner ensured that the depth prediction (i.e. the algorithm's output) could be compared with the actual position of the wire target.

Indeed the difference between true and estimated depth position reached similar values with the ones found in the simulation discussed above. Specifically it was possible to obtain depth estimates with approximately one micron's uncertainty for more than 10 mm of a scatterer's total displacement from an initial central position. Due to its nature the sharpness algorithm is only suitable for isolated point sources and cannot be implemented for any other kind of images or structures as the MV methods can.

7.1.3 Microbubble localization

In Chapter 6 both the two MV methods and the normalized sharpness algorithm were used to beamform experimental microbubble data for the first time. Single MBs can nowadays be distinguished in the ultrasound image and the contrast

agents are considered as efficient point scatterers. As a consequence the techniques discussed in this work are suited for microbubble localization that may eventually result in super-resolution contrast enhanced ultrasound. The MB data acquisition incorporated uncontrolled scatterer movement, at least compared to the simulation or experimental studies of the Chapters 2 to 5. Therefore equivalent performance to that noticed previously was not expected. The MBs are also likely to appear in high concentrations at certain locations rendering their separation difficult. Despite a number of experimental limitations the first preliminary results showed that each of the two methods has the potential to improve the accuracy of the lateral and the axial localization respectively beyond the conventional limits.

The adaptive apodization weights resulted into MB tube images that are laterally better resolved than the ones provided by conventional apodization. The used metrics improvement varied between 1.5 and 6-fold based on the known metrics used previously. At depths where single MBs were clearly distinguishable the measured FWHM was similar to that in the wire phantom and it was also possible to resolve pairs of MBs that were shown as a large one in the DAS images.

The normalized sharpness algorithm was applied to the same data and approximately 150 frames were used in order to provide sharpness curves including well-separated MBs. The sharpness curves were not as smooth as in the linear scatter work and it was not possible to evaluate the method's accuracy as before. This was due to:

- The acquisition setup that involved the use of two different scanners.
- The microbubble movement that was not only in the axial dimension.
- The absence of the scatterers actual position.
- The high microbubble concentration.

However, this preliminary investigation confirmed that Lorentzian-like shaped S-curves can be formed from MB data and that improved localization by a factor of 5 may be possible to achieve. The sharpness method is promising and requires additional work to develop into a microbubble method. The MV methods and the sharpness algorithm were tested on single emission RF data and depend on the ultrasound signals which are both very important advantages for the formation of a fast and accurate imaging scheme.

7.2 Future work

This section proposes suggestions for future research on the Minimum Variance beamforming and the normalized sharpness algorithm both separately, and in a framework for combined use.

7.2.1 Minimum Variance beamforming

The two separate Minimum Variance beamformer implementations that were analyzed and evaluated in this thesis provided, despite the computational cost, significant lateral resolution benefits. Similar improvement was occasionally recorded during the first microbubble measurements. However, this performance was not uniform throughout entire images in the latter case. Keeping in mind a future implementation of the method *in vivo*, further research is required in order to examine whether it is possible to reduce the dependance of the MV performance on the data type and hence maintain a constant MV high quality for all datasets.

This may be accomplished by investigating and applying additional algorithm modifications based in the current MV literature outwith the ultrasound field. Generally, the most common reason for the MV varying performance is a possible signal cancellation, where the signal of interest is mistakenly considered as interference and is therefore rejected. This is usually due to steering vector errors, wavefront distortions or intervening media between source and target [199, 200]. Even a small direction error may result into significant degradation. In fields such as passive sonar arrays, the use of specific array steering vectors or the calculation of their errors resulted in MV implementations of increased robustness [201–203]. This has also been achieved by adding multiple constraints [204] or by incorporating penalty weights due to the covariance matrix limited knowledge [205–207], that reformulate the optimization problem as this was originally introduced in Equation (2.4). Such studies could be replicated taking into account the nature of ultrasound imaging.

The work here showed that MV future implementations must be designed alongside the transducer that will be used for the measurements/scans incorporating its specific characteristics such as its bandwidth, its aperture and pitch size. All the above parameters were found to affect the efficiency of adaptive beamforming. Interestingly the computational time can be significantly reduced when beamforming small areas separately. Thus, parallel processing should be feasible, since multiple beamformers can be deployed simultaneously in different areas. The responses could then be summed providing whole images many times faster than the presented approaches allow.

There are in the ultrasound literature many different MV approaches tested for various applications, each one using different metrics and presenting different results. A general research platform generating ultrasound data that can be widely used by all researchers would be very useful allowing comparisons between the adaptive methods. The growing research in the adaptive beamforming field is currently motivated by the high processing times of the standard implementation. As a consequence the research is dominated by proposals for reduced-complexity implementations.

However, MV investigations may best focus in obtaining a robust high perfor-

mance beamformer regardless of the computational burden. The suggestion of faster implementations is of secondary importance and should follow the confirmation of the usufulness of the method. Accordingly, the findings here lead to the conclusion that the MV beamforming should be liaised (or combined) with contrast microbubbles and rapid (single or few emissions to provide an image), super-resolution imaging. Structural imaging or averaging over a large number of emissions did not seem to benefit from the adaptive apodization weighting and should only be considered as side MV objectives.

7.2.2 Normalized sharpness method

The normalized sharpness method, as developed above, has the potential to provide precise axial localization. Several improvements may help to create MB calibrated sharpness data of similar quality to those of the linear scatterer work. Those improvements summarized in Subsection 6.5.2 in the first instance, are mainly related to the microbubble concentration and the limitation of the microbubble movement only in the axial direction. Therefore the improvements do not refer to further development of the method but rather tailoring the experimental protocol to it. In addition, the possibility of parallel frame processing with the MV beamformers was discussed. The combined use of the two algorithms, would significantly assist the normalized sharpness method in the initial determination of the microbubbles centre coordinates. Further, in such a situation, precise localization in both (lateral and axial) directions based solely on the transducer element signals could be achieved.

Once the calibration of the MB S-curves has been finalized, a measured sharpness could be directly assigned to a depth with a specific uncertainty, based on those reference S-curves. The procedure would be valid for any microbubble included in an image. As an example, an improvement over the above measurement/method would be the use of an experimental setup in which microbubbles are inserted into a water tank completely free, without tubing. A straight vertical image line below the transducer centre could then be assumed. From this setup, all microbubbles that cross that line may be used in order to extract the sharpness data and translate them into axial position. It is important to note that those sharpness data will result from movement in the axial direction only. The process could be extended for more lines in various lateral distances given that the reference S-curve data remain unchanged or have been scaled accordingly (Subsection 4.9.1). The above setup would require the acquisition of a large number of frames but this method would allow a map of depths to be created for a whole image.

With a different implementation the normalized sharpness method could be applied in the lateral dimension. This is worth investigating in order to create a method for point source localization over the entire image and entirely based on sharpness. From the original definition of the algorithm in optics and the first ul-

trasound data received by standard one dimension probes, the metric of sharpness follows a particular shape only in respect to depth changes. The first step towards future development would be an initial Field II simulation as in Chapter 4 with the scatterer moving in the lateral direction. The changes in the x-axis are likely to have smaller effects on the measured sharpness but plotting the sharpness over lateral distance might reveal a trend between the two. At a later stage, the Field II simulation could be repeated with irregular scatterer movement from one scan to the next, involving simultaneous change in both axial and lateral directions. In that situation, the sharpness could be plotted over axial and lateral distance at the same time in $3D$ plots. With all the necessary alterations in the PDF model it will be possible to provide a scatterer position estimate. The uncertainty of the estimate could also be extracted in a similar manner as was shown in this work.

Furher, the acquisition of raw $3D$ ultrasound data is possible through the use of $2D$ ultrasound transducers. The use of such probes could potentially allow the expansion of the technique to capturing $3D$ volumes since the 3rd (additional) dimension is also a lateral one. This could also be possible to simulate. All studies should follow the same protocol used here, and every simulation should be verified experimentally before application to non-linear scatterers. The long-term objective is to create an imaging technique for fast (preferably single emission), super-resolution vascular imaging [208–210] with the use of microbubbles, that is based on fundamental beamforming and RF signals. Possible future limitations are related again to MB concentration, the unknown sharpness behavior in the lateral dimensions that needs to be studied first, and the limited at present use of $2D$ arrays. Despite the limitations, the normalized sharpness method appears to be less vulnerable than the MV beamformers in real-imaging conditions.

Should the use of $2D$ arrays become more common for ultrasound data acquisition, more optical super-resolution techniques may be considered for translation into ultrasound thus presenting alternatives for overcoming the diffraction limit or accurately correct aberration. Such techniques could include aperture synthesis where pairs of active transducer elements from different heights, emit spherical waves and are operated as interferometers [27, 48, 82, 211, 212]. The $2D$ arrays consisting of multiple rows of elements could render possible the formation of such transmitting apertures. Another alternative could be Multi-Conjugate Adaptive Optics (MCAO) that compensates for distortions in astronomy, by creating $3D$ profiles of atmospheric turbulence with the use of multiple guide stars [213, 214]. The technique already exists in ultrasound imaging for wavefront correction [83, 84, 89] as stated in the Introduction, but is limited to one dimension at the moment.

Appendix A

Ultrasound Transmission Protocols

Ultrasound imaging can be carried out using different transmit protocols. There are 3 main ways of transmission that were mentioned and studied in this work. These are illustrated in Figure A.1 and a short description of each one follows below.

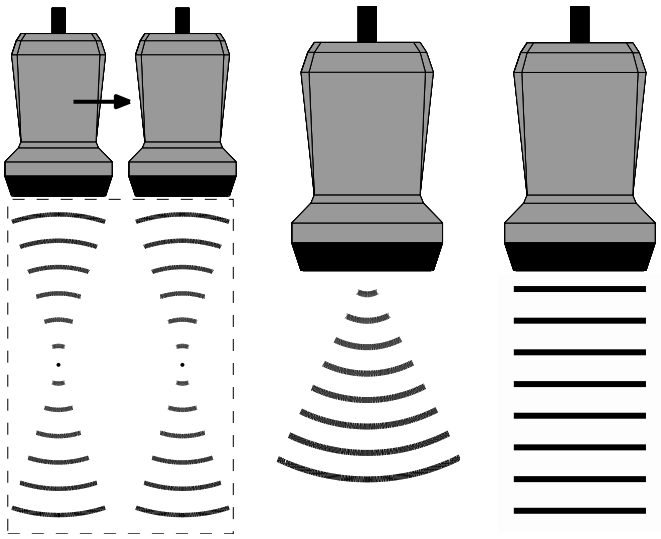

(a) Linear sweep (b) SAU imaging (c) PW imaging

Figure A.1: Illustration of the basic ways of ultrasound transmission: (a) Linear sweep, (b) Synthetic Aperture Ultrasound (SAU) imaging and (c) Plane Wave (PW) imaging.

A.1 Linear sweep

Transmission of ultrasound is performed through focused beams. A small part of the transducer (active aperture) transmits a narrow beam with a transmitting focus point. The active aperture is then moved across the array for the next transmission. From each transmission one line is formed by beamforming the received sensor

signals, and combining lines from multiple transmissions will then lead to image formation.

A.2 Synthetic aperture ultrasound

Synthetic aperture was originally developed for radar imaging, where imaging of the same target from different antenna positions results in high-quality images of the target [215–217]. In most radar systems only a single antenna is available, and Synthetic Aperture Radar (SAR) takes advantage of the radar antenna motion over a well-defined region to generate a larger synthetic aperture. The latter inherently results in higher spatial resolution. In practice, an aircraft is usually employed as a moving platform where the SAR is mounted on, data are recorded in each antenna position, and then signal processing of all the received radar echoes allows the formation of the high resolution images.

In ultrasound imaging, there is simultaneous access to all transducer elements, which may usually be used without any limitations. Therefore, a single or a small number of elements are used to emit an unfocused spherical wave that will cover the whole image region. Multiple emissions from adjacent elements (or group of elements) will produce multiple low-quality images that combined all together can result to a high-quality one with significantly improved sidelibe suppression. The principle of SAU was introduced in ultrasound by *Nikolov and Jensen*. An illustration of the SAU imaging is given in the Figure A.2.

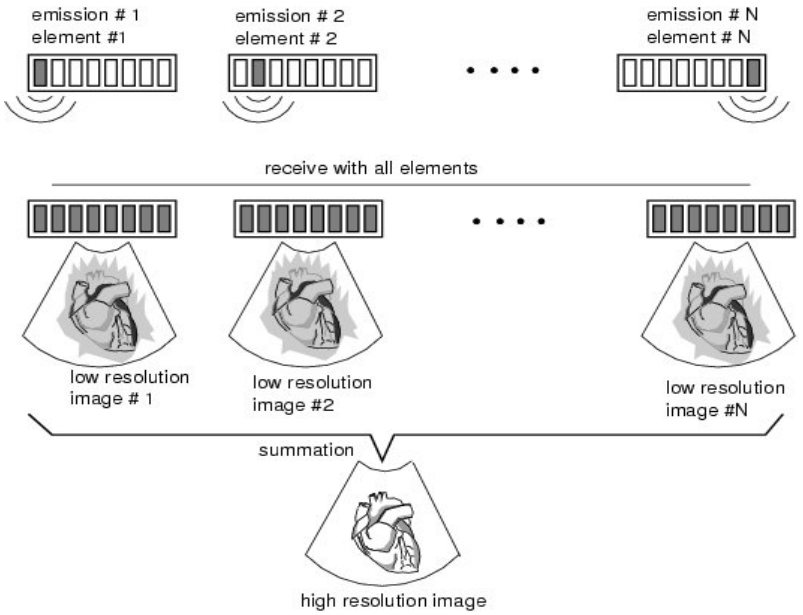

Figure A.2: The principle of synthetic aperture ultrasound imaging, adapted from [144]. A number of images are created from a single emission. These single emission images are combined to produce an image with a higher resolution and contrast.

The process is equivalent to using multiple antennas both in transmit and receive as in MIMO technology for wireless communications [146, 147]. Similar to SAR, in standard wireless communications, one antenna is traditionally used at the source (transmitter), and another one is used at the destination (receiver). In MIMO systems, multiple antennas at both communication circuit ends are combined to reduce ambiguities and allow the use of multiple signal paths to carry the acquired data.

A.3 Plane wave

Plane wave emission is being performed by utilizing all elements as both transmitting and receiving aperture. The transducer elements are transmitting unfocused waves and as a consequence, the entire image region can be covered in a single emission. Recent trends in ultrasound imaging involve the transmission of plane waves in multiple angles as shown in Figure A.3 that can be later summed to provide one image of higher resolution (spatial compounding).

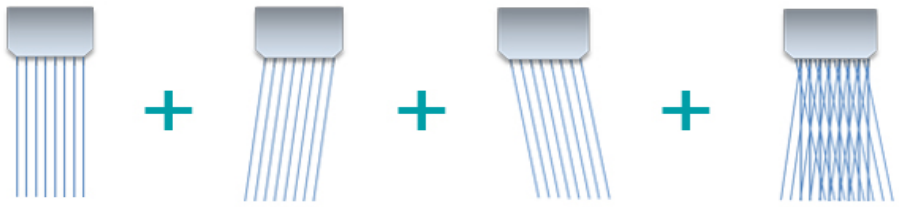

Figure A.3: An *EDAN Instruments, INC.* example of spatial compounding that combines several component images to provide an image of increased quality. The figure has been adapted from [218]. Three plane waves at 3 different angles are used and the received responses are summed to display a final image with reduced speckle noise and enhanced image contrast.

Appendix B

Conventional Apodization Weights

In ultrasound imaging, the presence of sidelobes (lobes at the edges of the main beam) is one of the main reasons causing image artefacts. The use of apodization weights aims to reduce the amplitude of these sidelobes and minimize their effect on the obtained images. Apodization is used mainly in receive processing but can also be employed during transmission. Four of the most common weighting functions that are used in ultrasonics are being described below.

B.1 Boxcar apodization

The Boxcar apodization is simply the rectangular function as shown in Figure B.1. For a transducer with $n = 192$ elements, the Boxcar weights, w_{boxcar} are given by:

$$w_{boxcar}(n) = 1 \,, \tag{B.1}$$

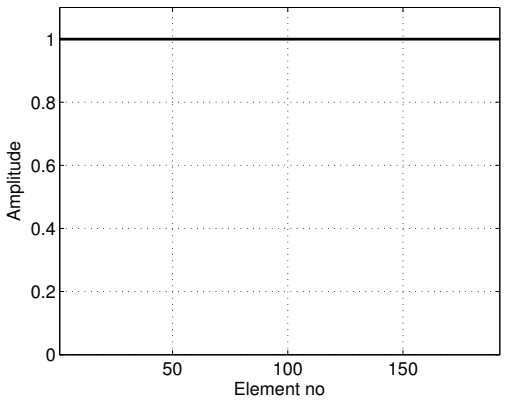

Figure B.1: Illustration of Boxcar apodization for a transducer with 192 active elements.

B.2 Hanning apodization

The Hanning apodization is one of the most commonly used window functions. It is shown in Figure B.2. It is a modified cosine function, and the Hanning weights, $w_{hanning}$, for a transducer with $n = 192$ elements are given by:

$$w_{hanning}(n) = 0.5 \times \cos(n\pi) + 0.5\,, \tag{B.2}$$

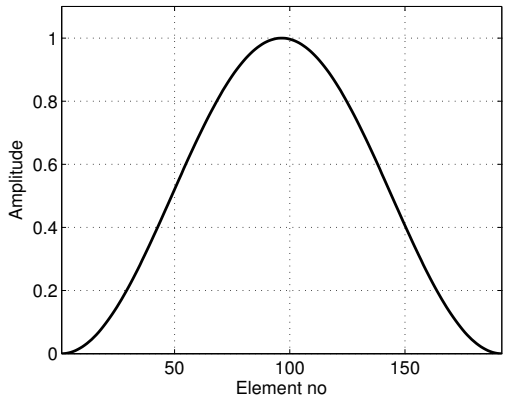

Figure B.2: Illustration of Hanning apodization for a transducer with 192 active elements.

B.3 Hamming apodization

As the Hanning apodization, the Hamming is another frequently used, cosine function. It is similar to Hanning as shown in Figure B.3 but with a slightly narrower main lobe. The Hamming weights, $w_{hanning}$, for a transducer with $n = 192$ elements are given by:

$$w_{hamming}(n) = 0.46 \times \cos(n\pi) + 0.54\,, \tag{B.3}$$

B.4 Tukey apodization

The Tukey window is again a tapered cosine which depends on the selection of a variable, r that can take values between 0 and 1. When $r = 0$, the Tukey window is equal to the rectangular, and when $r = 1$ it becomes equal to the Hanning window. The Tukey weights, w_{tukey}, for a transducer with $n = 192$ elements are given by:

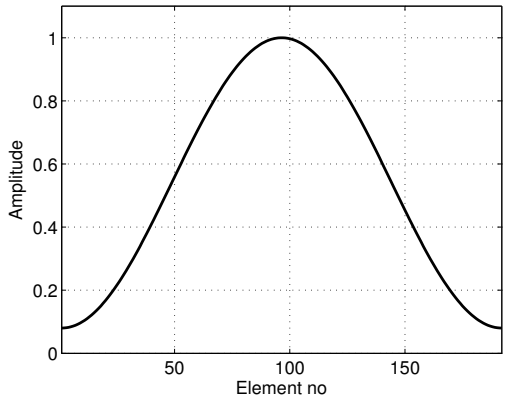

Figure B.3: Illustration of Hamming apodization for a transducer with 192 active elements.

$$w_{tukey}(n) = \begin{cases} 0.5 \times \{1 + \cos(\frac{2\pi}{r}[n - \frac{r}{2}])\}, & for \quad 0 \leq n < \frac{r}{2} \\ 1, & for \quad \frac{r}{2} \leq n < 1 - \frac{r}{2} \\ 0.5 \times \{1 + \cos(\frac{2\pi}{r}[n - 1 + \frac{r}{2}])\}, & for \quad 1 - \frac{r}{2} \leq n < 1 \end{cases} \tag{B.4}$$

Usually a value $r = 0.5$ is chosen which results into the curve of the Figure B.4.

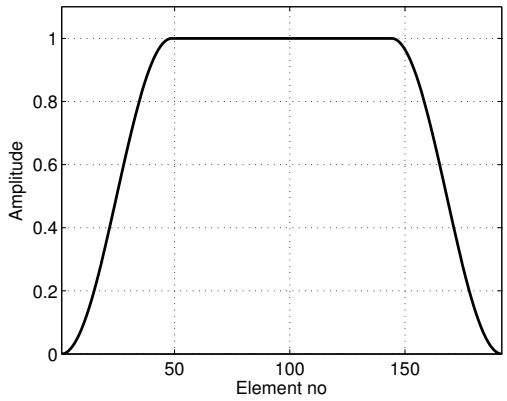

Figure B.4: Illustration of Tukey apodization with $r = 0.5$ for a transducer with 192 active elements.

Bibliography

[1] P. Hoskins, K. Martin, and A. Thrush. *Diagnostic Ultrasound: Physics and Equipment*. Cambridge University Press, 2nd edition, 2010.

[2] K. Attenborough and M. Postema. A pocket-sized introduction to acoustics. Technical report, University of Hull, January 2008.

[3] C. R. Hill, J. C. Bamber, and G. R. ter Haar. *Physical principles of medical ultrasonics, second edition*. John Wiley & Sons, Ltd, New York, USA, 2004.

[4] W. N. McDicken. *Diagnostic ultrasonics: Principles of use of instruments* . John Wiley and Sons, Inc. New York, 1976.

[5] M. L. Oelze and W. D. O'Brien Jr. Defining optimal axial and lateral resolution for estimating scatterer properties from volumes using ultrasound backscatter. *J. Acoust. Soc. Am.*, 115(6):3226–3234, 2004.

[6] J. A. Jensen. Deconvolution of ultrasound images. *Ultrasonic Imaging* , 14(1):1–15, 1992.

[7] N. J. Dudley, N. M. Gibson, M. J. Fleckney, and P. D. Clark. The effect of speed of sound in ultrasound test objects on lateral resolution. *Ultr. Med. Biol.*, 28(11-12):1561–1564, 2002.

[8] T. Szabo. *Diagnostic Ultrasound Imaging: Inside Out*. New York:Elsevier, 2004.

[9] D. A. Knapik, B. Starkoski, C. J. Pavlin, and F. S. Foster. A 100-200 MHz ultrasound biomicroscope. *IEEE Trans. Ultrason., Ferroelec., Freq. Contr.*, 47(6):1540–1549, November 2000.

[10] F. S. Foster, C. J. Pavlin, K. A. Harasiewicz, D. A. Christopher, and D. H. Turnbull. Advances in ultrasound biomicroscopy. *Ultr. Med. Biol.*, 26(1):1–27, January 2000.

[11] L. Pantoni. Cerebral small vessel disease: From pathogenesis and clinical characteristics to therapeutic challenges. *Lancet Neurol.*, 9(7):689–701, 2010.

[12] P. Carmeliet and R. K. Jain. Angiogenesis in cancer and other diseases. *Nature*, 407(6801):249–257, 2000.

[13] W. T. Cade. Diabetes-related microvascular and macrovascular diseases in the physical therapy setting. *Phys. Ther.*, 88(11):1322–1335, 2008.

[14] K. Wei. Contrast echocardiography: Applications and limitations. *Cardiol. Rev.*, 20(1):25–32, 2012.

[15] M. A. Pysz, K. Foygel, C. M. Panje, A. Needles, L. Tian, and J. K. Willmann. Assessment and monitoring tumor vascularity with contrast-enhanced ultrasound maximum intensity persistence imaging. *Invest. Radiol.*, 46(3):187–195, March 2011.

[16] M. Dunitz. *Ultrasound contrast agents*. B. B. Goldberg, Ed., London, 1997.

[17] E. Quaia. *Contrast media in ultrasonography: basic principles and clinical applications*. Springer, Berlin, 2005.

[18] L. Solbiati, A. Martegani, E. Leen, J.M. Correas, P.N. Burns, and D. Becker. *Contrast-enhanced ultrasound of liver diseases*. Springer, 2003.

[19] N. de Jong, F. J. ten Cate, C. T. Lancee, J. R. T. C. Roelandt, and N. Bom. Principles and recent developments in ultrasound contrast agents. *Ultrasonics*, 29(4):324–330, 1991.

[20] N. de Jong, P. J. A. Frinking, A. Bouakaz, M. Goorden, T. Schourmans, X. Jingping, and F. Mastik. Optical imaging of contrast agent microbubbles in an ultrasound field with a 100-mhz camera. *Ultr. Med. Biol.*, 26(3):487–492, 2000.

[21] M. C. Ziskin, A. Bonakdarpour, D. P. Weinstein, and P. R. Lynch. Contrast agents for diagnostic ultrasound. *Invest. Radiol.*, 7(6):500–505, 1972.

[22] E. Stride and N. Saffari. Microbubble ultrasound contrast agents: a review. *Proc. Inst. Mech. Eng. H.*, 217(6):429–447, 2003.

[23] A. Greco, M. Mancini, S. Gargiulo, M. Gramanzini, P. P. Claudio, A. Brunetti, and M. Salvatore. Ultrasound biomicroscopy in small animal research: applications in molecular and preclinical imaging. *Journal of Biomedicine and Biotechnology*, 2012:519238, 14 pages, 2012.

[24] T. G. Leighton. *The acoustic bubble*. Academic Press, London, 1997.

[25] Y. Yan, J. R. Hopgood, and V. Sboros. A novel estimation system for multiple pulse echo signals from ultrasound contrast microbubbles. In *Proc. IEEE Int. Conf. Acous., Speech, Sig. Pro.*, pages 601–604, 2008.

[26] Y. Yan, J. R. Hopgood, R. Steel, and V. Sboros. Statistical spectral analysis for echo signals from microbubbles and solid spheres. In *Proc. IEEE Ultrason. Symp.*, pages 1382–1385, 2008.

[27] Y. Yan, J. R. Hopgood, and V. Sboros. Bayesian spectral estimation applied to echo signals from nonlinear ultrasound scatterers. *EURASIP Journal on Advances in Sig. Proc.*, 2011:146175, November 2010.

[28] Konstantinos Diamantis. Super-resolution techniques for the analysis of ultrasound signals. Master's thesis, School of Medicine,University of Patras and Department of Medical Physics, University of Edinburgh, October 2011.

[29] K. Diamantis, M. A. Dhali, G. Gibson, Y. Yan, J. R. Hopgood, and V. Sboros. Super-resolution spectral analysis for ultrasound scatter characterization. In *Proc. IEEE Int. Conf. Acous., Speech, Sig. Pro.*, pages 903–907, 2016.

[30] M. B. Butler, D. H. Thomas, C. M. Moran, W. N. McDicken, V. Sboros, and S. D. Pye. Comparison of the acoustic response of attached and unattached BiSphere^{TM} microbubbles. In *Proc. IEEE Ultrason. Symp.*, pages 1683–1685, 2008.

[31] M. B. Butler, A. Dermitzakis, D. H. Thomas, S. D. Pye, and V. Sboros. Survival of single microbubbles insonated in solution and in narrow tubes. In *Proc. IEEE Ultrason. Symp.*, pages 1259–1261, 2009.

[32] D. H. Thomas, M. B. Butler, T. Anderson, R. Steel, S. D. Pye, M. Poland, T. Brock-Fisher, W. N. McDicken, and V. Sboros. Single microbubble response using pulse sequences: initial results. *Ultr. Med. Biol.*, 35(1):112–119, 2009.

[33] D. H. Simpson, C. T. Chin, and P. N. Burns. Pulse inversion Doppler: a new method for detecting nonlinear echoes from microbubble contrast agents. *IEEE Trans. Ultrason., Ferroelec., Freq. Contr.*, 46(2):372–382, March 1999.

[34] R. J. Eckersley, C. T. Chin, and P. N. Burns. Optimising phase and amplitude modulation schemes for imaging microbubble contrast agents at low acoustic power. *Ultr. Med. Biol.*, 31(2):213–219, February 2005.

[35] P. J. Phillips. Contrast pulse sequences (CPS): imaging nonlinear microbubbles. In *Proc. IEEE Ultrason. Symp.*, volume 2, pages 1739–1745, October 2001.

[36] M. Averkiou, M. Bruce, S. Jensen, P. Rafter, T. Brock-Fisher, and J. Powers. Pulsing schemes for the detection of nonlinear echoes from contrast microbubbles. In *9th European Symposium on Ultrasound Contrast Imaging*, pages 1–8, January 2004.

[37] S. R. Wilson and P. N. Burns. Microbubble-enhanced US in body imaging: what role? *Radiology*, 257(1):24–39, October 2010.

[38] L. Hoff. *Acoustic characterization of contrast agents for medical ultrasound imaging*. Kluwer Academic Publishers, 2001.

[39] Lars Hoff. *Ultrasound Contrast Bubble Simulation - Bubblesim*. Norwegian University of Science and Technology, December 2004.

[40] L. Hoff, P. Sontum, and J. M. Hovem. Oscillations of polymeric microbubbles: Effect of the encapsulating shell. *J. Acoust. Soc. Am.*, 107(4):2272–2280, 2000.

[41] V. Sboros, C. M. Moran, S. D. Pye, and W. N. McDicken. The behaviour of individual contrast agent microbubbles. *Ultr. Med. Biol.*, 29(5):687–694, 2003.

[42] V. Sboros, S. D. Pye, C. A. MacDonald, J. Gomatam, C. M. Moran, and W. N. McDicken. Absolute measurement of ultrasonic backscatter from single microbubbles. *Ultr. Med. Biol.*, 31(8):1063–1072, 2005.

[43] R. J. Eckersley, M. X. Tang, K. Chetty, and J. V. Hajnal. Microbubble contrast agent detection using binary coded pulses. *Ultr. Med. Biol.*, 33(11):1787–1795, 2007.

[44] S. Haykin, J. H. Justice, N. L. Owsley, J. L. Yen, and A. C. Kak. *Array Signal Processing*. Englewood Cliffs, NJ: Prentice Hall, 1985.

[45] D. G. Manolakis, V. K. Ingle, and S. M. Kogon. *Statistical and adaptive signal processing: spectral estimation, signal modeling, adaptive filtering and array processing*. McGrawHill Companies, Inc., 2000.

[46] I. J. Clarke, G. D. de Villiers, and J. L. Mather. Resolution limits of a two dimensional antenna array. In *Proc. SPIE Real-Time Signal Processing VIII, 15*, volume 0564, [Online] Available:10.1117/12.949698, January 1986.

[47] I. J. Clarke and G. Spence. A space-time estimator for the detection and estimation of multiple sinusoidal signals. In *High Res. Radar and Sonar (Ref. No. 1999/051), IEE Colloquium*, pages 9/1–9/6, 1999.

[48] A. H. Greenaway. Terrestrial optical aperture synthesis technique (TOAST). *Opt. Commun.*, 58(3):148–154, 1986.

[49] D. M. Pennington. Laser guided adaptive optics for high-resolution astronomy. In *Lasers and Electro-Optics. CLEO '02*, volume 1, pages 68–69, May 2002.

[50] E.N. Ribak and E. Gershnik. Stellar scintillation as a remote atmospheric wave-front sensor. *Opt. Lett.*, 21(6):435–437, March 1996.

[51] S. Djidel, J. K. Gansel, H. I. Campbell, and A. H. Greenaway. High-speed, 3-dimensional, telecentric imaging. *Opt. Expr.*, 14(18):8269–8277, 2006.

[52] G. Bienvenu and L. Kopp. Adaptivity to background noise spatial coherence for high resolution passive methods. In *Proc. IEEE Int. Conf. Acous., Speech, Sig. Pro.*, volume 5, pages 307–310, 1980.

[53] R. O. Schmidt. *A signal subspace approach to multiple emitter location and spectral estimation*. PhD thesis, Stanford University, 1981.

[54] A. Paulraj, R. Roy, and T. Kailath. A subspace rotation approach to signal parameter estimation. *Proc. IEEE*, 74(7):1044–1045, 1986.

[55] R. Roy and T. Kailath. ESPRIT-Estimation of signal parameters via rotational invariance techniques. *IEEE Trans. Acous., Speech, Sig. Pro.*, 37(7):984–995, 1989.

[56] A. Quinquis, E. Radoi, and F. C. Totir. Some radar imagery results using superresolution techniques. *IEEE Trans. Antennas. & Propagation*, 52(5):1–15, May 2004.

[57] K. G. Puschmann and F. Kneer. On super-resolution in astronomical imaging. *Astronomy & Astrophysics*, 436(1):373–378, 2005.

[58] X. Qu, D. Wu, L. Mets, and N. F. Scherer. Nanometer-localized multiple single-molecule fluorescence microscopy. *Proc. Natl. Acad. Sci. U.S.A.*, 101(31):11298–11303, 2004.

[59] E. Betzig, G. H. Patterson, R. Sougrat, O. W. Lindwasser, S. Olenych, J. S. Bonifacino, M. W. Davidson, J. Lippincott-Schwartz, and H. F. Hess. Imaging intracellular fluorescent proteins at nanometer resolution. *Science*, 313(5793):1642–1645, 2006.

[60] M. Bates, B. Huang, G. T. Dempsey, and X. Zhuang. Multicolor super-resolution imaging with photo-switchable fluorescent probes. *Science*, 317(5845):1749–1753, 2007.

[61] M. J. Rust, M. Bates, and X. Zhuang. Sub-diffraction-limit imaging by stohastic optical reconstruction microscopy (STORM). *Nature Methods*, 3(10):793–796, 2006.

[62] A. L. McEvoy, D. Greenfield, M. Bates, and J. Liphardt. Q&A: Single-molecule localization microscopy for biological imaging. *BMC Biology*, 8(106):1–9, 2010.

[63] M. Born and E. Wolf. *Principles of Optics*. Pergamon Press, 4th edition, 1970.

[64] P. Trk and F. J. Kao. *Optical imaging and microscopy*. Springer-Verlag, 2003.

[65] J. W. Goodman. *Introduction to Fourier Optics*. McGraw-Hill International Editions, Electrical Engineering Series, 2nd edition, 1996.

[66] R. K. Tyson. *Principles of adaptive optics*. Academic Press, 2nd edition, 1998.

[67] T. Sato, K. Uemera, and K. Sasaki. Super-resolution acoustical passive imaging system using algebraic reconstruction. *J. Acoust. Soc. Am.*, 67(5):1802–1808, 1980.

[68] Y. Sun, J. D. McKenna, J. M. Murray, E. M. Ostap, and Y. E. Goldman. Parallax: high accuracy three-dimensional single molecule tracking using split images. *Nano Lett.*, 9(7):2676–2682, 2009.

[69] R. McGorty, J. Schnitzbauer, W. Zhang, and B. Huang. Correction of depth-dependent aberrations in 3D single-molecule localization and super-resolution microscopy. *Opt. Lett.*, 39(2):275–278, 2014.

[70] M. Speidel, A. Jons, and E. L. Florin. Three-dimensional tracking of fluorescent nanoparticles with subnanometer precision by use of off-focus imaging. *Opt. Lett.*, 28(2):69–71, 2003.

[71] G. A. Lessard, P. M. Goodwin, and J. H. Werner. Three-dimensional tracking of individual quantum dots. *Appl. Phys. Lett.*, 91(22):224106, 2007.

[72] E. Herbert, M. Pernot, G. montaldo, M. Fink, and M. Tanter. Energy-based adaptive focusing of waves: application to noninvasive aberration correction of ultrasonic wavefields. *IEEE Trans. Ultrason., Ferroelec., Freq. Contr.*, 56(11):2388–2399, November 2009.

[73] G. W. McLaughlin. Practical aberration correction methods. *Ultrasound*, 15(2):99–104, 2007.

[74] S. W. Flax and M. O'Donnell. Phase-aberration correction using signals from point reflectors and diffused scatterers: Basic Principles. *IEEE Trans. Ultrason., Ferroelec., Freq. Contr.*, 35(6):758–767, November 1988.

[75] M. Hart, N. M. Milton, C. Baranec, K. Powell, T. Stalcup, D. McCarthy, C. Kulesa, and E. Bendek. A ground-layer adaptive optics system with multiple laser guide stars. *Nature Lett.*, 466:727–729, August 2010.

[76] R. C. Flicker. Sequence of phase correction in multiconjugate adaptive optics. *Opt. Lett.*, 26(22):1743–1745, November 2001.

[77] R. J. Purdy, P. E. Blankenship, C. E. Muehe, C. M. Rader, E. Stern, and R. C. Williamson. Radar signal processing. *Lincoln laboratory Journal*, 12(2):297–320, 2000.

[78] M. I. Skolnik. *Introduction to Radar Systems*. McGraw-Hill, New York, 1980.

[79] M. O'Donnell and S. W. Flax. Phase-aberration correction using signals from point reflectors and diffused scatterers: measurement. *IEEE Trans. Ultrason., Ferroelec., Freq. Contr.*, 35(6):768–774, November 1988.

[80] Y. Li. Phase aberration correction using near-field signal redundancy-part I: principles. *IEEE Trans. Ultrason., Ferroelec., Freq. Contr.*, 44(2):372–379, March 1997.

[81] Yue Li. Correction of Phase Aberrations in Medical Ultrasound Images Using Signal Redundancy, Ultrasound Imaging - Medical Applications, 2011.

[82] A. H. Greenaway. Optical aperture synthesis, review article. *Meas. Sci. Technol.*, 2:1–12, 1991.

[83] M. Fink. Time reversal of ultrasonic fields-part I: basic principles. *IEEE Trans. Ultrason., Ferroelec., Freq. Contr.*, 39(5):555–566, September 1992.

[84] M. Fink. Time reversal waves and super-resolution. *J. Phys.: Conf. Ser.* , 124(1):012004, 2008.

[85] M. Fink. Time reversal acoustics. *J. Phys.: Conf. Ser.* , 118(1):012001, 2008.

[86] M. Fink. Time reversal acoustics. *Phys. Today*, 50(3):34–40, May 1997.

[87] O. Couture, J. F. Aubry, M. Tanter, and M. Fink. Time-reversal focusing of therapeutic ultrasound on targeted microbubbles. *Appl. Phys. Lett.*, 94:173901, 2009.

[88] J. Robert and M. Fink. Spatio-temporal invariants time reversal operator. *J. Acoust. Soc. Am.*, 127(5):2904–2912, May 2010.

[89] M. Pernot, G. Montaldo, M. Tanter, and M. Fink. Ultrasonic stars for time-reversal focusing using induced cavitation bubbles. *Appl. Phys. Lett.*, 88:034102, 2006.

[90] M. A. O'Reilly and K. Hynynen. A super-resolution ultrasound method for brain vascular mapping. *Med. Phys.*, 40(11):110701, 2013.

[91] M. A. O'Reilly, R. M. Jones, and K. Hynynen. Three-dimensional transcranial ultrasound imaging of microbubble clouds using a sparse hemispherical array. *IEEE Trans. Biom. Eng.*, 61(4):1285–1294, 2014.

[92] M. A. O'Reilly, R. M. Jones, and K. Hynynen. Investigating a method for non-invasive ultrasound aberration correction through the skull bone. In *Proc. SPIE Med. Imag.*, volume 904013, [Online] Available:10.1117/12.2043832, March 2014.

[93] O. M. Viessmann, R. J. Eckersley, K. Christensen-Jeffries, M. X. Tang, and C. Dunsby. Acoustic super-resolution with ultrasound and microbubbles. *Phys. Med. Biol.*, 58(18):6447–6458, 2013.

[94] K. Christensen-Jeffries, R. J. Browning, M. X. Tang, C. Dunsby, and R. J. Eckersley. *In vivo* acoustic super-resolution and super-resolved velocity mapping using microbubbles. *IEEE Trans. Medical Imaging*, 34(2):433–440, February 2015.

[95] O. Couture, B. Besson, G. Montaldo, M. Fink, and M. Tanter. Microbubble ultrasound super-localization imaging (MUSLI). In *Proc. IEEE Ultrason. Symp.*, pages 1285–1287, 2011.

[96] M. Tanter and M. Fink. Ultrafast imaging in biomedical ultrasound. *IEEE Trans. Ultrason., Ferroelec., Freq. Contr.*, 61(1):102–119, 2014.

[97] Y. Desailly, O. Couture, M. Fink, and M.Tanter. Sono-activated ultrasound localization microscopy. *Appl. Phys. Lett.*, 103(17):174107, 2013.

[98] Y. Desailly, J. Pierre, O. Couture, and M. Tanter. Resolution limits of ultrafast ultrasound localization microscopy. *Phys. Med. Biol.*, 60(22):8723–8740, 2015.

[99] J. F. Synnevag, A. Austeng, and S. Holm. Adaptive beamforming applied to medical ultrasound imaging. *IEEE Trans. Ultrason., Ferroelec., Freq. Contr.*, 54(8):1606–1613, August 2007.

[100] I. K. Holfort, F. Gran, and J. A. Jensen. Broadband minimum variance beamforming for ultrasound imaging. *IEEE Trans. Ultrason., Ferroelec., Freq. Contr.*, 56(2):314–325, February 2009.

[101] J. Capon. High-resolution frequency-wavenumber spectrum analysis. *Proc. IEEE*, 57(8):1408–1418, August 1969.

[102] K. Diamantis, I. H. Voxen, A. H. Greenaway, T. Anderson, J. A. Jensen, and V. Sboros. A comparison between temporal and subband minimum variance adaptive beamforming. In *Proc. SPIE Med. Imag.*, volume 90400L, [Online] Available:10.1117/12.2043602, March 2014.

[103] K. Diamantis, I. H. Voxen, A. H. Greenaway, T. Anderson, J. A. Jensen, and V. Sboros. A phantom study on temporal and subband minimum variance adaptive beamforming. In *Proc. IEEE Ultrason. Symp.*, pages 1702–1705, September 2014.

[104] P. A. Dalgarno, H. I. C. Dalgarno, A. Putoud, R. Lambert, L. Paterson, D. C. Logan, D. P. Towers, R. J. Warbuton, and A. H. Greenaway. Multiplane imaging and three dimensional nanoscale particle tracking in biological microscopy. *Opt. Expr.*, 18(2):877–884, 2010.

[105] H. I. C. Dalgarno, P. A. Dalgarno, A. C. Dada, G. J. Gibson C. E. Towers, R. M. Parton, I. Davis, R. J. Warburton, and A. H. Greenaway. Nanometric depth resolution from multi-focal images in microscopy. *J. R. Soc. Interface*, 8(60):942–951, 2011.

[106] K. Diamantis, P. A. Dalgarno, A. H. Greenaway, T. Anderson, J. A. Jensen, and V. Sboros. High resolution depth-resolved imaging from multi-focal images for medical ultrasound. In *Proc. IEEE Eng. in Med. and Biol. Soc.*, pages 7067–7070, 2015.

[107] K. Diamantis, P. A. Dalgarno, A. H. Greenaway, T. Anderson, J. A. Jensen, and V. Sboros. A novel array processing method for precise depth detection of ultrasound point scatter. In *Proc. IEEE Int. Conf. Acous., Speech, Sig. Pro.*, pages 669–673, 2016.

[108] P. Stoica and R. L. Moses. *Introduction to Spectral Analysis*. Englewood Cliffs, NJ: Prentice Hall, 1997.

[109] J. Li and P. Stoica. *Robust Adaptive Beamforming*. John Wiley & Sons, New York, USA, 2006.

[110] T. J. Shan and T. Kailath. Adaptive beamforming for coherent signals and interference. *IEEE Trans. Acous., Speech, Sig. Pro.*, 33(3):527–536, 1985.

[111] F. Viola and W. F. Walker. Adaptive signal processing in medical ultrasound beamforming. In *Proc. IEEE Ultrason. Symp.*, volume 4, pages 1980–1983, 2002.

[112] J. A. Mann and W. F. Walker. A constrained adaptive beamformer for medical ultrasound: initial results. In *Proc. IEEE Ultrason. Symp.*, volume 2, pages 1807–1810, October 2002.

[113] O. L. Frost. An algorithm for linearly constrained adaptive array processing. *Proc. IEEE*, 60(8):926–935, 1972.

[114] C. C. Nilsen and I. Hafizovic. Beamspace adaptive beamforming for ultrasound imaging. *IEEE Trans. Ultrason., Ferroelec., Freq. Contr.*, 56(10):2187–2197, 2009.

[115] Z. Wang, J. Li, and R. Wu. Time-delay- and time-reversal-based robust Capon beamformers for ultrasound imaging. *IEEE Trans. Medical Imaging*, 24(10):1308–1322, 2005.

[116] P. Stoica, Z. Wang, and J. Li. Robust Capon beamforming. *IEEE Trans. Signal Process. Lett.*, 10(6):172–175, 2003.

[117] M. Sasso and C. Cohen-Bacrie. Medical ultrasound imaging using the fully adaptive beamformer. In *Proc. IEEE Int. Conf. Acous., Speech, Sig. Pro.*, volume 2, pages 489–492, March 2005.

[118] J. F. Synnevag, A. Austeng, and S. Holm. Benefits of minimum variance beamforming in medical ultrasound imaging. *IEEE Trans. Ultrason., Ferroelec., Freq. Contr.*, 56(9):1868–1879, September 2009.

[119] S. Holm, J. F. Synnevag, and A. Austeng. Capon beamforming for active ultrasound imaging systems. In *Proc. IEEE 13th Dig. Sig. Proc. Workshop*, pages 60–65, January 2009.

[120] O. M. H. Rindal, J. P. Asen, S. Holm, and A. Austeng. Understanding contrast improvements from Capon beamforming. In *Proc. IEEE Ultrason. Symp.*, pages 1694–1697, September 2014.

[121] I. K. Holfort, F. Gran, and J. A. Jensen. Investigation of sound speed errors in adaptive beamforming. In *Proc. IEEE Ultrason. Symp.*, pages 1080–1083, November 2008.

[122] M. Wax and Y. Anu. Performance analysis of the minimum variance beamformer in the presence of steering vector errors. *IEEE Trans. Signal Process.*, 44(4):938–947, April 1996.

[123] A. Austeng, T. Bjastad, J. F. Synnevag, S. E. Msøy, H. Torp, and S. Holm. Sensitivity of minimum variance beamforming to tissue aberrations. In *Proc. IEEE Ultrason. Symp.*, pages 1072–1075, 2008.

[124] I. K. Holfort, A. Austeng, J. F. Synnevag, S. Holm, F. Gran, and J. A. Jensen. Adaptive receive and transmit apodization for synthetic aperture ultrasound imaging. In *Proc. IEEE Ultrason. Symp.*, pages 1–4, September 2009.

[125] K. Kim, S. Park, Y. T. Kim, S. C. Park, J. Kang, J. H. Kim, and M. Bae. Flexible minimum variance weights estimation using principal component analysis. In *Proc. IEEE Ultrason. Symp.*, pages 1275–1278, 2012.

[126] H. So, J. Chen, B. Yiu, and A. Yu. Medical ultrasound imaging: To GPU or not to GPU? *IEEE Micro*, 31(5):54–65, September 2011.

[127] J. Chen, B. Y. S. Yiu, H. K. So, and A. C. H. Yu. Real-time GPU-based adaptive beamformer for high quality ultrasound imaging. In *Proc. IEEE Ultrason. Symp.*, pages 1–4, 2011.

[128] J. P. Asen, J. I. Buskenes, C. I. C. Nilsen, A. Austeng, and S. Holm. Implementing Capon beamforming on a GPU for real-time cardiac ultrasound

imaging. *IEEE Trans. Ultrason., Ferroelec., Freq. Contr.*, 61(1):76–85, January 2014.

[129] J. P. Asen, J. I. Buskenes, C. I. C. Nilsen, A. Austeng, and S. Holm. Implementing Capon beamforming on the GPU for real time cardiac ultrasound imaging. In *Proc. IEEE Ultrason. Symp.*, pages 2133–2136, 2012.

[130] I. K. Holfort, F. Gran, and J. A. Jensen. High resolution ultrasound imaging using adaptive beamforming with reduced number of active elements. *Proc. Int. Cong. on Ultrasonics*, 3(1):659–665, 2009.

[131] I. K. Holfort, F. Gran, and J. A. Jensen. Minimum variance beamforming for high frame-rate ultrasound imaging. In *Proc. IEEE Ultrason. Symp.*, pages 1541–1544, October 2007.

[132] J. F. Synnevag, A. Austeng, and S. Holm. A low-complexity data-dependent beamformer. *IEEE Trans. Ultrason., Ferroelec., Freq. Contr.*, 58(2):281–289, 2011.

[133] J. A. Jensen and N. B. Svendsen. Calculation of pressure fields from arbitrarily shaped, apodized, and excited ultrasound transducers. *IEEE Trans. Ultrason., Ferroelec., Freq. Contr.*, 39:262–267, 1992.

[134] J. A. Jensen. Field: A program for simulating ultrasound systems. *Med. Biol. Eng. Comp., vol. 10th Nordic-Baltic Conference on Biomedical Imaging, Supplement 1, Part 1*, 4:351–353, 1996.

[135] K. E. Thomenius. Evolution of ultrasound beamformers. In *Proc. IEEE Ultrason. Symp.*, pages 1615–1622, 1996.

[136] J. S. Arora. *Introduction to Optimum Design.* McGraw-Hill, Inc., New York, USA, 1989.

[137] M. E. Lockwood, D. L. Jones, R. C. Bilger, C. R. Lansing, W. D. Jr O'Brien, B. C. Wheeler, and A. S. Feng. Performance of time- and frequency-domain binaural beamformers based on recorded signals from real rooms. *J. Acoust. Soc. Am.*, 115(1):379–391, 2004.

[138] F. Arabshahi, S. Monajemi, H. Sheikhzadeh, K. Raahemifar, and R. Faraji-Dana. A frequency domain MVDR beamformer for UWB microwave breast cancer imaging in dispersive mediums. In *Proc. IEEE Sig. Proc. Inf. Tech.*, pages 362–367, 2013.

[139] F. Gran and J. A. Jensen. Multi element synthetic aperture transmission using a frequency division approach. In *Proc. IEEE Ultrason. Symp.*, pages 1942–1946, 2003.

[140] F. Gran and J. A. Jensen. Frequency division transmission imaging and synthetic aperture reconstruction. *IEEE Trans. Ultrason., Ferroelec., Freq. Contr.*, 53(5):900–911, May 2006.

[141] J. Chen, H. K.-H. So, and A. C. H. Yu. Towards establishing a design rule for aperture parameters in minimum-variance beamforming. In *Proc. IEEE Ultrason. Symp.*, pages 589–592, 2013.

[142] R. F. Wagner, S. W. Smith, J. M. Sandrik, and H. Lopez. Statistics of speckle in ultrasound B-scans. *IEEE Trans. Sonics Ultrasonics*, 30(3):156–163, 1983.

[143] F. J. Harris. On the use of windows for harmonic analysis with the discrete Fourier transform. *Proc. IEEE*, 66:51–83, 1978.

[144] S. I. Nikolov and J. A. Jensen. In-vivo Synthetic Aperture Flow Imaging in Medical Ultrasound. *IEEE Trans. Ultrason., Ferroelec., Freq. Contr.*, 50(7):848–856, 2003.

[145] J. A. Jensen. Field II simulation program (a web resource). `http://field-ii.dk/`. Field II home page.

[146] J. Li and P. Stoica. *MIMO Radar Signal Processing*. Hoboken, NJ:Wiley, 2009.

[147] D. Cristallini, D. Pastina, and P. Lombardo. Exploiting MIMO SAR potentialities with efficient cross-track constellation configurations for improved range resolution. *IEEE Trans. on Geo. and Rem. Sens.*, 49(1):38–52, Jan 2011.

[148] J. P. Asen, A. Austeng, and S. Holm. Capon beamforming and moving objects - An analysis of lateral shift-invariance. *IEEE Trans. Ultrason., Ferroelec., Freq. Contr.*, 61(7):1152–1160, 2014.

[149] S. A. I. Avanji, A. M. Far, and B. M. Asl. Investigation of the effects of transducer parameters on adaptive MV beamformers in medical ultrasound applications. In *Proc. Iranian Conf. on Electrical Eng. (ICEE)*, pages 1–6, 2013.

[150] B. M. Asl and A. Mahloojifar. Contrast enhancement and robustness improvement of adaptive ultrasound imaging using forward-backward minimum variance beamforming. *IEEE Trans. Ultrason., Ferroelec., Freq. Contr.*, 58(4):858–867, 2011.

[151] S. Cho, J. Kang, J. Kang, W. Lee, and Y. Yoo. Phantom and in vivo evaluation of sound speed estimation methods: Preliminary results. In *Proc. IEEE Ultrason. Symp.*, pages 1678–1681, 2014.

[152] H. Taki, K. Taki, T. Sakamoto, M. Yamakawa, T. Shiina, M. Kudo, and T. Sato. High range resolution ultrasonographic vascular imaging using frequency domain interferometry with the Capon method. *IEEE Trans. Medical Imaging*, 31(2):417–429, February 2012.

[153] B. Tracey, D. Penninck, D. Lemmerhirt, and J. Polak. Robust adaptive beamforming for artifact suppression in gastrointestinal ultrasonography. In *Proc. IEEE Ultrason. Symp.*, pages 1690–1693, 2014.

[154] J. A. Jensen, H. Holten-Lund, R. T. Nilsson, M. Hansen, U. D. Larsen, R. P. Domsten, B. G. Tomov, M. B. Stuart, S. I. Nikolov, M. J. Pihl, Y. Du, J. H. Rasmussen, and M. F. Rasmussen. SARUS: A synthetic aperture real-time ultrasound system. *IEEE Trans. Ultrason., Ferroelec., Freq. Contr.*, 60(9):1838–1852, 2013.

[155] J. Park, S. Wi, and J. S. Lee. Computationally efficient adaptive beamformer for ultrasound imaging based on QR decomposition. *IEEE Trans. Ultrason., Ferroelec., Freq. Contr.*, 63(2):256–265, 2016.

[156] X. Liu, J. Yu, H. Zhao, X. Liu, and X. Pang. An along-track sparse imaging method for forward-looking array SAR. In *IET International Radar Conference 2015*, pages 1–5, October 2015.

[157] Y. Chen, W. Zhao, G. Li, and Q. Zhang. Parametric sparse representation method for parameter estimation in SAR imaging. In *IET International Radar Conference 2015*, pages 1–5, October 2015.

[158] G. S. K. Wong and S. Zhu. Speed of sound in seawater as a function of salinity, temperature, and pressure. *J. Acoust. Soc. Am.*, 97(3):1732–1736, 1995.

[159] M. H. Pedersen, T. X. Misaridis, and J. A. Jensen. Clinical evaluation of chirp-coded excitation in medical ultrasound. *Ultr. Med. Biol.*, 29(6):895–905, 2003.

[160] J. Mamou, J. A. Ketterling, and R. H. Silverman. Chirp-coded excitation imaging with a high-frequency ultrasound annular array. *IEEE Trans. Ultrason., Ferroelec., Freq. Contr.*, 55(2):508–513, February 2008.

[161] N. K. Chern, P. A. Neow, and M. H. Ang Jr. Practical issues in pixel-based auto focusing for machine vision. In *Proc. IEEE Robotics and Automation*, pages 2791–2796, May 2001.

[162] R. A. Muller and A. Buffington. Real-time correction of atmospherically degraded telescope images through image sharpnening. *J. Opt. Soc. Am.*, 64(9):1200–1210, September 1974.

[163] P. M. Blanchard, D. Fisher, S. C. Woods, and A. H. Greenaway. Phase-diversity wave-front sensing with a distorted diffraction grating. *Appl. Opt.*, 39(35):6649–6655, 2000.

[164] P. M. Blanchard and A. H. Greenaway. Broadband simultaneous multiplane imaging. *Opt. Commun.*, 183(1-4):29–36, 2000.

[165] P. M. Blanchard and A. H. Greenaway. Simultaneous multiplane imaging with a distorted diffraction grating. *Appl. Opt.*, 38(32):6692–6699, 1999.

[166] M. Subbarao and J-K. Tyan. Selecting the optimal focus measure for autofocusing and depth-from-focus. *IEEE Trans. on Pattern Analysis and Machine Intelligence*, 20(8):864–870, 1998.

[167] Y. Yao, B. Abidi, N. Doggaz, and M. Abidi. Evaluation of sharpness measures and search algorithms for the auto focusing of high-magnification images. In *Proc. SPIE 6246, Visual Information Processing XV*, volume 62460G, [Online] Available:10.1117/12.664751, May 2006.

[168] X. Xu, Y. Wang, J. Tang, X. Zhang, and X. Liu. Robust automatic focus algorithm for low contrast images using a new contrast measure. *Sensors 2011*, 11(9):8281–8294, 2011.

[169] J. P. Hamaker, J. D. O'Sullivan, and J. E. Noordam. Image sharpness, Fourier optics, and redundant-spacing interferometry. *J. Opt. Soc. Am.*, 67(2):1122–1123, 1977.

[170] N. F. Zhang, M. T. Postek, R. D. Larrabee, A. E. Vladar, W. J. Keery, and S. N. Jones. Image sharpness measurement in the scanning electron-microscope–part III. *Scanning*, 21(4):246–252, 1999.

[171] J. Dijk, M. van Ginkel, R. J. van Asselt, L. J. van Vliet, and P. W. Verbeek. A new sharpness measure based on Gaussian lines and edges. In *Computer Analysis of Images and Patterns (Lecture Notes in Computer Science)*, volume 2756, pages 149–156, 2003.

[172] K. De and V. Masilamani. Image sharpness measure for blurred images in frequency domain. In *Int. Conf. on Design and Manufacturing (IConDM2013)*, volume 64, pages 149–158, 2013.

[173] N. Peters. Confocal information (a web resource), W. M. Keck microscopy center, University of Washington. `http://depts.washington.edu/keck/confocalgate.htm`.

[174] S. Johnson, Y. Gao, and B. Carlson. Light Microscopy Core Facility (a web resource), Duke University and Duke University medical center. `http://microscopy.duke.edu/`.

[175] S. Abrahamsson, J. Chen, B. Hajj, S. Stallinga, A. Y. Katsov, J. Wisniewski, G. Mizuguchi, P. Soule, F. Mueller, C. D. Darzacq, X. Darzacq, C. Wu, C. I. Bargmann, D. A Agard, M. Dahan, and M. G. L. Gustafsson. Fast multicolor 3D imaging using aberration-corrected multifocus microscopy). *Nature Methods*, 10(1):60–63, 2013.

[176] J. Yang, Z. Jingjing, S. Xu, and S. Chang. High-performance subwavelength grating coupler based on high reflectivity grating reflector. *Opt. Eng.*, 53(9):096107, 2014.

[177] H.I.C. Dalgarno. Introduction to Diffraction Gratings and their Application in 3D Imaging, training document. Technical report, Heriot-Watt University, Edinburgh, 2008.

[178] R. V. Hogg and A. T. Craig. *Introduction to mathematical statistics*. New York: Macmillan, 4th edition, 1978.

[179] M. V. Jambunathan. Some properties of Beta and Gamma distributions. *Ann. Math. Statist.*, 25(2):401–405, 1954.

[180] S. L. Hahn. *Hilbert Transforms in signal processing*. Artech House Signal Processing Library, Norwell, MA, 1996.

[181] J. A. Jensen. *Users' guide for the Field II program*. Center for Fast Ultrasound Imaging, Department of Electrical Engineering, Technical University of Denmark, 3.20 edition, November 2010.

[182] E. W. Weisstein. Full width at half maximum (a Wolfram web resource), from MathWorld. `http://mathworld.wolfram.com/FullWidthatHalfMaximum.html`.

[183] M. Lewandowski, Z. Klimonda, P. Karwat, M. Seklewski, A. Nowicki, L. Bassi, and P. Tortoli. Comparison of different schemes of synthetic transmit aperture using an ultrasound advanced open platform (ULA-OP). In *Proc. IEEE Ultrason. Symp.*, pages 1988–1991, October 2010.

[184] M. O'Donnell and Y. Wang. Coded excitation for synthetic aperture ultrasound imaging. *IEEE Trans. Ultrason., Ferroelec., Freq. Contr.*, 52(2):171–176, February 2005.

[185] J. P. Marques de Sa. *Applied statistics using SPSS, STATISTICA, MATLAB and R*. Springer-Verlag Berlin Heidelberg, 2nd edition, 2007.

[186] A. Tahmasbi, S. Ram, J. Chao, A. V. Abraham, F. W. Tang, E. S. Ward, and R. J. Ober. Designing the focal plane spacing for multifocal plane microscopy. *Opt. Expr.*, 22(14):16706–16721, 2014.

[187] Onda Corporation (Sunnyvale). Acoustic Intensity Measurement System (a web resource). `http://www.ondacorp.com/products_testingsol_scanningsystem.shtml`.

[188] J. M. Hansen, M. C. Hemmsen, and J. A. Jensen. An object-oriented multithreaded software beam formation toolbox. In *Proc. SPIE Med. Imag.*, volume 79680Y, [Online] Available:10.1117/12.878178, March 2011.

[189] V. Sboros, C. M. Moran, S. D. Pye, and W. N. McDicken. An in vitro study of a microbubble contrast agent using a clinical ultrasound imaging system. *Phys. Med. Biol.*, 49(1):159–173, 2004.

[190] A. L. Klibanov, P. T. Rasche, M. S. Hughes, J. K. Wojdyla, K. P. Galen, J. H. Jr Wible, and G. H. Brandenburger. Detection of individual microbubbles of ultrasound contrast agents: imaging of free-floating and targeted bubbles. *Invest. Radiol.*, 39(3):187–195, 2004.

[191] E. N. Marieb and K. N. Hoehn. *Human anatomy and physiology.* Pearson Education, 8th edition, 2010.

[192] W. T. Shi, F. Forsberg, A. Tornes, J. Ostensen, and B. B. Goldberg. Destruction of contrast microbubbles and the association with inertial cavitation. *Ultr. Med. Biol.*, 26(6):1009–1019, 2000.

[193] V. Sboros, C. A. MacDonald, S. D. Pye, C. M. Moran, J. Gomatam, and W. N. McDicken. The dependence of ultrasound contrast agents backscatter on acoustic pressure: theory versus experiment. *Ultrasonics*, 40(1-8):579–583, 2002.

[194] V. Sboros, S. D. Pye, T. A. Anderson, C. M. Moran, and W. N. McDicken. Acoustic Rayleigh scattering at individual micron-sized bubbles. *Appl. Phys. Lett.*, 91(90):123902, 2007.

[195] F. Vignon, W. T. Shi, J. E. Powers, E. C. Everbach, J.Liu, S. Gao, F. Xie, and T. R. Porter. Microbubble cavitation imaging. *IEEE Trans. Ultrason., Ferroelec., Freq. Contr.*, 60(4):661–670, 2013.

[196] J. A. Jensen, M. F. Rasmussen, M. J. Pihl, S. Holbek, C. A. Villagomez Hoyos, D. P. Bradway, M. B. Stuart, and B. G. Tomov. Safety assessment of advanced imaging sequences I: measurements. *IEEE Trans. Ultrason., Ferroelec., Freq. Contr.*, 63(1):110–119, 2016.

[197] J. A. Jensen. Safety assessment of advanced imaging sequences II: simulations. *IEEE Trans. Ultrason., Ferroelec., Freq. Contr.*, 63(1):120–127, 2016.

[198] V. Sboros, S.D. Pye, T. Anderson, C. M. Moran, M. Averkiou, C. A. MacDonald, and J. Gomatam. The measurement of backscatter from individual contrast agent microbubbles. In *Proc. IEEE Ultrason. Symp.*, volume 2, pages 1945–1947, October 2002.

[199] J. W. Kim and C. K. Un. An adaptive array robust to beam pointing error. *IEEE Trans. Signal Process.*, 40(6):1582–1584, 1992.

[200] L. C. Godara. The effect of phase-shift errors on the performance of an antenna-array beamformer. *IEEE Journal of Oceanic Engineering*, 10(3):278–284, 1985.

[201] S. Somasundaram. Reduced dimension robust Capon beamforming for large aperture passive sonar arrays. *IET Sonar Navigation*, 5(7):707–715, 2011.

[202] S. Somasundaram. Wideband robust Capon beamforming for passive sonar. *IEEE Journal of Oceanic Engineering*, 38(2):308–322, 2013.

[203] S. Somasundaram, N. Parsons, P. Li, and R. de Lamare. Reduced-dimension robust capon beamforming using Krylov-subspace techniques. *IEEE trans. Aerospace and Electronic Systems* , 51(1):270–289, 2015.

[204] S. A. Vorobyov. Principles of minimum variance robust adaptive beamforming design. *Signal Processing*, 93(12):3264–3277, 2013.

[205] Y. I. Abramovich. Controlled method for adaptive optimization of filters using the criterion of maximum SNR. *Radio Engineering and Electronic Physics*, 26:87–95, 1981.

[206] B. D. Carlson. Covariance matrix estimation errors and diagonal loading in adaptive arrays. *IEEE Trans. on Aerospace and Electronic Systems*, 24(4):397–401, 1988.

[207] H. Cox, R. M. Zeskind, and M. H. Owen. Robust adaptive beamforming. *IEEE Trans. on Acous., Speech, and Sig. Proc.*, 35(10):1365–1376, 1987.

[208] C. Errico, B. F. Osmanski, S. Pezet, O. Couture, Z. Lenkei, and M. Tanter. Transcranial functional ultrasound imaging of the brain using microbubble-enhanced ultrasensitive Doppler. *NeuroImage*, 124(Pt A):752–761, 2015.

[209] C. Errico, J. Pierre, S. Pezet, Y. Desailly, Z. Lenkei, O. Couture, and M. Tanter. Ultrafast ultrasound localization microscopy for deep super-resolution vascular imaging. *Nature letter*, 527(7579):499–502, 2015.

[210] B. Cox and P. Beard. Imaging techniques: Super-resolution ultrasound. *Nature News and Views*, 527(7579):451–452, 2015.

[211] D.M. Alloin and J.M. Mariotti. *Adaptive optics for astronomy*. British Crown, 1994.

[212] M. Kang, C. Yang, and J. Wu. Reconstruction of Uncompleted Frequency Spectrum Images Based on Fourier Telescopy. In *Proc. SPIE*, volume 74954G-7, [Online] Available:10.1117/12.832585, October 2009.

[213] B. L. Ellerbroek. First-order performance evaluation of adaptive-optics systems for atmospheric-turbulence compensation in extended-field-of-view astronomical telescopes. *J. Opt. Soc. Am.*, 11(2):783–805, 1994.

[214] T. Fusco, J.-M. Conan, G. Rousset, L. M. Mugnier, and V. Michau. Optimal wave-front reconstruction strategies for multiconjugate adaptive optics. *J. Opt. Soc. Am.*, 18(10):2527–2538, 2001.

[215] D. A. Ausherman, A. Kozma, J. L. Walker, H. M. Jones, and E. C. Poggio. Developments in radar imaging. *IEEE Trans. on Aero. and Elec. Sys.*, AES-20(4):363–400, July 1984.

[216] A. Ferretti, C. Prati, and F. Rocca. Permanent scatterers in SAR interferometry. *IEEE Trans. on Geo. and Rem. Sen.*, 39(1):8–20, Jan 2001.

[217] A. Moreira, P. Prats-Iraola, M. Younis, G. Krieger, I. Hajnsek, and K. P. Papathanassiou. A tutorial on synthetic aperture radar. *IEEE Geo. and Rem. Sens. Mag.*, 1(1):6–43, Mar 2013.

[218] Inc. EDAN Diagnostics. Advanced technologies: Spatial compounding (a web resource). `http://www.edan.com.cn/html/EN/products/ultrasound/CDUltrasound/201601/292173.html`. San Diego, CA, USA.